



This work is protected by copyright and other intellectual property rights and duplication or sale of all or part is not permitted, except that material may be duplicated by you for research, private study, criticism/review or educational purposes. Electronic or print copies are for your own personal, non-commercial use and shall not be passed to any other individual. No quotation may be published without proper acknowledgement. For any other use, or to quote extensively from the work, permission must be obtained from the copyright holder/s.



SUBMISSION OF THESIS FOR A RESEARCH DEGREE

Part I. DECLARATION by the candidate for a research degree. To be bound in the thesis

Degree for which thesis being submitted: **PhD in Physics**

Title of thesis: **“Evolution of electron capture supernova progenitors: new models, improved nuclear physics and hydrodynamic mixing uncertainties”**

This thesis contains confidential information and is subject to the protocol set down for the submission and examination of such a thesis.

NO

Date of submission: **09/06/14** Original registration date: **01/10/10**
(Date of submission must comply with Regulation 2D)

Name of candidate: **Samuel William Jones**

Research Institute: **EPSAM** Name of Lead Supervisor: **Dr. Raphael Hirschi**

I certify that:

- (a) The thesis being submitted for examination is my own account of my own research
- (b) My research has been conducted ethically. Where relevant a letter from the approving body confirming that ethical approval has been given has been bound in the thesis as an Annex
- (c) The data and results presented are the genuine data and results actually obtained by me during the conduct of the research
- (d) Where I have drawn on the work, ideas and results of others this has been appropriately acknowledged in the thesis
- (e) Where any collaboration has taken place with one or more other researchers, I have included within an ‘Acknowledgments’ section in the thesis a clear statement of their contributions, in line with the relevant statement in the Code of Practice (see Note overleaf).
- (f) The greater portion of the work described in the thesis has been undertaken subsequent to my registration for the higher degree for which I am submitting for examination
- (g) Where part of the work described in the thesis has previously been incorporated in another thesis submitted by me for a higher degree (if any), this has been identified and acknowledged in the thesis
- (h) The thesis submitted is within the required word limit as specified in the Regulations

Total words in submitted thesis (including text and footnotes, but excluding references and appendices) **37794**

Signature of candidate  Date **07/07/14**

Note
Extract from Code of Practice: If the research degree is set within a broader programme of work involving a group of investigators – particularly if this programme of work predates the candidate’s registration – the candidate should provide an explicit statement (in an ‘Acknowledgments’ section) of the respective roles of the candidate and these other individuals in relevant aspects of the work reported in the thesis. For example, it should make clear, where relevant, the candidate’s role in designing the study, developing data collection instruments, collecting primary data, analysing such data, and formulating conclusions from the analysis. Others involved in these aspects of the research should be named, and their contributions relative to that of the candidate should be specified (*this does not apply to the ordinary supervision, only if the supervisor or supervisory team has had greater than usual involvement*).

**Evolution of electron capture
supernova progenitors: new models,
improved nuclear physics and
hydrodynamic mixing uncertainties**

Samuel Jones

PhD in Physics

Keele University

October 2014

Abstract

Electron capture supernovae (EC-SNe) are the deaths of approximately 8–10 M_{\odot} stars. In this thesis, the evolution of 8–12 M_{\odot} stars is calculated using the MESA stellar evolution code. The aims of this thesis are to produce the most advanced and up-to-date progenitor models for electron capture supernovae (EC-SNe) and to study the behaviour of stars across the transition mass range between AGB stars and massive stars. These new stellar models will be the first of their kind since the 1980s and highlight new computational successes and persisting challenges in the field of stellar physics.

The thermal pulse phase of an 8.75 M_{\odot} super-AGB star is computed in its entirety from the end of the second dredge-up (2DUP) until the activation of electron captures by ^{20}Ne , which triggers its collapse. The most massive progenitors of electron capture supernovae are found to ignite neon and oxygen burning off-centre—a characteristic shared with the lowest mass iron core-collapse supernova (FeCCSN) progenitors. The behaviour of this shell burning is shown to be very sensitive to mixing across the formal convective boundary, where several types of instability are known to operate.

The evolution of the degenerate cores that are produced within 8–10 M_{\odot} stars following carbon burning is sensitive to changes in the electron fraction. Electron capture and β -decay reactions of nuclear species produced in the stellar core both modify the electron fraction and provide periods of strong cooling (the URCA process). Tabulated rates for these reactions available at the time of this work are too poorly resolved to accurately represent the physics. New calculations of the weak reaction rates are hence performed by nuclear physicists in a separate work motivated by the new results in this thesis. These rates are incorporated into the stellar models, where their impact is studied.

Acknowledgements

First and foremost, I would like to thank my supervisor Dr. Raphael Hirschi for his overwhelming enthusiasm, encouragement and patience. Thank you for the many interesting discussions about stars, supernovae and nucleosynthesis (amongst other things), for tolerating my eccentricities with a smile and for giving me so many opportunities to travel around the world to present my results and learn from others in the field. It has been an incredible three years.

I would also like to thank Ken'ichi Nomoto, Falk Herwig and Gabriel Martínez-Pinedo for hosting me on a number of occasions and for their kind hospitality during collaborative visits. I certainly learned a great deal during my visits to Tokyo, Victoria and Darmstadt and have many fond memories from Kyoto and Nikko, Waldemar-Peterson Haus, NuGrid collaboration meetings and discussing hydrodynamics late into the night.

I owe an enormous amount to Bill Paxton for creating and maintaining the stellar evolution code MESA, Michael Bertolli for his contribution to our weak reaction rate code, Calvin Johnson for providing nuclear physics data from his nuclear shell model code. Thanks to Marco Pignatari for his huge contribution to the NuGrid collaboration, and to Michael Bennett, Urs Frischknecht, Gyril Georgy, Nobuya Nishimura, Andréa Cristini, and everyone at TU Darmstadt for many interesting, useful discussions about stellar evolution, supernovae and nucleosynthesis.

In this Thesis the core of Chapter 3 has been published in Jones et al. (2013), *The Astrophysical Journal*, 772, 150, on which there are a total of twelve authors. Although I have calculated all of the stellar models (using the MESA code), created the figures and written the manuscript—for the aforementioned publication and of course, for this Thesis—I would like to thank each and every one of my co-authors. The eleven co-authors provided advice, suggestions for the structure of the paper and critique of the manuscript. I would also like to thank Dr. Christopher Tout—the referee of Jones et al. (2013)—for his input, without which the manuscript would not have reached

such a high standard. I am grateful in particular to Tobias Fischer, who performed a mapping between my progenitor model and the AGILE-BOLTZTRAN supernova code and followed the resulting collapse and explosion (this is an active work in progress, the results of which are not presented here and have not yet been published elsewhere; they are referred to as (Fischer 2014) in this Thesis). Chapter 4 of this Thesis describes the method for calculating weak interaction rates. It also presents the results of stellar models that have been computed using new weak reaction rates calculated using such a method. The rates that were used for the URCA process have been calculated for this work by Hiroshi Toki and Toshio Suzuki and published in Toki et al. (2013), *Physical Reviews C*, 88(1), 015806; the rates for the $A = 20$ and 24 nuclei were calculated for this work by Gabriel Martínez-Pinedo and Yi-Hua Lam using some transition strengths that were experimentally determined by Remco Zegers and Chris Sullivan, and have been submitted to *Physical Reviews* (Martínez-Pinedo et al. 2014) and made available on ArXiv, 1402.0793. During my PhD, I have also written a code to calculate weak interaction rates from nuclear transition strengths together with Michael Bertolli, with whom the work was shared roughly half and half; the transition strengths used by that code were calculated by Calvin Johnson. Although no results from the work with Michael Bertolli and Calvin Johnson are presented in this Thesis, it is a justification of the level of detail in section 4.2.

Thank you to my girlfriend, Katerina, and to my parents, sister and grandparents for their endless support stretching well beyond the three years of my Ph. D. Thanks to Tom Duncan and Simon Clarke for their hard work and perseverance both in and outside of the studio and for keeping me sane.

Samuel Jones, Keele Astrophysics Group

9 June 2014

Contents

Abstract	iv
Acknowledgements	v
1 Introduction	1
1.1 Stellar evolution: an overview	2
Low and intermediate mass stars.	4
Massive stars.	6
1.2 8–12 M_{\odot} stars	8
1.2.1 What are super-AGB stars?	8
1.2.2 The importance of understanding 8–12 M_{\odot} stars	11
1.2.3 Challenges and status of the field	23
1.3 The role of weak interactions in astrophysics	31
(i) The URCA process.	31
(ii) The neutron excess in advanced burning stages.	33
(iii) Collapse of the Fe-core and the supernova explosion.	34
(iv) Neutron-capture nucleosynthesis.	35
1.4 Mixing in the stellar interior	35
1.5 Thesis Outline	43
2 Numerical Modelling of stars and the MESA code	44
2.1 Key equations	44
2.2 Convection	48
2.2.1 Mixing length theory	51
2.2.2 Overshooting and convective boundary mixing	55
2.3 The nuclear reaction network and composition evolution	57
2.4 Essential physical and empirical data	59
2.4.1 EOS and opacities	60
2.4.2 Nuclear reaction rates	64
2.4.3 Mass loss	65
2.4.4 Neutrino energy losses	67
2.5 Modelling assumptions in this work	69
3 Models of 8–12 M_{\odot} stars	74
3.1 Evolution and fates	74
3.1.1 Evolution to the end of carbon burning	74
3.1.2 Late evolution of the 8.2, 8.7 and 8.75 M_{\odot} (super-AGB) models	85
3.1.3 Late evolution of the 8.8, 9.5 and 12.0 M_{\odot} (massive star) models	94
3.2 Neon-oxygen flashes and flame	100
3.2.1 Advance of the burning shell towards the stellar centre	103
3.2.2 Uncertainties due to mixing	106

Summary	115
3.3 Progenitor structure and importance for supernova explosions	118
3.4 Discussion and concluding remarks	123
4 Calculation, implementation and impact of new weak interaction rates	127
4.1 Case for the calculation of new weak reaction rates	128
4.1.1 What is involved?	128
4.1.2 The problem with currently available rates	130
4.1.3 Proposed solutions	133
4.2 Rate Calculations	136
4.2.1 General form	136
4.2.2 Phase space integrals	138
4.2.3 Nuclear Physics input: USDB shell model	138
4.2.4 Neutrino fluxes and γ -ray heating rates	139
4.2.5 Screening of weak reactions	140
4.3 Implementation in a stellar evolution code (MESA)	141
4.3.1 A quick reality check	142
4.3.2 Implementing weak reactions into the stellar evolution code	143
4.4 Impact of new weak reaction rates on the stellar models	148
4.4.1 URCA rates	148
4.4.2 $A = 20$ and 24 rates	157
4.4.2.1 Different behaviour from Nuclear physics	157
4.4.2.2 Results of the new calculations	163
5 Conclusions and future work	168
Publications	175
5.1 Refereed publications	175
5.2 Other Publications	175
5.3 Publications in preparation for submission to refereed journals	176
5.4 Talks	176
5.5 Conference Posters	177
Bibliography	178

List of Figures

1.1	Classification of stars by initial mass	4
1.2	Thermal pulses of AGB and super-AGB stars	6
1.3	Kippenhahn diagram showing the evolution of a $15 M_{\odot}$ star	7
1.4	The carbon burning flame of super-AGB stars	9
1.5	Illustrative Kippenhahn diagram showing the evolution of a super-AGB star towards an electron capture supernova	10
1.6	Cumulative mass distribution of core collapse supernova progenitors observed in M31	12
1.7	Distribution of neutron star spin periods in high-mass X-ray binary systems	13
1.8	The mass distribution of neutron stars	15
1.9	Abundance anti-correlations in metal-poor stars	17
1.10	Theoretical explosive yields for electron capture supernovae	18
1.11	Initial mass limits for the type II-P supernovae progenitors with direct detections	20
1.12	Association of various supernova types with emission typical of star forming regions	22
1.13	The transition masses as a function of initial metallicity	27
1.14	Hydrodynamical instabilities encountered in the stellar interior	39
2.1	Regions in the $\log \rho - \log T$ plane covered by the MESA EOS module .	62
2.2	Regions in the $\log \rho - \log T$ plane covered by the MESA opacity module	63
2.3	Dominant mechanisms of neutrino production across the $\rho - T$ plane .	68
2.4	The nuclear reaction network used in these calculations	73
3.1	Evolution of all the models in the Hertzsprung-Russell diagram	76
3.2	Effective temperature as a function of central helium abundance	78
3.3	Divergence of the models following C-burning in the $\log_{10}(\rho_c) - \log_{10}(T_c)$ plane	79
3.4	The dredge-out phenomenon in the $8.75 M_{\odot}$ model	82
3.5	Kippenhahn diagrams for the $8-12 M_{\odot}$ models	84
3.6	Impact of convective boundary mixing on the efficiency of the third dredge-up	87
3.7	Critical relationship between mass loss and core growth rate for the $8.7 M_{\odot}$ model	89
3.8	Radial profiles of the electron fraction, Y_e , in the progenitor structure of the 8.8 and $8.75 M_{\odot}$ models	96
3.9	Impact of the URCA process on the evolution of the $8.8 M_{\odot}$ model in the central density-temperature ($\rho_c - T_c$) plane	97

3.10	Rates of key neon- and oxygen-burning reactions as functions of temperature from the REACLIB compilation	101
3.11	Radial profiles with respect to mass co-ordinate of the radiative, conductive and total opacities following the extinction of the final neon-oxygen convective flash episode	104
3.12	The thermal adjustment timescale profile below the neon-burning shell in the $8.8 M_{\odot}$ model	107
3.13	Central density–temperature evolution of the $8.8 M_{\odot}$ model assuming different parameterisations of the convective boundary mixing	109
3.14	Diffusion coefficient profiles against mass coordinate during the second neon flash event in the $8.8 M_{\odot}$ model	110
3.15	Energy production from key neon- and oxygen-burning reactions during the peak of the first neon shell flash in the $8.8 M_{\odot}$ model with different CBM parameterisations	114
3.16	Density profiles as a function of mass coordinate and radius	120
4.1	$\lambda(^{24}\text{Mg} + e^-)$ at $T = 4 \times 10^8$ K from the compilations of Oda et al. (1994) and Takahara et al. (1989)	131
4.2	Reaction rates for $^{24}\text{Mg}(e^-, \nu)^{24}\text{Na}$ from the Oda et al. (1994) compilation as a function of electron density for various temperatures (T_9/GK)	132
4.3	$\log_{10}\langle ft \rangle$ values for the electron capture rates of ^{24}Mg and ^{20}Ne using the formalism of Fuller, Fowler & Newman (1985) at $T_9 = 0.7$	135
4.4	Schematic diagram illustrating the energetics of electron capture from Miyaji et al. (1980)	144
4.5	Evolution of the $8.8 M_{\odot}$ model in the $\rho_c - T_c$ plane along with the central abundances (right axis) of the key URCA process isotopes	149
4.6	^{25}Mg electron capture rate (top left panel) and ^{25}Na beta decay rate (top right panel) at $T = 4 \times 10^8$ K from the compilation of Oda et al. (1994) and the new calculation by Toki et al. (2013)	150
4.7	Product of electron-capture and β -decay rates for $A=23, 25$ and 27 (solid lines) using the newly calculated rates of Toki et al. (2013) including Coulomb corrections	152
4.8	Product of electron-capture and β -decay rates for $A=23, 25$ and 27 (solid lines) using the rates of Oda et al. (1994)	154
4.9	Central evolution of the failed massive stars at 3 metallicities ($Z = 0.014, 0.001$ and 10^{-5}) governed by the URCA process	155
4.10	Product of electron-capture and β -decay rates for $A = 20$ and $A = 24$ using the newly calculated rates of Martínez-Pinedo et al. (in prep.) including experimentally determined GT transition strengths	158
4.11	Binding energy per nucleon (MeV) as a function of proton number Z for $A = 23$ nuclei (odd-even or even-odd) calculated using the expression from the semi-empirical mass formula	161

4.12	Binding energy per nucleon (MeV) as a function of proton number Z for $A = 24$ nuclei (odd-odd or even-even) calculated using the expression from the semi-empirical mass formula	162
4.13	Late evolution of the failed massive star (FMS) models at three metallicities ($Z = 0.014, 10^{-3}$ and 10^{-5}) using the rates of Oda et al. (1994) and Martínez-Pinedo et al. (in prep)	165

List of Tables

3.1	Key properties of all six models	93
-----	--	----

1 Introduction

Stars and supernovae are responsible for the creation of the chemical elements (Burbridge et al. 1957). The majority of our own solar system is comprised of material produced or released in stellar explosions. In order to trace the evolution of the solar system back to its formation requires a detailed knowledge of the feedback of stars into the interstellar medium via supernovae.

The study of stars and supernovae involves several physical disciplines: thermodynamics, nuclear physics, fluid dynamics and magnetism. This makes them excellent benchmarks by which to test the current understanding of many physical fields and their interaction.

Exotic compact objects such as neutron stars and black holes are the remains of stars following a supernova explosion (see, e.g., Heger et al. 2003). These objects, the key components of X-ray binary systems being observed with such space-based missions as Chandra and XMM-Newton, still pose several challenging questions about the physics of extreme matter. Furthering our understanding of their formation will provide constraints on the properties of fundamental physics. There are also cosmological implications of supernovae. Supernova observations have, for example, recently provided evidence for the accelerating expansion of the universe (Riess et al. 1998).

In our present age of ever advancing technology, it is hoped that the first gravitational wave detections will be made when the next generation of ground (e.g. Advanced LIGO, Advanced Virgo) and space (LISA, DECIGO) interferometers and other facilities (e.g. MiniGRAIL and AURIGA) become fully operational. Until now, only the electromagnetic signals and a handful of neutrinos (Hirata et al. 1987; Bionta et al. 1987) from objects outside of our solar system had been detectable. These instruments will, however, be in their infancy and will only be able to detect ‘large’ perturbations in the gravitational field. Such signals are expected to be produced by supernovae and compact objects, providing an excellent opportunity to study further their complex behaviour. Neutrinos are also produced in abundance during the collapse of massive

stars and, as alluded to above, using instruments currently in development (IceCube, Super-Kamiokande), one hopes to be able to learn more about supernovae and their progenitors from neutrinos thanks to the enhancement of the neutrino detection rate from these advanced instruments.

1.1 Stellar evolution: an overview

Stars are important to all areas of astrophysics: hosting planets; chemically enriching the ISM and galaxies via winds and supernovae; contained in clusters, galaxies and galaxy clusters and responsible for the creation of almost all of the chemical elements. To fully understand the link between these phenomena and stars requires knowledge of stellar evolution.

The goal of stellar modelling is to accurately predict the structural and chemical evolution of stars. Beginning from some first principles in physics—mass conservation, energy conservation, hydrostatic equilibrium and energy transport—models can be calculated and the results compared to observations. Comparison with observations provides constraints for those models and informs their refinement. At present, most of the observational data (to which models could be compared) describe the conditions only at the surfaces of stars, e.g. luminosities, temperatures, gravitational field strengths, rotational velocities and chemical compositions. Thus, the predictions made by stellar models about the interiors of stars can, in general, only be validated if the predictions made about the surface are directly affected. In some exceptional cases—for example, in various stellar explosions or neutrino emission from the Sun—the stars expose a glimpse their interiors and the models are able to be validated in other ways¹.

During the 20th century, sophisticated theories of stellar structure (e.g. Eddington 1926; Chandrasekhar 1939) were fast emerging and were already able to account for many features of the observational data. From the principles of thermodynamics and

¹Modern developments in asteroseismology are also providing the opportunity to observe more directly the behaviour of the interior, e.g. convective core sizes.

Newtonian gravity, it was already understood that there must be some energy source deep within the star that could provide enough energy to the stellar material for it to balance its self-gravity with an outward pressure force, but a good theory describing this energy source was lacking. Hans Bethe proposed the first complete description of the proton-proton chain. This is the method by which hydrogen is converted into helium in the Sun's deep interior. The work built on George Gamow's description of quantum tunnelling, explaining how protons could be fused into deuterium under the temperatures and densities inside the Sun. In stars more massive than the Sun where the temperatures are higher, hydrogen is burnt predominantly by the CNO cycle.

When all of the hydrogen in the core of the star has been converted into (mostly) ${}^4\text{He}$, there can be no more release of nuclear binding energy from hydrogen fusion reactions and the star instead contracts, providing the necessary pressure gradient for hydrostatic balance by releasing gravitational potential energy. This increases the core temperature (and, of course, density). If the core reaches high enough temperatures, nuclear binding energy can once again be released - this time from fusing helium into carbon.

Stars evolve through this interplay between gravity and nuclear burning, and different burning stages have different threshold temperatures. Contraction ensues until either the central temperature exceeds the threshold required to ignite a new fuel that is abundant in the core region, or until the pressure from degenerate electrons provide a large majority of the pressure support. In the latter scenario, the temperature will gradually decrease, preventing the ignition of further nuclear burning in the core. If this is the case, the star will eventually shed its hydrogen-rich envelope to expose the strongly degenerate, inert core—a white dwarf.

Stars are most broadly classified by initial mass according to their fate. In this way, if one assumes a statistical initial mass function (IMF) for some star forming region, or indeed an entire galaxy, then it is possible to calculate the chemical (Chiappini, Matteucci & Gratton 1997; Cescutti et al. 2007) and population (e.g. Belczynski et al. 2008; Toonen, Nelemans & Portegies Zwart 2012) evolution of that region to a large extent from tables (Schaller et al. 1992) or analytical fits (Hurley, Pols & Tout 2000) of

stellar evolution calculations. The lower section of Figure 1.1 shows the classification scheme for the three main categories: low mass, intermediate mass and high mass stars.

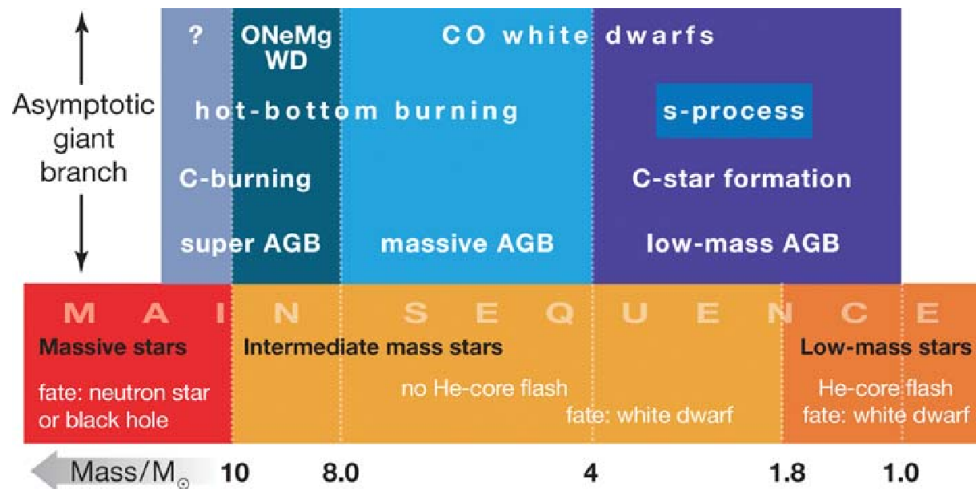


Figure 1.1: Classification of stars by (lower) main sequence mass and (upper) AGB mass from Herwig (2005). The limiting masses given at the bottom are approximate and depend upon the physical assumptions and metallicity. Also shown are the evolutionary fates and characterizing properties - note that the evolutionary fate of the super-AGB stars is still uncertain, marked in this figure with a question mark.

Low and intermediate mass stars. Although low and intermediate mass stars possess very similar evolutionary characteristics, their boundary is defined by the manner in which helium is ignited. Intermediate mass stars, having lower central density by virtue of their greater mass, will ignite helium centrally under non-degenerate conditions whereas low mass stars will contract further before the helium ignition temperature is reached, allowing for the onset of degeneracy. The pressure of the degenerate electrons is insensitive to the temperature and thus helium ignition in low mass stars is a violent event. The temperature increase caused by nuclear energy production accelerates the nuclear reaction rate—which has a temperature exponent of 40—until

the degeneracy is lifted and the core can expand (helium core flash, Sweigart & Gross 1978; see Mocák et al. 2009 for modern two and three dimensional simulations). When helium in the core of these stars is exhausted, envelope expansion associated with core contraction causes the star to move to the asymptotic giant branch (AGB). Further contraction is once again prevented by pressure from degenerate electrons in the CO core although nuclear burning continues in the helium and hydrogen shells above the core and a complex interplay between the two becomes the main evolutionary feature. Energy production from burning in the helium shell triggers an expansion of the outer layers causing them to cool and hydrogen burning is extinguished. When this helium burning episode is quenched an overall contraction re-ignites hydrogen in the shell above, the helium produced there is deposited onto the region where helium was burnt previously and at a critical point, helium shell burning is re-ignited and the cycle repeats (see Iben & Renzini 1983; Gallino et al. 1998 and Figure 1.2). There exists a thermal instability in the helium shell due to its thin profile causing a runaway process until the layer expands enough to alter the pressure or the energy is removed via convection; hence, this is called the *thermal pulse* (TP) cycle. During the thermal pulse cycle the envelope is losing mass to the interstellar medium and eventually the entire envelope may be lost. What remains at the end is a white dwarf (WD), the degenerate core of its parent star, its final chemical composition being predominantly a mixture of carbon and oxygen (CO-WD).

During the thermal pulse phase illustrated in figure 1.2, the envelope extends slightly down into the helium-rich layer as it expands (third dredge-up, 3DUP). This mixes protons into the region previously processed by helium burning and thus rich in carbon. If the conditions are right (i.e. an appropriate flux of protons), neutrons are released by the reaction chain $^{12}\text{C}(p, \gamma)^{13}\text{N}(\beta^+ \nu)^{13}\text{C}(\alpha, n)^{16}\text{O}$. The successive capturing of these neutrons builds the heavy elements (with $A > 60$), contributing to the main *s* process component.

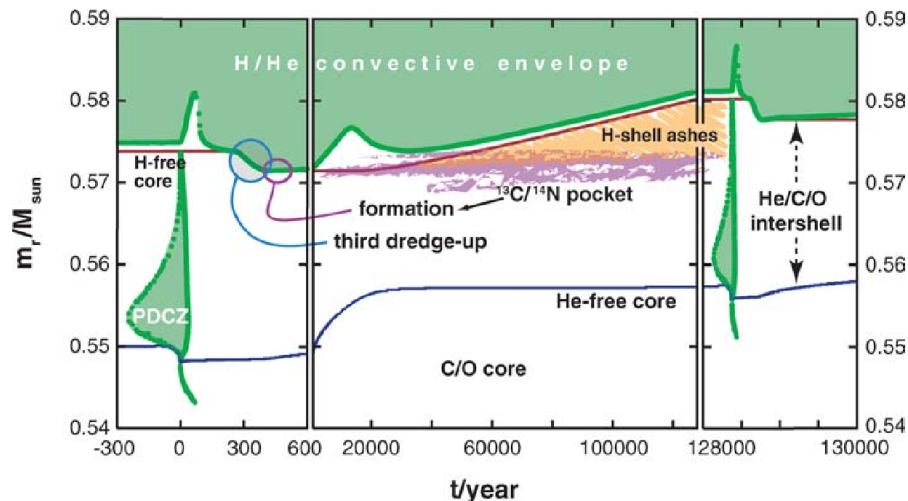


Figure 1.2: The structural profile during the 14th thermal pulse, the subsequent inter-pulse and the 15th thermal pulse for the $2M_{\odot}$ model from Herwig & Austin (2004). Green regions are convective, white are radiative. As the pulse-driven convective zone (PDCZ) develops, the envelope retracts periodically before deepening once more. After each thermal pulse, the envelope reaches down into the hydrogen-free layer in an event known as the third ‘dredge-up’ (3DUP). Figure taken from Herwig (2005).

Massive stars. Massive stars are those which possess enough gravitational potential energy to proceed through all possible burning stages (H, He, C, Ne, O, Si) and eventually reach core temperatures that enable the creation of iron-group elements from lighter elements (see, e.g., Chieffi, Limongi & Straniero 1998; Limongi, Straniero & Chieffi 2000; see Woosley, Heger & Weaver 2002a for a review; and for the effects of rotation, see Heger, Langer & Woosley 2000; Hirschi, Meynet & Maeder 2004; Chieffi & Limongi 2013). Silicon burning is unique to massive stars and proceeds quite differently to the other major burning stages², building heavier nuclei through a series of competing α -captures (α, γ) and photodisintegrations (γ, α). Even the simplest treatment of silicon burning must consider the abundances of ${}^4\text{He}$, ${}^{12}\text{C}$, ${}^{16}\text{O}$, ${}^{24}\text{Mg}$, ${}^{28}\text{Si}$, ${}^{32}\text{S}$, ${}^{36}\text{Ar}$, ${}^{40}\text{Ca}$, ${}^{44}\text{Ti}$, ${}^{48}\text{Cr}$, ${}^{52}\text{Fe}$ and ${}^{56}\text{Ni}$, through which the α -chains operate. Complicating

²Another exception here is neon burning, which will be discussed in Chapter 3.

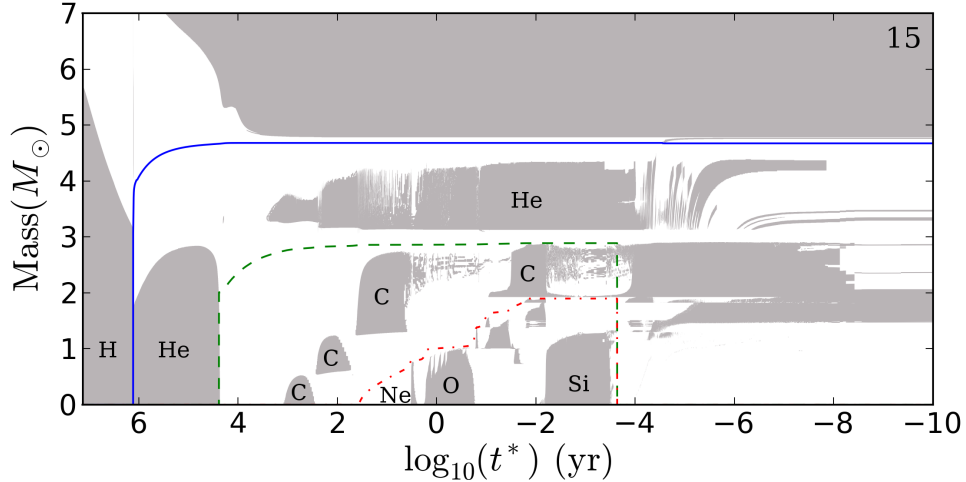


Figure 1.3: Convective structure evolution (‘Kippenhahn’) diagram of a $15 M_{\odot}$ massive star; illustrated is the interior $7 M_{\odot}$ of the star. t^* is the time until the iron core collapses (infall velocity exceeds 1000 km s^{-1}), grey regions are convective and white regions are radiative. Convective regions associated with the major burning stages are labelled by the fuel being burned at that time. The solid line marks the boundary of the helium core, the dashed line that of the CO core and the dot-dashed line that of the ONe core.

the picture of silicon burning further, the temperatures during silicon burning are in excess of 3 GK and many of the key reaction rates are extremely high. The iron cores produced during silicon burning are inert and as such can no longer produce energy to balance gravitational contraction. Furthermore, the pressure from degenerate electrons in the core is insufficient to balance the star’s weight and so collapse ensues. A Kippenhahn diagram illustrating the evolution of a $15 M_{\odot}$ star is shown in Figure 1.3.

During the helium and carbon burning phases in massive stars, neutrons are released via the reaction chain $^{14}\text{N}(\alpha, \gamma)^{18}\text{F}(\beta^+\nu)^{18}\text{O}(\alpha, \gamma)^{22}\text{Ne}(\alpha, n)^{25}\text{Mg}$ (Pignatari et al. 2010) and produce elements with $60 < A < 90$ (Raiteri et al. 1993). The solar abundance distribution in this atomic mass range is not produced exclusively by this process, the weak *s*-process component, but also from the main component in AGB stars (described earlier). Since the weak component relies on the presence of

^{14}N , the contribution from low metallicity stars should be small, however instabilities in differentially rotating massive stars have been shown to produce ^{14}N in a primary manner (Frischknecht, Hirschi & Thielemann 2012). This allows the weak s -process to operate at lower metallicities than previously thought and matches well with the observed abundances in galactic bulge stars (Chiappini et al. 2011).

The nucleosynthetic yields of massive stars are modified by the passing of the shock during the supernova explosion, and how the abundances are distributed throughout the core of the star by convection. Convection also modifies the entropy and electron fraction gradients, which have important consequences on the details of the supernova explosion and the properties of the forming neutron star.

1.2 8–12 M_{\odot} stars

The stellar mass range $8 \lesssim M_{\text{ini}}/M_{\odot} \lesssim 12$ corresponds to super-AGB stars and the most numerous massive stars. It is host to a variety of supernova progenitors and is therefore very important for galactic chemical evolution and stellar population studies.

1.2.1 What are super-AGB stars?

Super-AGB stars are the massive counterparts of AGB stars. Their evolution is characterized by the ignition of carbon fusion without progression to further nuclear burning stages (Ne, O, Si). The limiting masses (also called transition masses) for super-AGB stars are: M_{up} , the lowest initial mass for which carbon is ignited and M_{mas} , above which the star will burn through subsequent burning stages to produce an iron core and is therefore classified as a massive star. Classically, M_{up} and M_{mas} are about 9 and 11 M_{\odot} , respectively (Siess 2007), but depend upon the extent to which convective mixing operates beyond the formal boundary of the core (see section 1.4). Because super-AGB stars develop a degenerate core, carbon is ignited at an off-centre mass co-ordinate because of a temperature inversion (see section 3.1.2 for a detailed descrip-

tion). Ignition of a fuel in this way produces a flame front which propagates to the centre (Nomoto 1984; Garcia-Berro, Ritossa & Iben 1997; Siess 2007; see Figure 1.4), and the speed at which this flame travels will depend on the local degeneracy. More details of the propagation of nuclear flames are discussed in Chapter 3.

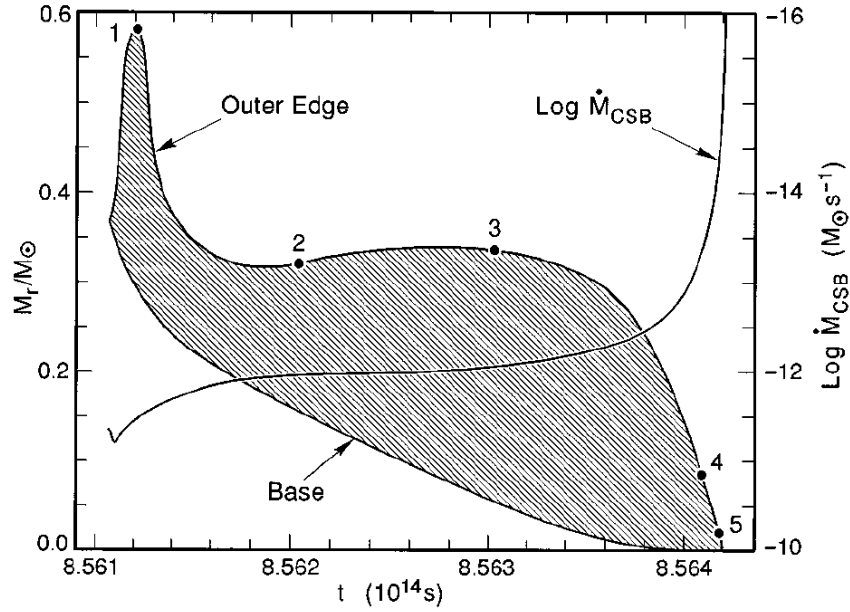


Figure 1.4: Propagation of a carbon-burning flame and its associated convective shell to the centre of a $9M_{\odot}$ model from Garcia-Berro, Ritossa & Iben (1997). $\dot{M}_{\text{CSB}}/M_{\odot}\text{s}^{-1}$ is the speed at which the flame (approximately the base of the convective shell) moves inwards during the second carbon burning episode.

Like their lower mass counterparts, super-AGB stars develop a thermal instability in their helium shell which leads to a helium shell flash, the recurrence of which indicates the beginning of a series of thermal pulses (TP). During this thermally pulsing phase (TP-SAGB) the envelope is losing mass and the products of nuclear burning in the helium shell are accumulating on the helium-free core. These two processes are in competition, the outcome of which will determine the fate of the star. Upon the loss of the envelope, nuclear production will cease and a white dwarf is left, however because its

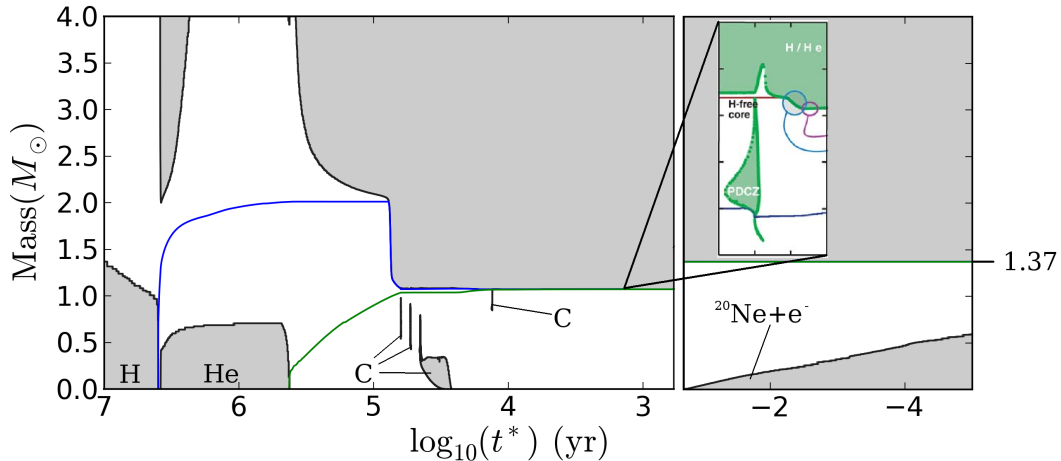


Figure 1.5: Convective structure evolution (‘Kippenhahn’) diagram of an $8 M_{\odot}$ super-AGB model; illustrated is the interior $4 M_{\odot}$ of the star. t^* is the time until the end of the calculation, grey regions are convective and white regions are radiative. The blue line marks the boundary of the H-depleted core, and the green line that of the He-depleted core. Following core helium burning, the star experiences a deep second dredge-up (at $\log_{10}(t^*) \approx 4.9$). Carbon ignites as flashes and later as a flame that propagates to the centre of the star (see section 1.2.3). The star evolves onto the TP-SAGB phase (inset panel). After several thousand of these thermal pulses, if the core reaches the critical mass (about $1.37 M_{\odot}$, Nomoto 1984) it will rapidly contract, reaching central densities exceeding the threshold for the $^{20}\text{Ne} + e^- \rightarrow ^{20}\text{F} + \nu_e$. While both panels show the result of an actual simulation, they come from two different simulations, and are arranged in this manner for illustrative purposes.

progenitor was sufficiently massive it has been processed by carbon burning and now has a chemical composition of primarily oxygen and neon (ONeWD). On the other hand, if the rate of nuclear burning in the helium shell allows the core to grow beyond the critical limit, $M_{\text{EC}} \approx 1.37 M_{\odot}$ (Nomoto 1984), electrons begin to be captured by isotopes in the core, removing electrons from the plasma. The removal of electrons alleviates the electron degeneracy pressure supporting the star and causes dynamical instability by which the star cannot readjust to balance the gravitational infall until the matter in the core has been compressed to nuclear density. When this density is reached in the core, the infalling material will have experienced nuclear transmutations due to

the rapid change in the thermodynamic environment (e.g. the ignition of an oxygen deflagration) and proceeds to explode and disrupt the structure of the progenitor star, leaving a neutron star remnant. This is an *electron capture* supernova (EC-SN, Miyaji et al. 1980). The pre-supernova evolution of a super-AGB star that will become an EC-SN is illustrated in Figure 1.5.

1.2.2 The importance of understanding 8–12 M_{\odot} stars

Electron capture supernovae (EC-SNe) are the deaths of approximately 8–10 M_{\odot} stars, and iron core-collapse supernovae (FeCCSNe) the deaths of most stars more massive than about 10 M_{\odot} (see Figure 1.1). Type II supernovae, such as the Crab and Vela supernovae and Cassiopeia A, are either electron-capture or core-collapse supernovae. The classical initial mass function of Salpeter (1955),

$$\frac{dN}{dM} \propto M^{-2.35},$$

is strongly weighted towards stars with lower masses and suggests that 8–12 solar mass stars should account for about half of all type II supernovae. A recent survey of supernova remnants in M31, the Andromeda galaxy, shows an even steeper (more bottom heavy) IMF than that of Salpeter (Jennings et al. 2012, see Figure 1.6).

Despite their significance, electron-capture supernovae and their progenitors are much less studied than iron core-collapse supernovae. One of the key reasons for this bias lies with the physical and computational complexities involved in modelling the evolution of the progenitor stars of electron-capture supernovae (see section 1.2.3). There are already a large number of observations that could potentially be explained by the occurrence of electron-capture supernovae, however the current status of electron-capture supernova theory is still catching up with observations due to these difficulties. These observations are summarised in this section along with some of the open questions that they present.

Knigge, Coe & Podsiadlowski (2011), observing X-ray binary systems (BeXs), found that they displayed a distinct bimodality in their orbital eccentricities and spin

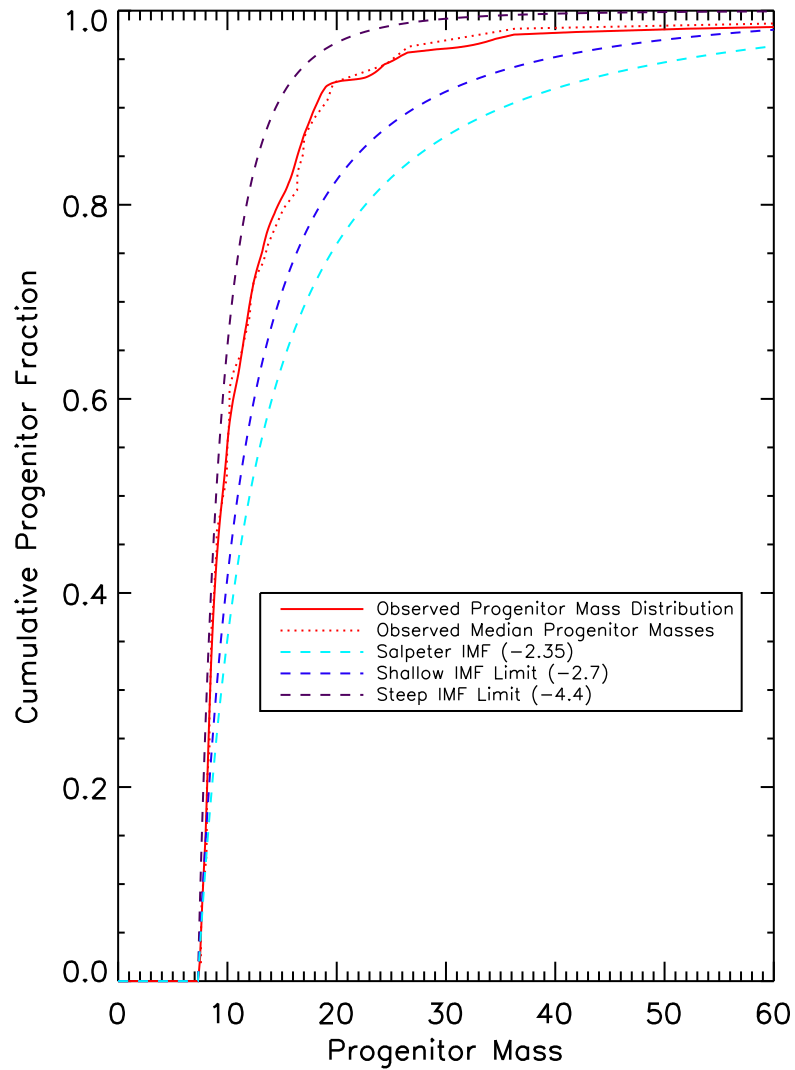


Figure 1.6: Observed cumulative progenitor distribution as observed in M31 by Jennings et al. (2012). The IMF appears to be steeper than that of Salpeter (1955) for high masses ($M \gtrsim 8M_{\odot}$). This statistical significance emphasises further the importance of studying stars in the mass range $8 - 12M_{\odot}$.

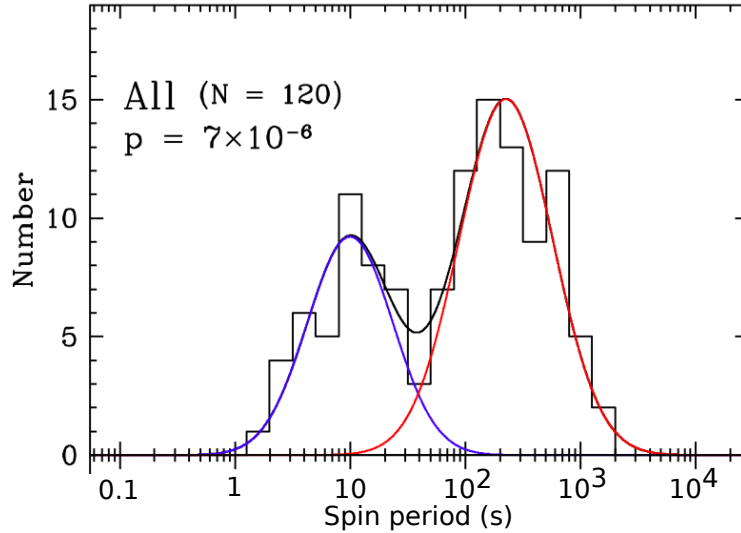


Figure 1.7: Distribution of neutron star spin periods in high-mass X-ray binary systems (Knigge, Coe & Podsiadlowski 2011).

periods (see Figure 1.7). The authors postulated that those neutron stars with lower orbital eccentricity are the remnants of electron-capture supernovae, and those with high orbital eccentricity are the remnants of core-collapse supernovae. The steeper density gradient in the EC-SN progenitors promotes a weaker, faster explosion in which asymmetries have less time to develop, giving the neutron star a weaker natal kick (Scheck et al. 2006, 2D; Wongwathanarat, Janka & Müller 2010, 3D) as suggested by Podsiadlowski et al. (2004). The two-dimensional EC-SN simulations of Wanaajo, Janka & Müller (2011), however, do show strong asymmetries and the details of the behaviour during the supernova explosion are still poorly understood. Mueller, Janka & Heger (2012) show that for low mass progenitors ($8.1 M_{\odot}$ in their study), the standing accretion shock instability (SASI) is not felt and hence large asymmetries may not persist in the explosion unless the progenitor star is sufficiently massive enough. A strong (unavoidable) caveat of all of the work on supernova theory is that the progenitor models with which their simulations begin are spherically symmetric. Thus, asymmetries are implicitly assumed to develop only during the bounce and explosion phase of

the supernova itself. Very recent work by Couch & Ott (2013) attempts to connect the explosion properties to progenitor asymmetries by introducing non-spherical 3D perturbations into 1D progenitor models. Indeed, some of the perturbed models yield successful explosions where the spherical models do not. This highlights the importance of asphericity in the progenitor models, for which it is desirable to have realistic predictions. Producing realistic 3D progenitor models for supernovae is a work actively in progress (see, e.g., Arnett & Meakin 2011).

Schwab, Podsiadlowski & Rappaport (2010) find a bimodality in the gravitational mass distribution of 14 well-measured (with accuracies better than about $0.025 M_{\odot}$) neutron stars (see Figure 1.8). The authors converted the measured masses into pre-collapse masses using a number of equations of state for neutron-star matter (since this EOS is still highly uncertain and remains a hot topic in astrophysics). The resulting peaks of the pre-collapse mass distribution were shown to be at about 1.37 and $1.48 M_{\odot}$. The mass of the neutron star that is formed in the supernova depends on the pre-supernova entropy structure, the explosion physics and whether or not material falls back onto the neutron star. There are still many uncertainties surrounding the pre-supernova – and in particular, the silicon-burning – evolution of massive stars that can affect the resulting neutron star mass. For example, if a silicon burning shell is active at the time where the iron core mass exceeds the Chandrasekhar limit, the core contracts and boosts energy production in the shell, causing an expansion (Timmes, Woosley & Weaver 1996). How the shell burning, and in particular convection during the late burning stages, behaves can make a significant difference to the iron core mass, and hence the mass of the neutron star formed in the subsequent explosion. To study the progenitor evolution of the $8\text{--}12 M_{\odot}$ stars is thus a much needed pursuit if one wants to constrain supernova theory, the nuclear equation of state and the understanding of the variety of compact objects.

The distribution of elemental abundances that is observed in the Sun (see, e.g., Asplund et al. 2009) is the result of many physical processes that have occurred in many different astrophysical sites. At present, the components of the distribution that are produced by the slow neutron-capture process (*s* process) in both low-mass and massive

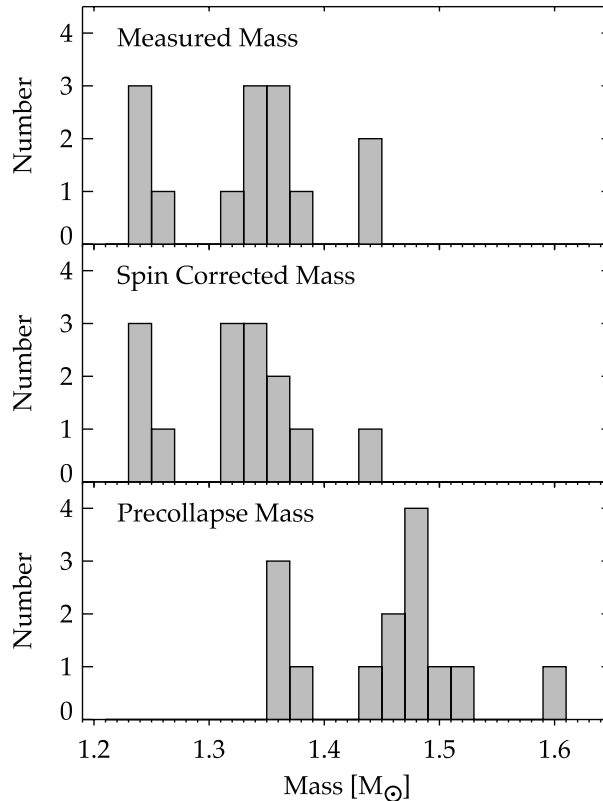


Figure 1.8: The neutron star mass distribution as observed by Schwab, Podsiadlowski & Rappaport (2010). There is a distinct bimodality in the distribution which is hypothesised to be the result of two neutron star formation mechanisms - electron capture and iron-core collapse supernovae. It is not clear whether the bimodality would persist once a larger sample size has been obtained.

stars are able to be reasonably well determined (see Käppeler et al. 2011 for a review), however there still remain large sections of the distribution that are inexplicable from the current picture. Anti-correlations in the observed abundances of metal-poor stars suggest that there are more than one site for heavy element production (Hansen et al. 2012; Figure 1.9), of which electron-capture supernovae likely play an important role. It

is known that the extreme physical conditions reached during the supernova explosion can drive the production of exotic nuclei, however there are still no robust quantitative results concerning the nucleosynthesis in electron-capture and core-collapse supernovae because of the uncertainties in the progenitor models and explosion physics. Recently, the r process signature in the solar abundance distribution has been shown to be reproduced by both the neutron star merger scenario (Rosswog et al. 2014) and some rare jet-driven supernovae of massive stars (Winteler et al. 2012).

The conditions that are experienced in the neutrino-driven wind during an EC-SN create a potential site for r -process nucleosynthesis, which is thought to be responsible for the production of half of the elements heavier than iron. Many recent studies of electron-capture supernovae (e.g. Ishimaru & Wanajo 1999; Wanajo et al. 2003; Ning, Qian & Meyer 2007; Wanajo et al. 2009; Wanajo, Janka & Müller 2011) model the collapse and associated explosive nucleosynthesis of stars that develop degenerate ONeMg cores. Ishimaru & Wanajo (1999) investigate the r -process via europium enrichment in galactic halo stars having a large $[\text{Eu}/\text{Fe}]$, highlighting the SNe from stars either in the mass range $8\text{--}10 M_{\odot}$ or $M \gtrsim 30 M_{\odot}$ as potential production sites. Wanajo et al. (2003) were able to produce r -process nucleosynthesis by artificially enhancing the shock-heating energy during the explosion; highly neutronised matter with an electron fraction (electrons per baryon) of $Y_e \approx 0.14$ was ejected, allowing for strong r -process nucleosynthesis. Ning, Qian & Meyer (2007) find that the steep density gradient in the surface layers of the core is responsible for a rapid expansion during the collapse of the core. This speed of the expansion causes the free nucleons, alpha particles and heavier nuclei to fall out of equilibrium and free nucleons in this state will facilitate the formation of seed nuclei with $A \sim 140$ (Meyer 2002). Other signatures in the yields of electron-capture supernovae are found by the 1-D collapse model of Wanajo et al. (2009), including a small amount of ^{56}Ni in comparison with core-collapse supernovae. Following this study, a 2-D hydrodynamic calculation was performed (Wanajo, Janka & Müller 2011), finding EC-SNe to be likely sources of Zn, Ge, As, Se, Br, Kr, Rb, Sr, Y and Zr, but r -process elements were not produced without an artificial reduction of the minimum Y_e in the simulation (see Figure 1.10). Assuming that EC-SNe

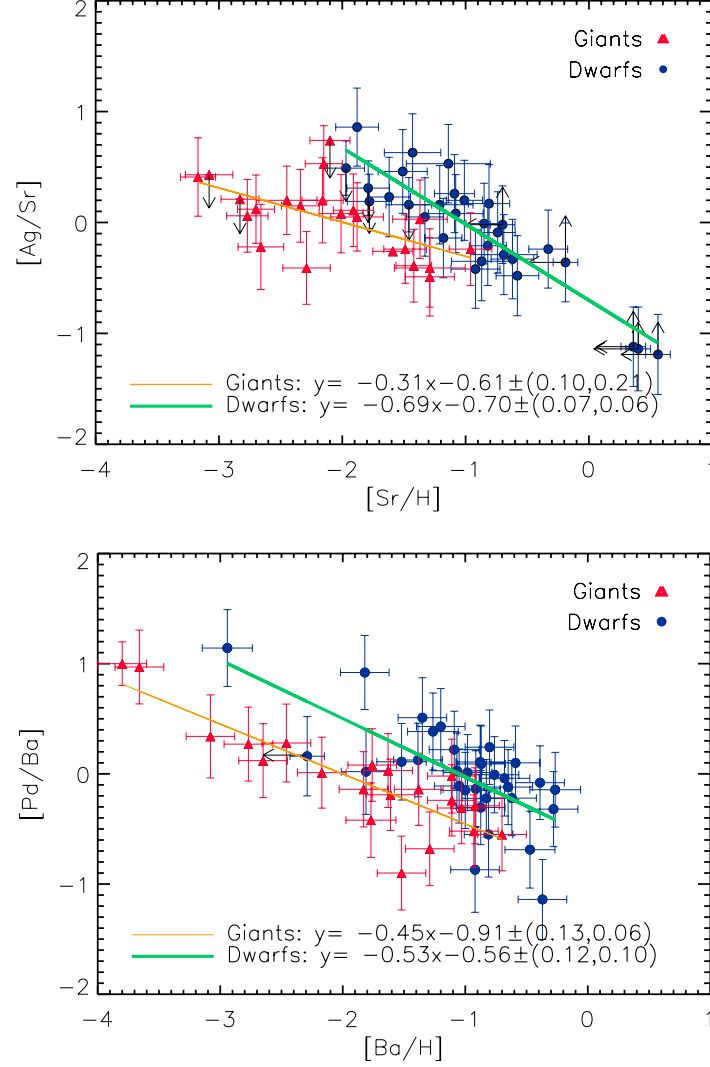


Figure 1.9: Observations of metal-poor stars show anti-correlations of Ag and Pd (silver and palladium) with Sr and Ba (strontium and barium). Ratios in parentheses are logarithmic abundance ratios with respect to the solar value, i.e. $[A/B] = \log_{10}(X_A/X_B) - \log_{10}(X_A/X_B)_{\odot}$, where X_A and X_B are the abundances of A and B . Strontium and barium are formed almost entirely in the weak and main s-process, respectively. If Ag were also formed primarily in the weak s-process, then the trend in the top panel would be flat. So too would the trend in the bottom panel, were Pd to be formed primarily in the main s-process along with Ba. These elements (Ag and Pd) also show anti-correlations with Eu (europium), which is an r-process element. The origins of elements in the region of Ag and Pd are thus not clear, and it has been postulated that electron-capture supernova explosions are a potential site for their production. Figure taken from Hansen et al. (2012)

are the sole contributors of ^{86}Kr in the galaxy, Wanajo et al. estimate that EC-SNe account for $\sim 4\%$ of all core collapse supernovae, which suggests that the progenitor channel for EC-SNe is relatively narrow given the statistical significance of stars in the $8\text{--}12 M_{\odot}$ mass range.

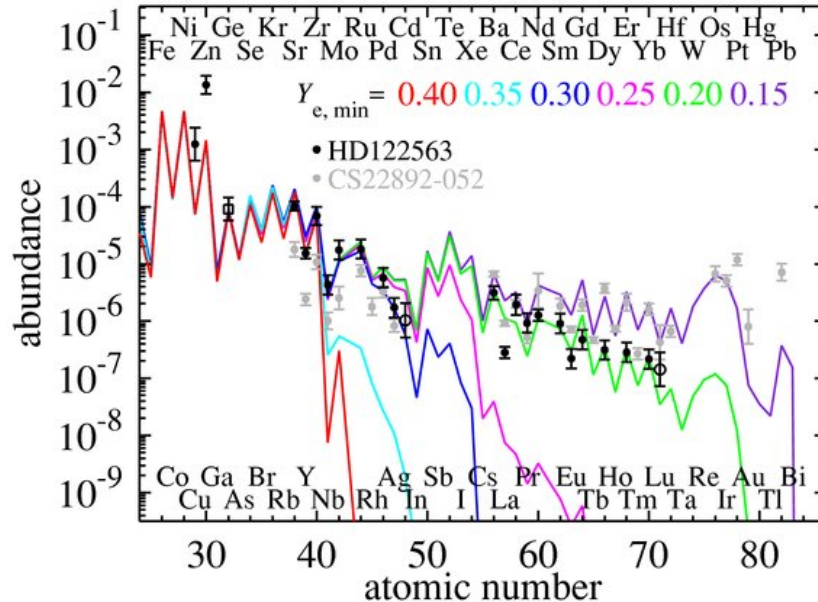


Figure 1.10: Abundance as a function of atomic mass number for the yields of electron-capture supernovae resulting from the 2D (axially symmetric) supernova simulation of Wanajo, Janka & Müller (2011). The minimum electron fraction found in the simulation was $Y_e = 0.4$ (red line), while the other lines show the results when the minimum Y_e is artificially reduced.

Although it is looking less likely that electron capture supernovae can contribute to the main r process, their nucleosynthesis yields are still important. For example, the production of ^{48}Ca in recent simulations of electron capture supernovae is high enough to explain the solar abundance – a long standing problem that was thought to be attributed to some rare type Ia events (Wanajo, Janka & Müller 2013a). From the same simulation, Wanajo, Janka & Müller (2013b) found ^{60}Fe to be produced during the EC-SN explosion. Quantitative comparisons to other calculations suggest that EC-SNe could contribute between 4 and 30% of the ^{60}Fe in the Milky Way.

Smartt 2009 (and references therein) have raised difficult questions for the stellar evolution community by providing direct detection data for supernova progenitors. For each transient detected that is thought to be a supernova, it is possible to search the Hubble Space Telescope’s archival data for the past few years, looking for a source at the precise coordinates where the transient was detected. If the source has now disappeared following the transient, then the supernova is confirmed and moreover, one now has photometric data for the star during the final years (or less) before it exploded. From the photometry, Smartt and collaborators determine the ZAMS mass of the progenitor star by comparing the derived luminosity and effective temperatures to those computed using stellar evolution codes. Figure 1.11 shows the derived ZAMS masses of type II-P supernova progenitors using the direct detection method and comparing the photometry to stellar models calculated using the Cambridge STARS code (Eggleton 1971). In this study, the lower limit for the initial mass of a type II-P progenitor is found to be $8.5_{-1.5}^{+1} M_{\odot}$. The problem is complicated for type II-P supernovae because the contribution could be from either CCSNe or EC-SNe. The progenitors of EC-SNe are super-AGB stars that undergo deep second dredge-up (see section 1.2.3 and Figure 1.5). During the second dredge-up of super-AGB stars, hydrogen is mixed down to temperatures that are not reached by the envelope in massive stars, and provides a large boost in the star’s luminosity. The relationship between the initial stellar mass and the luminosity at the pre-supernova stage is thus non-monotonic and a degeneracy arises. For example, models calculated using the stellar evolution code MESA show that for a given pre-supernova luminosity, the progenitor could be a massive star with $M_{\text{ZAMS}} \approx 15 M_{\odot}$ or a super-AGB star with $M_{\text{ZAMS}} \approx 8 M_{\odot}$.

It has already been suggested that the transients SN2008S, NGC300-OT2008 and M85-OT2006 are examples of EC-SNe (Smartt 2009; Botticella et al. 2009), but their nature has yet to be confirmed. Type IIP supernovae with low explosion energies and relatively small ^{56}Ni yield are generally thought to be either the EC-SNe of roughly $8 - 10 M_{\odot}$ stars or weak FeCCSNe of roughly $20 - 25 M_{\odot}$ stars whereby a black hole is formed and a large fraction of the ejecta falls back onto the remnant. Supernovae with the classification of type II_n-P are also electron capture supernova candidates.

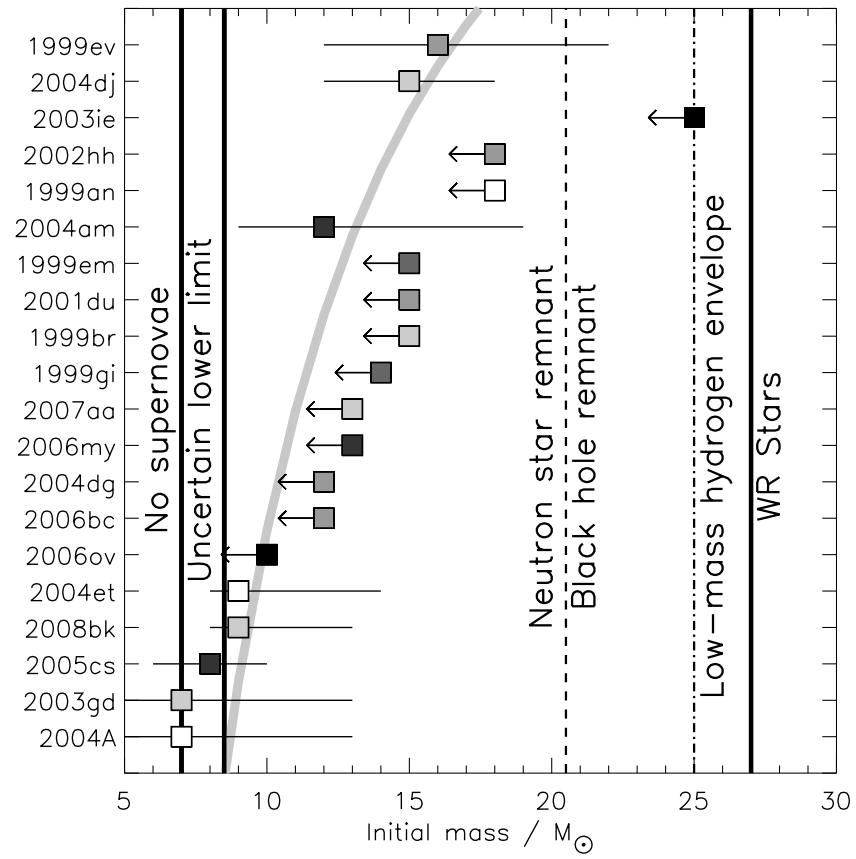


Figure 1.11: Initial mass limits for the type II-P supernovae progenitors with direct detections (Smartt et al. 2009).

They exhibit narrow (n) spectral features, indicating an interaction with slow-moving circumstellar material and a plateau (P) in the light-curve (Smith 2013). Indeed, if one assumes association of supernova locations with regions of H_α and UV emission (as indicators of star formation) to be a good indicator of the progenitor mass, the majority of type II_n supernovae would have progenitors in the mass range $8\text{--}12 M_\odot$ (Anderson et al. 2012; Figure 1.12). In addition, Anderson et al. find that a significant fraction of type II supernovae appear to arise from progenitor stars with $M_{\text{ini}} < 10M_\odot$ by the same method.

The white dwarfs that are produced during the deaths of super-AGB stars that do not develop cores of the critical mass for EC-SNe may be in binary configurations. Their accretion induced collapse (AIC; Nomoto & Kondo 1991) is triggered by growth of the accreting core up to the critical mass for electron captures by ^{20}Ne to be activated. Realistic white dwarf models can only be produced by simulating the evolution of super-AGB stars, adding to the growing list of reasons to accurately simulate $8\text{--}12 M_\odot$ stars. The AIC channel is potentially a contributor to the population of millisecond pulsars (MSPs), offering the unique scenario in which a neutron star is formed after being spun up due to angular momentum transfer from its donor companion (Hurley et al. 2010). It has been shown, however, that the strong vorticities encountered as a result of the deposition of angular momentum in SASI-driven explosions can produce rapidly rotating neutron star remnants (Blondin & Mezzacappa 2007). As mentioned earlier, Mueller, Janka & Heger (2012) show the SASI to be dominant in the core collapse supernovae of massive stars (a $23 M_\odot$ star in their study).

There are at present too many uncertainties involved in the simulated explosions, many of which are related to uncertainties in the progenitor models calculated by stellar physicists, and challenges in the progenitor modelling itself to be able to know the contribution of EC-SNe to GCE, stellar populations and supernovae with the currently available progenitors. In fact, all simulations of EC-SNe to date, with the exception of Ishimaru & Wanajo (1999), begin from the same classical pre-supernova model of Nomoto (1987). New progenitor models of electron-capture and low mass core-collapse supernovae are thus highly desirable.

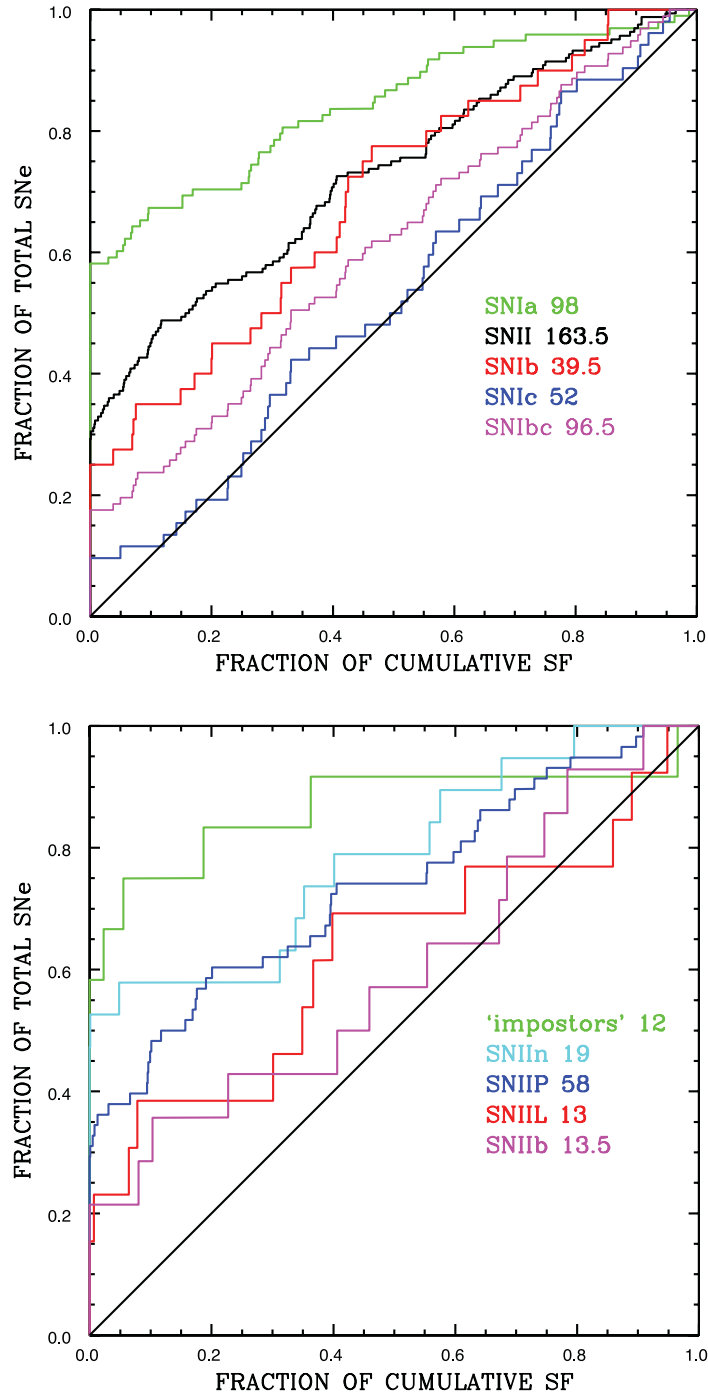


Figure 1.12: Association of various supernova types with emission typical of star-forming regions. The black lines show hypothetical, infinite size distributions that perfectly trace the emission. The further above and to the left a line lies, the less associated with a star-forming region that supernova type appears to be. Association with star-forming regions is an indicator of the progenitor mass, with more massive stars being more associated due to their shorter lifetimes.

1.2.3 Challenges and status of the field

Early numerical studies of stellar evolution in the (super-) AGB regime (e.g. Hofmeister, Kippenhahn & Weigert 1964; Kippenhahn, Thomas & Weigert 1965; Kippenhahn, Thomas & Weigert 1966) showed evolution towards central carbon ignition under relatively non-degenerate conditions, due to the lack of a more modern treatment of neutrino emission (see section 2.4.4). The effects of composition on the evolution of stars in the (super-) AGB mass range are investigated in detail by Becker & Iben (1979) and Becker & Iben (1980), formerly in the pre-AGB regime and latterly during the thermal pulses with emphasis on the surface abundance evolution and formation of planetary nebulae.

During the 1980s, several studies attempted to investigate the evolution of stars at the transition between massive stars that produce neutron stars and AGB stars that produce white dwarfs. These studies largely involved the computation of helium stars. The electron capture supernova phenomenon first peaked interest with the publication of a helium star model that evolved through to core collapse induced by electron captures (Miyaji et al. 1980). These calculations did not follow the thermal pulse phase in detail; instead the core was assumed to grow by steady shell burning. Further calculations were completed by Nomoto (1984) in which the hydrogen envelope was then fitted to the core, and the first progenitor models for EC-SNe were produced. Soon after, Hillebrandt, Nomoto & Wolff (1984) simulated the resulting collapse and explosion from the point at which the oxygen deflagration had processed the inner $0.32 M_{\odot}$ into NSE composition. Nomoto (1987), in his follow-up publication, presented details of the oxygen deflagration during the very late phases of the pre-supernova evolution of the helium star. Since this result has not been replicated to date, these models are still actively used as input for supernova simulations³ (e.g. Ning, Qian & Meyer 2007; Janka et al. 2008a; Wanajo, Janka & Müller 2011).

³Ritossa, García-Berro & Iben (1999) presented in great detail the evolution of a super-AGB star through this phase as part of a series of papers by the same group. However, models have never been used by the supernova community.

Habets (1986) also computed the evolution of helium stars for a range of initial masses, finding that those with $M = 3.2, 3.5$ and $4.0 M_{\odot}$ eventually ignited neon burning in the centre, while those with $M = 2.2, 2.5$ and $2.9 M_{\odot}$ experienced the ignition of neon off-centre. The off-centre ignition proceeded as a flash, as in the most massive model of Nomoto (1984), case 2.6, but both studies agreed that the flash did not induce dynamical effects. Woosley, Weaver & Taam (1980), on the other hand, evolving a full $10 M_{\odot}$ stellar model ($2.7 M_{\odot}$ helium core) from the main sequence (as opposed to pure helium stars) found that the neon flashes were sufficient to cause the ejection of the hydrogen envelope. Woosley and collaborators were also able to simulate the propagation of the neon-burning shell to the stellar centre, concluding that the model would become an FeCCSN. The model from Nomoto (1984), case 2.6, was not followed any further than the ignition of off-centre neon-burning shells, however subsequently, Nomoto & Hashimoto (1988) followed the propagation of the neon-burning shell in a helium star of $3.0 M_{\odot}$ (case 3.0) to the stellar centre, also concluding that the star would produce an Fe core before collapsing. The fact that the models of Woosley, Weaver & Taam (1980) eject the envelope about ten years before the explosion could lead to the production of a peculiar supernova exhibiting strong interaction with the circumstellar medium (CSM; Smith 2013), however Woosley et al. themselves strongly state that poor zoning in their calculations may have led to such a result. Timmes & Woosley (1992) and Timmes, Woosley & Taam (1994) studied in detail the properties of nuclear flames in degenerate compositions of C+O and O+Ne+Mg. In these studies it was proposed that, should neon and oxygen burning ignite off-centre in the core of a star significantly far from the centre, then it may compete with the contraction of the centre to determine its fate – EC-SN or FeCCSN.

A few years later, detailed simulations of a super-AGB star were published describing the characteristics of super-AGB evolution such as off-centre carbon ignition, deep second dredge-up and the convective flash and flame during carbon burning (Garcia-Berro & Iben 1994). Garcia-Berro & Iben (1994) also found $X(^{23}\text{Na})$ to be an order of magnitude higher in the core following carbon burning than in previous studies, and suggested that electron captures by this ^{23}Na could trigger the collapse

of the star. Ritossa, Garcia-Berro & Iben (1996), extending this body of work, found that the balanced-power condition assumed by Timmes, Woosley & Taam (1994) for conductively propagating flames (carbon-burning luminosity = neutrino luminosity) is not fulfilled, although the flame speed agreed well with those computed by Timmes and collaborators. The study also found that the $^{22}\text{Ne}(\alpha, n)^{25}\text{Mg}$ neutron source is activated in the thermal pulse (TP) cycle of super-AGB stars. Iben, Ritossa & Garcia-Berro (1997), simulating the evolution of a super-AGB star with slightly higher M_{ini} than in their previous studies, find the dredge-out phenomenon to occur. Luminosity produced via carbon burning, gravitational contraction and helium burning cause the development of a convection zone in the helium layer that grows in mass and merges with the descending base of the convective envelope. The final publication in this series of works studying super-AGB evolution simulated a star with still larger M_{ini} (Ritossa, García-Berro & Iben 1999). A description of the URCA process (see section 1.3) operating in the ONe core of their model was presented. The authors also find transient neon shell burning in the outer layers of the core. In this $11 M_{\odot}$ model, the core reaches $0.014 M_{\odot}$ shy of the critical mass for electron captures by ^{20}Ne to be activated (based on the calculations of Miyaji et al. 1980) and the model would evolve to an electron capture supernova as long as the envelope is not lost entirely.

Siess (2006) confirmed the characteristics of super-AGB evolution found in the body of work produced by the Spanish group discussed in the previous paragraph. The chemical signature of the second dredge-up was found to be indistinguishable from that of lower mass AGB stars that do not experience carbon burning. In the calculations with the STAREVOL code used by Siess, the carbon flame is treated by forcing adaptive fine zoning informed by the calculation of flame speeds in degenerate materials by Timmes & Woosley (1992) and Timmes, Woosley & Taam (1994). As mentioned earlier, Ritossa, Garcia-Berro & Iben (1996) found the steady state assumption of Timmes et al. to be invalid, however it is not clear that this is a strong caveat of the STAREVOL code since the flame speeds calculated by Ritossa et al. agree well with those found in Timmes et al.'s simulations. Siess (2007) extended his study to several lower metallicities. He shows that while the transition masses decrease when initial

metallicity is decreased, there exists a minimum point at $Z \approx 10^{-4}$ below which the transition masses begin to increase again with further reduction of the initial metallicity (Figure 1.13). This phenomenon was briefly explained by Tornambe & Chieffi (1986), and is caused by the final size of the helium core, which is determined by the size of the core during the main sequence and the strength of the H-burning shell thereafter. The reduction in the abundances of CNO elements with decreasing Z means that a star with a given initial mass must burn hydrogen with higher temperatures in order to provide supporting luminosities. The size of the convective hydrogen core is thus larger. Below the critical metallicity of $Z \approx 10^{-4}$, the CNO abundances are so low that energy generation from proton-proton chain reactions are the dominant source of luminosity. The convective core size thus has little dependence on the CNO abundances—and hence on the metallicity—while the proton-proton chain is providing the bulk of the energy. However, the energy generation in the hydrogen-burning shell is dominated by the CNO cycle for metallicities well below $Z = 10^{-4}$. This is because the temperature in the hydrogen-burning shell is consistently higher than in the convective hydrogen-burning core owing to the shell being thinner and radiative and to the star being more luminous during the shell-burning phase than on the main sequence. It is for this reason—that the temperature is high enough in the hydrogen-burning shell for the CNO cycle to dominate while in the convective hydrogen-burning core it was not—that the shell hydrogen-burning rate is a monotonic increasing function of the metallicity. Thus, for lower metallicity the helium (hydrogen-free) core grows more slowly and a larger initial mass is required to give the same final helium core mass.

Pumo & Siess (2007) briefly analysed a grid of models calculated with the STAREVOL code (Siess & Pumo 2006), predicting the electron capture supernova channel to be at most $1 M_{\odot}$ wide at any metallicity. In Pumo, Siess & Zappalà (2007), the authors revised the maximum width of the channel to $1.5 M_{\odot}$. The results of these studies are largely inconclusive and only highlight issues that are already well known: (i) with a fixed ratio of core growth to mass loss, the minimum initial mass to have an EC-SN shows non-linear behaviour with Z , the metallicity, (ii) the minimum initial mass for an EC-SN depends on the ratio of core growth rate to mass loss rate and

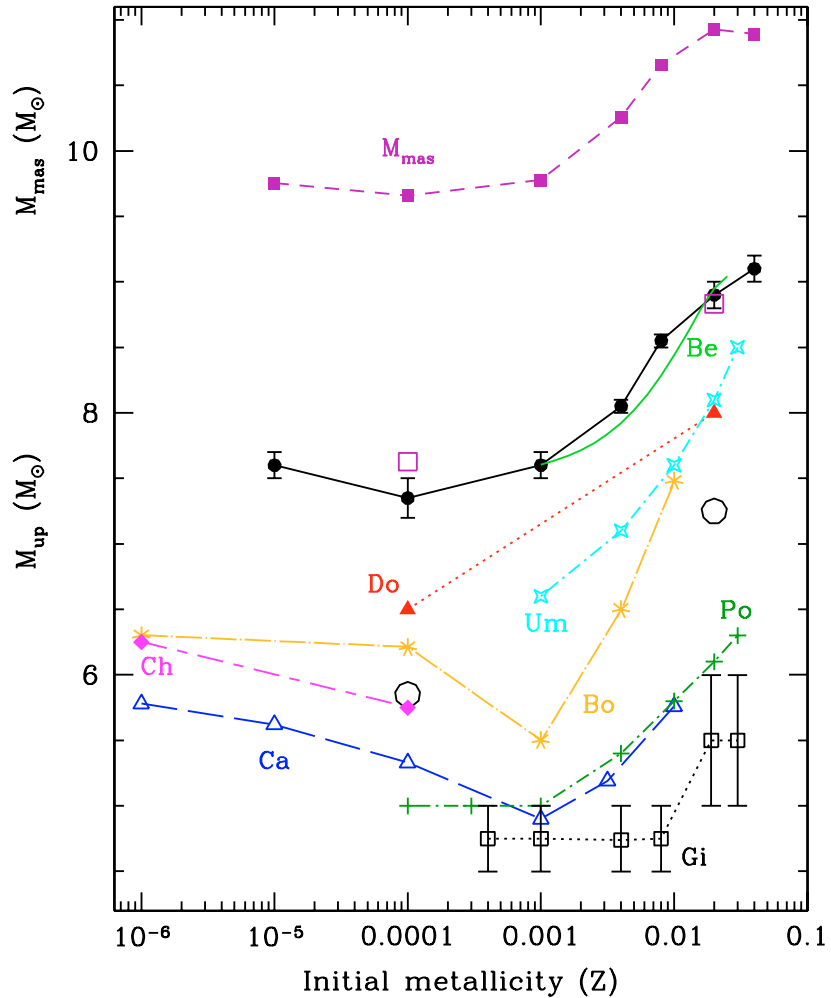


Figure 1.13: Transition masses M_{mas} (minimum initial mass for which neon is ignited; filled squares connected by a dashed line) and M_{up} (minimum initial mass for which carbon is ignited; dots connected by a solid line) as a function of Z taken from Siess (2007). The values of M_{mas} and M_{up} for models with overshooting are represented by big open squares and circles, respectively. Results from several other studies are included for comparison: Do (Dominguez et al. 1999), Um (Umeda et al. 1999), Bo (Bono et al. 2000), Ca (Cassisi & Castellani 1993), Ch (Tornambe & Chieffi 1986), Be (Becker & Iben 1979), Gi (Girardi et al. 2000), and Po (Pols et al. 1998).

(iii) the inclusion of overshooting shifts the transition masses. Poelarends et al. (2008), building on this work, computed super-AGB models with three stellar evolution codes (KEPLER, EVOL and STERN), having different physical treatments of mixing, up to the start of the thermal pulse regime. From this point, the models are evolved through the TP-SAGB phase for a few pulses with EVOL and STERN. The TP-SAGB phase for all the models was then computed synthetically, considering various mass loss rates from the literature and dredge-up efficiencies informed by the numerical TP-SAGB calculations. The final fates of a multitude of models were examined and the contribution of electron capture supernovae from super-AGB stars to all supernovae at solar metallicity was found to have an upper limit of 20%. If the mass loss rate is an increasing function of metallicity, then the EC-SN channel from super-AGB stars is expected to be wider at lower metallicities. Further discussion of this prediction is presented in section 3.1.2.

Efforts to better understand the evolution of super-AGB stars through numerical modelling are ongoing (see, e.g., Siess 2010; Doherty et al. 2010; Doherty et al. 2014) and it is now computationally possible to follow several thousands of thermal pulses in order to explore the complex evolution that can be compared with observations. The shortcomings of hydrostatic one dimensional modelling of the TP-AGB and TP-SAGB phase were historically (Wagenhuber & Weiss 1994) and recently (Lau et al. 2012) brought to the attention of stellar physicists. Wagenhuber & Weiss (1994) found that the conditions in the heavily extended hydrogen envelope may become such that the ionised hydrogen recombines. This introduces complications for stellar modelling because the opacity will be dominated by the recombined hydrogen and absorb radiation from the star. The stellar envelope becomes dynamically unstable, and although one dimensional hydrostatic modelling of this phase cannot properly treat the physics involved, the simulations published at the time suggested that this instability could lead to the complete ejection of the stellar envelope to form a planetary nebula with a white dwarf remnant at its centre. Wood & Faulkner (1986) found in their simulations (again, assuming hydrostatic equilibrium) that low-mass stars developing cores with masses greater than $0.86 M_{\odot}$ would eventually reach a helium shell flash producing lu-

minosities in excess of the Eddington luminosity. The pressure would be completely dominated by the radiation component and the envelope would become dynamically unstable and be ejected. Similarly, Lau et al. (2012) found high opacities due to the Fe content of the envelope to be a major contributor to the instability at solar metallicity. The treatment of convection is well known to be incomplete in stellar models (see 1.4) and by increasing the mixing length parameter, α (see section 2.2.1), the authors were able to reach convergence at this stage by enhancing the transport of energy by convection. However, this only deferred the instability for a few thermal pulses. Although a better theory of mixing in stars is required, it is a reasonable assumption to make that the mixing length parameter characterising the convection would be different for different evolutionary phases (Meakin & Arnett 2007).

A commonly-made assumption in super-AGB stellar modelling is to use a global rate for carbon fusion ($^{12}\text{C} + ^{12}\text{C}$) and calculate the abundances of its various products via branching ratios. For example, Doherty et al. (2010) in their study of super-AGB evolution model carbon burning by implicitly including many reactions to express the overall abundance evolution associated with this phase. Their final composite reaction (equation 1.1) allows the tracking of ^{20}Ne and ^{24}Mg abundances as a function of the ^{12}C and ^{16}O abundances alone.



This calculation is performed in instantaneously mixed regions using a one-zone approximation. As such, the effects of mixing at the edges of the convective zones are ignored, affecting the burning of unstable isotopes especially in the advanced stages. The final composition of the He-free core will also be compromised as a result of this assumption, burning more helium by $3\alpha \rightarrow ^{12}\text{C}$ and less by $^{12}\text{C}(\alpha, \gamma)^{16}\text{O}$.

In the first and only study to model the ‘entire’ TP-SAGB phase, Siess (2010) also assumes instantaneous mixing in convective zones, employing a one-zone treatment of nucleosynthesis in those regions using mass-averaged reaction rates. Although the calculation proceeded through 4000 thermal pulses requiring about 10^7 timesteps, the models still fail to converge during a sufficiently strong thermal pulse. Siess cites a

physical (rather than purely numerical) reason for the termination of the TP-SAGB phase, as discussed earlier in this section.

On the progress of linking supernovae and stellar models, for the transients SN2008ha and SN2008S Pumo et al. (2009) have proposed evidence for super-AGB progenitors exploding as electron capture supernovae. The authors show that for 2008ha, the progenitor could have spent a long time on the TP-SAGB phase, stripping almost its entire envelope before the SN stage, concluding that the ejecta would be ‘non-H-rich’ and show no CSM interaction. Although the latter is consistent with observations, the former is not yet confirmed. The dense shell of material surrounding SN2008S (Boticella et al. 2009) could be reproduced by Pumo et al. (2009) in a scenario where mass loss was temporarily boosted during a thermal pulse. This mechanism has been investigated by Mattsson, Höfner & Herwig (2007), who find that changes in the mass loss rate and wind velocity are adequate for sweeping up material into detached shells around the star.

Podsiadlowski et al. (2004) suggested that the modified evolution of super-AGB stars in interacting binary systems could lead to an enhanced galactic EC-SN rate if the envelope was stripped before the occurrence of second dredge-up. It is not immediately clear what the result of the envelope stripping is, however, since without the hydrogen envelope the helium layer should expand, and the core–envelope interface should change. The conclusions of Podsiadlowski et al. generally suggest that binary interaction (i.e. the stripping of the envelope before dredge-up) would produce larger cores for a given initial mass and hence the transition masses would be effectively shifted to lower initial masses. Thus, the contribution of EC-SNe would be greater, given a non-linear, bottom-heavy statistical IMF. Moreover, with 70 percent of massive stars in interacting binary systems (Sana et al. 2012), the motivation for exploring the binary channels of EC-SNe and FeCCSNe is strong. The main effect of mass transfer on the internal evolution of stars (unless there is a common envelope phase, e.g. Iben & Livio 1993) is the transport and distribution of angular momentum. The work in this thesis does not concern itself with the calculation of rotating stellar models, since the non-rotating cases are already riddled with uncertainties. Thus, the effects of

binary interaction on the evolution of 8–12 M_{\odot} stars can be considered negligible in the present work, other than to make quantitative predictions about the rate of EC-SNe in the universe. Of course, in reality, explaining all of the observed details of stars and supernovae would include the effects of binary interaction, rotation and magnetic fields.

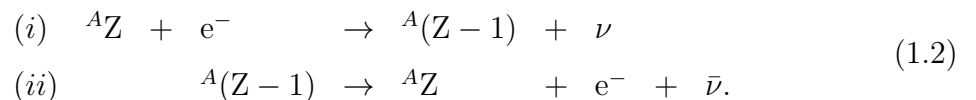
1.3 The role of weak interactions in astrophysics

Weak interactions are of crucial importance to several astrophysical processes. Some of the key phenomena relevant to stellar evolution and supernovae are:

- (i) The URCA process
- (ii) The neutron excess in advanced burning stages
- (iii) Collapse of the Fe-core and the supernova explosion
- (iv) Neutron-capture nucleosynthesis

In this short section the impacts of weak reactions are described in accordance with this list. (i) and (ii) are directly relevant to this work and are described in more details throughout chapters 3 and 4. (iii) and (iv) are briefly described for completeness and to illustrate the breadth of impacts that weak reactions have on closely related disciplines in astrophysics.

(i) The URCA process. The URCA process is the name famously given by George Gamow to the strong cooling caused by energy losses as neutrinos produced in nuclear reactions escape from the stellar interior. The URCA process pair of reactions are simply (i) electron capture and (ii) β -decay:



Of course, all weak nuclear processes (electron and positron capture, β^\pm decay) produce neutrinos. In general, the reactions are exothermic when the reaction rate is significantly high. This is due to the relationship between the chemical potential of the electrons in the local material and the Q-value of the reaction (see section 4.3). If the reaction rate is high and the reaction is exothermic then by definition it cannot directly cause cooling. However, electron captures can still proceed endothermically when the rate is lower and only those from the tail end of the Fermi-Dirac distribution can contribute. In this regime, the reverse beta-decay channel may not yet be completely blocked, and the reaction will be exothermic. When both forward (electron capture) and reverse (β -decay) rates for a relatively abundant pair of isotopes are similar and significantly high, there is little change in the composition and little net energy generation (since $Q_{ec} = -Q_\beta$). The process is important, however, because for every electron-capture and decay, a neutrino removes some energy from the region in which the URCA process is taking place. The main URCA process pairs and their respective activation densities ($\rho/10^9 \text{ g cm}^{-3}$) at $T = 0$ are as follows: $^{27}\text{Al} \leftrightarrow ^{27}\text{Mg}$ (0.13), $^{25}\text{Mg} \leftrightarrow ^{25}\text{Na}$, (1.18), $^{23}\text{Na} \leftrightarrow ^{23}\text{Ne}$ (1.68); Ritossa, García-Berro & Iben 1999). The ground state to ground state transition for the $A = 27$ pair is forbidden, and so the electron capture proceeds from the first two excited states of ^{27}Al . At relevant temperatures in super-AGB stars, $kT \approx 0.04 \text{ MeV}$ ($\log(T/\text{K}) \approx 8.67$), and so the electron capture by ^{27}Al does not proceed until the density is significantly higher than the threshold density. By the time the density is high enough for the reaction to produce ^{27}Mg , the Fermi surface is far higher than the energies of the first two excited states of ^{27}Al and the β -decay channel is blocked. For the $A = 23$ and $A = 25$ pairs, it is also the electron-capture parents (^{23}Na and ^{25}Mg) that are abundant in the stellar core. As the density increases to, crosses and surpasses the thresholds, each URCA pair generally produces a period of cooling followed by a period of heating. While the amount of cooling depends on the contraction timescale (the longer spent at a density where the product of the electron capture and β -decay rates, $\lambda^{ec}\lambda^\beta$, is high, the more neutrino cooling the material is subjected to), the amount of heating is limited by the abundance of the electron capture parent when the β -decay channel of the daughter

nucleus becomes blocked.

The importance of the URCA process in the evolution of 8–12 M_{\odot} stars is discussed and explored in depth in chapters 3 and 4. The URCA process is also important in dense CO white dwarfs and, by proxy, type Ia supernovae (Paczynski 1973; Barkat & Wheeler 1990). The convection induced by carbon-burning in the pre-explosive evolution becomes a numerical burden when coupled with the URCA process. Recent attempts have been made to properly account for this behaviour (Lesaffre, Podsiadlowski & Tout 2005).

(ii) The neutron excess in advanced burning stages. Thielemann & Arnett (1985) demonstrated that during the advanced burning stages of massive stars (particularly oxygen and silicon burning), the inclusion of isotopes with seemingly negligible abundances in the nuclear reaction network (see section 2.3) significantly lowered the neutron excess of the composition. The neutron excess,

$$\eta = \sum_i (N_i - Z_i) Y_i, \quad (1.3)$$

and the electron fraction,

$$Y_e = \sum_i Z_i Y_i, \quad (1.4)$$

are indicative of how neutron-rich the composition is. N_i and Z_i are the neutron and proton numbers of species i and $Y_i = n_i/\rho N_A$ is its number abundance. The neutron excess and the electron fraction are thus related by

$$Y_e = \frac{1 - \eta}{2}.$$

A neutron excess of 0 implies that the composition consists completely of nuclei with $N = Z$, giving an electron fraction of $Y_e = 0.5$. A composition with a neutron excess of $\eta > 0$ (or $Y_e < 0.5$) implies via charge neutrality that there are fewer free electrons in the system. As will be described in detail in Chapter 3, this lowers the electron density ρY_e and hence lowers the contribution of degenerate electrons to the pressure.

(iii) Collapse of the Fe-core and the supernova explosion. In massive stars, the collapse of the iron core is accelerated as electrons are driven into iron-group nuclei and free protons. Martínez-Pinedo, Langanke & Dean (2000), in their shell model calculations, found that previously determined β -decay rates were underestimated and electron-capture rates overestimated. The authors predicted that the electron fraction would drop more slowly due to the lower electron-capture rates, and that when the electron fraction reached $Y_e \approx 0.46$, the β -decay and electron capture rates of several iron-group nuclei would be comparable, enhancing neutrino cooling as in the URCA process. Langanke & Martínez-Pinedo (2000) determined new electron-capture and β -decay rates for 100 nuclei in the mass range $A = 45 - 65$, motivated by their previous work. The differences between these rates and the classical rates of Fuller, Fowler & Newman (1980, 1982a, 1982b, 1985) indeed resulted in higher electron fractions in the iron core at the time of collapse (Heger et al. 2001, to which the interested reader is referred for more information of which ions produce increases and decreases in the electron fraction for various evolutionary stages of massive stars). Juodagalvis et al. (2010) produced a multitude of new weak rates for the iron-group including the effects of Coulomb corrections (see chapter 4) that should now be the standard set.

The explosion mechanism of core-collapse supernovae is related to the revival of the stalled shock by neutrino heating (Janka 2001). The source of these neutrinos is largely the neutronisation of the composition by weak processes and the cooling of the proto-neutron star. The temperature of the material during the supernova is so hot (> 6 GK) that the composition is in nuclear statistical equilibrium (NSE). Weak reactions during this phase will produce a large burst of neutrinos that will become trapped in the high density in falling material and deposit their energy. For this reason, accurate treatment of weak interactions in the supernova simulation itself is important for precise evaluation of the neutrino luminosity, which is the driving mechanism of the standard explosion.

(iv) **Neutron-capture nucleosynthesis.** Neutron-capture processes build heavy nuclei from seeds typically in the iron-group ($A \approx 60$) for which fusion is not energetically favourable. The slow neutron-capture process (s process; Käppeler et al. 2011 and references therein) operates during the thermal pulse phase of AGB stars (main component) and the helium- and carbon-burning phases of massive stars (weak component). The site of the rapid neutron-capture process (r process) is currently an open question, however rare/exotic magneto-rotationally driven supernovae (Winteler et al. 2012) and neutron star mergers (Rosswog et al. 2014) are the most likely candidates. Accurate β -decay rates are thus crucial to simulating the nucleosynthesis of the heavy elements. Moreover, eliminating uncertainties in nucleosynthesis calculations by using the most accurate, up-to-date weak rates helps to break degeneracies between the nuclear reaction rates and the physics of the supernova or merger simulation.

1.4 Mixing in the stellar interior

From a far enough distance, it is easy to think of stars as quiescent and peaceful. In reality, the stellar interior is a dynamic, often turbulent and chaotic place where huge convective plumes rise and fall, rush past one another and slam into more stable parts of the star. The stellar material is fluid, and as such experiences all of the instabilities of fluid dynamics with varying degrees of severity. These instabilities affect the physical properties of the star and how they evolve in time. Mixing of a fluid transports and distributes entropy, which will modify the thermal structure of the star, leading to its re-adjustment. Mixing of chemical elements can replenish fuel in a region of nuclear burning and transport the ashes of previous burning to other regions in the star, where they may experience other, different, nuclear processes. Deep convection in the stellar envelope can bring the products of nuclear burning up to the surface of the star, where they may be observed using spectroscopy.

Astrophysics aside, the nature of convection requires simply the solution of the Navier-Stokes equations of fluid dynamics. Since there is no known analytical solution

to these equations in 3-D, numerical solutions must be found, and problems arise thick and fast. In comparison to the lengthy timescales of stellar evolution, the important nuances of dynamical, turbulent and advective processes occur extremely quickly. Convection on a stellar scale can be, and has been, simulated in two and three dimensions (Herwig et al. 2006; Meakin & Arnett 2007; Mocák et al. 2009; Arnett & Meakin 2011; Herwig et al. 2011; Mocák et al. 2011; Stancliffe et al. 2011), however the explicit nature of the numerical methods involved mean that the simulated time rarely exceeds the order of hours. Compared to even the oxygen-burning timescale in massive stars (the second shortest burning stage, on the order of weeks to months), this is a short time, which makes it difficult to conclude whether or not what is seen in the simulations is transient behaviour, i.e. not representative of the average conditions.

Furthermore, the hydrodynamical processes of key interest to stellar physicists are often occurring deep within the stellar interior, making them difficult processes to observe. Convection in these situations is almost always coupled to several nuclear reactions and requires a detailed equation of state (EOS). One must then include a nuclear reaction network in the simulation and incorporate new EOS tables, which causes further numerical complications. Progress continues to be made, however, in simulating the surface convection of the Sun (Freytag et al. 2012; Trampedach et al. 2013), whose granulation and activity can be more easily measured and where nuclear reactions are barely present. The added complication with surface convection is the coupling of rotation and magnetic fields with the convection⁴.

Using basic considerations of physics to average or approximate the effects of recurrent short-timescale events within the star is regrettably still the only viable option when simulating several million years of evolutionary time. The most commonly used prescription at present to approximate the effects of convection in stellar models is called the mixing length theory (MLT) of convection (Böhm-Vitense 1958). The fundamental principles of MLT and how it accounts for convection are described in section 2.2.1. The most well-known formulation is extensively detailed in Cox & Giuli

⁴Of course, rotation and magnetic fields are also important in the deep interior.

(1968). Although MLT is a reasonable approximation for the behaviour of convection in the deep interior, it is still a parameterised treatment which one would like to be able to automate based on physical considerations, informed by fluid dynamics.

The Full Spectrum of Turbulence (FST) model (Canuto & Mazzitelli 1991; Canuto, Goldman & Mazzitelli 1996) (CM, hereafter) is an attempt to improve upon the basic MLT treatment of convection by considering the behaviour of eddies with all possible sizes (and kinetic energies given by some turbulent energy spectrum function), while MLT effectively only considers one large eddy. The authors show that the standard MLT of, e.g., Böhm-Vitense (1958) is a reasonable approximation only for high viscosity flows that are not found in the stellar interior, and that for efficient (inefficient) convection the actual convective flux is ten times higher (lower) than is given by MLT. Both the MLT and CM models assume convection to be incompressible ($\nabla \cdot \mathbf{v} = 0$), but the CM model is not parameterised like MLT (where, for one, the mixing length itself contains a free parameter, α , see section 2.2.1) since it is shown that the mixing length should not be a function of the local scale height of pressure in the incompressible, inviscid flow of the stellar interior. Instead, the mixing length is simply set to the distance of the local shell from the upper boundary of the convective region in the CM model.

The use of the CM model and subsequent mutations thereof in the place of MLT has only been studied for only low-, intermediate-mass and solar-like stars, especially concerning the behaviour of the surface convection, with the exception of Stothers & Chin (1995) and Ventura et al. (1998). Stothers & Chin (1995) found the CM model to succeed in fitting models in the HRD for a range of initial masses and no parameterisation of the mixing length, but found there to be negligible effects on the evolution of the deep interior, although the models were not computed beyond helium burning. Ventura et al. (1998) have shown some results for the early evolutionary stages of a $15 M_{\odot}$ model (up to the ignition of carbon burning) with and without a parameterised overshoot, but do not provide any useful conclusions concerning the CM model of convection. While the CM model of convection is compelling, and surely more physical than the standard MLT model, it is a potentially large undertaking in

itself to fully test the model for massive stars (particularly in the advanced stages). Partially because that has not yet been completed, and partially because the work of Stothers & Chin (1995) suggests that there will be little impact, in this work (as for all other modern 1D studies of massive stars) the standard MLT model for convection is used.

While MLT treats the effects of convection itself, it is a local treatment that is used to inform a diffusive scheme of where to calculate mixing. This means that it requires external knowledge of where the boundaries of the convection zones lie. How one determines where the boundaries of convection are situated within stellar models is described in section 2.2. Once the notion of a convective boundary has been established, material from the stable layer may still be entrained into the convective zone depending upon the stiffness of that boundary relative to the turbulence strength. This is a well established phenomena in fluid dynamics applied to geo, atmospheric and ocean physics (see Turner 1986 for a concise review). If material can be entrained, then the location of the boundary is dynamic in time and advances at an entrainment rate; the problem becomes complicated further.

A schematic diagram depicting a few mixing processes that can operate in the stellar interior is shown in Figure 1.14. Shear flows (like the one depicted in the top-left corner of Figure 1.14) induce mixing at the boundary with the stable layer, as is seen in multidimensional simulations of helium shell flash convection (Herwig et al. 2006; Herwig et al. 2011). The shear is induced by horizontal turbulence and, if the turbulent kinetic energy is high enough, causes a deformation of the convective boundary. Stresses in the fluid arising from the shear produces turbulence, and if the velocities are high enough the fluid becomes unstable by the Kelvin-Helmholtz instability, causing mixing directly (Strang & Fernando 2001). In fluid dynamics, the Richardson number, Ri , is the ratio of the potential energy of material in the stable layer to the turbulent kinetic energy of the unstable later at the interface. High Richardson numbers therefore indicate a stiff boundary; low Richardson numbers indicate that the interface is eroded on an advective timescale. Indeed, Thorpe (1968) found through experiment that for $Ri < 0.25$ the Kelvin-Helmholtz instability appears. Mixing by the Kelvin-Helmholtz

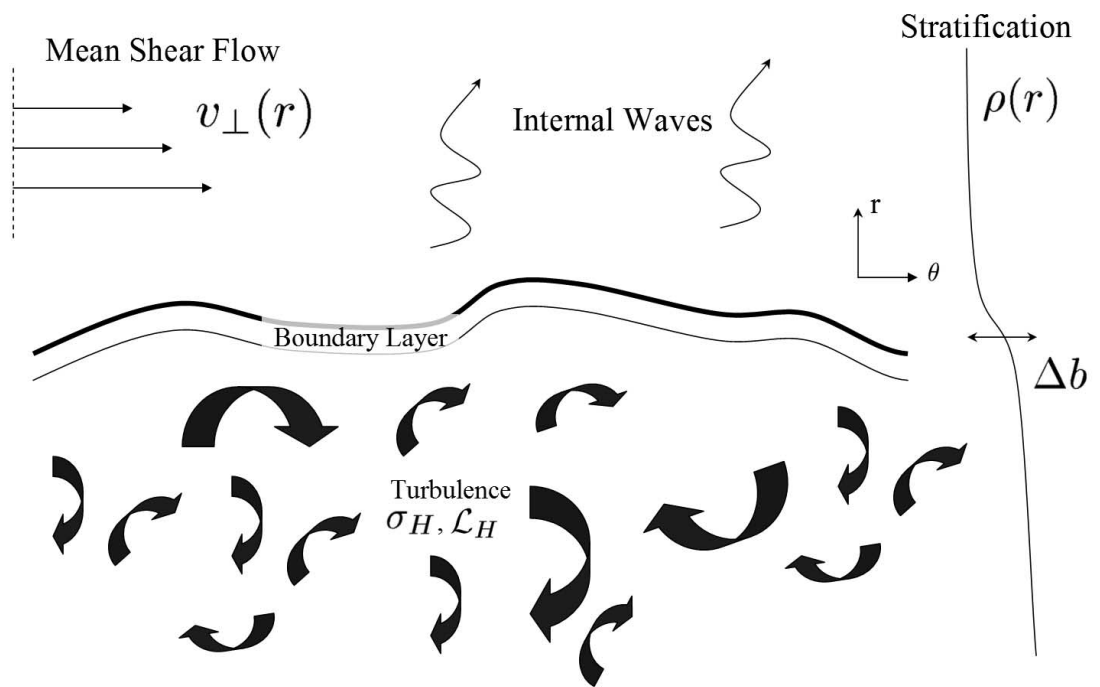


Figure 1.14: Schematic diagram depicting several hydrodynamical instabilities encountered at the boundary between the region exhibiting turbulent convection and the stable layer (Meakin & Arnett 2007).

instability operates in the locality of the boundary layer. Large-scale convective cells are also required to transport the mixed material over large distances in the star where they may have an impact on the observables or on the structure. The density profile of the stellar material across the interface (right hand side of Figure 1.14) characterises the stiffness of the convective boundary. The drop in density at the interface Δb is called the buoyancy jump. The steeper the buoyancy jump, the higher the entropy of the convective material must be in order to cross the boundary. Deformation of the convective boundary occurs due to the rapid deceleration of convective plumes at the interface. This induces internal wave motions that cause mixing in the stable layer (upper middle of Figure 1.14).

A fluid element is dynamically unstable if its density is different to that of its new surroundings following a small radial perturbation. This consideration of convective stability is described in more detail in Chapter 2. The equation of motion for a first order radial perturbation of a fluid element is

$$\rho \frac{\partial^2 r}{\partial t^2} = -g \left(\left. \frac{\partial \rho}{\partial r} \right|_s - \frac{\partial \rho}{\partial r} \right) r,$$

where the subscript s indicates the adiabatic change (at constant entropy) and g is the local acceleration due to gravity. The equation of motion can be written as

$$\frac{\partial^2 r}{\partial t^2} + N^2 r = 0, \quad (1.5)$$

where N is the buoyancy (Brunt-Väisälä) frequency,

$$N^2 = -g \left(\left. \frac{\partial \ln \rho}{\partial r} \right|_s - \frac{\partial \ln \rho}{\partial r} \right). \quad (1.6)$$

The solution to the equation of motion (1.5) is thus

$$r = \begin{cases} r_0 e^{Nt} & N^2 < 0 \\ r_0 e^{iNt} & N^2 > 0 \end{cases}. \quad (1.7)$$

The displacement of the perturbed fluid element grows exponentially when $N^2 < 0$, i.e. when the adiabatic density gradient is steeper than the density gradient of the surrounding stratified medium. In a stable configuration $N^2 > 0$, the adiabatic density

gradient is shallower than the surrounding stratified medium and the solution is the oscillating one. The buoyancy frequency is the maximum frequency of internal gravity waves, whose propagation and dispersion are an important facet of asteroseismology (Aerts, Christensen-Dalsgaard & Kurtz 2010, section 3.1.4.2), but this will not be discussed here. Rather, I will discuss the implications of the magnitude of the buoyancy frequency (when $N^2 > 0$) for characterising the degree of stability of the fluid. This is nicely illustrated by examining its relation with the entropy gradient in the star (Maeder 2009 p 85–86, 5.9–5.17). The relationship is (Maeder 2009, equation 5.16)

$$N^2 = \frac{g\delta}{C_P} \frac{ds}{dr}, \quad (1.8)$$

where C_P is the specific heat at constant pressure and δ is a thermodynamic property of the material (see chapter 2). The convection criteria for instability becomes $ds/dr < 0$ – a negative entropy gradient. Since adiabatic changes are at constant entropy, this condition is quite intuitive. In material that is stable, the buoyancy frequency is a measure of the steepness of the positive entropy gradient.

Another factor to consider is the composition of the material. The gradient of the mean molecular weight $\nabla_\mu \equiv \partial \ln \mu / \partial \ln P$ can provide either a stabilising or a destabilising effect within the star. For example, for $\nabla_\mu > 0$ the mean molecular weight decreases as a function of radius, providing a stabilising effect acting against the rise of a perturbed fluid element. If a region would be convective in the absence of this stabilising ∇_μ but is dynamically stable in its presence, the material is considered to be *semiconvective* (see section 2.2). This is because the material can achieve thermal stability while only being partially mixed (i.e. its composition has not been completely homogenised). If $\nabla_\mu < 0$, heavier particles sit atop lighter ones. In this situation, mixing can arise when the heavier particles sink. This situation does not necessarily lead immediately to mixing, since the weak gravitational settling can easily be balanced by, for example, a supporting temperature gradient. The classic example is that of warm, salty water sitting atop a beaker full of pure, cold water. The salty water has a higher mean molecular weight than the pure water, however its temperature excess makes it still the lower density fluid. If a fluid parcel of the warm, salty water was

spatially perturbed in such a way that its new position was deeper in the beaker, the parcel would be buoyantly restored to its original height. Left alone, the warm, salty water will exchange heat energy with the colder water below (and lose heat energy to the surrounding air), and as the system thermalises, the salty water would become the denser of the two fluids and begin to sink. This process is called *thermohaline* mixing, and is a slow process exhibiting fingering.

It is quite evident that the treatment of mixing in the stellar interior is not a closed problem and requires detailed studies of many hydrodynamical and thermal instabilities in order to constrain its behaviour. While it remains the task of 3D hydrodynamics simulations to provide the insights needed, by performing stellar evolution simulations in 1D with a range of different parameterisations it is possible to highlight situations where a targeted study is required. As has been described in this section, such works have already begun (e.g. Meakin & Arnett 2007; Mocák et al. 2009; Herwig et al. 2011). While different mixing considerations in stellar models do produce photometric variations that can be compared directly with observations, coupling mixing, nucleosynthesis and spectroscopy is a vital test of their accuracy. If the boundary is deformed, interfacial gravity waves appear in the stable layer (see illustration in Figure 1.14). Modern asteroseismological instruments are now able to measure properties of these gravity waves as they propagate through the star and cause the excitement of oscillatory modes. This gives the opportunity to compare hydrodynamical simulations of convection in stars with real data in order to constrain the stellar behaviour. Asteroseismology is the best tool presently available to directly observe processes within the deep stellar interior. In the coming years, characteristics of the internal stellar structure will be able to be tested by direct comparison to asteroseismological observations. These observations will be crucial to constrain the behaviour of mixing at the convective boundary.

1.5 Thesis Outline

In this thesis, new models of electron capture supernova progenitors calculated using the MESA code will be presented. In chapter 2, the methodology behind calculating stellar models is outlined and the physical assumptions involved are described in detail. The results of the calculations are presented and described in chapter 3, along with a discussion of the uncertainties of the results, linked to the methods and assumptions made in chapter 2. Two such uncertainties are the hydrodynamic mixing properties and the accuracy of the physics—and indeed of the numerical representation of the physics—with which weak reaction rates are calculated. The nuclear physics uncertainties are addressed in chapter 4, which describes new calculations of weak reaction rates including Coulomb corrections that were performed by collaborators for this study. The differences between these newly calculated rates and those available in the literature are discussed in chapter 4 along with a demonstration of their impact in the stellar evolution models presented in chapter 3. Finally, in chapter 5 the key results of this work are summarised and some of the outstanding problems are presented together with a discussion about how they may be addressed in the future.

2 Numerical Modelling of stars and the MESA code

In the Introduction, a background to stellar evolution including recent observational and theoretical results concerning 8–12 M_{\odot} stars was presented. This chapter will focus on the methodology used when performing detailed numerical simulations of stars and describes the the methods and tools that were used to produce the results that are presented later in this thesis.

Modules for experiments in stellar astrophysics (Paxton et al. 2011) is an open-source distribution of physics modules developed and maintained largely by the scientific community. *MESA/star* is a stellar evolution code in which the equations outlined in this section are solved in a fully coupled manner (structure + burning + mixing). This is advantageous for the accuracy of the converged solution at each time step because there is feedback between these three main sets of equations.

2.1 Key equations

Mathematically, the structure and evolution of stars is described by a system of well-known differential equations that require approximate physical treatments and data for their solution. The derivation of these differential equations can be found in any good stellar astrophysics text book, but for completeness their final Lagrangian (mass coordinate as independent variable) forms are described below.

One begins with the equation of mass conservation,

$$\frac{dm}{dr} = 4\pi r^2 \rho(r), \quad (2.1)$$

which is used to translate the structure equations from a Eulerian coordinate system (radius as independent variable) to Lagrangian. It gives the relationship between m , r and $\rho(r)$: the mass coordinate, radius and density of a given point in the star,

respectively. Firstly we consider the conservation of momentum,

$$\frac{dP}{dm} = \frac{1}{4\pi r^2} \left[\frac{d^2 r}{dt^2} - \frac{GM_r}{r^2} \right], \quad (2.2)$$

where P and M_r are the pressure and the mass enclosed in a sphere of radius r , respectively. G is the gravitational constant. The forces provided by gravity and the internal pressure gradient on a mass element oppose one another, and in the case of their imbalance, the mass element will receive an acceleration of $d^2 r/dt^2$. For stellar interiors where the evolutionary timescales of interest are much longer than the sound crossing time, it can be assumed that the star is always in pressure (hydrostatic) equilibrium. As such, the acceleration term is excluded and Eq. 2.2 reduces to the equation of hydrostatic equilibrium,

$$\frac{dP}{dm} = -\frac{GM_r}{4\pi r^4}. \quad (2.3)$$

The next consideration is the conservation of energy. L_r is the luminosity (erg s^{-1}) of the stellar material enclosed within radius r . Unless a shell is generating or losing additional energy, $dL_r/dr = dL_r/dm = 0$. However, in certain regions within the star energy will be produced by nuclear processes and work will be done on or by the material in the shell. If neutrinos are created in the stellar material (by various processes including the nuclear reactions that are generating energy), energy will be removed from the system very efficiently since neutrino scattering is greatly improbable at such densities. These three considerations yield the equation of energy conservation,

$$\frac{dL}{dm} = \epsilon_{\text{nuc}} - \epsilon_{\nu} + \epsilon_{\text{grav}}, \quad (2.4)$$

where ϵ_{nuc} and ϵ_{ν} are the specific nuclear energy generation and thermal neutrino losses, respectively, with units of $\text{erg g}^{-1} \text{s}^{-1}$. ϵ_{grav} is the specific amount of work done on or by the shell during expansion or contraction,

$$\epsilon_{\text{grav}} = -\frac{dq}{dt} = -c_P \frac{dT}{dt} + \frac{\delta}{\rho} \frac{dP}{dt}, \quad (2.5)$$

where c_P is the specific heat at constant pressure and $\delta = -\partial \ln \rho / \partial \ln T$ is a thermodynamic property of the material (see below for more details about the thermodynamic

derivatives). Lastly, a description of the temperature stratification as a function of mass coordinate is required, given by

$$\frac{dT}{dm} = -\frac{GmT}{4\pi r^4 P} \nabla, \quad (2.6)$$

where ∇ is the temperature gradient

$$\nabla = \frac{\partial \ln T}{\partial \ln P}. \quad (2.7)$$

∇ is evaluated depending upon whether the region is convective or radiative. If the region is radiative, the temperature gradient is given as

$$\nabla \equiv \nabla_{\text{rad}} = \frac{3}{16\pi acG} \frac{\kappa L_r P}{mT^4}. \quad (2.8)$$

In the radiative case, ∇_{rad} is derived by considering the radial diffusion of thermalised photons. a is the radiation density constant, c is the speed of light and κ is the combined radiative and conductive opacity of the stellar material, $\kappa = (\kappa_\gamma^{-1} + \kappa_c^{-1})^{-1}$. If the region is convectively unstable, then ∇ is unknown and must be determined using the mixing length theory of convection. This is described in section 2.2.1.

The equation of state (EOS) describes how the thermodynamic properties of the stellar material are related, and is usually of the form

$$P = P(\rho, T, X), \quad (2.9)$$

where X contains information about the elemental/isotopic composition of the material from which one is interested in the mean molecular weight, μ . A general EOS is given by

$$P^\alpha = \frac{\rho}{\mu^\varphi} kT^\delta, \quad (2.10)$$

where the exponents are

$$\alpha = \left(\frac{\partial \ln \rho}{\partial \ln P} \right)_{\mu, T}; \quad \varphi = \left(\frac{\partial \ln \rho}{\partial \ln \mu} \right)_{P, T}; \quad \delta = - \left(\frac{\partial \ln \rho}{\partial \ln T} \right)_{P, \mu} \quad (2.11)$$

and for an ideal, non-interacting gas, $\alpha = \varphi = \delta = 1$. In reality, the EOS used in stellar evolution codes must account not only for gas pressure but also for radiation,

$$P_{\text{rad}} = \frac{1}{3} aT^4 \quad (2.12)$$

and electron degeneracy pressure (Phillips 1999, p. 58, eq. 2.31 and 2.34),

$$P_e = \begin{cases} \frac{h^2}{5m} \left[\frac{3}{8\pi} \right]^{2/3} n_e^{5/3} & \text{non - relativistic} \\ \frac{hc}{4} \left[\frac{3}{8\pi} \right]^{1/3} n_e^{4/3} & \text{relativistic,} \end{cases} \quad (2.13)$$

where n_e is the electron number density. In the cooler outer layers of the star, the material may only be in a state of partial ionisation, which must also be accounted for in the EOS.

A simple approximation to the EOS is to consider the stellar material as a polytrope,

$$P = K\rho^{(n+1)/n}, \quad (2.14)$$

a solution to the Lane-Emden equation for the gravitational potential. From 2.13, one can see that the equation of state of a completely electron-degenerate gas ($P_e \gg P_{\text{gas}}$) is well represented by polytropes of $n = 3/2$ (non-relativistic) and $n = 3$ (relativistic). With some light manipulation of the polytropic relation and the equations of hydrostatic equilibrium and mass conservation, one arrives at the mass-density relation

$$M \propto \rho^{(3-n)/2n}, \quad (2.15)$$

with which it becomes clear that there is no dependence of the mass on the density for an $n = 3$ polytrope. Instead, the mass is defined by the values of the polytropic constant K and index n (see Kippenhahn & Weigert 1990 eq. 19.27). The only solution for the mass of a relativistically degenerate polytrope is the Chandrasekhar mass,

$$M_{\text{Ch}} = 5.836 Y_e^2 M_{\odot}. \quad (2.16)$$

Chandrasekhar's more rigorous derivation, considering the effects of partial degeneracy, reduces to this same limiting mass, since the fully-relativistic case represents an $n = 3$ polytrope.

2.2 Convection

The treatment of convection and mixing in stellar models arises from considerations of dynamical and secular stability. Since we are modelling in hydrostatic equilibrium, we are assuming that the evolutionary timescale is much longer than the sound crossing time and therefore any fluid element will always be in pressure equilibrium with its surroundings. Any fluid element being heated will experience a density change $\Delta\rho_e$ and will be buoyantly accelerated upwards by its surroundings. Considering the upward movement of this fluid element by Δr as a small perturbation, convective stability of the fluid is then defined by whether the perturbation is suppressed, or whether it grows. A perturbation of Δr from the original position involves a change in pressure of the fluid element, $(\Delta P)_e$, which is equal to the change in pressure of the surroundings, $(\Delta P)_s$,

$$(\Delta P)_e = (\Delta P)_s = \frac{\partial P}{\partial r} \Delta r, \quad (2.17)$$

because of the hydrostatic equilibrium assumption. We must also consider the change in density of the element (e) and of the surroundings (s) over the perturbation,

$$(\Delta\rho)_e = \left(\frac{\partial\rho}{\partial r}\right)_e \Delta r \quad (2.18)$$

$$(\Delta\rho)_s = \left(\frac{\partial\rho}{\partial r}\right)_s \Delta r. \quad (2.19)$$

If the density of the perturbed fluid element decreases more than the density of the surroundings across an upwards radial displacement Δr , i.e. if

$$-\left(\frac{\partial\rho}{\partial r}\right)_e > -\left(\frac{\partial\rho}{\partial r}\right)_s, \quad (2.20)$$

then the perturbation grows as the fluid element receives a larger and larger buoyancy acceleration, and the fluid is convectively unstable. The general EOS from Eq. 2.10 in differential form is

$$\frac{1}{\rho} \frac{\partial\rho}{\partial r} = \frac{\alpha}{P} \frac{\partial P}{\partial r} + \frac{\varphi}{\mu} \frac{\partial\mu}{\partial r} - \frac{\delta}{T} \frac{\partial T}{\partial r}, \quad (2.21)$$

and by assuming that the composition of the convective element does not change as a function of radius (mixing timescale \ll burning timescale), $(\partial\mu/\partial r)_e = 0$. The pressure term also cancels since we are assuming hydrostatic equilibrium and thus 2.20 becomes

$$\left(\frac{\partial \ln T}{\partial \ln P}\right)_e - \left(\frac{\partial \ln T}{\partial \ln P}\right)_s < -\frac{\varphi}{\delta} \left(\frac{\partial \ln \mu}{\partial \ln P}\right)_s \quad (2.22)$$

where radial derivatives have been converted to derivatives with respect to pressure by multiplying by the pressure scale height, $-\partial r/\partial \ln P$. This relation is commonly written more simply as

$$\nabla_e - \nabla_s < -\frac{\varphi}{\delta} \nabla_\mu, \quad (2.23)$$

where

$$\nabla = \left(\frac{\partial \ln T}{\partial \ln P}\right); \quad \nabla_\mu = \left(\frac{\partial \ln \mu}{\partial \ln P}\right)_s. \quad (2.24)$$

Since in the absence of convection the stellar temperature gradient is given by considering only radiative (and conductive) transport, $\nabla_s \equiv \nabla_{\text{rad}}$ is referred to as the radiative temperature gradient. ∇_{ad} is the adiabatic temperature gradient and describes the temperature of the convective element should it rise adiabatically. ∇_e describes the actual temperature of the fluid element as it rises. To a very good approximation, $\nabla_e = \nabla_{\text{ad}}$ in the deep stellar interior, however in the convective envelope convection can become very inefficient and this assumption becomes poor. There are then two definitions of convective instability: one where the surroundings are of uniform composition, the Schwarzschild criterion,

$$\nabla_{\text{rad}} > \nabla_{\text{ad}}, \quad (2.25)$$

and one where the composition gradient is non-zero, the Ledoux criterion,

$$\nabla_{\text{rad}} > \nabla_{\text{ad}} + \frac{\varphi}{\delta} \nabla_\mu. \quad (2.26)$$

One can see that when the mean molecular weight of the surrounding material is decreasing radially, the radiative (and conductive) temperature gradient will become steeper before inducing convection than for a uniform composition of the material. This is typically the case in the cores of stars whereby nuclear burning has been ignited at

the centre, raising the mean molecular weight in that region. The material in this situation is then unstable by the Schwarzschild criterion but stable by the Ledoux criterion. The stabilising effect of the composition gradient leads to a slow mixing, known as semi-convection. On the other hand, if the mean molecular weight of the surrounding material is increasing radially, mixing will be induced where there is a shallower radiative (and conductive) temperature gradient than if the material was of uniform composition. In this case, the material is stable by the Schwarzschild criterion and unstable by the Ledoux criterion. In this situation, mixing can be induced by the composition gradient alone, and is known as thermohaline mixing (see, e.g., Charbonnel & Zahn 2007).

Semi-convection in stars has in the past been defined to be a result of an over-stable oscillation of a perturbed fluid element in the presence of a stabilising mean molecular weight gradient when there is heat exchange between the element and the surroundings (Kato 1966). The growth of the instability depends upon the rate of heat diffusion over a convective element, having a typical timescale τ_{HD} while the timescale for some evolutionary phase producing the convection within the star would be τ_{SE} : when $\tau_{HD} \ll \tau_{SE}$, the over-stable region can be assumed to be efficiently mixed, the composition gradient is destroyed and the convection criterion becomes identical to that of Schwarzschild. Conversely, if $\tau_{HD} \gg \tau_{SE}$, then one might assume that mixing in the over-stable region is so inefficient that it will never mix in the present situation and the convection criteria is strictly that of Ledoux (Langer, Fricke & Sugimoto 1983). For everything in-between, one would like to characterise the rate of mixing using a diffusive approximation, for which the diffusion coefficient of semi-convective mixing is needed. Semi-convection has been shown to have an impact on the evolution of the convective helium core (Castellani, Giannone & Renzini 1971) and the surface abundance of carbon in low-mass AGB stars (Iben & Renzini 1982). Langer, Fricke & Sugimoto (1983) and Spruit (1992) have provided prescriptions to calculate the semi-convective diffusion coefficient for use in stellar models. The numerical values obtained using these prescriptions are similar in magnitude to diffusion coefficients representing the effects of dynamical shear due to differential rotation (i.e. where $d\omega/dr \neq 0$).

Semi-convection and rotation both have a strong impact on the stellar models during, for example, the crossing of the Hertzsprung-Russell diagram from the hot side to the cool side. Hence, it is difficult to calibrate the efficiency of semi-convection—which is a free parameter—by comparing stellar models with observations due to a degeneracy with parameterisations of other mixing processes. One specific example of such an observation is the blue-to-red supergiant ratio; at present no single treatment and parameterisation of mixing is able to predict the observed ratio of blue supergiants to red supergiants (see, e.g., Woosley, Heger & Weaver 2002a and references therein).

As will be explained later, in the MESA code I assume the Schwarzschild criterion for convection except for in the very late stages, where a strong μ gradient develops in the core due to the rapid electron captures, in keeping with previous studies of similar stars (Miyaji et al. 1980; Nomoto 1984; Nomoto 1987; Gutierrez et al. 1996). For sure, the seemingly more physical Ledoux criterion with semiconvection would be ideal in the future, by which time hopefully a sound treatment for convection is available that also incorporates the effects of overshooting and convective boundary mixing.

2.2.1 Mixing length theory

Stellar convection is quite undeniably a 3-D phenomenon. However, it is impossible to properly model convection in 3-D for an entire stellar lifetime. The difference in the orders of magnitude of convective (on the order of minutes) and evolutionary timescales in stars (millions of years) is simply too large to ever achieve such a feat. Instead, if one is to include the effects of convection in 1-D stellar models at present, a treatment known as ‘mixing length theory’ (MLT) must be employed. Mixing length theory considers the macroscopic bulk motions of convective mass elements to have a mean free path ℓ , the mixing length. MLT is used to provide the local gradient of temperature across a convectively unstable zone of the stellar model, which is required for the solution of the equation of energy transport (equation 2.6). For mixing of the composition, the principle is to approximate convection as a diffusive process using the convective velocity calculated from MLT to predict an appropriate diffusion coefficient for each

zone in the discretised stellar model. Once this has been achieved, the diffusion equation can be solved in order to give the new distribution of nuclear species as a result of the mixing.

MLT is a local treatment for a non-local phenomenon, making it necessary to average several quantities. The method by which this averaging is included in the treatment is quite poor, however the treatment does well to reproduce many observables given the appropriate parameterisation for the mixing length, $\ell = \alpha H_P$.

By substituting the radiative temperature gradient from Eq. 2.8 into the Schwarzschild stability criterion (Eq. 2.25), we can define a critical luminosity,

$$L_{r,\text{crit}} = \frac{16\pi acG}{3} \frac{mT^4}{\kappa P} \nabla_{\text{ad}}, \quad (2.27)$$

above which convective flux is required in addition to radiation and conduction in order to maintain energy balance. For $L_r < L_{r,\text{crit}}$, the actual temperature gradient is given by the radiative one, $\nabla \equiv \nabla_{\text{rad}}$, but for $L_r > L_{r,\text{crit}}$ convective flux is required to carry the excess luminosity and the actual temperature gradient ∇ is unknown. In order to address this we need to determine what the convective flux will be.

The local luminosity of the star, L_r , must be provided by a combination of radiative, conductive and convective energy transport. The total energy flux is then given by

$$F = \frac{L_r}{4\pi r^2} = F_{\text{rad}} + F_{\text{conv}}, \quad (2.28)$$

where F , the total flux, can be given by assuming that all of the energy flux is in fact transported radiatively and is related to a (‘fictitious’) local radiative temperature gradient ∇_{rad} (as defined in 2.8) that would be required to carry that flux radiatively,

$$F = \frac{4acG}{3} \frac{mT^4}{\kappa P r^2} \nabla_{\text{rad}}, \quad (2.29)$$

giving

$$\frac{4acG}{3} \frac{mT^4}{\kappa P r^2} \nabla_{\text{rad}} = F_{\text{rad}} + F_{\text{conv}}, \quad (2.30)$$

where F_{rad} is the actual radiative flux given by the actual temperature gradient,

$$F_{\text{rad}} = \frac{4acG}{3} \frac{mT^4}{\kappa P r^2} \nabla. \quad (2.31)$$

We now require an expression for the convective flux as a function of the local thermodynamic conditions. Starting from the initial assumption that a convective fluid element will rise a radial distance ℓ , the mixing length, before its thermalisation with the surroundings, one assumes that the average fluid parcel will have travelled a distance $\ell/2$ before reaching the local shell. The temperature excess of such an average fluid parcel over the surrounding material in this shell is given by

$$\begin{aligned}\overline{DT} &\approx \left[\left(\frac{\partial T}{\partial r} \right)_e - \left(\frac{\partial T}{\partial r} \right)_s \right] \frac{\ell}{2} \\ &= T(\nabla - \nabla_e) \frac{\ell}{2H_P}\end{aligned}\tag{2.32}$$

where H_P is the local scale height of pressure. The pressure excess of the element over the surroundings $DP = 0$ from hydrostatic equilibrium, and the (average) density difference $\overline{D\rho}$ is given by

$$\frac{\overline{D\rho}}{\rho} = -\delta \frac{\overline{DT}}{T},\tag{2.33}$$

where δ is defined in 2.11. During its thermalisation, the amount of heat per unit mass transferred from the convective element to its surroundings is

$$\Delta Q = c_P \overline{DT},\tag{2.34}$$

and assuming the average velocity of a convective element to be $\bar{v} = v(\ell/2)$, the heat flux from convection is

$$\begin{aligned}F_{\text{conv}} &= \bar{v} \rho \Delta Q \\ &= \bar{v} \rho \frac{T\ell}{2H_P} c_P (\nabla - \nabla_e).\end{aligned}\tag{2.35}$$

The buoyancy force on the fluid element is equal to the weight of the displaced surroundings, giving a net force per unit volume on the convective element of

$$\begin{aligned}K &= -g \overline{D\rho} \\ &= g \delta \rho \frac{\overline{DT}}{T}.\end{aligned}\tag{2.36}$$

It is then assumed that the average force acting on the convective element as it rises from its original position is simply $\bar{K} = \frac{1}{2}K(\ell/2)$, and that half of the work done on the fluid element by this force is converted to the kinetic energy of the element while the other half displaces the surrounding fluid and dissipates. This gives an expression for the convective velocity from the work done in moving the fluid parcel (on average) a distance of $\ell/2$ to our local shell,

$$\bar{v}^2 = \frac{1}{8}g\delta(\nabla - \nabla_e)\frac{\ell^2}{H_P}, \quad (2.37)$$

giving an expression for the convective flux,

$$F_{\text{conv}} = \ell^2 \rho T c_P \frac{\sqrt{g\delta}}{4\sqrt{2}} (\nabla - \nabla_e)^{\frac{3}{2}} H_P^{-\frac{3}{2}}. \quad (2.38)$$

An expression for ∇_e is now required. As the fluid element rises, it will cool both adiabatically and, more realistically, also due to radiative losses into the surroundings. The cooling rate (erg s^{-1}) of a convective element with surface area S is

$$\lambda = S j \quad (2.39)$$

where j is the radiative flux of energy into the surroundings from the element. j is expressed using the diffusive formulation where the temperature gradient in the normal direction from the convective element is approximated to be $2\overline{DT}/d$, where d is the diameter of the element, giving

$$\lambda = -\frac{8}{3}acT^3 \frac{\overline{DT} S}{\rho \kappa d}. \quad (2.40)$$

This flux becomes a correction to the temperature gradient thusly,

$$\begin{aligned} \left(\frac{\partial T}{\partial r}\right)_e &= \left(\frac{\partial T}{\partial r}\right)_{\text{ad}} - \frac{\lambda}{\rho V c_P \bar{v}}, \\ \nabla_e &= \nabla_{\text{ad}} - \frac{\lambda H_P}{\rho V c_P \bar{v} T}. \end{aligned} \quad (2.41)$$

After substituting in for λ and \overline{DT} and using the dimensional approximation $\ell S/Vd \approx 9/(2\ell)$, we obtain a final equation,

$$\frac{\nabla_e - \nabla_{\text{ad}}}{\nabla - \nabla_e} = \frac{6acT^3}{\rho^2 \kappa c_P \bar{v} \ell}. \quad (2.42)$$

It is now possible to find analytical solutions to the 5 unknown quantities, ∇_e , ∇ , \bar{v} , F_{conv} and F_{rad} using the 5 equations 2.30, 2.31, 2.37, 2.38 and 2.42 given the local thermodynamic quantities. Also needed is an appropriate mixing length, which is parameterised by setting it to be some fraction α of the pressure scale height of order unity,

$$\ell = \alpha H_P. \quad (2.43)$$

Once the equations above have been solved, the diffusion coefficient is given by

$$D = \frac{1}{3} \bar{v} \ell \quad (2.44)$$

and can be used to solve for the mixing of the composition due to convection.

2.2.2 Overshooting and convective boundary mixing

In section 1.4, the complexity of hydrodynamic mixing in stellar interiors was discussed, and so far in this section the principles of mixing length theory (MLT)—the simplification by which convective mixing is generally included in 1-D stellar models—have been described. It was explained that the general principle of MLT is to calculate the actual temperature gradient in convective regions along with the average convective velocity, from which a diffusion coefficient can then be used to solve the diffusion equation for the mixing of composition, X , along with the reaction network.

MLT is limited to act in regions where the local radiative temperature gradient needed to provide the supporting luminosity by radiative transport alone, ∇_{rad} , satisfies either

$$\nabla_{\text{rad}} \equiv \left(\frac{\partial \ln T}{\partial \ln P} \right)_{\text{rad}} > \nabla_{\text{ad}} \quad (2.45)$$

(Schwarzschild criterion) or

$$\nabla_{\text{rad}} > \nabla_{\text{ad}} + \frac{\varphi}{\delta} \nabla_{\mu} \quad (2.46)$$

(Ledoux criterion), where ∇_{μ} is the gradient of mean molecular weight in the surrounding stellar material, $\partial \ln \mu / \partial \ln P$ and φ and δ are thermodynamic derivatives

from 2.11. An important physical inaccuracy of MLT is its failure to provide a treatment for what happens at the convective boundary with the radiative layer. In section 1.4, physical considerations relevant to the behaviour at convective boundaries were discussed in detail. The general conclusion is that at the convective boundaries, even though the criteria for convection are no longer satisfied, mixing processes can still operate. These more complex considerations of hydrodynamical instability I refer to as convective boundary mixing.

In order to reproduce the radius and luminosity of a star with a given mass, a certain amount of extra mixing into the radiative layer is needed in the stellar models. In some stellar evolution codes, such as GENEC (Eggenberger et al. 2008), this is implemented as a radial extension of the Schwarzschild boundary by a fraction of the pressure scale height (typically about one fifth). This extension of the convective core is referred to as penetrative overshooting, since the convection penetrates into the stable radiative layer. One might describe a related physical picture as ballistic overshooting. Earlier, it was described how MLT predicts a diffusion coefficient with which the diffusion equation is solved for the mixing of the nuclear composition. In GENEC, during the hydrogen, helium, carbon and neon burning phases the convective turnover timescale is assumed to be so short in comparison to the nuclear burning timescale that the mixing of composition in convective regions is not solved using the diffusion equation, but instead the composition is assumed to be uniformly mixed throughout the region. Although a seemingly simplistic model for overshooting, models calculated using GENEC are robust in reproducing many evolutionary characteristics of massive stars. GENEC also has a sophisticated 1D implementation of rotation, allowing for the effects of shear mixing to be included in simulations of rotating stars, which are indeed treated diffusively. The assumption of instantaneous mixing in the convective regions propagates to the region where overshooting takes place, meaning that the composition in this region is instantly homogenised with the convective core.

Convective velocities in 2-D (Herwig et al. 2006) and 3-D (Herwig et al. 2011) hydrodynamical simulations of convective boundaries have shown relatively good agreement with those calculated with 1-D mixing length theory, but also yield velocity pro-

files that exponentially decay as a function of radial distance into the radiative layer. Because mixing is treated as a diffusive process, where the diffusion coefficient and the convective velocity are related by 2.44, convective boundary mixing in MESA is treated using an exponentially decaying diffusion coefficient. The diffusion coefficient of mixing is assumed to decrease exponentially from the strict Schwarzschild boundary radially into the radiative zone. The diffusion coefficient is then

$$D = D_0 \exp\left(-\frac{2z}{f_{\text{CBM}}\lambda_{P,0}}\right) \quad (2.47)$$

where D_0 is the diffusion coefficient, taken equal to the mixing length diffusion coefficient value (D_{MLT}) at a distance $f_{\text{CBM}}\lambda_{P,S}$ inside the convection zone from the Schwarzschild boundary. At this location, the pressure scale height is $\lambda_{P,0}$, while $\lambda_{P,S}$ is the pressure scale height at the Schwarzschild boundary. This is because the value of D_0 drops sharply towards zero at the Schwarzschild boundary. D is the diffusion coefficient as a function of distance z from this location and f_{CBM} is a free parameter. The values of f_{CBM} used in this work are given and discussed in section 2.5.

2.3 The nuclear reaction network and composition evolution

The principal role of the nuclear reaction network is to evolve the composition of the stellar material according to the nuclear reactions that are activated in certain regions of the star at a given temperature, density and existing composition. The rate of change of the number of species i in a zone within the stellar model due to nuclear reactions is given by

$$\dot{Y}_{i,\text{burn}} = \sum_j c_i(j)\lambda_j Y_j + \sum_{j,k} c_i(j,k)\lambda_{j,k}\rho Y_j Y_k + \sum_{j,k,l} c_i(j,k,l)\lambda_{j,k,l}\rho^2 Y_j Y_k Y_l, \quad (2.48)$$

where the three terms on the right hand side correspond to sums over all one-body, two-body and three-body reactions that create or destroy species i , respectively (see, e.g., Arnett & Thielemann 1985). The subscripts j , k and l denote quantities pertaining

to the first, second, or potentially third reactants in the reaction, respectively. $c_i(j)$, $c_i(j, k)$ and $c_i(j, k, l)$ are statistical and prevent double counting of reactants:

$$\begin{aligned} c_i(j) &= \pm N_i, \\ c_i(j, k) &= \pm \frac{N_i}{N_j! N_k!}, \\ c_i(j, k, l) &= \pm \frac{N_i}{N_j! N_k! N_l!}, \end{aligned}$$

where N_i , N_j , N_k and N_l are numbers indicating how many particles of type i , j , k or l are involved in the reaction and the expression is positive or negative depending upon whether the reaction creates or destroys species i , respectively. λ is the rate of the reaction and ρ is the density of the stellar material. The first term on the right hand side of equation 2.48 (the one-body term) accounts for photodisintegration reactions and weak reactions—e.g. $^{20}\text{Ne}(\gamma, \alpha)^{16}\text{O}$ and $^{23}\text{Na}(e^-, \nu)^{23}\text{Ne}$, respectively—for which λ_j has units of s^{-1} . The value of λ for weak reactions is one of the key quantities that are calculated for this work using the methodology outlined in Chapter 4. The second term on the right hand side of equation 2.48 (the two-body term) accounts for the reactions in which two nuclei are considered to fuse together; the majority of the reactions considered are part of this category. For this kind of reaction,

$$\lambda_{j,k} = N_A \langle \sigma v \rangle_{j,k}$$

and has units of $\text{cm}^3 \text{s}^{-1} \text{mol}^{-1}$; N_A is Avagadro's number and $\langle \sigma v \rangle_{j,k}$ is the velocity-integrated cross-section of the reaction. While the third term on the right hand side of equation 2.48 accounts for all reactions in which there are three reactants, it is usually only relevant for the rate of change in the abundances of ^4He and ^{12}C due to the triple-alpha reaction ($3\alpha \rightarrow ^{12}\text{C}$). In this case, $\lambda_{j,k,l}$ has the units of $\text{cm}^6 \text{s}^{-1} \text{mol}^{-2}$ (see Cyburt et al. 2010).

While evolving the composition, the nuclear reaction network must also calculate ϵ_{nuc} —the net specific energy gained or lost by the zone due to these nuclear processes—for the equation of energy conservation (2.5). This is given by

$$\epsilon_{\text{nuc}} = -N_A \sum_i \mu_i \dot{Y}_i - \epsilon_{\nu, \text{nuc}},$$

where μ_i is the chemical potential of species i and $\epsilon_{\nu,\text{nuc}}$ is the specific neutrino luminosity produced by reactions involving the weak nuclear force. In Chapter 4 the method with which $\epsilon_{\nu,\text{nuc}}$ is calculated is described in great detail hence such a description is not included here.

The equations presented thus far in this section describe the time-evolution of the composition for a single zone. In stellar evolution codes the numerical models of stars are discretised into several hundreds or thousands of zones. In some codes the different ‘operators’ (structure, burning and mixing) are split, or decoupled, meaning that they are solved separately. For example in GENE (The Geneva stellar evolution code), firstly the structure equations, followed by the nuclear burning and finally the mixing are calculated in turn in an iterative scheme until the desired precision is reached. In the nuclear burning step, the composition is evaluated for each zone by solving equation 2.48. There are significant differences for codes in which the burning and mixing are coupled (such as the MESA code), where the rate of change of the abundance of species i in a zone is given by

$$\dot{Y}_i = \dot{Y}_{i,\text{burn}} + \dot{Y}_{i,\text{mix}},$$

where $\dot{Y}_{i,\text{burn}}$ is the rate of change due to nuclear reactions (equation 2.48) and $\dot{Y}_{i,\text{mix}}$ is the rate of change due to mixing, which—since all mixing is approximated as a single diffusive process—is given by Fick’s second law of diffusion:

$$\dot{Y}_{i,\text{mix}} = \frac{\partial}{\partial m} \left(\sigma_D \frac{\partial Y_i}{\partial m} \right), \quad (2.49)$$

where σ_D is the 1-D (radial) Lagrangian diffusion coefficient with units of $\text{g}^2 \text{s}^{-1}$ and m is the mass coordinate.

2.4 Essential physical and empirical data

Previously in this section, I have highlighted how extra information about the properties and behaviour of the stellar material under a range of conditions is required in order to solve the equations quantitatively. Unlike other stellar evolution codes, such

as GENEC, STERN, KEPLER and FRANEC (for massive stars), MESA does not have one relatively fixed set of physical treatments and assumptions (e.g. the choice of Schwarzschild or Ledoux criterion to determine convective stability). Instead, several prescriptions are typically available and the user is given the choice of which to use. Stellar evolution codes other than MESA often do have the option to choose between different sets of input physics however the breadth of choice in the MESA code is particularly extraordinary. Indeed, the fact that the MESA code provides so many choices is one of its defining characteristics, making it somewhat of a stellar evolution ‘sandbox’. In one sense, this makes the MESA code difficult to place in the field of stellar evolution where for years the long-standing codes have been defined by the choices of these physics that they make. In a more positive light, the existence of something like the MESA code enables the scientific community to push currently accepted physical treatments to their breaking point and provide new treatments in their place. Some of the key sources and origins of the data, tables and physical treatments to support the structure equations in their solution in MESA are explained below. Afterwards, I will summarise the choices, where applicable, that were made for the simulations that produced the results presented in this thesis.

2.4.1 EOS and opacities

In Eq. 2.6, the equation of energy transport or temperature stratification for example, it is clear that two main physics inputs are needed - the opacity of the stellar material $\kappa(T, \rho, X)$, and the equation of state of the stellar material $P(T, \rho, X)$, giving the pressure. The opacity and pressure of the stellar material are both quantities whose evaluations in turn require detailed calculations. However, since both $\kappa(T, \rho, X)$ and $P(T, \rho, X)$ are fixed properties of the material, their calculation can be pre-processed and provided to the stellar evolution code in tabular format. In MESA, the `eos` module gives the pressure as a function of density and temperature, which are the independent variables. The `kap` module gives the opacity as a function of density, temperature and composition. The coverage of the MESA EOS and κ modules in the $\log \rho - \log T$ plane

is shown in Figs. 2.1 and 2.2, respectively. The MESA EOS tables are constructed from OPAL (Rogers & Nayfonov 2002) tables and for lower temperatures, SCVH (Saumon, Chabrier & van Horn 1995) tables are used and account for the partial dissociation and ionisation of the composition. For intermediate conditions, these two tables are blended in a pre-processing manner, the blended region being illustrated in Figure 2.1 by the blue dotted line. Outside of the regions covered by these tables in the density–temperature plane, the HELM (Timmes & Swesty 2000) and PC (Potekhin & Chabrier 2010) EOSs are employed, again being blended at the boundaries of the MESA table. This blending region is shown in Figure 2.1 by the black dashed line. The blending is performed using a sinusoidal function for each of the physical quantities provided by the EOS (see Paxton et al. 2011 for further details).

MESA offers the choice either to use the OPAL Type 1 (Iglesias & Rogers 1993) or Type 2 (Iglesias & Rogers 1996) radiative opacity tables. The type 2 opacity tables account for varying abundances of C and O, rather than assuming the C and O abundances to scale directly with the metallicity. This is especially important for the AGB and super-AGB stars, whose deep second dredge-up mixes primary C and O to the surface. The MESA opacity tables are constructed in a pre-processing manner from several sources, including the equations of (Buchler & Yueh 1976) for $\log_{10}(T/\text{K}) > 8.7$ where Compton scattering becomes the dominant source of radiative opacity. Electron conduction opacities for $-6 \leq \log_{10}(\rho/\text{g cm}^{-3}) \leq 9.75$ and $3 \leq \log_{10}(T/\text{K}) \leq 9$ are those of Cassisi et al. (2007). Outside of the regions covered by Cassisi et al. (2007) two different fits to the electron conduction tables of Hubbard & Lampe (1969) are used. In the non-degenerate case, the fits of Iben (1975) are used, while in the degenerate case the fits of Yakovlev & Urpin (1980) are used. In the region where there is an absence of radiative opacity calculations (between the lines labelled $\log R = 1$ and $\log R = 8$ in Figure 2.2), the radiative opacities are fixed at their value of $\log R = 1$ and combined with the electron conduction opacities. For further details of the MESA opacity tables outside of the regions discussed here and of the table boundary blending schemes, the reader is referred to Paxton et al. (2011).

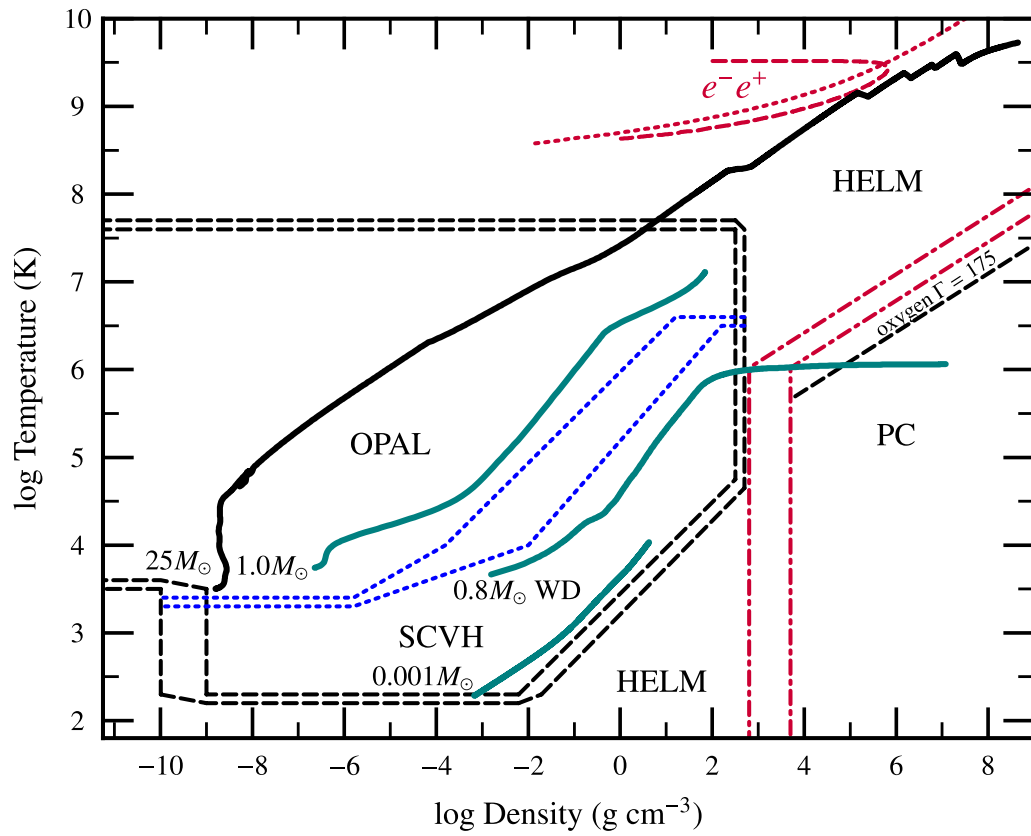


Figure 2.1: Regions in the $\log \rho - \log T$ plane covered by the MESA EOS module (Paxton et al. 2011). The dotted blue lines show the region where the OPAL and SCVH tables are blended to produce the MESA EOS tables. The dashed black lines show the region where the MESA EOS is blended with either the HELM or PC EOS, and the red dot-dashed lines where the HELM and PC EOSs are blended.

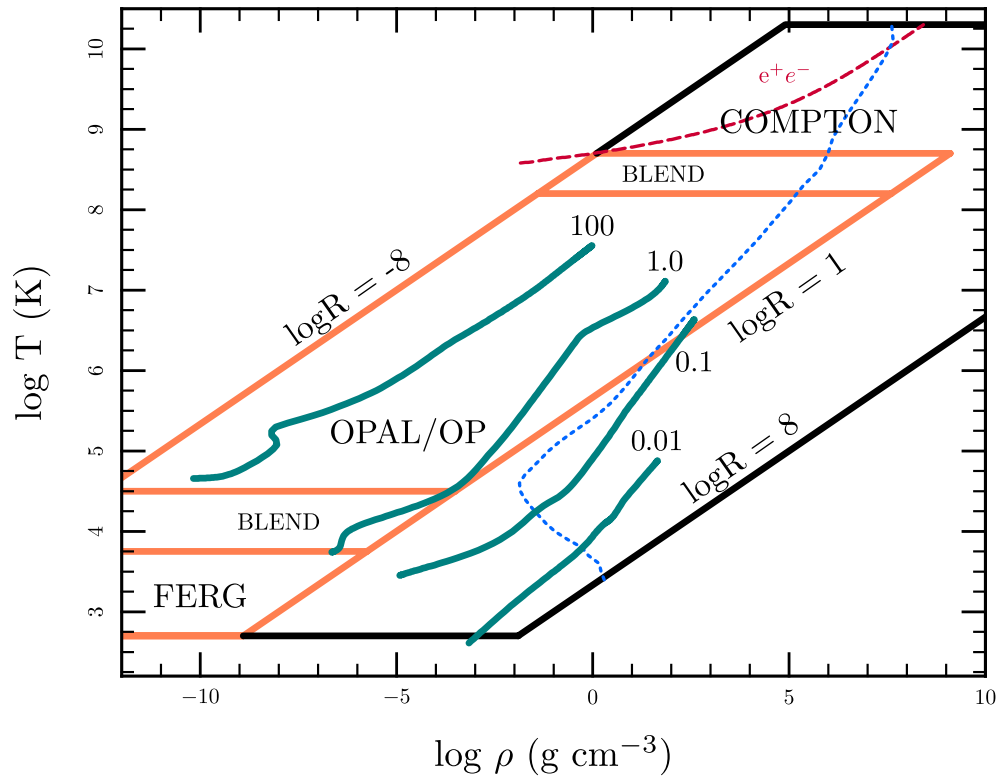


Figure 2.2: Regions in the $\log \rho - \log T$ plane covered by the MESA opacity module (Paxton et al. 2011). The orange lines bound regions for which tabulated radiative opacities are available. The blue dotted line marks the region for which electron conduction becomes the dominant source of opacity and the solid black line extends to regions where total opacities are a combination of the radiative opacity at the line $\log R = 1$ and electron conduction opacities (see text for details).

2.4.2 Nuclear reaction rates

In the MESA code, most reaction rates were taken from the REACLIB compilation (Cyburt et al. 2010). These rates are supplied as functions of the temperature in GK (T_9),

$$\lambda = \exp \left[a_0 + \sum_{i=1}^5 a_i T_9^{\frac{2i-5}{3}} + a_6 \ln T_9 \right], \quad (2.50)$$

where a_{0-6} are the fitting parameters from the compilation. For each reaction, λ is computed from the fits and can be used in equation 2.48 for the nuclear reaction network. In equation 2.50, λ has units of s^{-1} for single-body reactions. For two-body reactions, the quantity provided by the formula in 2.50 is actually $N_A \langle \sigma v \rangle$ with units of $\text{cm}^3 \text{mol}^{-1} \text{s}^{-1}$, where $\langle \sigma v \rangle$ is the velocity-integrated reaction cross section and N_A is Avagadro's number. With each of the sets of fitting parameters, a Q-value for the reaction is also supplied for the purposes of calculating the release of nuclear energy production from each reaction in the network. REACLIB provides sets of recommended reaction rates including those with both theoretical and experimentally measured contributions. Indeed, preference is given to the experimentally determined rates where applicable and often the experimental rates are provided by the NACRE compilation¹ (Angulo 1999; Angulo et al. 1999).

There are some exceptional reactions for which the recommended rates provided by the REACLIB compilation are not used. These include the rate for $^{14}\text{N}(p, \gamma)^{15}\text{O}$ measured at the LUNA facility in Dresden (Imbriani et al. 2004), which is important in the hydrogen-burning CNO cycle. The rate of Fynbo et al. (2005) was used for the triple- α (3α) reaction during helium burning. This rate was calculated using measurements of the $^{12}\text{C} \rightarrow 3\alpha$ decay, which showed a dominant resonance in the ^{12}C nucleus with an energy of about 11 MeV. This is also directly relevant to supernova explosions, in which the photodisintegration of carbon into α -particles is of paramount importance for explosive nucleosynthesis. The rate of Kunz et al. (2002) was used for

¹<http://pntpm3.ulb.ac.be/Nacre/nacre.htm>

$^{12}\text{C}(\alpha, \gamma)^{16}\text{O}$, in which several interfering resonances are shown to contribute to the rate.

Weak reaction rates and associated neutrino-loss rates are those of Fuller, Fowler & Newman (1985), Oda et al. (1994) for *sd*-shell nuclei, Langanke & Martínez-Pinedo (2000) for *pf*-shell nuclei and, as will be discussed in sections 3.1.3 and 4.4, Toki et al. (2013) for *sd*-shell nuclei.

2.4.3 Mass loss

The stellar wind is still a very uncertain phenomenon. Mass is lost from the outer layers of the star into the interstellar medium by several mechanisms. The microphysics behind some of these processes involve line-dominated opacities (i.e. from specific isotopes, atoms, molecules and dust) and the generation and regeneration of magnetic field lines. Rotation also contributes to mass loss: the addition of centrifugal force modifies the amount of momentum needed to drive a unit of mass from the surface (Maeder 2009). In addition, rotation implies asymmetrical mass loss in some cases. Mass loss rates are generally prescribed separately for the hot and cool side of the Hertzsprung-Russell diagram (HRD), where the surface conditions are quite different. Hot stars on the main sequence with radiative envelopes experience line-driven mass loss. This type of mass loss is caused when the components of the stellar plasma exhibit high opacities at the relevant temperatures and thus momentum is imparted to the material by photons (Vink, de Koter & Lamers 2001). Hence, the mass loss rate is sensitive to the surface temperature and composition of the star. Cool stars on the RGB or AGB have very extended envelopes with deep convection zones. The material at the surface is more loosely bound and the mass loss is much harder to constrain physically. Pulsations and the formation of dust are known to become important in this situation (van Loon et al. 2005).

About 70% of massive stars will have some degree of interaction with a binary companion over the course of their lives (Sana et al. 2012). Mass transfer further complicates the problem of mass loss and greatly enriches the spectrum of types of

stars, evolutionary paths and supernova types. I highlight this here out of necessity - binary interaction is the elephant in the room of stellar evolution calculations, and although it is fair to say that binary interaction could be simulated by enhanced mass loss in 1D stellar models, one third of the massive stars in interacting binaries will experience merger events.

In MESA, the mass loss scheme for massive stars is taken from Glebbeek et al. (2009). For effective temperatures of $\log(T_{\text{eff}}/\text{K}) < 4$, it uses de Jager, Nieuwenhuijzen & van der Hucht (1988). For $\log(T_{\text{eff}}/\text{K}) > 4$ there are two prescriptions used, depending on the abundance of hydrogen at the surface: for $X_{\text{S}}(^1\text{H}) > 0.4$, Vink, de Koter & Lamers (2001) is used and for $X_{\text{S}}(^1\text{H}) < 0.4$, the Nugis & Lamers (2000) prescription is used. The Nugis & Lamers (2000) rate is used for quite massive stars ($M \gtrsim 30M_{\odot}$) that will become the Wolf-Rayet star progenitors of type Ibc supernovae. The rate of de Jager, Nieuwenhuijzen & van der Hucht (1988) is used for the red supergiant phase, while the rate of Vink, de Koter & Lamers (2001) is used mostly during the main sequence. Although there is not a free parameter in the mass loss rate of de Jager, Nieuwenhuijzen & van der Hucht (1988), it is worth reiterating that the mass loss rates for stars on the cool side of the Hertzsprung-Russell diagram are very uncertain. Typically, a factor of 0.8 is applied to empirically-determined rates in non-rotating models. This is to compensate for the fact that the observations from which the rates are determined are of rotating stars (see Maeder & Meynet 2001).

For lower mass stars (AGB, super-AGB), the prescription of Reimers (1975) is used for the red giant branch. Although quite an old mass loss rate, the mass lost in this phase is only about 1 – 3% of the total stellar mass for stars with $M_{\text{ini}} \gtrsim 3M_{\odot}$ and the rate agrees with more recent calculations (Blöcker 1995). For the AGB, the rate of Blöcker (1995) is preferred, since it is derived from dynamical calculations of Mira-type variables and fits the observed initial–final mass relation for AGB stars.

2.4.4 Neutrino energy losses

At the densities encountered in stellar interiors, to an excellent approximation, the neutrino mean free path will be much longer than the stellar radius. As a result, any neutrino production in a region of the star will result in a direct energy loss from that region. The energy loss from non-nuclear neutrino processes are prescribed in the code by using the fits of Itoh et al. (1996). For each zone, these fits give the energy loss ϵ_ν (MeV g⁻¹ s⁻¹) that is to be used in the energy conservation equation (2.5). These fits do not include energy losses due to neutrinos produced by weak nuclear reactions. Weak reaction rates could be considered more complex than thermonuclear fusion rates in the sense that they are strongly dependent upon the electron number density of the stellar material and must also be provided together with neutrino loss rates. These neutrino loss rates are included in the term ϵ_{nuc} (MeV g⁻¹ s⁻¹) in the energy conservation equation (2.5). The method of calculation of these neutrino losses will be described in detail in Chapter 4, while in this short section I will outline the non-nuclear neutrino production mechanisms.

The neutrino production processes are categorised as follows (Fowler & Hoyle 1964; Itoh et al. 1996):

$$\begin{aligned}
 \textit{Neutrino bremsstrahlung} : & \quad e^\pm + {}^A\text{Z} \rightarrow e^\pm + {}^A\text{Z} + \nu + \bar{\nu} \\
 \textit{Pair annihilation} : & \quad e^+ + e^- \rightarrow \nu + \bar{\nu} \\
 \textit{Plasmon decay} : & \quad \gamma_{\text{pl}} \rightarrow \nu + \bar{\nu} \\
 \textit{Photoneutrino process} : & \quad e^- + \gamma \rightarrow e^- + \nu + \bar{\nu}
 \end{aligned} \tag{2.51}$$

The dominant mechanisms of neutrino production across the $\rho - T$ plane are shown in Figure 2.3.

The pair creation process dominates at high temperatures where electron–positron pairs are produced in dynamic equilibrium with the black-body radiation and are converted directly to a neutrino–anti-neutrino pair (Chiu & Morrison 1960). A plasmon is a quanta of plasma oscillation, which is an oscillation in the electron density. Plasmons are quasi-particles that are unstable to decay, which can produce a neutrino–anti-

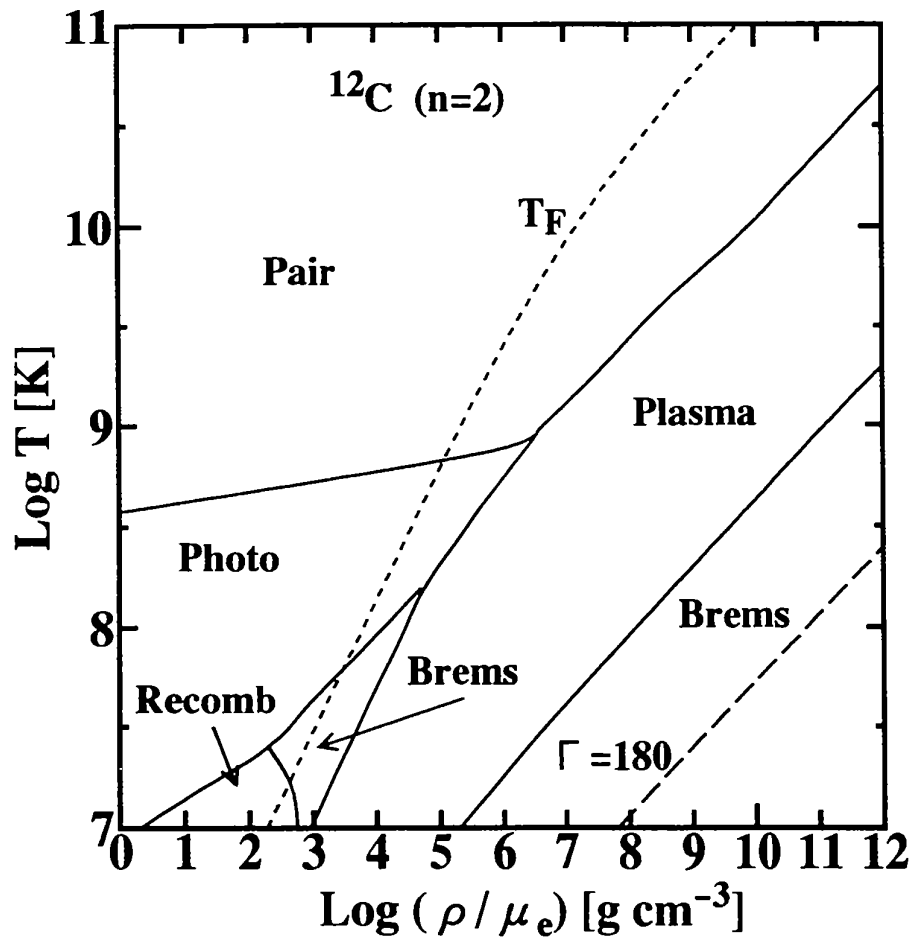


Figure 2.3: Dominant mechanisms of neutrino production across the $\rho - T$ plane, from Itoh et al. (1996). T_F is the Fermi temperature and $\Gamma = 180$ (dashed line) is the melting curve of the ionic Coulomb solid.

neutrino pair (see Adams, Ruderman & Woo 1963 and Beaudet, Petrosian & Salpeter 1967 for further details about plasmons, and in particular their transverse and longitudinal components). The neutrino production rate due to plasmon decay is a strongly peaked function of the electron density ρY_e ; it is a maximum in the domain where $\hbar\omega_0 \gg kT$, where ω_0 is the plasma frequency. The plasma neutrino energy loss rate is therefore peaked at higher electron densities for higher temperatures (see Figure 2.3 and Beaudet, Petrosian & Salpeter 1967). A small region of the $\rho - T$ plane is dominated by the recombination process, where an electron in a continuum state undergoes a transition to a bound state (Kohyama et al. 1993).

2.5 Modelling assumptions in this work

The stellar models presented in this thesis were calculated with the *Modules for Experiments in Stellar Astrophysics* (MESA) stellar evolution code (Paxton et al. 2011), revision 3709. The models were calculated from the pre-main sequence assuming a uniform initial composition with a metal fraction of $Z = 0.014$ (solar metallicity) and elemental abundances taken from Asplund et al. (2004). The effects of rotation are not considered in the present work.

In MESA, convective mixing is treated as a time-dependent, diffusive process with a diffusion coefficient, D_{MLT} , as described in detail in section 2.2.1 and 2.3. The mixing length parameter used for these models is $\alpha_{\text{MLT}} = 1.73$, calibrated from fitting the parameters of the Sun (see, e.g., Herwig et al. 2012). While it is considered standard procedure to calibrate the mixing length parameter in order to reproduce the solar parameters, it is important to keep in mind that there is no particularly good reason that one should expect the parameter to be insensitive to the initial mass of the model, the location in the star or the evolutionary phase. During the entire evolution sequence convective stability is defined by the Schwarzschild criterion (2.25) with the exception of the late stages of the $8.75 M_\odot$ and $8.8 M_\odot$ models (when electron captures begin to dominate the evolution of the core) where instead the Ledoux criterion (2.26) is

used (Miyaji & Nomoto 1987, see section 2.2). Mixing at convective boundaries is treated with an exponentially decaying diffusion coefficient (Freytag, Ludwig & Steffen 1996; Herwig 2000) of the form shown in 2.47. For all convective boundaries the free parameter of this treatment is taken as $f_{\text{CBM}} = 0.014$ with the exception of the base of convective shells burning nuclear fuel, for which a stricter value of $f_{\text{CBM}} = 0.005$ is used. This includes the lower boundary of the convective envelope in the super-AGB models because the hydrogen-burning shell extends into the convective layer (hot-bottom burning; see, e.g., Boothroyd, Sackmann & Ahern 1993). Such a reduced efficiency of convective boundary mixing across the base of convective shells in which nuclear fuel is burning is indicated from both He-shell flash convection in AGB stars (Herwig 2005) as well as nova shell flashes (Denissenkov et al. 2013a). Exactly how much the f_{CBM} parameter should be reduced for these kinds of boundaries (for example, at the base of the carbon-burning or neon-burning shells) is at present not clear. What the 3D simulations do show, however, is that the velocity profile at the boundary is never discontinuous and some extra mixing should occur. During the silicon-burning stage of the $12 M_{\odot}$ model, no convective boundary mixing is assumed ($f_{\text{CBM}} = 0$). This choice is not informed by considerations of physics or astrophysical observations, but can be instead thought of as a conservative approach with two motivating factors. Firstly, since the $12 M_{\odot}$ model is the canonical massive star in this set of models, an attempt was made to use similar assumptions to the ones made in well-established codes during silicon-burning (e.g., the Geneva stellar evolution code GENECE and the KEPLER code). Secondly, as will be described below, a simplified nuclear reaction network is used for the silicon-burning phase in the $12 M_{\odot}$ model because it is a practical impossibility to include all of the (important) details of silicon burning in the MESA code at the present time. Taking stock of the many short-comings in stellar models of silicon-burning stars, I decided that it was better not to introduce new uncertainties into a model that will ultimately serve as a comparator for the others. That being said, I have begun to compare models of massive stars computed with some of the leading stellar evolution codes (GENECE and KEPELR) with those I have calculated with MESA in order to quantify some of the key differences and their impact on the

nucleosynthesis. Quantitative predictions of the impact of different physics assumptions on the nucleosynthesis in stars can be compared with observations, either directly or indirectly (e.g. via simulations of galactic chemical evolution). Future 3D simulations are also required to constrain the behaviour of convective boundary mixing under the wide range of physical conditions that are encountered in stars and hence in stellar models, in particular for the advanced burning stages.

MESA solves the coupled stellar structure, nuclear burning, and abundance mixing equations simultaneously. In cases where the burning timescale is much longer than the mixing timescale, as for example during core H-burning on the main sequence, then MESA's coupled calculation and an operator-split calculation will agree. In cases where the nuclear burning time scale is similar or shorter compared to the mixing time scale, the coupled method provides consistent abundance profiles in convection zones, whereas operator-split calculations require a special treatment for chemical species with short nuclear timescales and smaller time steps. Note that in exceptional cases where the energy release by simultaneous burning and mixing is so large that the approximations of MLT are violated, then all 1D methods become inaccurate and 3D hydrodynamic simulations are necessary (see, e.g., Herwig et al. 2011).

The nuclear energy production and composition evolution is followed with a nuclear reaction network of 114 isotopes from ^1H to ^{61}Co including the NeNa cycle, URCA processes, alpha chains and electron-captures by ^{24}Mg , ^{24}Na , ^{20}Ne and ^{20}F along with their inverses. Figure 2.4 shows the detail of the network. Such a large network is required to follow both nucleosynthesis and energy production in these models. For example ^{30}Si and ^{34}S are the main products of O-burning in the lowest-mass massive stars as opposed to ^{28}Si and ^{32}S in more massive stars owing to higher degeneracies and thus higher electron capture rates (see, e.g., Thielemann & Arnett 1985). In stars with degenerate cores close to the Chandrasekhar limit (2.16), accurately calculating the electron fraction, Y_e , is very important because only a slight reduction in Y_e can cause significant contraction. Further isotopes are included implicitly to account for non-negligible reaction channels, for example $^{44}\text{Ti}(\alpha, p)^{47}\text{V}(p, \gamma)^{48}\text{Cr}$ is included but the abundance of ^{47}V is not explicitly calculated. These implicit isotopes can be seen

in Figure 2.4 where there is an arrow junction on an unshaded isotope.

For the 8.2, 8.7 and 8.75 M_{\odot} models that become SAGB stars, a network optimised for the AGB phase, including 37 isotopes and the relevant nuclear processes listed above, is employed from the time of completion of second dredge-up. During the silicon-burning stage of the 12 M_{\odot} model the simplified 21-isotope network `approx21.net`, that is available in the MESA code, is used. It is common for simplifications to the nuclear reaction network to be made in order to efficiently deal with the many high rates of forward and reverse reactions. The mass-loss rates used in this work are those of Reimers (1975; $\eta = 0.5$) for the red giant branch (RGB) phase and Blöcker (1995; $\eta = 0.05$) during the asymptotic giant branch (AGB) phase.

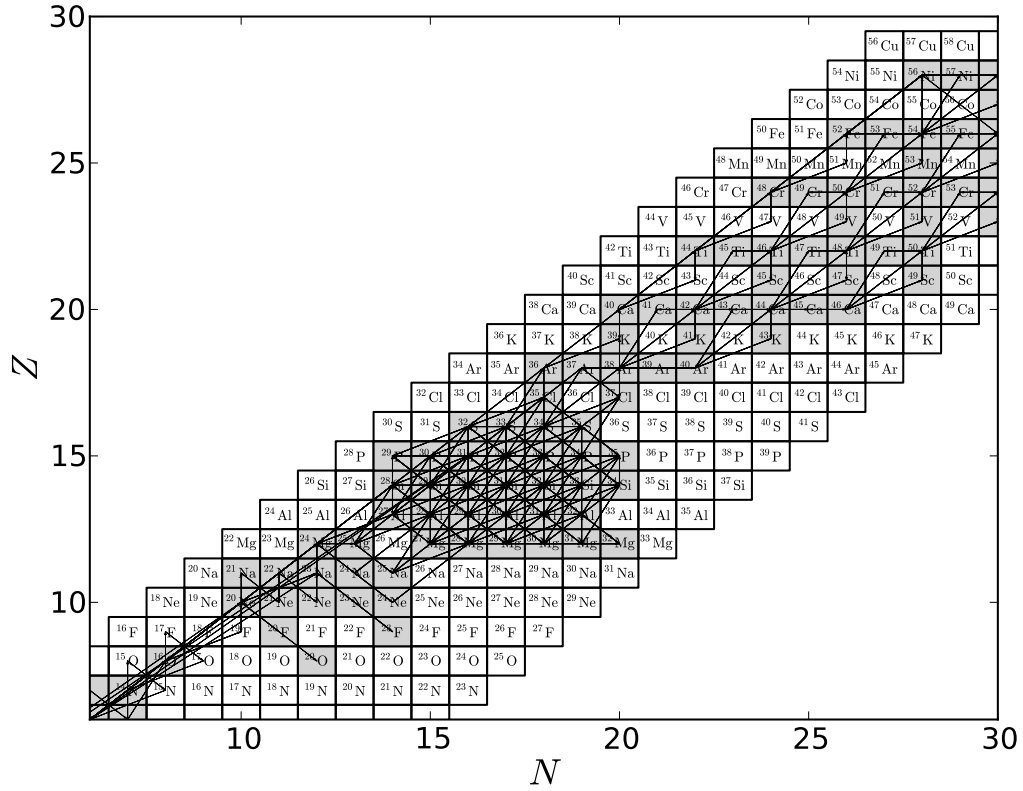


Figure 2.4: The nuclear reaction network used in these calculations. The abundances of the shaded isotopes are followed explicitly. Reactions are shown with arrows, and implicitly included isotopes (ones whose abundances are not calculated explicitly but through which reactions are considered to proceed) can be seen where there is an arrow junction on an unshaded isotope. This network was used for all of the models with the exception of the TP-SAGB phase in the 8.2, 8.7 and 8.75 M_{\odot} models and the post oxygen-burning phase in the 12 M_{\odot} model. In these phases, appropriate smaller, more efficient networks are used (see text for details).

3 Models of 8–12 M_{\odot} stars

In this chapter, newly computed models of solar metallicity ($Z = 0.014$) stars at the transition between super-AGB stars and massive stars are described in detail. The models were computed with the stellar evolution code MESA, which is a community-developed tool. The MESA code was described in chapter 2 along with the modelling assumptions that have been tuned for the simulation of stars across the transition mass range between AGB stars and massive stars. The general evolution of the six models is discussed and later the properties of neon and oxygen shell burning that occur in the 8.8 and 9.5 M_{\odot} models are analysed. The effects of hydrodynamical processes that are poorly constrained in 1D models on the behaviour of shell burning and hence the fate of the stars are examined and tested. This chapter contains results that were published in the *Astrophysical Journal* this year (Jones et al. 2013).

3.1 Evolution and fates

In this section, the evolution and fate of the models is described in the following order. In section 3.1.1 the early evolution of the models from the main sequence to the end of carbon burning is briefly outlined. Sections 3.1.2 and 3.1.3 then describe in detail the late evolution of the super-AGB and massive star models, respectively.

3.1.1 Evolution to the end of carbon burning

During the main sequence, fusion of hydrogen into helium in the convective core results in a reduced opacity and increased mean molecular weight, μ . The increase in μ leads to an increase in luminosity ($L \propto \mu^4$ for an ideal gas with negligible radiation pressure, e.g. Prialnik 2000 eq. 5.47 with $\beta \approx 1$). The pressure decreases modestly as μ^{-1} for an ideal gas, and the core contracts. The reduction in opacity dominates over the increase in luminosity during the main sequence and because $\nabla_{\text{rad}} \propto \kappa L_r P$, the

radiative temperature gradient decreases. The adiabatic temperature gradient on the other hand, increases slightly. As a result, the material at the edge of the core becomes convectively stable and therefore the mass of the convective core decreases during the main sequence lifetime of the star.

Another way of considering the decrease in mass of the convective core during the main sequence involves entropy. The entropy in an ideal gas and radiation mixture is (Clayton 1983, 2-136)

$$S = \text{const} + \frac{N_A k}{\mu} \ln \frac{T^{\frac{3}{2}}}{\rho} + \frac{4a}{3} \frac{T^3}{\rho}, \quad (3.1)$$

with the second and third terms from the gas and radiation, respectively, a is the radiation density constant and the other symbols have their usual (thermodynamic) meanings. The thermodynamic conditions remain in a steady state during the main sequence because the Kelvin-Helmholtz time-scale ($\tau_{\text{KH}} = E_g/L$) is much shorter than the nuclear timescale ($\tau_{\text{nuc}} = \epsilon_{\text{nuc}} M_{\text{core}}/L$). If this was not the case, the star would be contracting in order to provide the luminosity required to support the star while fuel was burning (see, e.g. Kippenhahn & Weigert 1990, section 30.5). Thus, on the main sequence the star is in equilibrium and hydrogen-burning energy production is in a steady-state, where the nuclear reactions are self-regulating in the following way. The nuclear reactions produce energy and thus increase the temperature of the material. The pressure increases and the core expands, lowering the temperature and moderating the reaction (and thus energy production) rates. The temperature, density and pressure remain reasonably constant due to this self-regulation. As discussed earlier, the mean molecular weight increases from roughly $\frac{1}{2}$ to $\frac{4}{3}$ during hydrogen burning, and equation 3.1 thus shows that the entropy in the convective core will decrease as a result of the mean molecular weight increase. The entropy can be thought of as a measure of how intrinsically hot the material is. Consider that a fluid parcel is displaced into new surroundings and expands to reach pressure equilibrium adiabatically (i.e. at constant entropy). If the entropy of the fluid parcel is higher than that of the surroundings, the parcel will also have a higher temperature than the surroundings. For an ideal gas in which $P \propto \rho T$, this means that the parcel will have a lower density than its

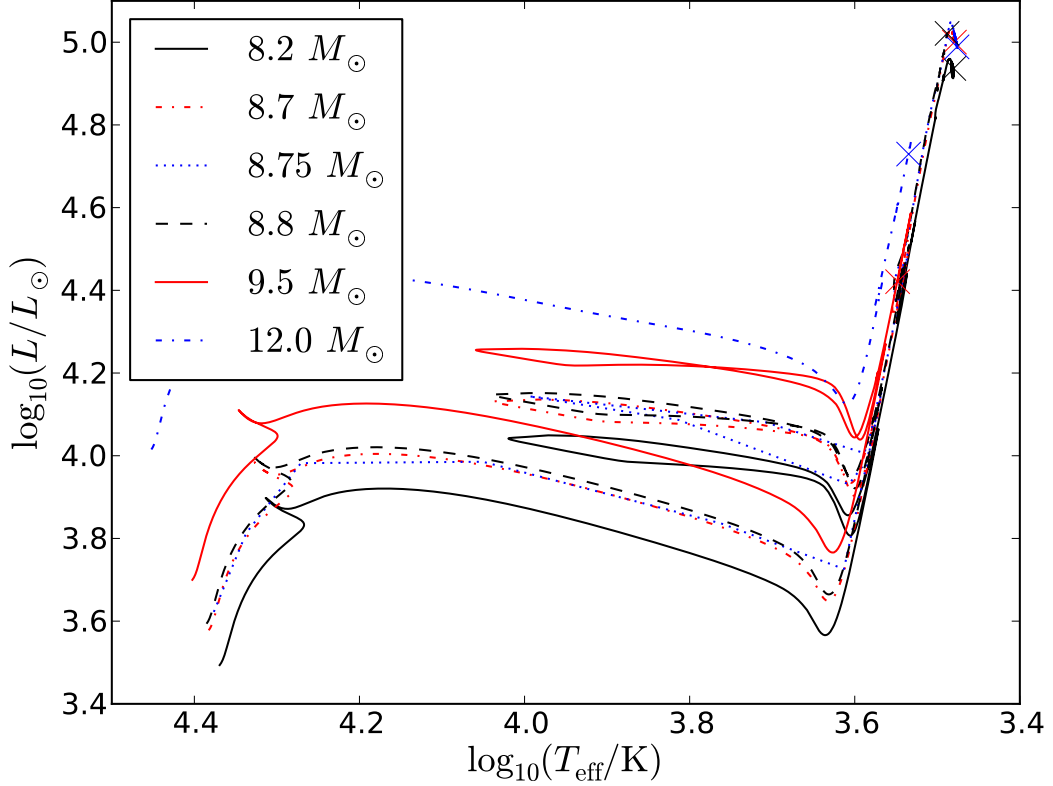


Figure 3.1: Evolution of all the models in the Hertzsprung-Russell diagram; final luminosities are indicated by crosses. The $12 M_{\odot}$ model is the only model not to exhibit a blue loop (see text for details). By virtue of their deep second dredge up and subsequent dredge-out, the 8.2 , 8.7 , 8.75 and $8.8 M_{\odot}$ stars become much more luminous than the $9.5 M_{\odot}$ and even the $12 M_{\odot}$ stars during the late stages.

new surroundings and will thus be dynamically unstable. With this consideration in mind, the lowering of the entropy of the material in the convective core—caused by the reduction in μ —makes it more difficult for the core material to mix with the overlying layer. As a result, the material at the edge of the convective core becomes convectively stable.

The evolution of all the models in the Hertzsprung-Russell diagram (HRD) and the central density–temperature ($\rho_c - T_c$) plane are shown in Figures 3.1 and 3.3,

respectively. The HRD in Figure 3.1 shows that with the exception of the $12 M_{\odot}$, all of the models evolve blue-wards during helium burning (after ascending the red giant branch, RGB). This evolutionary feature is called a blue loop. The behaviour of the effective temperature as a function of central helium abundance is shown in Figure 3.2, with the helium-burning evolution beginning in the lower right of the Figure, and ending in the lower left. The blue loop is clearly shown by the arc between roughly $X_c(^4\text{He}) = 0.5$ and 0. The location in the HRD after the main sequence turn-off is determined by a complex interplay between the helium core, the hydrogen-burning shell and the opacity of the envelope. In general, as the core contracts the envelope will expand—a mirroring effect. During the core helium-burning evolution the structure is more complicated than during the main sequence. This is because there is a hydrogen-burning shell between the core and the envelope. The hydrogen-burning shell in fact provides a large fraction of the stellar luminosity during core helium-burning. The occurrence of the blue loop has been shown to be sensitive to the hydrogen profile encountered by the hydrogen-burning shell as it burns outwards in mass, strongly linked to the proximity of the shell source to the lower extent of the convective envelope (Lauterborn, Refsdal & Weigert 1971). More recently, studies have shown that the behaviour of the blue loop is sensitive to the amount of convective overshooting at the base of the envelope (Stothers & Chin 1991), the CNO abundances (Xu & Li 2004), metallicity and mass loss (Meynet et al. 2013). This phenomenon is still rather uncertain, for example on the observational side the blue-to-red supergiant ratio as a function of metallicity shows the opposite trend to theoretical models, and on the theoretical side the results of the models depend very strongly on the parameters of very uncertain physical prescriptions (in particular, mixing and mass loss). Following hydrogen burning in all the models, the core is well-represented by an isothermal monatomic ideal gas and its mass well exceeds the Schönberg-Chandrasekhar limit. As the core contracts, the pressure at the core/envelope interface decreases as the core radius decreases. As the instability becomes more severe in this way, the central pressure, temperature and density are increasing and eventually helium burning is ignited at the stellar centre. The convective core grows in mass during the helium-

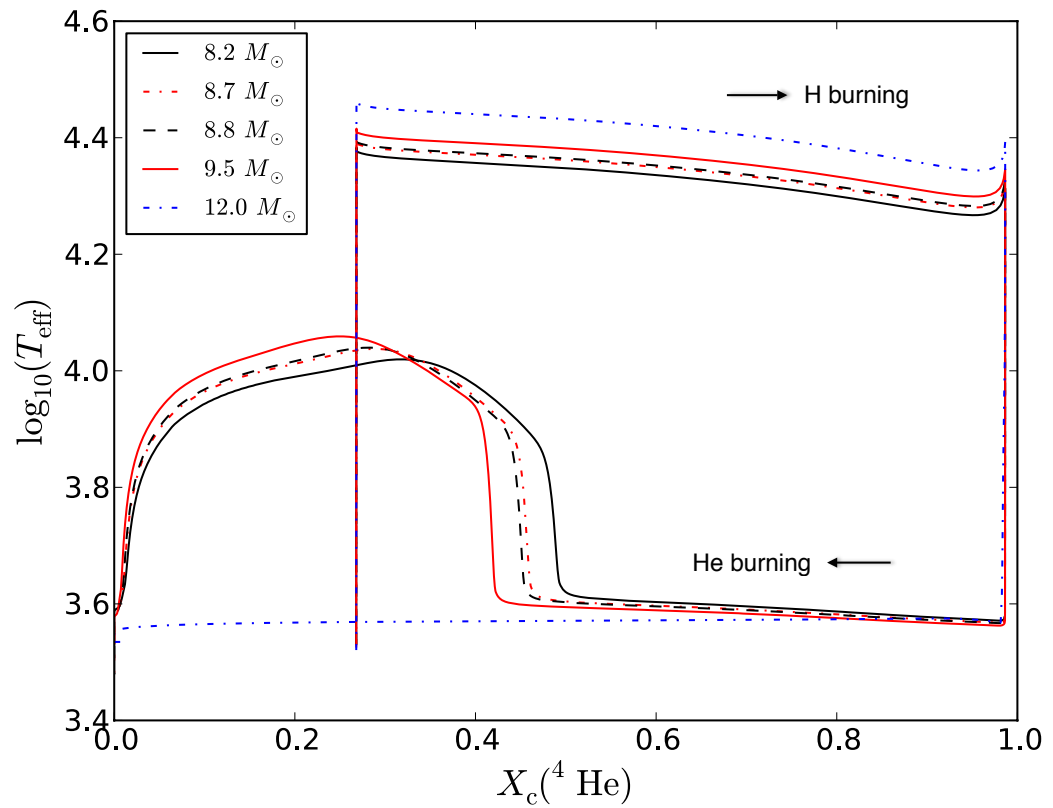


Figure 3.2: Effective temperature as a function of central helium abundance. The models evolve clockwise around the figure, with left-to-right evolution during hydrogen burning, and right-to-left evolution during helium burning. The arc during helium burning between central helium abundances of roughly 0.5 and 0.0 shows blue-wards evolution (seen as a blue loop in the HRD).

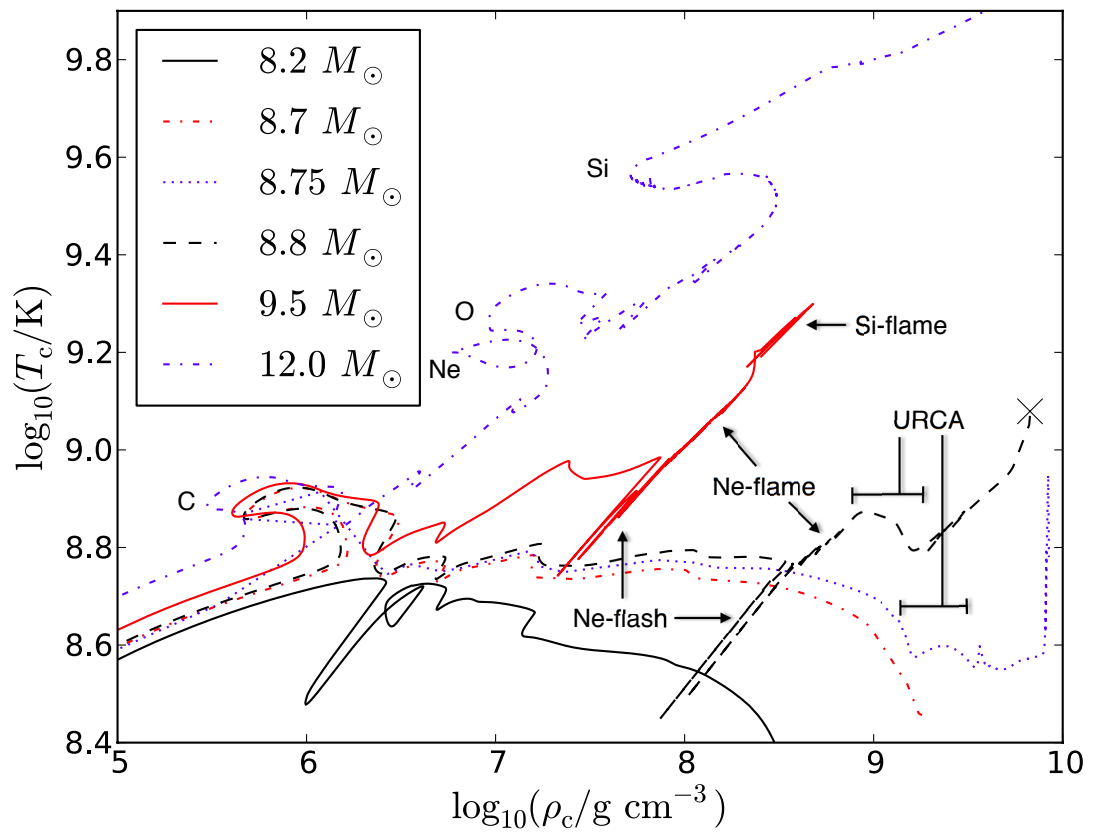


Figure 3.3: The divergence of the models following C-burning in the $\log_{10}(\rho_c) - \log_{10}(T_c)$ plane; the cross shows from where the evolution of the $8.8 M_\odot$ model was continued with the AGILE-BOLTZTRAN 1-D hydro-code.

burning lifetime. This is because the mass of the helium core (or hydrogen-free core) is also growing in mass due to (radiative) shell hydrogen burning. The core luminosity therefore increases and more helium-rich material becomes convectively unstable.

Following the core He-burning stage, core contraction is accompanied by an expansion of the envelope seen in Figure 3.5 as a deepening of the base of the convective envelope in mass. The penetration of the envelope convection into the helium core—the so-called second dredge-up—is not intuitive. Returning to the considerations of entropy that were discussed in Chapter 1, convection occurs when $ds/dr < 0$ and the mixing redistributes the entropy. As the pressure at the edge of the (helium) core decreases as the (helium) core contracts, the density also decreases while the temperature changes only a little, increasing the specific entropy of the material. Assuming adiabatic convection in the envelope, Sugimoto (1970) showed that when the entropy at the core–envelope interface was less than that in the envelope itself, indeed the mixing should not occur. In that case, the core mass should increase due to hydrogen shell burning. Sugimoto (1970) also showed that the inclusion of neutrino losses in a $10 M_{\odot}$ model accelerated the evolution of the core so strongly that $0.01 M_{\odot}$ of material was mixed into the envelope during the advanced burning stages, as opposed to $2.6 M_{\odot}$ when neutrino losses were not included.

Carbon is ignited centrally in all but the $8.2 M_{\odot}$ model, in which it is ignited at a mass coordinate of $0.15 M_{\odot}$ away from the centre and the C-burning front propagates to the centre (see Figure 3.5a). The off-centre ignition of carbon and its propagation to the stellar centre is a characteristic feature of super-AGB stars (Nomoto 1984; Ritossa, García-Berro & Iben 1999; Siess 2006; Siess 2009; Denissenkov et al. 2013b), and comes about in the following way. After helium is exhausted in the centre of the star, helium burning proceeds in a shell and as the core contracts, gravitational energy is released and acts to heat up the material. During the contraction between helium and carbon burning, the electrons in the central region of the core become partially degenerate, providing an additional source of pressure with which to counteract the gravitational contraction. As a result, the contraction is slowed down. More to the point, as the density increases and degeneracy comes into play, the plasma frequency

is significantly modified (see Clayton 1983, 3-305 and 3-306 for non-degenerate and degenerate expressions for the plasma frequency and section 2.4.4 for a description of neutrino loss processes). This means that the radiative transport of energy is carried by plasmons, which are unstable to neutrino-decay, rather than free photons, which are not (see section 2.4.4). Neutrinos are only likely to interact with matter at densities approaching $10^{11} \text{ g cm}^{-3}$, i.e. nuclear densities, which are astrophysically relevant only in the conditions arising during a core-collapse supernova (Janka 2001). The neutrinos produced from the plasmon interactions then freely stream from the core of the star with, to an excellent approximation, no interaction with the stellar material. In general, neutrino losses accelerate the evolution of stellar cores. The neutrino luminosity appears in the equation of energy conservation (equation 2.5), and one can see that to provide luminosity support in the absence of nuclear energy release (i.e. $\epsilon_{\text{nuc}} \approx 0$), the rate of gravitational energy release must increase. Neutrino processes compete with, and dominate over, gravitational energy release in the central regions of the contracting CO core (because contraction is inhibited by the degenerate electrons), producing a net cooling. The maximum temperature moves outwards from the centre and carbon burning ignites when and where the peak temperature reaches about $7 \times 10^8 \text{ K}$ (Siess 2006).

After the exhaustion of carbon in the centre, carbon burning proceeds in shells and from this point onwards the behaviour of the envelope begins to diverge across the $8 - 12 M_{\odot}$ mass range. In the models with $M \leq 8.8 M_{\odot}$ the timescale for expansion of the H-envelope is comparable to the evolutionary timescale. The core of the $8.2 M_{\odot}$ model is more degenerate than in the other, more massive models. As a result, electron degeneracy pressure provides a larger fraction of the total pressure in the $8.2 M_{\odot}$ model; the contraction of the core is thus slower. Helium burns in a shell on top of the carbon-oxygen (CO) core with periods of more vigorous burning coinciding with the extinguishing of carbon shells in the core below. At no point does helium burning produce a steep enough temperature gradient for the helium shell to become convectively unstable. Ultimately, the base of the envelope deepens in mass and engulfs the entire helium shell. Whether or not material from the CO

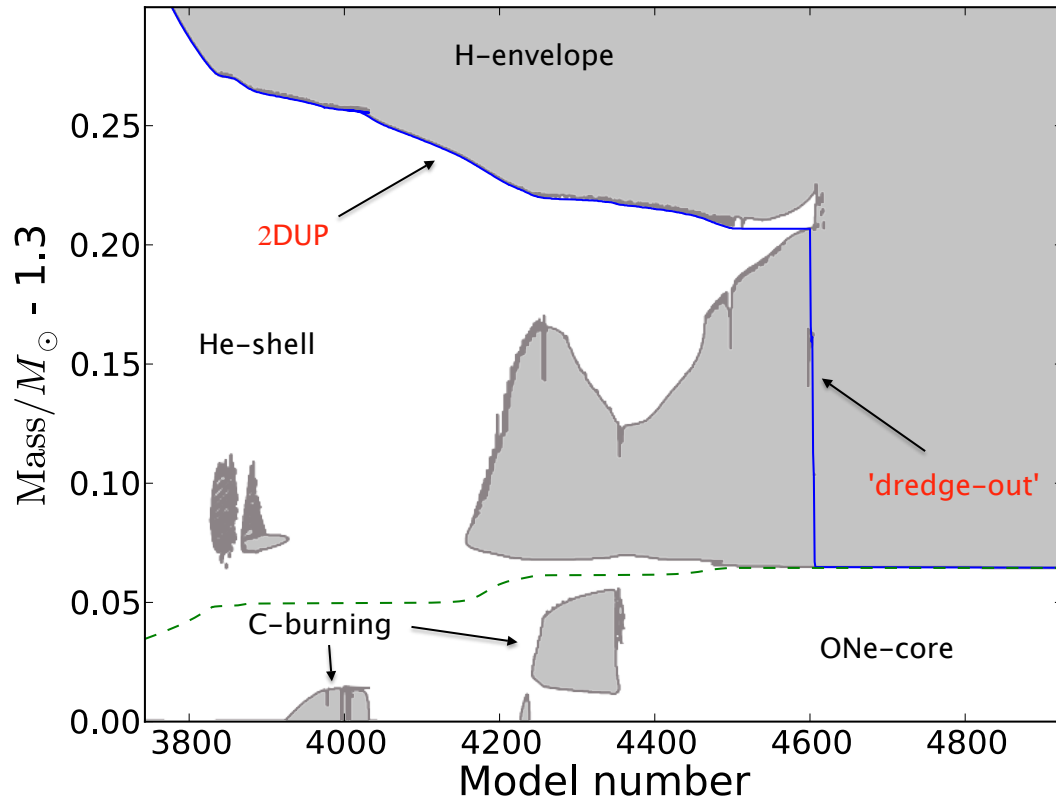


Figure 3.4: Kippenhahn (convective structure evolution) diagram of the dredge-out episode in the $8.75 M_{\odot}$ model. As the hydrogen envelope deepens in mass during the second dredge-up (2DUP), helium burning ignites in the helium shell, inducing convection. Hydrogen is not burning as the base of the envelope descends. The convective helium-burning region becomes more extended after the extinction of the last carbon-burning shell due to gravitational energy release and ultimately coalesces with the descending envelope. The hydrogen-free boundary mass—below which there is no hydrogen—is drawn with a solid blue line and the helium-free boundary mass is drawn with a dashed green line.

core is also mixed up into the envelope is still an open question. In the 8.7, 8.75 and 8.8 M_{\odot} models, the temperatures in the helium-burning shell are higher than in the 8.2 M_{\odot} model; helium burning is more energetic and induces convection before the base of the envelope can reach the edge of the CO core. The convection zone grows in mass due to the input of gravitational energy following the extinction of the last carbon-burning shell in the CO core below (see Figure 3.4). The convective helium shell merges with the hydrogen envelope, which becomes enriched with the products of complete hydrogen burning and incomplete helium burning. This phenomenon was given the name *dredge-out* by Ritossa, García-Berro & Iben (1999) in order to distinguish it from the second dredge-up. The second dredge-up experienced in the 8.2 M_{\odot} model mixes the helium-shell material into the envelope on a much longer time scale than the convective turnover time scale. The dredge-out in the 8.7, 8.75 and 8.8 M_{\odot} models, on the other hand, causes the enrichment to take place on the convective turnover time scale of the envelope. In addition, the rapid transport of protons down to helium-burning temperatures that takes place during dredge-out merits further study—such conditions are favourable for the production of neutrons and hence neutron-capture elements. Previous studies (Iben, Ritossa & Garcia-Berro 1997; Ritossa, García-Berro & Iben 1999) also find the formation of a semi-convective layer between the base of the envelope and the growing helium-burning convection zone in some models, however the outcome (*dredge-out*) is the same whether this layer is formed or not. In the 8.8 M_{\odot} model, as much as 0.8 M_{\odot} of He-rich material is mixed into the envelope. Aside from the huge increase in the amount of helium and helium-burning products that now resides at the surface following this deep mixing event, there are many other observable quantities resulting from dredge-out. In particular, the dredge-out is accompanied by a large increase in luminosity, inducing luminosities at the pre-SN stage larger than for the 12 M_{\odot} model as shown in Figure 3.1 (see also Eldridge & Tout 2004; Eldridge, Mattila & Smartt 2007).

In the 12 M_{\odot} model, the evolution of the core is accelerated by neutrino energy losses whereas the envelope expands on a thermal timescale. As a result the convective envelope remains unaltered after carbon burning. With decreasing initial mass, the

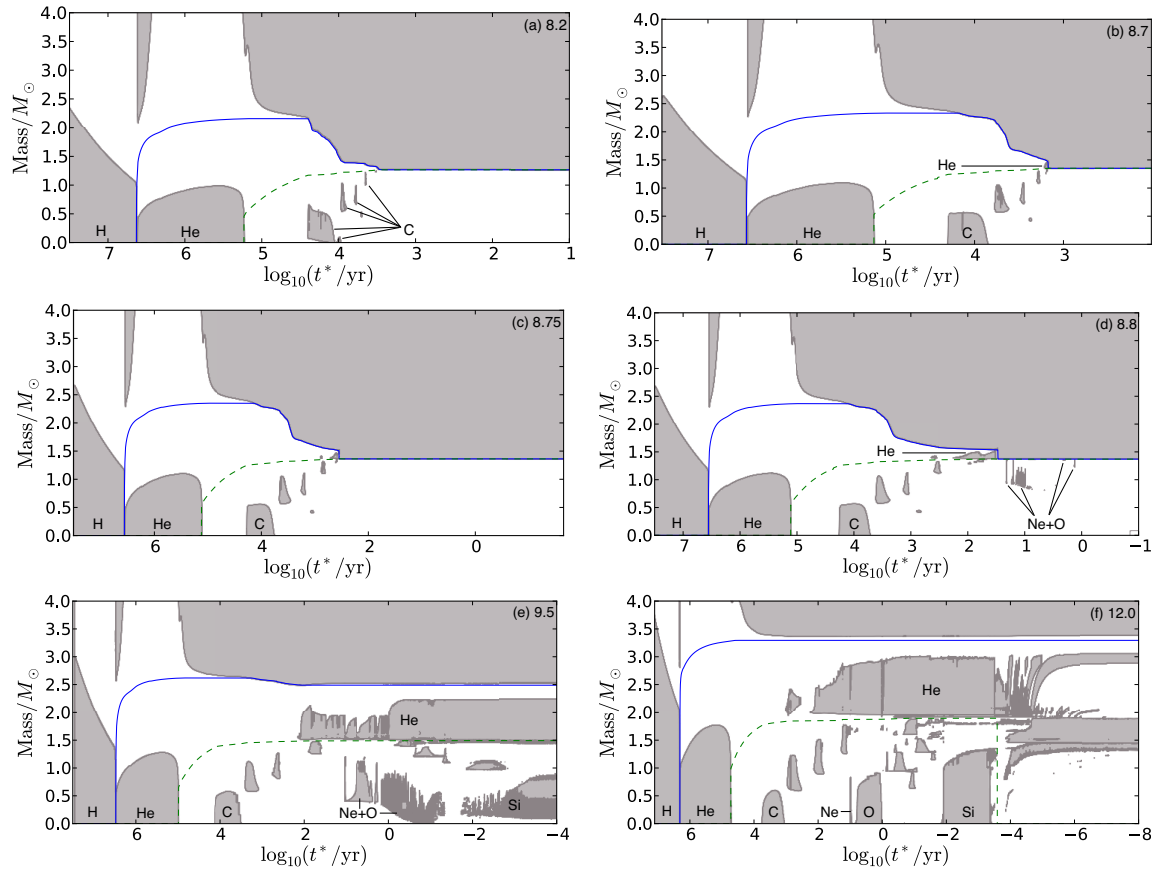


Figure 3.5: Evolution of convective structure (solid grey shapes) for the H-, He- and advanced burning phases of the models. t^*/yr is the time left until the end of the calculation. Solid blue and dashed green lines show the locations of the He- (H-free) and CO- (He-free) core boundaries respectively. Only the inner $4 M_{\odot}$ are shown.

core is more degenerate and compact following carbon burning and thus contraction is slower. This provides further energy and time for the expansion of the envelope, as can be seen at $\log_{10}(t^*/\text{yr}) \approx 4 - 3$ in Figure 3.5a-e.

3.1.2 Late evolution of the 8.2, 8.7 and 8.75 M_{\odot} (super-AGB) models

The 8.2 M_{\odot} , 8.7 M_{\odot} and 8.75 M_{\odot} models develop cores with masses that fall short of the critical mass for neon ignition (see § 3.1.3) following 2nd dredge-up ($M_{\text{CO}} = 1.2670$, 1.3509 and 1.3621 M_{\odot} respectively), developing thin (of the order of $10^{-5} - 10^{-4} M_{\odot}$) helium shells that soon develop a recurrent thermal instability producing transient He-fuelled convection zones (thermal pulses, TP). The 8.2 M_{\odot} star expels its envelope to become an ONe white dwarf (WD). It is uncertain whether the 8.7 M_{\odot} star would produce an ONe WD like the 8.2 M_{\odot} star, or whether its core would reach the critical central density for electron captures on ^{24}Mg , $\rho \approx 10^{9.6} \text{ g cm}^{-3}$, before the envelope is lost. The 8.75 M_{\odot} star has been simulated through the entire TP-SAGB phase (about 2.6×10^6 time steps) including the URCA process and electron captures by ^{24}Mg and ^{20}Ne (see Figure 3.3), which means that its fate is an electron capture supernova (EC-SN).

The outcomes of these models are highly sensitive to the mass-loss prescription during the thermal pulse phase and the rate at which the core grows (Poelarends et al. 2008). The TP-SAGB phase of the 8.7 M_{\odot} star has been modelled for about 240 pulses, at which point $\rho_{\text{c}} = 10^{9.34} \text{ g cm}^{-3}$. Though still far from $\rho_{\text{crit}}(^{24}\text{Mg} + \text{e}^-)$, the central density has exceeded the thresholds for both major URCA process reactions, accelerating the contraction of the core towards $\rho_{\text{crit}}(^{24}\text{Mg} + \text{e}^-)$. Due to this acceleration in contraction and comparison with literature (Nomoto 1984; Nomoto 1987; Ritossa, García-Berro & Iben 1999; Poelarends et al. 2008), the most probable outcome for the 8.7 M_{\odot} model is an EC-SN.

The efficiency of the third dredge-up during the thermal pulse phase is the key factor in determining the growth rate of the core. The dredge-up efficiency,

$$\lambda_{3\text{DUP}} = \frac{\Delta M_{3\text{DUP}}}{\Delta M_{\text{c}}}, \quad (3.2)$$

is the ratio of mass dredged up into the envelope during the third dredge-up ($\Delta M_{3\text{DUP}}$) to mass deposited onto the helium core through hydrogen burning during the inter-

pulse period (ΔM_c ; see, e.g., Karakas, Lattanzio & Pols 2002 and Figure 3.6). The dredge-up efficiency ranges between $\lambda_{3\text{DUP}} = 0$ and 1, where $\lambda_{3\text{DUP}} = 1$ is an extremely efficient dredge-up in which all the material deposited onto the core during the inter-pulse is mixed back into the envelope. $\lambda_{3\text{DUP}} \ll 1$ is, on the other hand, an extremely inefficient dredge-up resulting in the maximum possible core growth rate.

In order to demonstrate the sensitivity of the fate of super-AGB stars to the convective boundary mixing and mass loss rate uncertainties, I re-computed the $8.7 M_\odot$ model from the completion of second dredge-up. This time, the calculation assumed an exponential overshoot beneath the convective envelope characterised by equation 2.47 and $f_{\text{CBM}} = 0.02$ as opposed to the original value of 0.005. Kippenhahn (convective structure evolution) diagrams in Figure 3.6 show the drastically increased dredge-up efficiency for the model with deeper mixing of the convective envelope ($f_{\text{CBM}} = 0.02$, bottom panel). The net core growth between two thermal pulses and the inter-pulse period for each of the convective boundary mixing parameterisations ($\dot{M}_{\text{core}}/M_\odot \text{ yr}^{-1}$) is plotted against different mass loss rates ($\dot{M}_{\text{env}}/M_\odot \text{ yr}^{-1}$) for red (super-)giants from the literature (Reimers 1975; Blöcker 1995; van Loon et al. 2005) in Figure 3.7. The dividing line separating the white dwarf and neutron star fates is the critical (average) core growth rate,

$$\overline{\dot{M}}_{\text{core}}^{\text{crit}} = \frac{M_{\text{EC}} - M_{\text{core}}^{\text{EAGB}}}{M_{\text{tot}}^{\text{EAGB}} - M_{\text{EC}}} \overline{\dot{M}}_{\text{env}}, \quad (3.3)$$

which is a function of the mass of the core and envelope at the start of the thermal-pulse phase ($M_{\text{core}}^{\text{EAGB}}$ and $M_{\text{env}}^{\text{EAGB}}$, respectively, where $M_{\text{tot}}^{\text{EAGB}} = M_{\text{core}}^{\text{EAGB}} + M_{\text{env}}^{\text{EAGB}}$) and the average mass loss rate, $\overline{\dot{M}}_{\text{env}}$.

M_{EC} is the critical core mass needed to be reached before an EC-SN is inevitable. Several factors make the determination of M_{EC} complicated. For an electron fraction of $Y_e = 0.5$, Chandrasekhar's limiting mass for a relativistically degenerate core is $M_{\text{Ch}} = 1.46 M_\odot$ (see equation 2.16). During the very late stages of the progenitor evolution, electron captures severely reduce the average core electron fraction, decreasing the limiting mass well below the mass of the core (Miyaji et al. 1980). This reduction of the electron fraction is driven by the electron captures of ^{20}Ne and later, material

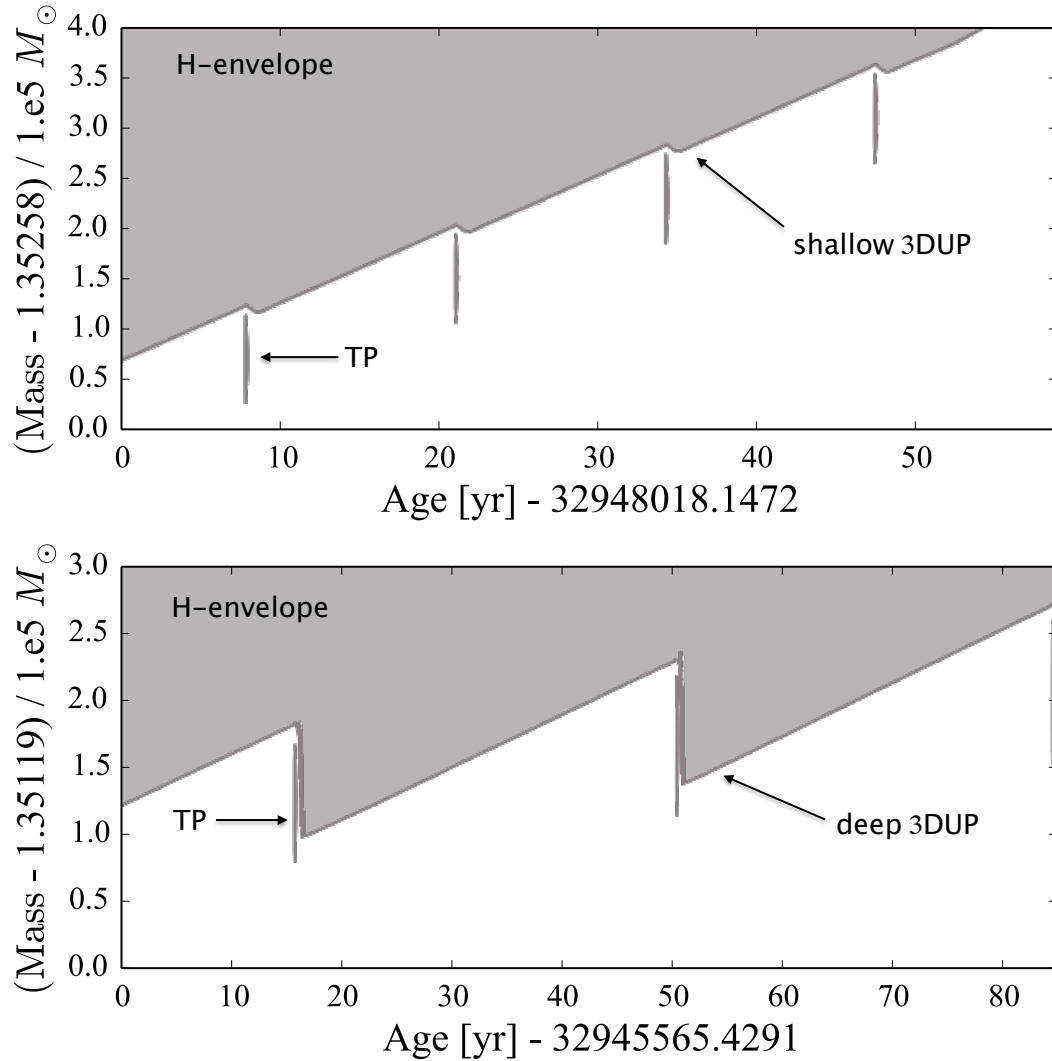


Figure 3.6: Kippenhahn (convective structure evolution) diagrams of the thermal pulse phase of the $8.7 M_{\odot}$ model with $f_{\text{CBM}} = 0.005$ (top panel) and $f_{\text{CBM}} = 0.02$ (bottom panel). The thermal pulse (TP) and third dredge-up (3DUP) events are labelled. Arguably, 3DUP is the name given to the deepening in mass of the convective envelope following the extinction of the helium shell-flash convection zone. While these events in the top panel for $f = 0.005$ are shallow, they nevertheless reach into the helium core and dredge up the products of complete hydrogen burning.

burnt into nuclear statistical equilibrium (NSE) composition by the oxygen deflagration. Evolution towards this point (the critical density for electron captures by ^{20}Ne to be activated) is driven by contraction due to electron captures by ^{24}Mg , which have a threshold at lower densities. Assuming that the criterion for producing an EC-SN is the core mass within which the central density is high enough for electron captures by ^{24}Mg to be activated, I assume $M_{\text{EC}} = 1.37$ in accordance with previous work (Miyaji et al. 1980; Nomoto 1984; Ritossa, García-Berro & Iben 1999; Poelarends et al. 2008).

Figure 3.7 shows that assuming the mass loss rates of van Loon et al. (2005) and Reimers (1975), even with the high third dredge-up efficiency arising in the model with $f_{\text{CBM}} = 0.02$ the $8.7 M_{\odot}$ model would still produce an EC-SN. This conclusion is void if indeed the envelope would be ejected during the TP phase due to some dynamical instability (see section 1.2.3). Another interesting conclusion from Figure 3.7 is that even for the case with $f_{\text{CBM}} = 0.005$ (lower 3DUP efficiency and hence greater core growth rate per pulse), the $8.7 M_{\odot}$ model would become an ONeWD assuming the mass loss rate of Blöcker (1995). This would make the EC-SN channel extremely narrow at solar metallicity.

In order to maintain numerical stability in the $8.75 M_{\odot}$ model, after the depletion of ^{24}Mg at the centre by electron captures, the input physics assumptions were simplified. First, the effects of mass-loss were excluded from the calculation and secondly the surface was relocated to a region where the optical depth is an order of magnitude greater than that at the photosphere (which is where the surface had previously been defined). Choosing to set the boundary at a larger optical depth is one way to deal with the inappropriate way the final stages of these massive super-AGB envelopes are being simulated in this work. In a 1-D code (and probably in the real star) large pulsations occur signalling an increasing instability of the envelope which may lead to enhanced mass loss or even ejection phases, such as the super-wind. These issues have been alluded to recently by Lau et al. (2012), as I discussed in section 1.2.3. Choosing the photosphere to be at a larger optical depth indeed lets the star be hotter and smaller, and the mass loss calculated from the stellar parameters, if it were still included, will not be the same as for the default photosphere parameters. Through this treatment,

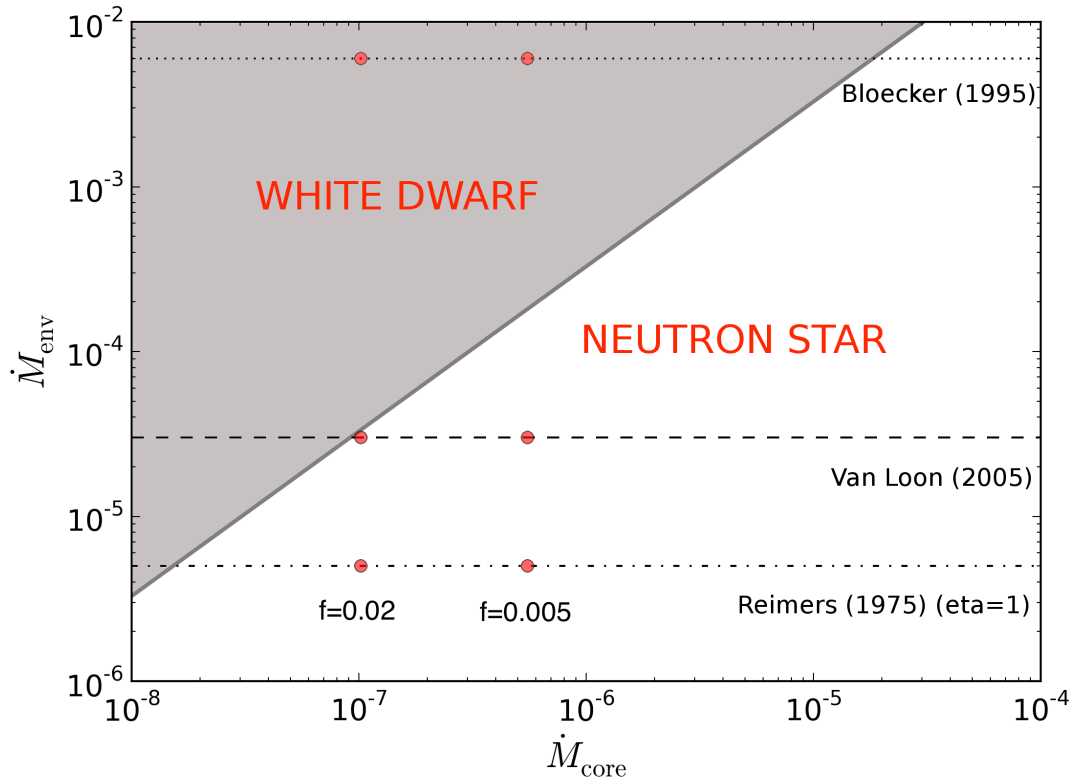


Figure 3.7: Mass loss rate against core growth rate for the $8.7 M_{\odot}$ super-AGB model during the TP-SAGB phase. The critical relationship between the two rates is plotted with a solid line, above and to the left of which the envelope is lost before the core reaches the critical mass to produce an electron capture supernova and an ONeWD is formed (shaded grey). Below and to the right of the solid line, all combinations of mass loss and core growth rates in the white region will result in an EC-SN from the $8.7 M_{\odot}$ model. Horizontal lines show typical mass loss rates from literature (Poelarends et al. 2008). The red dots correspond to two average net core growth rates extracted from the present model assuming two parameterisations of convective boundary mixing (and hence two different 3DUP efficiencies): $f = 0.02$ and $f = 0.005$.

the details of the envelope evolution are increasingly inaccurate from this point. When these changes were made, the remaining envelope mass was $4.48 M_{\odot}$ and the central density $\rho_c = 4.67 \times 10^9 \text{ g cm}^{-3}$. For further discussion of numerical instabilities and their physical interpretation, the reader is referred to Wagenhuber & Weiss (1994) and Lau et al. (2012). A simple calculation involving the mass of the envelope at the first thermal pulse of the $8.75 M_{\odot}$ model (see Table 3.1) and the time spent on the TP-SAGB yields a critical mass-loss rate of

$$\dot{M}_{\text{env}}^{\text{crit}} = \frac{M_{\text{env}}^{\text{EAGB}} - M_{\text{EC}}}{\tau_{\text{TP-SAGB}}} = 6.75 \times 10^{-4} M_{\odot} \text{ yr}^{-1}. \quad (3.4)$$

That is to say, a mass-loss rate higher than $\dot{M}_{\text{env}}^{\text{crit}}$ would have reduced the star to an ONe WD before it could produce an EC-SN. This critical mass-loss rate is within the wide realms applied to super-AGB stars (see Figure 3.7, Poelarends et al. 2008 and references therein). Mass loss clearly has a strong impact on the width of the super-AGB channel which, along with the efficiency of the third dredge up, was explored by Poelarends et al. (2008) using three stellar evolution codes (KEPLER, STERN and EVOL). Numerical models were computed for the complete pre-AGB evolution, while only part of the AGB was computed with the STERN and EVOL codes. Synthetic models were employed for the AGB thereafter, where the numerical models left off. Poelarends et al. found the upper limit to the contribution of EC-SNe to all supernovae as 20%. The contribution from accretion-induced collapse of the ONeWDs formed when the mass loss rate is too high for a single star to produce an EC-SN (e.g. Nomoto & Kondo 1991), or from binary systems in which the envelope is stripped before the second dredge-up (Podsiadlowski et al. 2004), is not considered in the figure.

It has been suggested that mass loss rates should scale with metallicity because the content of metals that strongly influence the strength of line-driven and some pulsation-driven winds will be lower (Poelarends et al. 2008). This would make the EC-SN channel wider for lower metallicities. However, this is not a simple consideration: in RSG stars, C and O can be enriched in the envelope by mixing up material from the helium-burning shell during the third dredge-up. The dredge-out in the most massive super-AGB stars also enriches the envelope with carbon and oxygen. C and O

enrichment taking place in such a primary manner would not show strong metallicity dependence if the mass loss is driven by dust formation. At low metallicity in massive AGB stars, Chieffi et al. (2001) and Herwig (2004) have shown that the vigorous burning of protons during hot dredge-up episodes increases the efficiency of 3DUP, which would impede the core growth rate. Furthermore, the luminosity boost from such hot dredge-ups could in turn boost the mass loss periodically. In some simulations of the TP-AGB phase of low metallicity stars, the third dredge-up occurs while the pulse-driven convection zone (PDCZ) is still active (Cassisi, Castellani & Tornambe 1996; Lau, Stancliffe & Tout 2009). In this scenario, protons are ingested into the PDCZ, releasing a huge amount of energy in a short time scale. The huge luminosity boost from this event is known to have dynamical effects which have uncertain consequences in 1D stellar models. Herwig et al. (2011), using simulations of the late thermal pulses of Sakurai’s object in 3D to inform 1D mixing prescriptions, found that protons ingested into the PDCZ resulted in neutron densities a factor of 10^4 higher than predicted by 1D simulations alone. These neutron densities were required to reproduce the abundance distribution that is observed for Sakurai’s object, demonstrating that violent mixing events with dynamical consequences (that are certainly difficult to predict from 1D simulations alone) are not negligible phenomena. Thus, the efficiency of the 3DUP and the mass loss rate of stars during the thermal pulse phase is very uncertain, particularly at low metallicities where the lower metal fraction is thought to generally reduce the mass loss rate. It is not so easy to jump to such conclusions about the width of the EC-SN channel when the physics of these events, particularly reactive hydrodynamics, is still uncertain.

In contrast to the $8.8 M_{\odot}$ model, which is discussed in §3.1.3, there is no significant Y_e reduction in the outer core, since there was no Ne-O flash. Instead, the contraction is driven by the steady growth of the core during each thermal pulse and the contraction is slower. Heating competes with neutrino losses so that the core resumes cooling until electron captures by ^{24}Mg are activated (see Figure 3.3). The difference can again be seen following the depletion of ^{24}Mg at the centre of both models, where the $8.8 M_{\odot}$ model continues to heat while the $8.75 M_{\odot}$ model again cools down.

This difference in temperature between the centre of the $8.8 M_{\odot}$ and $8.75 M_{\odot}$ models is important when considering the next phase of their evolution - electron captures by ^{20}Ne .

	8.2 M _⊙	8.7 M _⊙	8.75 M _⊙	8.8 M _⊙	9.5 M _⊙	12.0 M _⊙
$M_{\text{ign}}^{\text{C}}/M_{\odot}^a$	0.15	0.00	0.00	0.00	0.00	0.00
$M_{\text{ign}}^{\text{Ne}}/M_{\odot}^b$	–	–	–	0.93	0.42	0.00
$T_{\text{ign}}^{\text{Ne}}/GK^c$	–	–	–	1.318	1.311	1.324
$\psi_{\text{c}}^{\text{Ne}d}$	–	–	–	46.0	15.2	5.6
$\rho_{\text{c}}^{\text{Ne}}/\text{gcm}^{-3e}$	–	–	–	3.343×10^8	7.396×10^7	1.730×10^7
$M_{\text{tot}}/M_{\odot}^f$	7.299	7.910	8.572	8.544	9.189	11.338
$M_{\text{env}}/M_{\odot}^g$	6.032	6.559	7.210	7.174	6.702	8.022
$M_{\text{He}}/M_{\odot}^h$	1.26721	1.35092	1.36230	1.36967	2.48733	3.31580
$M_{\text{CO}}/M_{\odot}^i$	1.26695	1.35086	1.36227	1.36964	1.49246	1.88602
Remnant	ONe WD	ONe WD / NS	NS	NS	NS	NS
SN Type	–	– / EC-SN (IIP)	EC-SN (IIP)	EC-SN (IIP)	CC-SN (IIP)	CC-SN(IIP)

Table 3.1: ^a Mass coordinate of carbon ignition. ^b Mass coordinate of neon ignition. ^c Temperature at locus of neon ignition. ^d Central degeneracy at time of neon ignition. ^e Central density at time of neon ignition. ^f Total mass at time of first thermal pulse or neon ignition. ^g Envelope mass at time of first thermal pulse or neon ignition. ^h Helium core mass (H-free core mass) at time of first thermal pulse or neon ignition. ⁱ Carbon-oxygen core mass (He-free core mass) at time of first thermal pulse or neon ignition.

3.1.3 Late evolution of the 8.8, 9.5 and 12.0 M_{\odot} (massive star) models

The mass of the CO core, M_{CO} , continues to grow for the entire lifetime of the secondary C-burning shells in all models due to helium shell burning. Previous studies (see Nomoto 1984 and references therein) show that the core mass limit for neon ignition is very close to $1.37 M_{\odot}$, which the present models confirm. Indeed, in all models with initial mass greater than $8.8 M_{\odot}$, a CO-core develops with a mass that exceeds the limit for neon ignition, $M_{\text{CO}}(8.8 M_{\odot}, 9.5 M_{\odot}, 12.0 M_{\odot}) = 1.3696, 1.4925, 1.8860 M_{\odot}$ (whereas in the $8.75 M_{\odot}$ model, which does not ignite neon, $M_{\text{CO}} = 1.3623 M_{\odot}$).

A temperature inversion develops in the core following the extinction of carbon-burning in both the $8.8 M_{\odot}$ and $9.5 M_{\odot}$ models. The process by which this arises is similar to that described for off-centre carbon ignition in section 3.1.1. The neutrino emission processes that remove energy from the core are generally (over-) compensated by heating from gravitational contraction in more massive stars. However in these lower-mass stars the onset of partial degeneracy moderates the rate of contraction and hence neutrino losses dominate, cooling the central region. As I discussed earlier, the energy losses from neutrinos accelerates the evolution of the star during the advanced stages (from carbon burning and onward), which is why the completion of the second dredge-up (reaching the CO core boundary) appears to occur at later evolutionary phases in more massive stars and not at all in the $12 M_{\odot}$ model (or indeed any model with $M > 12 M_{\odot}$). Essentially, the evolutionary timescale is short compared to the rate at which the envelope reaches into the core (see Sugimoto & Nomoto 1974 for more details and an expression for the rate of dredge-up and its dependency upon the radiative heat absorption and mixing timescale).

As a result of the net cooling in the central region, the ignition of neon in the 8.8 and $9.5 M_{\odot}$ models takes place off centre, at mass coordinates of $0.93 M_{\odot}$ and $0.40 M_{\odot}$ respectively. This result confirms the work of Nomoto (1984) (case 2.6), but diverges from that of Eldridge & Tout (2004), which I will discuss later. In both models the temperature in the neon-burning shell becomes high enough to also ignite $^{16}\text{O} + ^{16}\text{O}$.

As I mention in section 2.5, owing to the high densities in the cores of these stars, the products of neon and oxygen burning are more neutron-rich than in more massive stars. This results in an electron fraction in the shell of as low as $Y_e \approx 0.48$ (see section 3.3 and Figure 3.8). Such low Y_e causes the adiabatic contraction in the following way. If the temperature is high during the flash, the flashing outer layer expands and exerts lower pressure (less weight) on the central region (as can be seen in Figure 3.3 labelled ‘Ne-flash’, ρ_c decreases due to the almost adiabatic expansion of the central region). However, when the flashed region has cooled down by neutrino emission following the extinction of nuclear burning, the outer layer shrinks and exerts more weight on the core, which is less able to provide support than before the flash because there are fewer electrons available to contribute to the degeneracy pressure. The centre then reaches higher densities, and hence temperatures, than before (see the $\rho_c - T_c$ evolution in Figure 3.3). As mentioned above, for this reason the reduction in Y_e is important for cores so close to M_{Ch} ($M_{\text{Ch}} \propto Y_e^2$, see equation 2.16).

As illustrated in Figure 3.5e, following the neon shell flashes the $9.5 M_\odot$ model recurrently ignites neon- and oxygen-burning in shells at successively lower mass coordinates that eventually reach the centre, following which Si-burning is ignited off-centre. Although neon burning (and oxygen burning) in the $8.8 M_\odot$ model begins as a flash and later propagates toward the centre, the evolution of the $8.8 M_\odot$ model diverges from that of the $9.5 M_\odot$ star when its centre reaches the conditions necessary for the first URCA process pair to become significant (whereas the $9.5 M_\odot$ model avoids such dense conditions). More details of the neon and oxygen shell burning episodes are discussed in section 3.2.

The CO core (or equivalently He-free core) in the $8.8 M_\odot$ model at the time of neon ignition is $1.36964 M_\odot$, very close to M_{Ch} , while that of the $9.5 M_\odot$ model is $1.49246 M_\odot$ (see Table 3.1). Under these conditions, the $8.8 M_\odot$ model experiences a much more marked contraction due to the reduction in Y_e . The central density at this time is as high as $3.43 \times 10^8 \text{ g cm}^{-3}$, which is exceedingly close to the threshold density for $^{27}\text{Al}(e^-, \nu)^{27}\text{Mg}$. Although there is no cooling effect from the A=27 pair because the reverse decay channel is blocked, the further removal of electrons from the

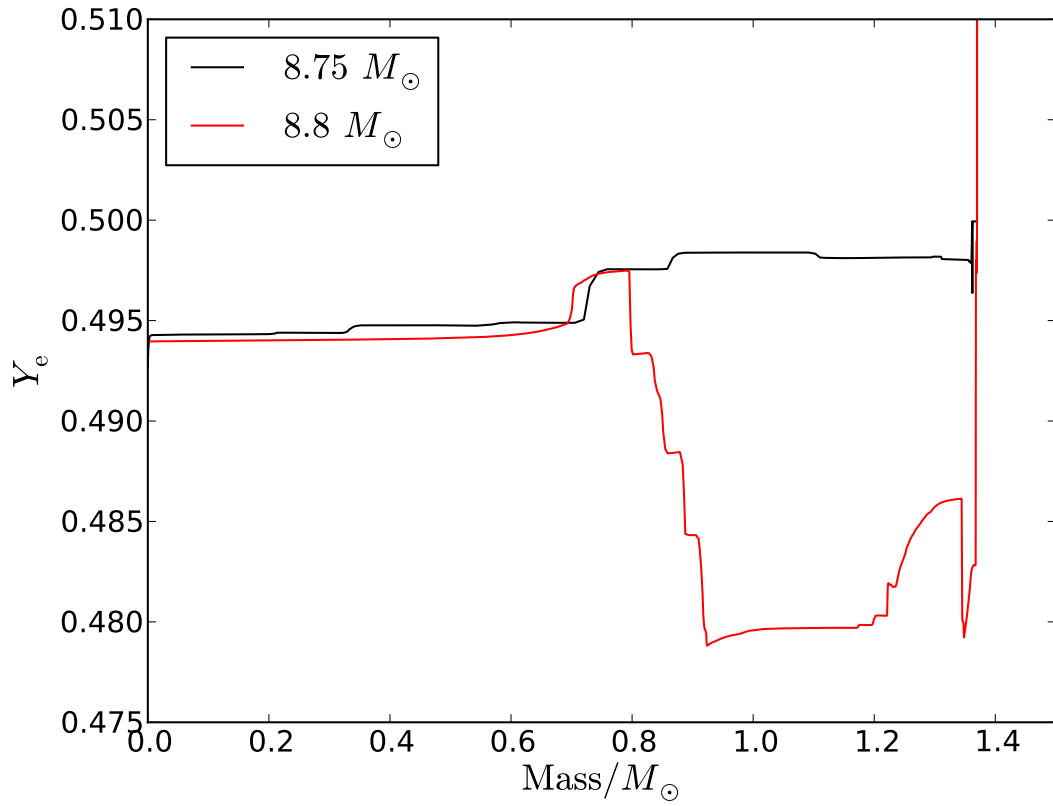


Figure 3.8: Radial profiles of the electron fraction, Y_e , in the progenitor structure of the $8.8 M_{\odot}$ model and the $8.75 M_{\odot}$ model after central ^{24}Mg depletion. The silicon-rich shell of the $8.8 M_{\odot}$ model, where the material has been processed by the neon-oxygen shell flashes, displays a severely reduced electron fraction, reflected by high ratios of $^{30}\text{Si}/^{28}\text{Si}$ and $^{34}\text{S}/^{32}\text{S}$.

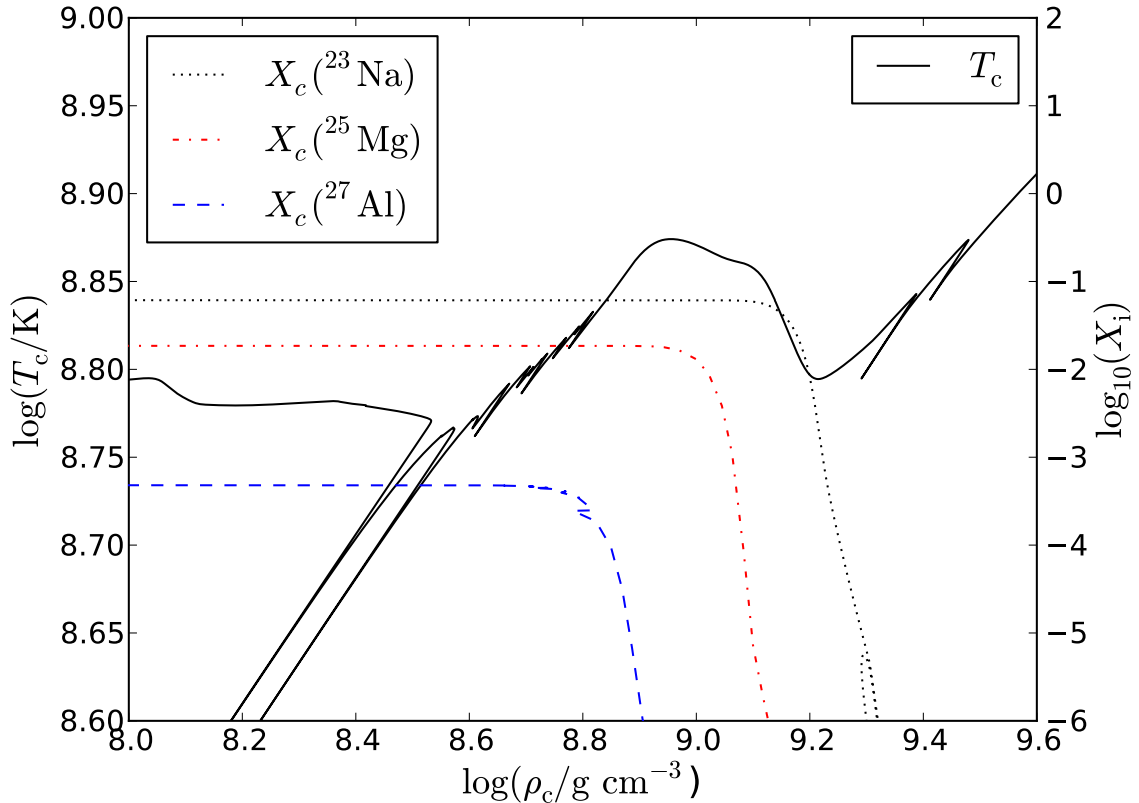


Figure 3.9: Impact of the URCA process on the evolution of the $8.8 M_{\odot}$ model in the central density–temperature ($\rho_c - T_c$) plane. The impact of each pair, $A = 27, 25$ and 23 in order of increasing threshold density, can be seen coinciding with the depletion of the abundance of its electron capture parent.

core causes contraction toward the threshold densities of the second and third URCA pairs ($A=25$ and $A=23$ respectively). There is also a slight heating effect from the electron captures on ^{27}Al (see Figure 3.9). The cooling effect supplied by the $A=25$ URCA pair (and later the $A=23$ pair, shown in Figs. 3.3 and 3.9) allows for a small amount of contraction but again it is the associated change in the electron fraction that enables the largest contraction when the core is so close to the Chandrasekhar limit ($M_{\text{Ch}} \propto Y_e^2$). As a result, the core of the $8.8 M_{\odot}$ model continuously contracts until

the centre reaches the critical density for electron captures by ^{24}Mg , quickly followed by further contraction to the critical density for those by ^{20}Ne (see Figure 3.3).

There is a discrepancy between the URCA-process trajectories of the present models and those of Ritossa, García-Berro & Iben (1999). This is due to the under-sampling of weak reaction rates for the URCA process that are employed in the MESA code (Oda et al. 1994). In chapter 4 I discuss the implications of this under-sampling and show that, by using new well sampled weak rates (Toki et al. 2013), the URCA process central trajectory of Ritossa, García-Berro & Iben (1999) is qualitatively reproduced in the $8.8 M_{\odot}$ case.

This central evolution is significantly different from that for the $8.75 M_{\odot}$ model, which is described in section 3.1.2 and experiences stronger plasmon-neutrino cooling due to the slower rate of contraction. The difference in the contraction timescales following the URCA process in the 8.75 and $8.8 M_{\odot}$ models also has implications for the $A = 24$ weak reactions ($^{24}\text{Mg}(e^{-}, \nu)^{24}\text{Na}$, $^{24}\text{Na}(e^{-}, \nu)^{24}\text{Ne}$ and their reverse decays) when using the rates of Oda et al. (1994). In the rapidly contracting $8.8 M_{\odot}$ model the impact of the under-sampled weak rates tends to be smoothed out, and almost no trace can be seen in the $T_c - \rho_c$ plane (Figure 3.3). In the slower contracting $8.75 M_{\odot}$ model, the $A = 24$ rates produce a peak in the $T_c - \rho_c$ plane (Figure 3.3) at $\log_{10}(\rho_c/\text{g cm}^{-3}) \approx 9.65$, as in previous studies (e.g. Gutierrez et al. 1996). A second contributing factor to the differences in response of the two models to the $A = 24$ reactions is the central temperature. The weak rates are strongly density-dependent, however for higher temperatures the transition low to high rate with increasing density is less pronounced. Combined with the under-sampling of the Oda et al. (1994) rates, this again tends to smooth out their impact, particularly in the $8.8 M_{\odot}$ model. The energy release from both the rapid contraction and the γ -decays from electron-capture products raise the temperature high enough to ignite neon and oxygen burning in quick succession.

The $8.8 M_{\odot}$ model has been modelled onwards from the resulting oxygen deflagration with the AGILE-BOLTZTRAN hydrodynamics code and has been confirmed to result in core collapse (Fischer 2014). Although Eldridge & Tout (2004) report the

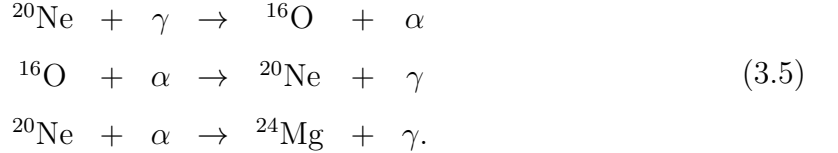
same fate for their $10 M_{\odot}$ model in which a limited network was used, there is no neon shell flash following the completion of the second dredge-up. In these models, neon burning was found to take place at the edge of the core during the last carbon-shell flash, reducing the core mass to M_{Ch} (Eldridge 2005). Subsequently, the core contracted directly to central densities of about $\log_{10}(\rho_c/\text{g cm}^{-3}) = 9.8$ (roughly the critical density for electron captures by ^{20}Ne to start) with no further neon-shell flashes, though electron captures were not included in the nuclear reaction network. Neon-burning reaction rates were artificially limited to prevent numerical problems and a low spatial resolution was used. I believe these two caveats to be the reason that the neon-oxygen shell flashes that are found to occur in such stars in the present work were not found in these earlier models. In this work the MESA code was able to follow the evolution all the way to oxygen deflagration by using a very large network of 114 nuclei including all the relevant fusion and weak reactions. The models thus highlight the importance of neon-shell burning in determining the path to collapse. Indeed, by reducing the detail of the nuclear reaction network in the MESA simulations to include only the reactions used by Eldridge & Tout (2004), an $8.8 M_{\odot}$ model does not develop a neon shell flash.

As mentioned above, the $9.5 M_{\odot}$ model starts silicon burning off centre in a shell that later propagates toward the centre. This is another example of the continuous transition towards massive stars, in which all the burning stages begin centrally. Since this model has not been evolved to its conclusion, it is uncertain whether silicon-burning will migrate to the centre, producing an iron core. If indeed that is the case, it will finally collapse as an iron core-collapse supernova (FeCCSN). Such a low-mass progenitor would make for interesting explosion simulations (see section 3.3 and Mueller, Janka & Heger 2012). The $12 M_{\odot}$ is the canonical massive star in this set of models, igniting C, Ne, O and Si burning centrally (see Figure 3.5f). It eventually collapses, and would produce an FeCCSN.

3.2 Neon-oxygen flashes and flame

As described in detail earlier, following the extinction of the final carbon burning shell, a degeneracy/neutrino-induced temperature inversion arises in the core in a similar way to the temperature inversion in SAGB stars. Neon is thus ignited off-centre at mass coordinates of $0.93M_{\odot}$ and $0.40M_{\odot}$ for the $8.8M_{\odot}$ and $9.5M_{\odot}$ models respectively. Some of the important model properties are given in Table 3.1 at this time. At the point of Ne-shell ignition, the density profile of the 8.8 and $9.5 M_{\odot}$ models is very different (see Figure 3.16). While the $8.8 M_{\odot}$ model is structured more like a super-AGB star due to the previous dredge-out episode, the $9.5 M_{\odot}$ model resembles more a massive star, with a distinct He-shell and C-shell still present.

In the simulations of the NeO flame in low-mass massive stars performed as part of this work, the situation is more complicated than that of the carbon flame in super-AGB stars. Rather than proceeding via the fusion of two similar nuclei, neon-burning is driven by photodisintegration. The key reactions are



The neon photodisintegration reaction ${}^{20}\text{Ne}(\gamma, \alpha){}^{16}\text{O}$ has a Q-value of -4.73 MeV and is thus endothermic. When this reaction first becomes significant, the inverse reaction, ${}^{16}\text{O}(\alpha, \gamma){}^{20}\text{Ne}$, proceeds much faster, returning the energy to the stellar material and replenishing the ${}^{20}\text{Ne}$ abundance. When the temperature becomes high enough however (see Figure 3.10), the α -particle released is quickly captured by another ${}^{20}\text{Ne}$ nucleus, producing ${}^{24}\text{Mg}$. This reaction has a Q-value of 9.32 MeV and is the primary energy source during neon-burning.

At the point where the heat accumulates, ${}^{20}\text{Ne}$ is more efficient at capturing the α -particles released slowly via the photodisintegration of neon. The energy release is dictated by the photodisintegration rate and the burning proceeding effectively as the net reaction $2({}^{20}\text{Ne}) \rightarrow {}^{16}\text{O} + {}^{24}\text{Mg} + 4.59$ MeV. Woosley, Heger & Weaver (2002a),

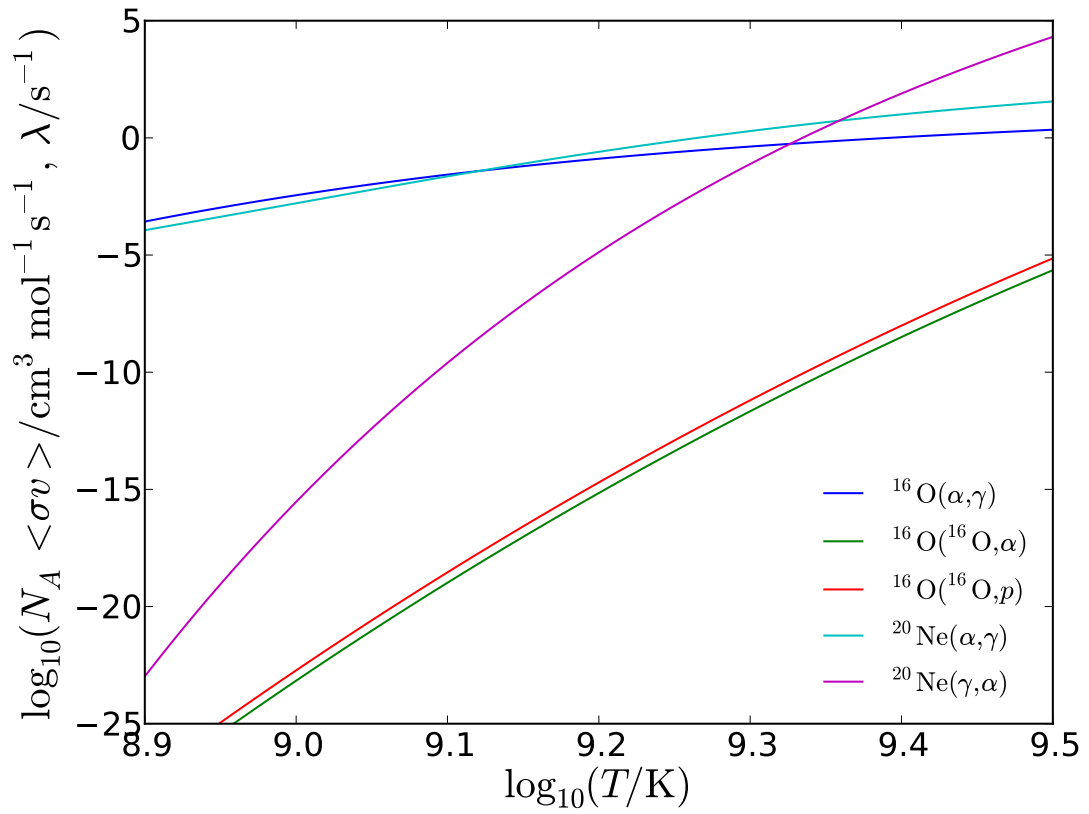


Figure 3.10: Reaction rates, λ (one-body reactions) and $N_A \langle \sigma v \rangle$ (two-body reactions) of key neon- and oxygen-burning reactions as functions of temperature from the REACLIB compilation.

using the steady-state α -particle abundance derive an analytical expression for the energy generation from neon burning as

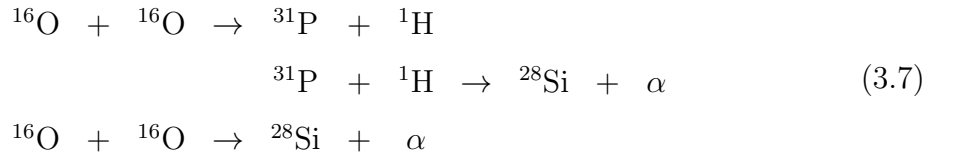
$$\epsilon \approx 2.5 \times 10^{29} T_9^{3/2} \left(\frac{Y^2(^{20}\text{Ne})}{Y(^{16}\text{O})} \right) \lambda_{\alpha,\gamma}(^{20}\text{Ne}) \exp(-54.89/T_9) \text{ erg g}^{-1} \text{ s}^{-1}. \quad (3.6)$$

When the rate of energy generation from neon burning is high enough, the material above the region of nuclear burning becomes convectively unstable. When the fuel ignites off-centre, like in the carbon flame of super-AGB stars (Siess 2006), the base of the convective zone does not develop at the coordinate of the peak temperature, but a small distance above it. This is because of the dependence of the luminosity on the temperature gradient, $L_r \propto dT/dr$. Of course, $dT/dr = 0$ at the coordinate of the peak temperature and the criterion for convection,

$$L_r > \frac{16\pi acG}{3} \frac{mT^4}{\kappa P} \nabla_{\text{ad}},$$

is satisfied at a point somewhere above the peak temperature where $\nabla_{\text{rad}} = \nabla_{\text{ad}}$.

In the convective region, however, a constant supply of fresh ^{20}Ne is being mixed down to the higher temperatures at the its base. The temperature there is 1.26 GK, where the $^{16}\text{O}(\alpha, \gamma)^{20}\text{Ne}$ and $^{20}\text{Ne}(\alpha, \gamma)^{24}\text{Mg}$ reaction rates are incredibly similar. As fresh ^{20}Ne is mixed down to this region, the success of the ^{20}Ne over ^{16}O to capture the α -particle raises the temperature enough to ignite oxygen burning, which proceeds by the following reactions:



The development of a convective zone provides luminosity to support the outer layers of the core and temporarily halts the contraction of the core. The central regions thus expand and cool (see Figure 3.3). The lifetime of the shell burning episode is lengthened while convection brings in fresh fuel to be burnt at the base of the shell where the temperature is high. This contraction continues until the temperature becomes high enough where neon and oxygen is abundant, re-igniting the nuclear burning and

producing a new convective shell. After a few flashes, the region previously engulfed by the shell convective shell as it extended radially outwards has become heavily depleted in Ne and O and so the closest fuel is in the direction of the centre. At this point the burning shell begins to propagate to the centre of the star.

3.2.1 Advance of the burning shell towards the stellar centre

After the last flash has extinguished and contraction begins, the two models begin to diverge, as best illustrated in Figs 3.3 and 3.5(d, e). The $9.5M_{\odot}$ star once again contracts and a thin shell of neon and oxygen is ignited below the base of the previously convective shell. Any convection developing at this time does not bring any fresh fuel (only the ashes of the previous shells) into the burning region. The core is so dense that the photon mean free path is too short for radiative transfer to play an important role in the inward propagation of the flame and instead compressional heating due to core contraction and local heating due to electron conduction are largely responsible for intermittent periods of nuclear energy production that move towards the centre.

It is a different story for the $8.8M_{\odot}$ star. Contraction, following the final ONe-shell flash, at first acts to heat the material locally and to burn neon and oxygen moderately as in the $9.5M_{\odot}$ model, except that the core is more degenerate in the $8.8M_{\odot}$ star. Electron conduction is therefore much more efficient and initially, it seems as though the localised effect of heat generation due to contraction and any subsequent nuclear burning is diluted across the core. This smoothing of the temperature profile across the core would prevent the region directly below the previously ONe-burning shells from reaching temperatures in excess of the Ne-burning threshold. Instead of a flame developing as in the $9.5M_{\odot}$ star, the core contraction, driven by the neutron-rich composition in the NeO shell, would then cause local heating much further from the centre where the degeneracy is lower, where a new neon and oxygen burning shell ignites (where the fuel is still abundant) above the outermost extent of the previous ONe-shells.

To test this hypothesis, I firstly inspect the opacity profiles of the cores of the 8.8

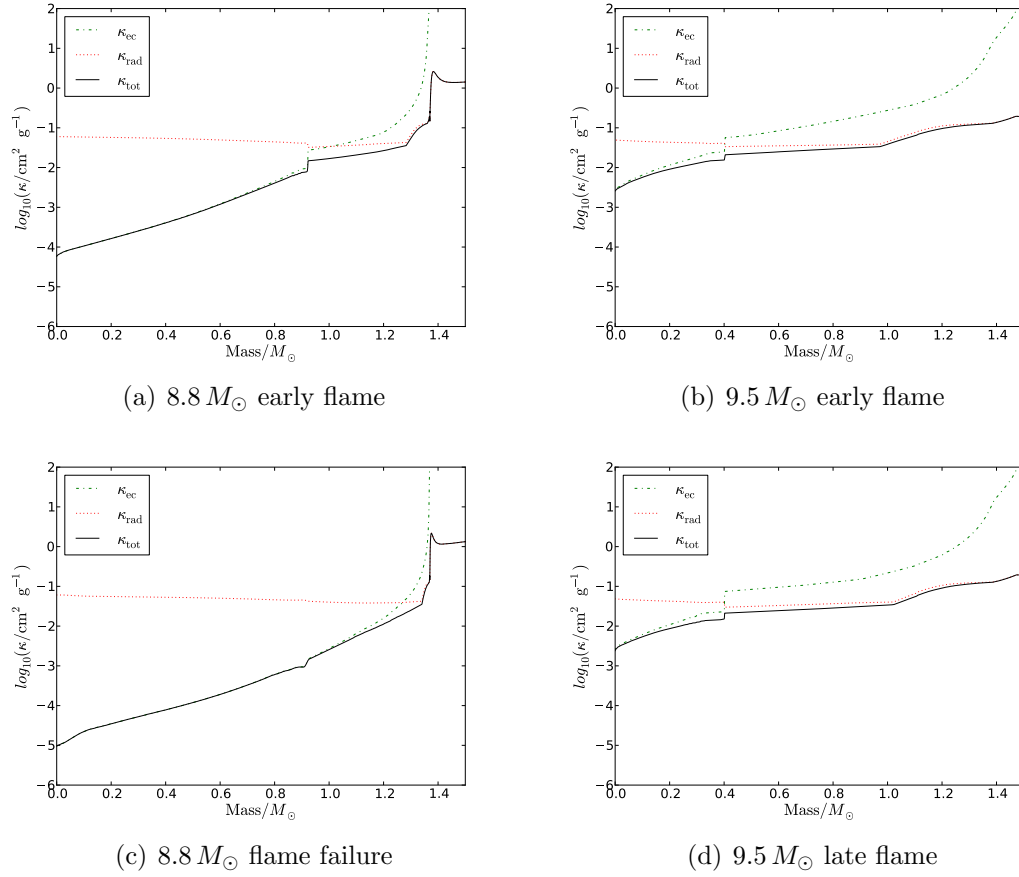


Figure 3.11: Radial profiles with respect to mass co-ordinate of the radiative (κ_{rad}), conductive (κ_{ec}) and total ($\kappa_{\text{tot}} = [1/\kappa_{\text{rad}} + 1/\kappa_{\text{ec}}]^{-1}$) opacities following the extinction of the final neon-oxygen convective flash episode. The heat transport in both stars is dominated by conduction (lower κ), however the $9.5 M_{\odot}$ model by virtue of its higher total opacity allows for heating to take effect on a more local scale than in the $8.8 M_{\odot}$ model.

and $9.5 M_{\odot}$ models. These are shown in Figure 3.11 following the extinction of the last neon-oxygen flash and at a later time in each model. Although electron conduction dominates the heat transfer in both cases, it is more efficient (lower κ) by a factor of about 3 in the $8.8 M_{\odot}$ model's early flame and by a factor of more than 10 later, meaning that any energy production from subsequent radiative neon-oxygen burning or contraction could be diluted across the core. In contrast, the higher conductive opacities in the $9.5 M_{\odot}$ model could allow for the nuclear and compressional energy to take effect much more locally. This examination, although physical, is largely qualitative and lacks causality.

While it is not under dispute that the lower opacity would allow for more efficient heat transport in the $8.8 M_{\odot}$ model, it is important to examine whether this effect is important or not for the timescales involved in the star's evolution. The flux of energy due to radiation and conduction is given by

$$\mathbf{F} = -\frac{4acT^3}{3\rho} \left(\frac{1}{\kappa_{\text{rad}}} + \frac{1}{\kappa_{\text{ec}}} \right) \nabla T$$

(Kippenhahn & Weigert 1990, p. 33, eq. 5.3). For a thin shell across which T , κ and ρ can be considered constant, the heat diffusion equation is

$$\frac{dT}{dt} = K \nabla^2 T,$$

where K is the thermal diffusivity,

$$K = \frac{4acT^3}{3\kappa\rho^2 C_P} \quad \text{cm}^2 \text{ s}^{-1}$$

(Maeder 2009, p. 46, eq. 3.46). In order to get an idea of whether the rate of energy transport due to low, electron dominated opacities removes enough heat from the burning front to prohibit its propagation, one can examine the thermal adjustment timescale of the stellar material below the flame. The thermal adjustment timescale,

$$\tau_{\text{therm}} \approx \frac{\ell^2}{K} \quad \text{s},$$

is the time taken for a perturbation in temperature to be felt at a distance ℓ from the source. In this case, the source is the neon-burning shell and ℓ is the distance from

the burning front towards the centre of the star. The thermal adjustment timescale is plotted as a function of mass coordinate in Figure 3.12, where the timescale for a given distance is calculated using the value of the thermal diffusivity, K , averaged over the distance ℓ from the burning front.

To draw a conclusion, the thermal adjustment timescale must be compared with some evolutionary timescale. The most appropriate in this case is the nuclear burning timescale of neon. Per gram of the stellar material, with composition roughly 60% ^{16}O and 40% ^{20}Ne , the amount of energy released by neon-burning is approximately

$$4.59 \times \frac{X(^{20}\text{Ne})}{2m_{20}} \text{ MeV},$$

where $m_{20} \approx 20$ amu is the mass of the ^{20}Ne nucleus in grams. Taking a typical neon-shell burning energy generation rate per gram from the simulation gives an order-of-magnitude estimate for the nuclear timescale during neon-burning of 3.6×10^7 s, about one year. This is much shorter than the thermal adjustment timescale across the core. So, although it is true that stronger degeneracies boost the energy transport by electron conduction below the burning front, the timescale for the energy transport is too long in comparison with the nuclear timescale to affect the energetics of the burning front.

Even in the $9.5 M_{\odot}$ model, where the burning front reaches the centre of the star, the behaviour of the shell is not that of a convective zone trailing burning front being driven by a smoothly propagating conductive flame. The propagation is instead interrupted by periods of quenching and contraction. This behaviour will be illuminated in the following section, where I examine the properties of mixing at the lower boundary of the convective neon–oxygen burning shell.

3.2.2 Uncertainties due to mixing

Still one of the largest uncertainties in any 1-D stellar evolution calculation is the treatment of convection. Extra mixing at convective boundaries may explain many observed phenomena, for example the abundances of CNO elements and the s-process abundance distribution in AGB stars (see, e.g., Busso, Gallino & Wasserburg 1999

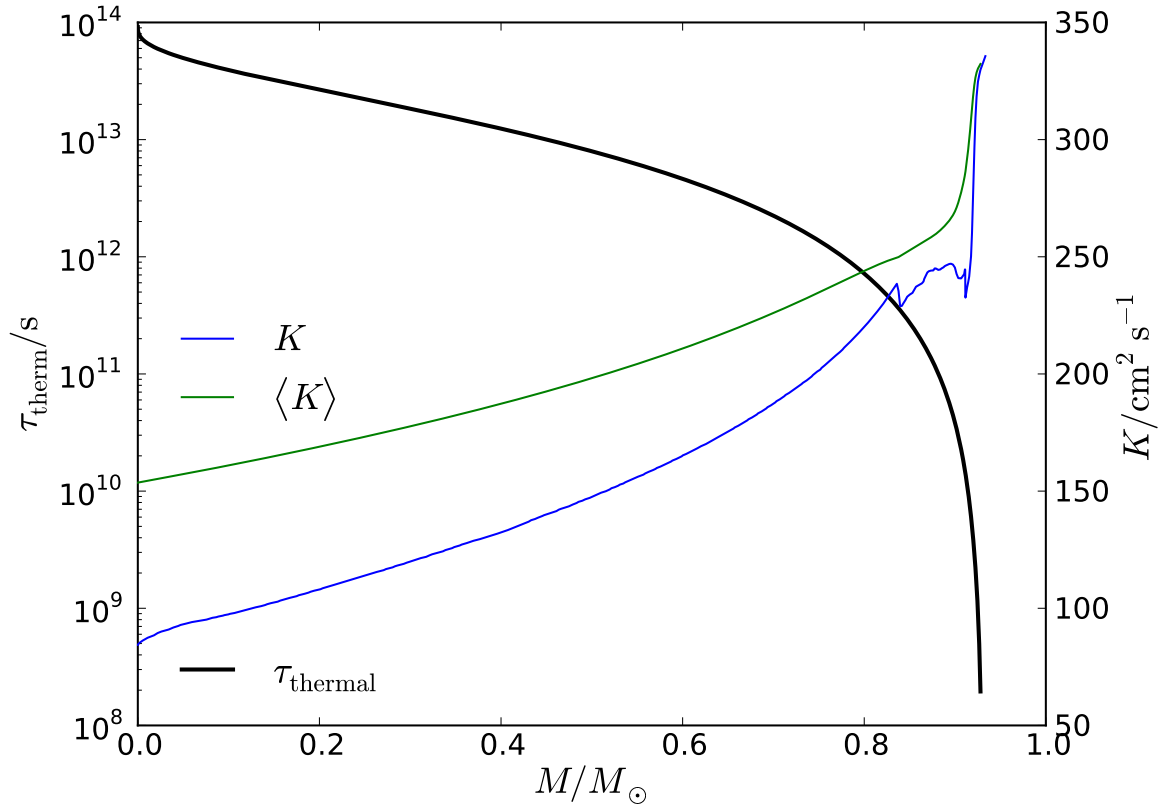


Figure 3.12: The thermal adjustment timescale profile below the neon-burning shell in the $8.8 M_{\odot}$ model. Plotted on the twin axis is the thermal diffusivity, K , as a function of distance inwards from the burning front and its mass-averaged value with which the thermal adjustment timescale is calculated.

and Käppeler et al. 2011 for reviews of this topic), and hence such mixing is included in the present models. Due to the turbulent and advective nature of convection, it is physically plausible to infer some extra mixing across the boundary between convective and radiative layers but without the benefit of 3-D hydrodynamical simulations of the physical conditions it is difficult to quantify its extent. We use the term convective boundary mixing rather than overshooting for the advanced evolution phases of the deep stellar interior, such as convective shells. This is because the term overshooting suggests a physical picture in which coherent convective structures or blobs cross the Schwarzschild boundary before they notice the reversal of buoyancy acceleration. It seems that the term overshooting is typically used as more of a numerical ‘fix’ for fitting stellar models in the HRD. However, in the deep interior hydrodynamic instabilities, such as Kelvin-Helmholtz or internal gravity wave induced turbulence dominate mixing at the convective boundary. It is these real, physical considerations that motivate the consideration of convective boundary mixing. Largely, the effect of including convective boundary mixing is to shift the transition masses due to increased core sizes. However it is intuitive to hypothesise that increased amounts of extra mixing below the ONe-burning shells would have a crucial effect on their inward propagation. To test this, extra mixing below the convective ONe-burning shells was assumed to behave as an exponentially decaying diffusion process as outlined in Eq. 2.47 with $f_{\text{flame}} = 0.005$ (the original assumption), 0.014, 0.028 and 0.100. In this treatment, although mixing is assumed to take place beyond the formal Schwarzschild convective boundary, the effects of this extra mixing upon the heat transport is not considered. Instead, in the region where the convective boundary mixing takes place, the temperature gradient is the radiative one, $\nabla = \nabla_{\text{rad}}$. The central density–temperature evolution from the flame’s ignition for all of these assumptions is shown in Figure 3.13. It should be noted that setting $f_{\text{flame}} = 0.100$ is likely an extremely unphysical assumption that is adopted here simply to test the uncertainty of these conclusions.

Although the central evolution behaves slightly differently for each mixing assumption, all the models reach central densities of $\rho_c = 10^{9.6} \text{ g cm}^{-3}$ at temperatures well below the neon-ignition threshold. The model with the largest amount of mixing

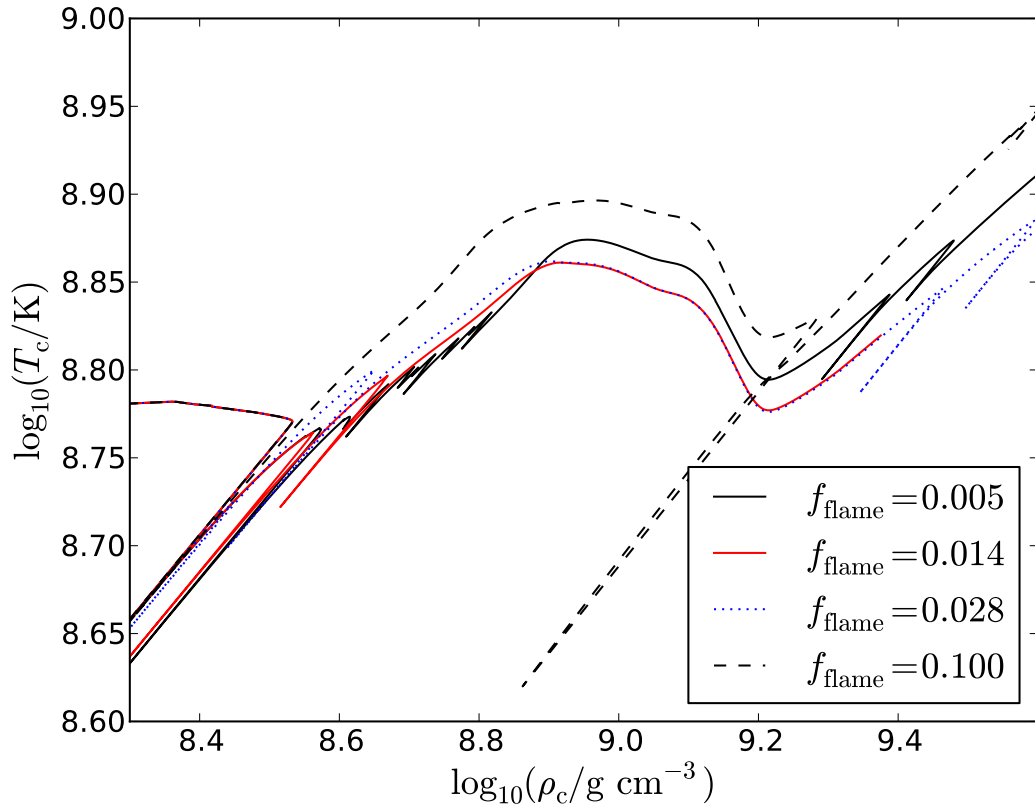


Figure 3.13: Central density–temperature evolution of the $8.8 M_{\odot}$ model showing the differences created during the neon shell flashing phase when $f_{\text{flame}} = 0.005$ was assumed (the original assumption), 0.014, 0.028 and 0.100 (extreme), where f_{flame} is the value of the parameter f in Eq. 2.47 at the base of the ONe-burning shell.

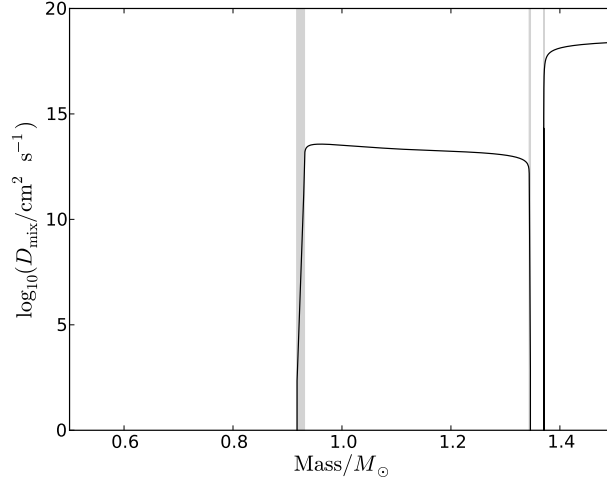
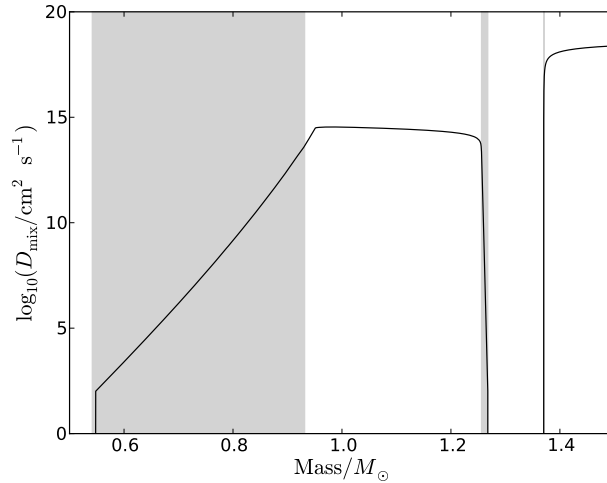
(a) $f_{\text{flame}} = 0.005$ (b) $f_{\text{flame}} = 0.100$

Figure 3.14: Diffusion coefficient profiles against mass coordinate during the second neon flash event in the $8.8M_{\odot}$ model. Shaded grey areas represent the regions of convective boundary mixing. Although the flame re-ignites in the case with $f_{\text{flame}} = 0.100$, the fuel is brought in on the mixing timescale which, during this phase, is shorter than the central contraction timescale and the critical density is already reached for $^{24}\text{Mg} + e^{-}$, leaving the outcome of the model unaltered. It should also be noted that $f_{\text{flame}} = 0.100$ is an extreme assumption adopted purely for the purpose of testing the robustness of the models presented in this work.

($f_{\text{flame}} = 0.100$) is unique because although all models undergo a few flashes after the extent of the URCA process has been exhausted, it is the only one to re-ignite an ONe shell at a mass co-ordinate in-keeping with the original location of the flashes¹. At this point, the centre is already extremely close to the threshold density for $^{24}\text{Mg}(e^-, \nu)^{24}\text{Na}$ at $\rho_c \approx 10^{9.6} \text{ g cm}^{-3}$. The change in extent of the convective boundary mixing between the $f_{\text{flame}} = 0.005$ and $f_{\text{flame}} = 0.100$ models is shown in Figure 3.14.

So far, I have shown that a large range of extra mixing extents at the convective boundary does not affect the qualitative evolutionary outcomes of failed massive stars – EC-SNe. The next logical steps would be (i) to determine whether the presence or absence of a convective boundary mixing prescription affects the evolutionary outcome of failed massive stars in 1D simulations and (ii) to determine the nature of the strength and extent of convective boundary mixing at the interface between the NeO-burning shell and the stable radiative layer.

In super-AGB stars, it has been shown that the nuclear burning front propagates inwards (towards the centre of the star) from the ignition point because the peak energy generation from $^{12}\text{C} + ^{12}\text{C}$ fusion resides below the peak temperature (Siess 2006; Denissenkov et al. 2013b). This is due to the dependency of the fusion rate on the density and the square of the ^{12}C abundance. Energy generation heats the material, dragging the peak temperature inwards and thus the peak energy generation also moves inwards. The location of the base of the convective shell above the flame is determined instead by the luminosity produced above the peak temperature, as discussed above.

Siess (2009) studied the effect of thermohaline mixing on the evolution and propagation of the carbon flame in super-AGB stars. Across the flame front, there is a steep mean molecular weight gradient transitioning between the unburnt composition (^{12}C and ^{16}O) and the composition after it has been processed by the flame (^{20}Ne and ^{16}O). As I have described in Chapter 1, the stratification of a fluid where material of higher mean molecular weight is situated atop material of lower mean molecular weight can

¹All of the other models in this test ignite further shells at the locus of maximum extent of the original ONe-shell flashes, similar to the standard $8.8M_{\odot}$ case.

induce mixing, depending on the steepness of the temperature gradient. Siess found that thermohaline mixing at the carbon flame front could choke off the propagation of nuclear burning, and the carbon flame would thus fail to reach the centre of the star.

Thermohaline mixing is treated as a diffusive process in one dimensional stellar evolution models. The size of the diffusion coefficient depends upon the assumption of the efficiency of the mixing. Thermohaline mixing is typically characterised by the salt-finger aspect ratio, $a = l/d$ where l and d are the length and diameter of the salt fingers (see, e.g., Denissenkov 2010 and references therein), from which the efficiency of the mixing is determined.

Stellar evolution calculations have previously shown that thermohaline mixing characterised by a salt-finger aspect ratio of $a \approx 7$ can reproduce the observed decrease of the surface ^{12}C abundance and $^{12}\text{C}/^{13}\text{C}$ ratio in RGB stars (Charbonnel & Zahn 2007). Siess (2009) assumed the same efficiency of thermohaline mixing in his simulations in which the carbon flame is quenched. More recent two and three dimensional simulations of thermohaline mixing (Denissenkov 2010; Traxler, Garaud & Stellmach 2011) have shown the mixing to be much less efficient, characterised by a value of $a < 1$. Denissenkov et al. (2013b), treating thermohaline mixing with the lower efficiency determined from multi-dimensional simulations, find that this kind of mixing alone is not enough to quench the propagation of the carbon flame in super-AGB stars, and the flame successfully reaches the centre of the star. Furthermore, Denissenkov and collaborators test the stability of the carbon flame against the exponential convective boundary mixing treatment in equation 2.47 assuming values of $f_{\text{CBM}} = 0.014$, 0.007 and 0.004 below the carbon-burning convective shell. In all cases, the flame was quenched, even when accounting for the additional heat transport in the boundary mixing region. The reason for the quenching of the flame in the presence of convective boundary mixing is the flattening of the ^{12}C abundance profile. The conditions for the propagation of the flame are no longer satisfied and the burning front does not reach the centre. Under these circumstances, the super-AGB star will produce a hybrid white dwarf, with an inner core of CO composition and an outer core of ONe composition.

Figure 3.15 shows the energy production due to the key neon- and oxygen-burning

reactions during the peak of the first neon shell flash episode in the $8.8 M_{\odot}$ model. The top panel is the case assuming $f_{\text{CBM}} = 0.005$ below the shell flash convection zone and the bottom panel is for the case with $f_{\text{CBM}} = 0$ (no convective boundary mixing). Note the difference in scale of the x-axis for the plots.

In the case with $f_{\text{CBM}} = 0$ (pure Schwarzschild criterion, bottom panel), there are two distinct peaks in the energy production, separated by a thin region strongly depleted in neon. Just below this region (to the left in the plot), the temperature is about 1.35 GK and the $^{20}\text{Ne}(\alpha, \gamma)^{24}\text{Mg}$ and $^{16}\text{O}(\alpha, \gamma)^{20}\text{Ne}$ reaction rates are very similar. The peak in energy production of each rate at this location traces the abundance of the fuel, and so the peak in $^{20}\text{Ne}(\alpha, \gamma)^{24}\text{Mg}$ lies just below that of $^{16}\text{O}(\alpha, \gamma)^{20}\text{Ne}$. The production of energy must be proportional to $Y(^{20}\text{Ne})^2/Y(^{16}\text{O})$ since the net reaction for neon burning requires two neon nuclei as the reactants (equation 3.6).

In the region where neon has been depleted, the temperature reaches 2 GK and $^{16}\text{O} + ^{16}\text{O}$ becomes significant. α -particles are released by $^{16}\text{O}(^{16}\text{O}, \alpha)^{28}\text{Si}$ and $^{16}\text{O}(^{16}\text{O}, p)^{31}\text{P}(p, \alpha)^{28}\text{Si}$. As the α -particles are released in this way, $^{16}\text{O}(\alpha, \gamma)^{20}\text{Ne}$ and $^{20}\text{Ne}(\alpha, \gamma)^{24}\text{Mg}$ quickly turn ^{16}O into ^{24}Mg and because the $^{20}\text{Ne}(\alpha, \gamma)^{24}\text{Mg}$ reaction is much quicker than $^{16}\text{O}(\alpha, \gamma)^{20}\text{Ne}$ at this temperature, neon is completely depleted. $^{24}\text{Mg}(\alpha, \gamma)^{28}\text{Si}$ proceeds at about half the rate of the $^{20}\text{Ne}(\alpha, \gamma)^{24}\text{Mg}$ reaction and so the region starts to become enriched with ^{24}Mg and ^{28}Si . It happens, then, that producing silicon from oxygen in this way is quicker than oxygen-oxygen fusion, however it must rely upon the oxygen-oxygen fusion reactions as the source of α -particles.

After the neon is processed into ^{24}Mg , ^{28}Si and ^{16}O by the radiative pre-cursor neon flame, the burning moves inwards towards the centre because of its strong dependence on the neon abundance. Above the neon-depleted region (to the right in the plot), neon-burning energy production had previously boosted the luminosity above L_{crit} and the material is convectively unstable, as I described earlier. The temperature in the convective region increases and oxygen-burning reactions ($^{16}\text{O} + ^{16}\text{O}$) are activated.

In the case with $f_{\text{CBM}} = 0.005$, the evolution up to the development of the convective shell is the same for the case with $f_{\text{CBM}} = 0$, since there is no mixing. However,

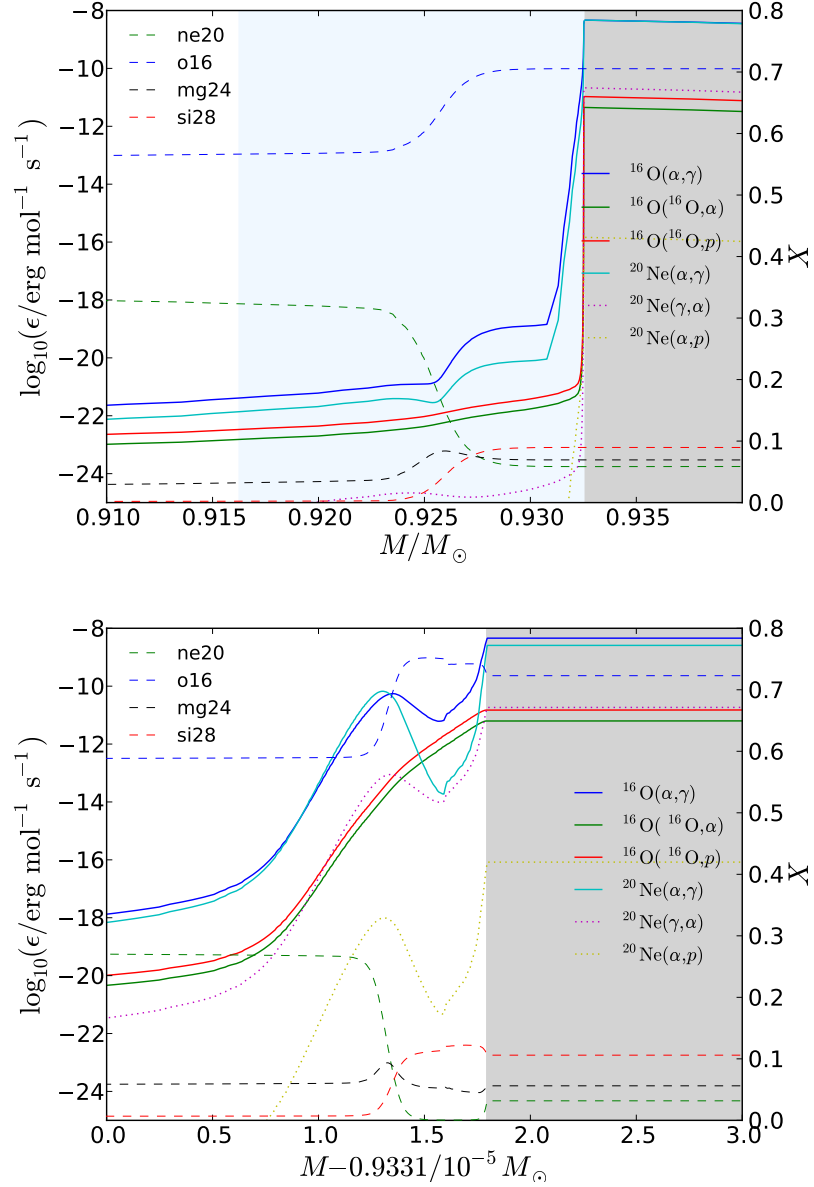


Figure 3.15: Energy production from key neon- and oxygen-burning reactions during the peak of the first neon shell flash in the $8.8 M_{\odot}$ model with $f_{\text{CBM}} = 0.005$ (top panel) and $f_{\text{CBM}} = 0$ (bottom panel) as functions of mass coordinate (absolute values are plotted, with negative quantities plotted with a dotted line style). The abundances of ^{20}Ne , ^{16}O , ^{24}Mg and ^{28}Si are plotted on the right axis. Note the difference in the scale of the x-axis for the two plots. Regions of convection are shaded grey and the extent of convective boundary mixing is shaded for the $f_{\text{CBM}} = 0.005$ model (top panel) in light blue.

the situation evolves differently once the shell becomes convectively unstable. The extra mixing at the lower boundary of the convective shell homogenises the composition across the thin radiative neon-burning shell with that in the convective oxygen-burning shell. This mixing feeds the convective shell with neon, which proceeds to burn there via the net reaction $2^{20}\text{Ne} \rightarrow ^{16}\text{O} + ^{24}\text{Mg} + 4.59 \text{ MeV}$ at much higher temperatures than are usually found during neon burning. This can be seen in the higher rate of energy production by $^{20}\text{Ne}(\alpha, \gamma)^{24}\text{Mg}$ in the convective shell in the top panel of Figure 3.15 ($f_{\text{CBM}} = 0.005$) compared to the bottom panel ($f_{\text{CBM}} = 0$), and the higher abundances of ^{20}Ne and ^{24}Mg . As discussed above, the peak in the energy generation of the radiative pre-cursor neon flame follows closely the sharp increase in the abundance of neon towards the centre. If there is mixing at the convective boundary between the radiative layer and the convective shell, however, the step in the $X(^{20}\text{Ne})$ profile is (i) smoothed out and (ii) displaced towards the centre of the star. With the mixing assumed to be characterised by an exponentially decaying diffusion coefficient with $f_{\text{CBM}} = 0.005$, the temperature at the new location of the step-up in neon abundance towards the centre is 1.07 GK ($\log_{10}(T/\text{K}) \approx 9.03$), and thus ^{16}O dominates ^{20}Ne in the capturing of any α -particles (see Figure 3.10) and neon-burning barely proceeds at all.

The shell burning episode continues to bring neon and oxygen into the convective shell from the radiative layer below until both the convective region and the region in which the mixing had extended are rich in silicon-group composition (^{28}Si , ^{30}Si , ^{32}S and ^{34}S) and depleted in ^{16}O and ^{20}Ne . The convective shell persists until there is no longer sufficient luminosity to sustain it. Upon the extinction of the convective shell, the core contracts as described earlier. Neon burning re-ignites just below the extent of the boundary mixing where fuel is abundant as the core heats up.

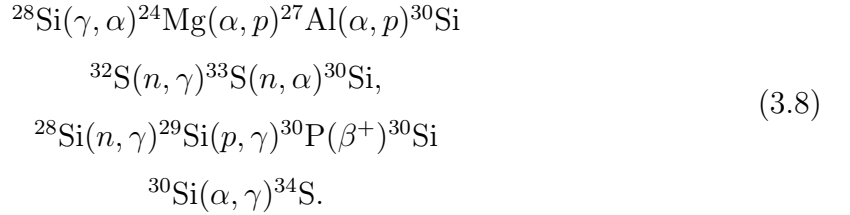
Summary So far, I have discussed how

- The net reaction $2(^{20}\text{Ne}) \rightarrow ^{16}\text{O} + ^{24}\text{Mg} + 4.59 \text{ MeV}$ is the source of energy during neon burning.
- Neon-burning thus proceeds when the $^{20}\text{Ne}(\alpha, \gamma)^{24}\text{Mg}$ rate dominates over the

$^{16}\text{O}(\alpha, \gamma)^{20}\text{Ne}$ rate.

- Once neon is depleted, ^{24}Mg and ^{28}Si are present, and although lots of ^{16}O is produced, there is a ‘freeze-out’ where neon can no longer be produced by $^{16}\text{O}(\alpha, \gamma)^{20}\text{Ne}$ because the source of the α -particles was $^{20}\text{Ne}(\gamma, \alpha)^{16}\text{O}$, and there is no more neon.
- Because of the net reaction for neon burning, the energy production is proportional to $Y(^{20}\text{Ne})^2/Y(^{16}\text{O})$.
- Once ^{20}Ne is depleted in the thin radiative shell, it burns radiatively inwards, following the steep $X(^{20}\text{Ne})$ gradient.
- The luminosity increases radially and a convective zone develops above the flame, mixing down and burning ^{20}Ne , raising the temperature high enough to ignite oxygen burning.
- The presence of convective boundary mixing below the convection zone removes the conditions for a thin radiative ‘pre-cursor’ neon flame, as is the case for the carbon-burning flame in super-AGB stars (Denissenkov et al. 2013b).
- The boundary mixing brings the neon into the convection zone to be burned there instead, and the steep $X(^{20}\text{Ne})$ gradient is smoothed out and displaced towards the centre at temperatures of about 1.07 GK, where α -particles are captured much more efficiently than ^{16}O than by ^{20}Ne , thus preventing neon burning.
- With boundary mixing, the convective shell persists until it, and the boundary mixing region, are depleted in neon and oxygen. The shell extinguishes, support of the outer layers of the core is removed and the core contracts, re-igniting neon and then oxygen in a similar manner closer to the centre.
- With no boundary mixing, the neon flame propagates towards the centre, trailing a convection zone burning both neon and oxygen.

Pulling the focus to the composition of the neon and oxygen shell-burning ashes, I will briefly discuss their impact on the structure of the star and the importance of weak interactions. Thielemann & Arnett (1985) published an in-depth study of the key nuclear reactions that occur during neon, oxygen and silicon burning in massive stars. They showed that amongst those key oxygen-burning reactions are the following reactions that change the electron fraction:



As Thielemann and Arnett emphasise, the abundances of minor nuclei are needed in order to correctly predict the neutron excess (equation 1.4). Three of the reactions in 3.8 involve neutrons as reactants. These neutrons are released by the (p, n) channels of the following reactions:



which are initiated firstly by electron captures and secondly by protons being released by both the (α, p) reactions and the ${}^{16}\text{O}({}^{16}\text{O}, p){}^{31}\text{P}$ reaction. In the lowest mass massive stars,



also contribute to raising the neutron excess (lowering the electron fraction).

Indeed, ${}^{34}\text{S}$ is the most abundant product of oxygen burning in the NeO shells of the present models. The lowering of the electron fraction, Y_e (i.e. increase of the neutron excess, η) lowers the value of the Chandrasekhar mass for the core. During the enhanced contraction, the $8.8 M_\odot$ model reaches the critical density for electron captures by ${}^{27}\text{Al}$ to dominate the central evolution. As I have described in section 3.1.3, the star becomes an electron capture supernova.

3.3 Progenitor structure and importance for supernova explosions

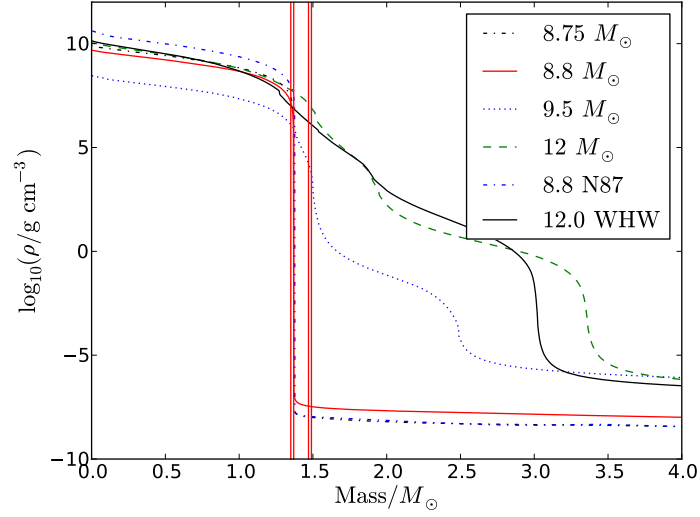
It is becoming clearer that the mechanism driving the explosion of core collapse supernovae is the deposition of energy by neutrino scattering and its revival of the stalled shock (see Janka et al. 2012 for a recent review). The structure of the progenitor star, in terms of density and electron-fraction profiles of the stellar core, has a strong impact on the timescale at which the later supernova explosion may develop as well as on the explosion energetics. Core-collapse supernova explosions are related to the revival of the stalled shock wave, which forms when the contracting core reaches normal nuclear matter density and bounces back. In massive stars that produce iron cores in the conventional manner—through core and shell silicon burning—the characteristic structure of the core that will influence the dynamics of the supernova explosion concerns the material inside the inner edge of the carbon shell. However, in practice the profiles of the entropy and the electron fraction are taken into account when determining the boundary between the material that will comprise the neutron star and the material that will be ejected into the ISM during the supernova explosion (this boundary is commonly referred to as the ‘mass cut’). In general, a sharp density gradient separating iron-core and silicon layer results in a strong acceleration of the bounce shock at the onset of shock revival early after core bounce on a timescale of only few 100 ms. Progenitors with a shallower density gradient suffer from a more extended mass accretion period after core bounce, during which the standing bounce shock oscillates, driven by neutrino-energy deposition behind and mass accretion from above. This results in a delayed onset of shock revival by several 100 ms and more energetic explosions due to the larger heat deposition behind the shock via neutrinos before shock expansion. In more massive stars with shallower density gradients, the standing accretion shock instability (SASI) has been shown to excite various modes and could potentially drive the explosion (see Mueller, Janka & Heger 2012), however this mechanism could have strong dimensional dependencies (i.e. the instability is triggered due to numerical

artefacts).

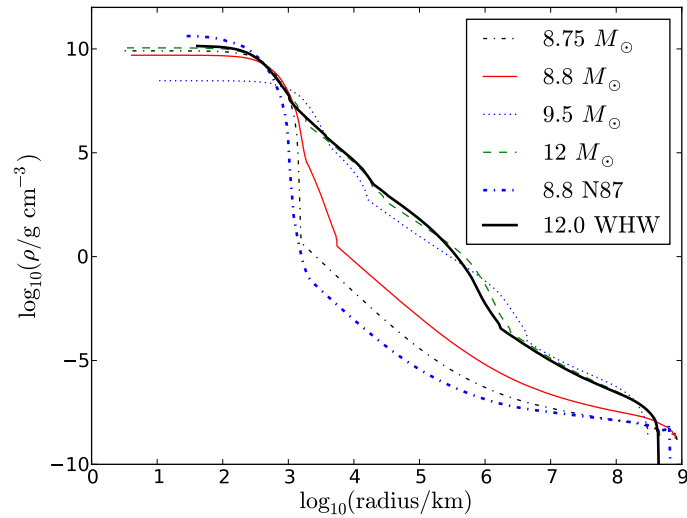
In addition to the standard iron-core progenitors commonly explored in core-collapse supernova studies, a selection of new models of lower zero-age main-sequence mass that belong to the SAGB class have been calculated as well as failed massive stars and low-mass massive stars. Therefore, in Figure 3.16, the structures of the SAGB model ($8.75 M_{\odot}$) after central ^{24}Mg depletion, electron-capture SN progenitor ($8.8 M_{\odot}$, failed massive star) at ignition of oxygen deflagration, low-mass massive star ($9.5 M_{\odot}$) at the point of neon-shell ignition, and standard iron-core progenitor ($12 M_{\odot}$) at the onset of core contraction/collapse (maximum infall velocity across the core exceeds 1000 km s^{-1}) are compared. Note that the $9.5 M_{\odot}$ progenitor is not then as evolved as the other models and hence its central density is still lower than those of the other models. It is therefore only used as a reference case. The major difference between the low-mass (8.75 and $8.8 M_{\odot}$) and the more massive iron-core progenitors is the very steep density gradient separating the core and the envelope. There the density drops about 16 orders of magnitude, from about 10^8 to $10^{-8} \text{ g cm}^{-3}$.

Distinguishing the $8.75 M_{\odot}$ and $8.8 M_{\odot}$ progenitor structures becomes clearer when inspecting the density profiles with respect to radius, Figure 3.16(b). The bulge from $\log_{10}(R/\text{km}) \approx 3.2$ to 3.8 that features in the $8.8 M_{\odot}$ structure but is absent in the $8.75 M_{\odot}$ structure, is a carbon-burning shell. One would expect that, since the $8.8 M_{\odot}$ model experienced several neon-oxygen flashes, the structure within the core should be significantly different from that of the super-AGB model. Aside from the abundance profiles showing a large region in which the composition is dominated by Si-group isotopes, the most striking difference is in the electron fraction, Y_e , which is shown in Figure 3.8.

In Figure 3.16 the progenitor structures of the (SAGB-like) Nomoto (1987) $8.8 M_{\odot}$ and the Woosley, Heger & Weaver (2002b) $12 M_{\odot}$ models have been included for comparison. The Nomoto (1987) structure is at a later evolutionary stage compared to the present models. A fraction of the core has already been burnt to a nuclear statistical equilibrium (NSE) composition, but the core structure is qualitatively similar to the $8.75 M_{\odot}$ SAGB model presented in this work. It is also clear from Figure 3.16, bottom



(a)



(b)

Figure 3.16: Density profiles as a function of mass coordinate (a) and radius (b) for 8.75, 8.8 and 12 M_{\odot} models after central ^{24}Mg depletion, ignition of oxygen deflagration and collapse, respectively. The 9.5 M_{\odot} density profile at the point of neon ignition is also plotted for reference. While the 8.8 M_{\odot} model possesses an SAGB-like structure following dredge-out, the 9.5 M_{\odot} is more reminiscent of a massive star with distinct He- and C- shells. Vertical red lines in (a) show derived pre-collapse masses for the two peaks in the observed neutron star distribution of Schwab, Podsiadlowski & Rappaport (2010). The blue dot-dashed line shows the structure of the Nomoto (1987) progenitor and the black solid line shows that of the 12 M_{\odot} progenitor from Woosley, Heger & Weaver (2002b).

panel, that there are differences in the structure of the (Nomoto 1987, SAGB-like) model and the new $8.8 M_{\odot}$ (failed massive star) model, where there is a CO-rich layer at the edge of the core. As discussed previously, there is a neutron-rich layer in the new $8.8 M_{\odot}$ model where the Ne-O shell flash consumed previously that is not a feature of the Nomoto (1987) model. There is a clear clustering of the SAGB EC-SN progenitor structures and the CCSN progenitor structures in the density profiles as a function of radius (Figure 3.16, bottom panel), while the $8.8 M_{\odot}$ model lies in-between.

The iron-core progenitors have extended high-density silicon as well oxygen and carbon layers above the core. These result in a shallower transition from iron core to helium envelope. The density decreases steadily step-wise according to the different composition interfaces (see Figure 3.16, top panel). Moreover, different evolutionary tracks for the 8.75 , and $8.8 M_{\odot}$ progenitor cores lead to low-mass cores of only about $1.376 M_{\odot}$, which is significantly lower than for the $12 M_{\odot}$ model of $1.89 M_{\odot}$ (see Table 3.1). Note that the $12 M_{\odot}$ iron-core results are in qualitative agreement with those of the KEPLER code (Woosley, Heger & Weaver 2002b) and, as a function of radius, match very well. The reason for the discrepancy between the two as a function of mass is the difference in assumption for convective overshooting, which has led to the production of larger cores in the MESA model. Currently in progress is a code comparison study of MESA, KEPLER and the Geneva stellar evolution code (Hirschi, Meynet & Maeder 2004) for the evolution, explosion and nucleosynthesis of massive stars in order to quantify some of the related uncertainties. The resulting steep density gradient at the edge of the core of the EC-SN progenitor models presented in this work are expected to accelerate the supernova shock on a short timescale after core bounce, producing a weak explosion with little ^{56}Ni ejecta, as in previous studies (e.g. Wanajo et al. 2009). Such an explosion should produce qualitatively similar results as obtained for the $8.8 M_{\odot}$ progenitor from Nomoto (1987) (for details about electron-capture supernova explosions, see Kitaura, Janka & Hillebrandt 2006, Janka et al. 2008b and Fischer et al. 2010). The split between weaker, more rapid EC-SN explosions and stronger, slower FeCCSN explosions is a possible explanation for the observed bi-modality in the spin period and orbital eccentricity of X-ray binaries, although it is not clear how this

is manifested (Knigge, Coe & Podsiadlowski 2011). The consensus is that in the slower explosions, asymmetries can develop more strongly and give a larger natal kick to the star (Scheck et al. 2006; Wongwathanarat, Janka & Müller 2010).

3.4 Discussion and concluding remarks

I have begun to explore in detail stellar evolution at the transition mass range between super-AGB stars and massive stars at solar metallicity. Using the MESA code, I was able to model stars across the transition (AGB, super-AGB, EC-SN progenitors and massive stars) with a consistent set of input physics, while current published stellar evolution calculations limit themselves to either massive stars or super-AGB stars. In addition, I have calculated full stellar models rather than computing the evolution of helium stars.

I was able to follow the evolution of the entire star from pre-main sequence up to the ignition of an oxygen deflagration for the $8.8 M_{\odot}$ model and up to the activation of electron captures by ^{20}Ne for the $8.75 M_{\odot}$ model, both of which become EC-SNe. The $8.75 M_{\odot}$ case is the first EC-SN progenitor model published including the envelope and the TP-SAGB phase, and the $8.8 M_{\odot}$ case is the first EC-SN progenitor model from a failed massive star. Using the AGILE-BOLTZTRAN hydrodynamics code together with supernova theorists, the $8.8 M_{\odot}$ model has been confirmed to result in core collapse—an EC-SN (Fischer 2014). While such a confirmation has not been performed for the $8.75 M_{\odot}$ super-AGB model, the model has an evolution relatively consistent with the existing literature.

The $8.8 M_{\odot}$ model confirms the notion that failure to establish a stable neon-oxygen laminar flame that propagates to the centre can result in an electron-capture supernova proposed by Timmes, Woosley & Taam (1994). The main difference in the pre-SN evolution when compared with the generally accepted (super-AGB) EC-SN progenitors is that following dredge-out (and neon-burning), the core contracts directly to the threshold density for electron captures by ^{24}Mg and ^{20}Ne as opposed to first undergoing episodic core growth through thermal pulses in the He-shell.

Although the main conclusions of the chapter should not change, it is important to stress that the initial mass for which the evolutionary paths described depend on the choices made for convective boundary mixing at the edge of the convective core. This would, however, affect the statistical contribution of these types of stars to a complete

population because of the shape of the IMF.

Also noteworthy is the fact that the rates of weak reactions in *sd*-shell nuclei of Oda et al. (1994) are available in very sparse grids with respect to temperature and electron density. Finer grids for weak interaction rates are necessary to precisely follow the URCA and other weak reaction processes. In chapter 4, I will show that by using new, well sampled weak rates for the $A = 23, 25$ and 27 URCA pairs the central evolution presented by Ritossa, García-Berro & Iben (1999) is qualitatively reproduced.

Schwab, Podsiadlowski & Rappaport (2010) present a sample of 14 neutron stars for which the masses are well-measured. The authors calculate the pre-collapse masses of the stars in their sample, the distribution of which is distinctly bimodal and is attributed to the two birth mechanisms, EC-SNe and FeCCSNe. In Figure 3.16, the two peaks of the pre-collapse mass distribution are plotted as red vertical lines. Because each NS birth mechanism is coupled intrinsically to the pre-supernova evolution of the star, it is an interesting result that the peaks should agree relatively well with the pre-SN structure of the two models in the present set that undergo off-centre ignition of neon. Between 8.8 and $9.5 M_{\odot}$ (from the present set of models), an initial mass range of only $0.7 M_{\odot}$ contains about 15% of all single stars with the potential to give birth to a NS (assuming a Salpeter IMF and that single stars in the mass range $8.5 \leq M/M_{\odot} \leq 20$ produce neutron stars in their deaths). For this reason, the importance of further investigation into the initial mass range between 8.8 and $9.5 M_{\odot}$ is strengthened. From examination of these two models in the set, there may be an interesting correlation between the propagation of the neon-oxygen flame and the URCA process.

If both failed massive stars and super-AGB stars have the potential to produce electron capture supernovae then the EC-SN channel is wider than is thought at present. It is my intention to produce EC-SN progenitor models from both super-AGB stars and failed massive stars for several metallicities. Detailed supernova simulations with the models and including full nucleosynthesis will help constrain what observational features and nucleosynthesis one can expect from EC-SNe.

There are three main factors determining the evolution of stars in the mass range between super-AGB stars and massive stars, which ignite neon and oxygen burning off-centre: mixing at the convective boundary, lowering of the electron fraction by burning oxygen into a composition with relatively high neutron excess, and the approach of the central density to the threshold for the $^{27}\text{Al}(e^-, \nu)^{27}\text{Mg}$ reaction. As I have shown, the boundary mixing prohibits the conductive propagation of the radiative burning front after off-centre ignition. The propagation of the shell towards the centre under these conditions is instead driven by compressional heating between each convective shell-burning episode. This behaviour, where the pressure support provided by the shell is switched recurrently on and off provides the perfect opportunity for the core to reach higher densities, facilitated by the lower average electron fraction due to oxygen burning. If, during this evolution, the density reaches the threshold density for electron captures on ^{25}Mg to be activated in the centre of the star, then the contraction of the core is accelerated by the removal of electrons, and the star will produce an electron capture supernova.

In the absence of mixing at the convective boundary (pure Schwarzschild criterion), it is not yet confirmed that the burning front will propagate conductively all the way to the centre, however the simulations in the present work indicate that if this is the case, then the star may not reach the densities for the URCA process to operate. Instead, the burning shell could provide support of the outer layers until the flame reached the centre. The core would then be rich in silicon-group composition and therefore not produce an electron capture supernova. However, such simulations having never been completed with such a detailed reaction network, it is difficult to predict the effect of the increasing neutron excess in the core due to shell burning on the contraction of the core.

Convective boundary mixing is at present still a very uncertain phenomenon. While the timescales for stellar evolution restrict theoretical models to only one dimension, there is an emergence of effort to explore specific phases of the evolution in two (Herwig et al. 2006; Herwig et al. 2007) and three (Meakin & Arnett 2007; Mocák et al. 2011; Herwig et al. 2011) dimensions in order to properly quantify the extent of

convective mixing and its behaviour at the boundary with a radiative zone. The long term goal is to further constrain the parameters of the diffusive treatment by analysing the results of 3D simulations, or indeed to implement new schemes in the 1D models, as informed by 3D simulation.

4 Calculation, implementation and impact of new weak interaction rates

In the previous chapter and briefly in the introduction, it was shown how weak interactions play a crucial role in the advanced evolution of stars. In particular, the URCA process in CO white dwarfs – the progenitors of thermonuclear type Ia (carbon-deflagration) supernovae – and ONe white dwarfs – the progenitors of the AIC scenario. In chapter 3 it was also shown that the advanced evolution of super-AGB stars and failed massive stars as progenitors of electron capture supernovae is strongly influenced by the URCA process. In the case of stars that ignite neon and oxygen off-centre, the fate is dependent upon whether or not the star experiences the URCA process.

The Chandrasekhar limit is strongly dependent upon the electron fraction ($M_{\text{Ch}} \propto Y_e^2$, see equation 2.16) and thus the removal of electrons from the stellar material reduces the Chandrasekhar mass. The collapse of the cores of these electron capture supernova (EC-SN) progenitors (in the AIC scenario and in both super-AGB and failed massive star progenitors) is a direct result of the effective Chandrasekhar limit becoming smaller than the actual core mass. Electrons are removed from the material by capturing onto ^{24}Mg , ^{24}Na , ^{20}Ne and ^{20}F in the high density environment where degenerate electrons provide the majority of pressure support for the stellar core. A similar process where electrons are captured by iron-group nuclei and free protons, combined with the rapid photodisintegration of those same nuclei, trigger the collapse of the iron core in massive stars and resulting in iron core collapse supernovae (FeCCSNe).

The electron fraction is set by the rate of weak interactions and charge exchange reactions (e.g. (p, n) and (n, p) reactions). It is one of the key quantities determining the abundance distribution of nuclei that are synthesised during the supernova explosion, along with the temperature. It determines the distribution of material in nuclear statistical equilibrium (NSE). This distribution is important for linking supernova observations and theory because the amount of nickel that is synthesised in and ejected by the explosion is linked to the peak luminosity of the supernova light curve.

The NSE distribution at the time when the material begins to fall into disequilibrium also determines the neutron-to-seed ratio, which is a crucial factor in determining the behaviour of neutron-capture nucleosynthesis in the supernova.

In this chapter, firstly the case is made in favour of calculating new tables of weak reaction rates for *sd*-shell nuclei relevant to the evolution of 8–12 M_{\odot} stars (section 4.1). The method with which the new reaction rates have been calculated by Toki et al. (2013) including Coulomb corrections (section 4.2), and how they have implemented into the MESA stellar evolution code (section 4.3) is described. Finally, section 4.4 provides a description of the results from these new rate calculations and their impact on the evolution of failed massive stars.

4.1 Case for the calculation of new weak reaction rates

This section describes the nuclear physics uncertainties associated with modelling the progenitors of electron capture supernovae. These uncertainties provide the motivation for improving the accuracy of the treatment of weak reaction rates for *sd*-shell nuclei in stellar models. Firstly, the characteristics that differentiate weak reaction rates from charged particle fusion rates are discussed. The uncertainties introduced into stellar evolution models by using weak reaction rates available in the literature at the time of this work are then described. Finally, the rationale behind the choice to calculate updated reaction rates in tabular form with finer resolution is explained.

4.1.1 What is involved?

The rates of two- and three-body nuclear reactions vary by many orders of magnitude with respect to temperature due to the sensitivity of the velocity-integrated reaction cross section, $\langle \sigma v \rangle$. However, the rate of these types of charged particle fusion reactions are only linearly dependent upon the mass density ρ (two-body) or dependent

upon mass density to the second power (three-body; see section 2.3 and equation 2.48). This is not the case for weak interactions, whose rates depend upon the product of the mass density and the electron fraction, ρY_e , in a more complex, non-linear fashion. The strong density dependence of the weak reaction rates is manifested in the electron chemical potential μ_e , which appears in the Fermi-Dirac distribution. The exact manner in which the rate relates to the chemical potential of the electron will be described in section 4.2.

Nuclear reaction rates are required by the nuclear reaction network module of any stellar evolution code (see chapter 2). In section 2.4.2 I described how the REACLIB scheme (Cyburt et al. 2010) can be used to calculate the rates of various nuclear reactions as a function of the temperature in GK using a set of seven fitting coefficients (equation 2.50). The alternative is to interpolate tabulated rates for which the λ (one-body) or $N_A \langle \sigma v \rangle$ (two-body) is given for a number of temperatures. Indeed, REACLIB rates are largely the results of fitting tabulated rates in such a way. As a consequence of the non-linear density dependence of the weak reaction rates, there will be an extra dimension to the tabulated reaction rates for weak reactions compared to those for charged particle fusion reactions. The procedure is a little more complicated if one wishes to include weak reactions in the nuclear reaction network since now there are rates with two-dimensional dependencies. In order to avoid large memory usage when computing stellar evolution models with a large nuclear reaction network, weak reaction rates are usually tabulated on the order of 10×10 co-ordinates in $(\log_{10} Y_e \rho, T_9)$ space, for the ranges

$$\begin{aligned} 1 &\leq \log_{10} Y_e \rho \leq 11 \\ 0.001 &\leq T_9 \leq 30. \end{aligned} \tag{4.1}$$

As I have already briefly mentioned, under degenerate conditions in the stellar interior the distribution of electron energies is given by Fermi-Dirac statistics and hence weak interaction rates become very steep functions of density, an effect that is even stronger with decreasing temperature.

4.1.2 The problem with currently available rates

Figure 4.1 shows an example of the available tabulated weak reaction rates that have been published in the literature. The rate of $^{24}\text{Mg}(e^-, \nu)^{24}\text{Na}$ is shown as a function of $\log_{10}(\rho Y_e)$ at a fixed temperature of $T_9 = 0.4$ GK, and the two types of points show the results from the calculations of Takahara et al. (1989) and Oda et al. (1994). The lines joining the points in Figure 4.1 show the rate that would result from a linear interpolation of $\log_{10}(\lambda/s^{-1})$, which is the technique that is used in the code to obtain the rate for a given temperature, density and electron fraction.

It becomes clear from Figure 4.1 that when using a log-interpolation technique, the sparsity of the Oda et al. (1994) tables is insufficient to properly resolve the degeneracy threshold in the rate, which is better represented by the tables of Takahara et al. (1989) since there is a better sampling of the calculated rates. The figure highlights the numerical errors that are introduced into the code because the reaction rate will strongly depend upon the resolution of the reaction rate tables. The extent to which these numerical errors propagate through to the results is shown in section 4.4. The rate of $^{24}\text{Mg} + e^-$ jumps by about 20 orders of magnitude from $\log_{10}(\rho Y_e/g \text{ cm}^{-3}) = 9.0$ to 10.0 at the temperature of interest ($T = 0.4$ GK). This is a problem for resolving the rate at the threshold density and interpolation results in a significant underestimation of the rate.

One may achieve a smoother rate with more continuous behaviour by changing the technique of interpolation. For example, the result of using a cubic spline interpolation instead of the linear is shown in Figure 4.2 for the ^{24}Mg electron capture rate. The cubic spline method introduces new errors into the rate, giving an overestimation in the crucial regime where the rate jumps several orders of magnitude at the threshold. Simply using the sparsely sampled rates with different interpolation routines is thus not a viable option. There are still more shortcomings of calculations involving electron capture rates that are poorly resolved in the $\rho - T$ plane. For example, the vast majority of widely used rate tables for *sd*-shell nuclei possess a grid spacing of 1 dex in ρY_e .

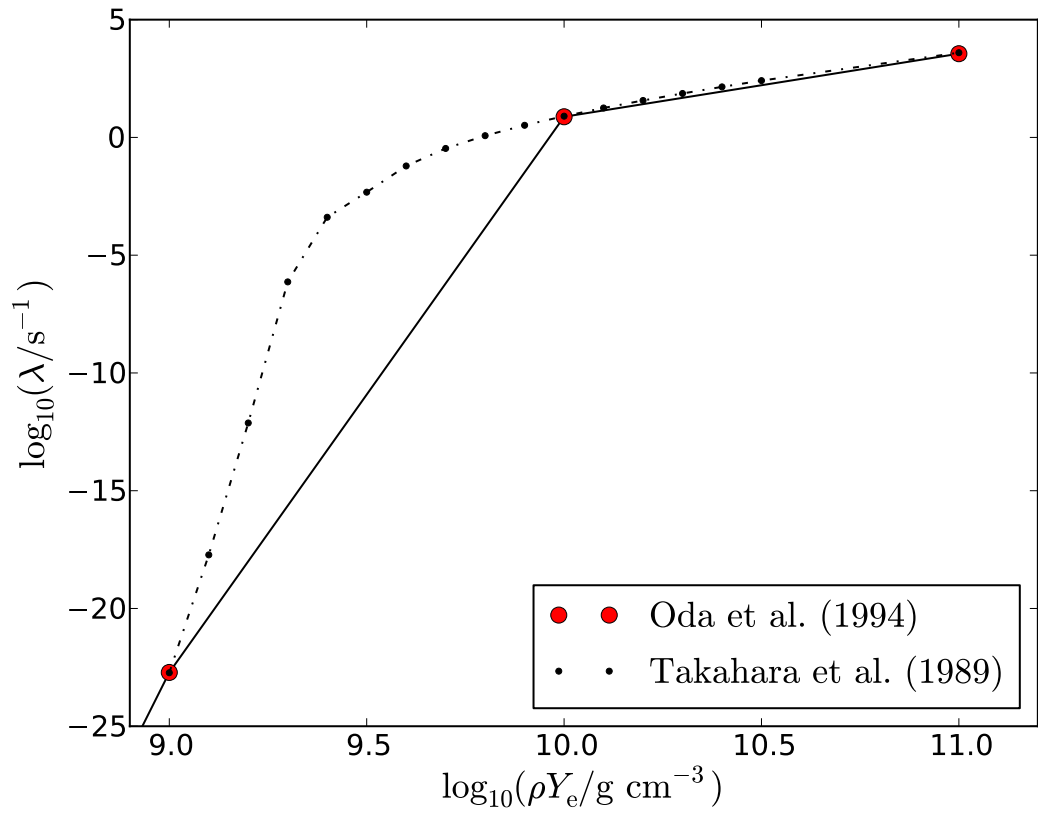


Figure 4.1: $\lambda(^{24}\text{Mg} + e^-)$ at $T = 4 \times 10^8$ K from the compilations of Oda et al. (1994) and Takahara et al. (1989). It is immediately clear that the denser sampling in the rate of Takahara et al. (1989) better represents the threshold density for the rate. The lines show the resulting interpolation of these rates that is used in the code.

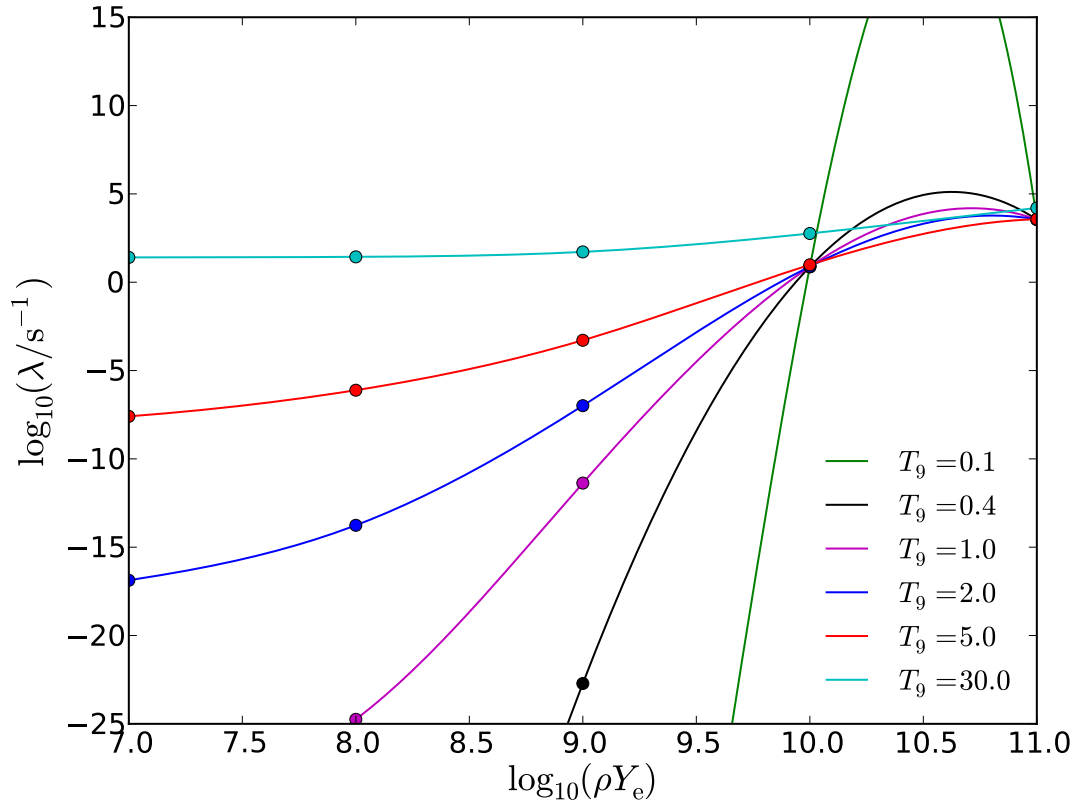


Figure 4.2: Reaction rates for $^{24}\text{Mg}(e^-, \nu)^{24}\text{Na}$ from the Oda et al. (1994) compilation as a function of electron density for various temperatures ($T_9 \equiv T/10^9 \text{ K}$). The solid lines show the result of a cubic spline interpolation for fixed temperature. The rate resulting from the interpolation is vastly overestimated in the crucial regime (in particular for $T_9 = 0.4$ and 0.1 , which are appropriate central temperatures for the super-AGB progenitors of EC-SNe).

4.1.3 Proposed solutions

In order to overcome the issue of under-sampled weak interaction rates outlined above, there are two general approaches one can take: (i) use the rates from existing tables with a more intelligent interpolation technique informed by nuclear physics or (ii) create new tables with the desired resolution in $\log_{10}(\rho Y_e) - T_9$ space with the latest nuclear physics, and continue to use the log-interpolation method.

An example of method (i) with which to vastly reduce the error that is introduced into the rates by interpolation of sparsely sampled rates was proposed by Fuller, Fowler & Newman (1985). The ft value is the product of the phase space integral, f , and the half-life, t (or $t_{1/2}$), for a single transition—from a specific state in the parent nucleus to a specific state in the daughter. The ft value is a quantity that depends only on the strength of the transition (i.e. on the transition matrix element, B_{ij} ; see section 4.2.1). Fuller, Fowler & Newman (1985) demonstrated that one could produce *effective* ft^1 values by using an efficient analytical approximation to the ground-state to ground-state phase space integral, ϕ_{GS} (the expression for ϕ under various conditions is given by Fuller, Fowler & Newman 1985 as functions of the degeneracy parameter), normalising the rate to produce a quantity that varied smoothly with respect to $\log_{10}(\rho Y_e)$. The relationship between the rate λ , ground-state to ground-state phase space integral ϕ_{GS} and the effective ft value $\langle ft \rangle$ is

$$\langle ft \rangle = \phi_{\text{GS}} \frac{\ln 2}{\lambda}. \quad (4.2)$$

More details of what comprises the phase space integral are given in section 4.2, but for now its relevance need only be summarised by considering that the density dependence of the reaction rate λ is introduced by the ϕ term. Thus, interpolating the $\log_{10}\langle ft \rangle$ values and converting them back into a rate, λ/s^{-1} , using the relation in equation 4.2 should provide a much more accurate representation of the rate. However, this formalism has a major caveat in that it will only be appropriate when the rate is

¹The use of triangular brackets, e.g. $\langle ft \rangle$, indicates the effective value of ft in this discussion.

dominated by ground-state to ground-state transitions. In order to demonstrate that $\log_{10}\langle ft \rangle$ is not a smoothly varying quantity with respect to $\log_{10}(\rho Y_e)$, I have calculated its values for the Oda et al. (1994) compilation. For the ground-state to ground-state phase space integral, ϕ_{GS} , I used the analytical formulae of Fuller, Fowler & Newman (1985). The resulting $\langle ft \rangle$ values are shown in Figure 4.3. While for the ^{20}Ne electron capture rate, the $\langle ft \rangle$ values vary by less than an order of magnitude, the rate of electron capture by ^{24}Mg produces a much less smoothly varying value. The $\langle ft \rangle$ value jumps more than two orders of magnitude between $\log_{10}(\rho Y_e) = 7$ and 9, and then falling 4 orders of magnitude between $\log_{10}(\rho Y_e) = 9$ and 10. Thus, the $\log_{10}\langle ft \rangle$ formalism does not produce a smoothly varying function of T_9 and $\log_{10}(\rho Y_e)$ for some of the weak interactions involved in the evolution of electron capture supernova progenitors where transitions other than ground-state to ground-state have large contributions to the rate. The same is true for β -decays; the rate of which is in fact dominated by transitions other than those from ground-state to ground-state. One always wishes to use a consistent format of input for the rates together with a consistent method of interpolation in order to best quantify the error in the calculation and without the possibility of introducing new sources of error. For this reason, I find the $\log_{10}\langle ft \rangle$ formalism redundant in this scenario and thus choose not to employ it, even for nuclear and thermodynamical regimes in which an accurate physical representation of a number of rates may be achieved in this manner.

In light of the previous discussion, I find it preferable to calculate new weak reaction rates for a more appropriate grid in $\log_{10}(\rho Y_e) - T_9$ space, option (ii). I will still use a linear log-interpolation technique to provide rates in-between the grid points. In the regime where the degeneracy is mild, electron chemical potential is much lower than the reaction threshold ($\mu_e \ll Q_{ij}$), the reaction rate will be very low and will not vary much as a function of the density. This means that the new tabulated rates need not be so densely resolved in all regions. Focussing on the URCA process reactions ($A = 23, 25$ and 27), I have determined that an appropriate grid would require:

$$\Delta \log_{10}(\rho Y_e / \text{g cm}^{-3}) = 0.02$$

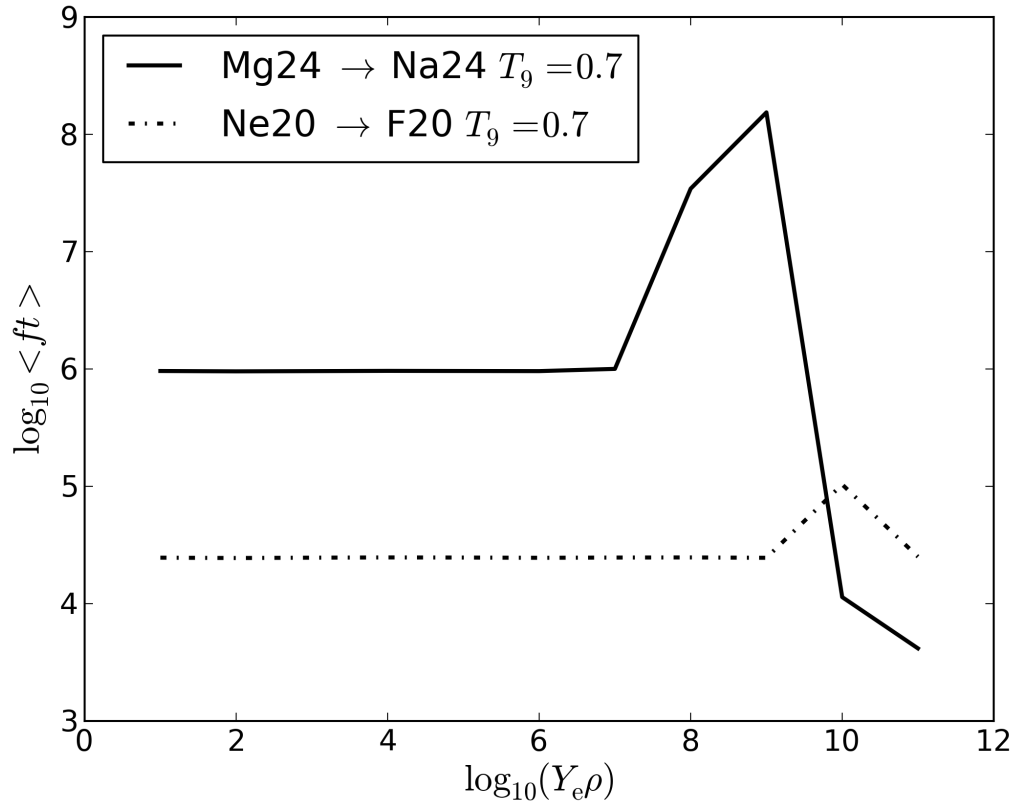


Figure 4.3: $\log_{10}\langle ft \rangle$ values for the electron capture rates of ^{24}Mg and ^{20}Ne using the formalism of Fuller, Fowler & Newman (1985) at $T_9 = 0.7$. For $^{24}\text{Mg}(e^-, \bar{\nu})^{24}\text{Na}$, $\log_{10}\langle ft \rangle$ is not a smoothly varying function of $\log_{10} Y_e \rho$ since a significant contribution to the rate is made by transitions to (from) excited states in the daughter (parent) nucleus.

$$\Delta \log_{10}(T/\text{K}) = 0.05$$

for the conditions

$$7.0 \leq \log_{10}(T/\text{K}) \leq 9.2$$

$$8.0 \leq \log_{10}(\rho Y_e/\text{g cm}^{-3}) \leq 9.2.$$

For the nuclei with $A = 20$ and 24 , the density range should be revised to have an upper limit at $\log_{10}(\rho Y_e) = 11$.

4.2 Rate Calculations

The last section outlined the motivation for calculating new weak reaction rates for sd -shell nuclei, particularly the $A = 23, 25$ and 27 URCA process nuclei and the $A = 20$ and 24 nuclei that are important during the late evolutionary stages of electron-capture supernova progenitors. This section will briefly describe the calculations performed by collaborators to evaluate weak interaction rates for sd -shell nuclei for this study (Toki et al. 2013).

4.2.1 General form

The methodology employed for the calculation of new β^\pm -decay, e^\mp -capture, ν -loss and $\bar{\nu}$ -loss rates from nuclear quantities (energy levels, transition strengths, spins) is similar to that in the literature (Fuller, Fowler & Newman 1980; Oda et al. 1994; Langanke & Martínez-Pinedo 2000; Toki et al. 2013), however I will briefly describe the general method here for completeness.

The rate for a weak reaction, λ^α , where α denotes the type of reaction (β^- -decay, e^- -capture, β^+ -decay or e^+ -capture; bm , ec , bp and pc respectively) is given by the general formula

$$\lambda^\alpha = \frac{\ln 2}{K} \sum_i \left[\frac{(2J_i + 1)e^{-E_i/k_B T}}{G(Z_p, A_p, T)} \sum_j B_{ij} \phi_{ij}^\alpha \right] \quad (4.3)$$

where $K = 6146 \pm 6$ s is a constant related to fine structure (Langanke & Martínez-Pinedo 2000), i and j denote quantities pertaining to the parent and daughter nuclei respectively, and

$$G(Z_p, A_p, T) = \sum_l (2J_l + 1) e^{-E_l/k_B T} \quad (4.4)$$

is the partition function of the parent nucleus. B_{ij} is the transition matrix element – the strength of the transition from state i in the parent nucleus to state j in the daughter nucleus (sometimes called the transition strength) – and is a probability given by

$$B_{ij} = B_{ij}^{Fermi} + B_{ij}^{GT}. \quad (4.5)$$

B_{ij}^{Fermi} and B_{ij}^{GT} are the Fermi and Gamow-Teller contributions to the transition probability respectively. The total spin quantum number of the electron and neutrino is 0 for Fermi transitions and 1 for Gamow-Teller transitions. B_{ij}^{GT} is calculated using the spin and isospin operators ($\boldsymbol{\sigma}$ and \mathbf{t} respectively) and an experimentally observed quenching factor. Further details of the transition strength calculations are beyond the scope of this thesis and are therefore not discussed. ϕ_{ij}^α is the phase space integral, in which information about the density dependence of the rate is introduced into the calculation. The expression is slightly different depending upon the reaction type (see § 4.2.2), but the general form is

$$\phi_{ij}^\alpha = \int (Q_{ij} \pm w)^2 w p F(Z, w) S_{e,p} (1 - S_\nu) dw. \quad (4.6)$$

In 4.6 and throughout this description, $w = \frac{1}{m_e c^2} (m_e c^2 + E_K)$ is the energy of the electron in units of $m_e c^2$, and $p = \sqrt{w^2 - 1}$ is the electron momentum, in units of $m_e c$. $Q_{ij} = \frac{1}{m_e c^2} (M_p - M_d + E_i - E_j)$ is the transition Q -value in units of $m_e c^2$, where M_p and M_d are the nuclear rest masses of the parent and daughter nuclei respectively. Hence, the term $(Q_{ij} \pm w)$ pertains to the energy of the reaction neutrino, depending upon α . $S_{e,p}$ and S_ν are the distributions of electrons/positrons and neutrinos respectively, however based on the relevant conditions in the stellar interior one assumes non-interaction of neutrinos and hence S_ν is always zero. For reference, the electron distribution function is given by

$$S_e = [e^{(E_e - \mu_e)/k_B T} + 1]^{-1}, \quad (4.7)$$

where μ_e is the chemical potential of the electron and $E_e = wm_e c^2$. Finally, the Fermi function $F(Z, w)$ corrects for the Coulomb distortion of the electron wavefunction by the nuclear potential.

4.2.2 Phase space integrals

The phase space integrals have different forms depending on α (bm , ec , bp or pc). These are:

$$\phi_{ij}^{ec} = \int_{w_l}^{\infty} (Q_{ij} + w)^2 wp F(Z, w) S_e(w) (1 - S_\nu(Q_{ij} + w)) dw. \quad (4.8)$$

$$\phi_{ij}^{pc} = \int_{w_l}^{\infty} (Q_{ij} + w)^2 wp F(-Z, w) S_p(w) (1 - S_\nu(Q_{ij} + w)) dw. \quad (4.9)$$

$$\phi_{ij}^{bm} = \int_1^{Q_{ij}} (Q_{ij} - w)^2 wp F(Z + 1, w) (1 - S_e(w)) (1 - S_\nu(Q_{ij} - w)) dw. \quad (4.10)$$

$$\phi_{ij}^{bp} = \int_1^{Q_{ij}} (Q_{ij} - w)^2 wp F(-Z + 1, w) (1 - S_p(w)) (1 - S_\nu(Q_{ij} - w)) dw. \quad (4.11)$$

For electron and positron captures, the lower limit w_l is set to

$$w_l = \begin{cases} 1 & Q_{ij} > -1 \\ |Q_{ij}| & Q_{ij} < -1 \end{cases}. \quad (4.12)$$

The phase space integrals are evaluated numerically at each $\log_{10}(\rho Y_e, T_9)$ coordinate, which is by far the most time consuming task and presents the strongest case against computing the rates in real-time during the stellar evolution calculations.

4.2.3 Nuclear Physics input: USDB shell model

Using equation 4.3, one can calculate the rates of β^\pm -decays and e^\mp captures. In order to do this, one requires the energy stratification of the states of the parent and daughter nuclei, the spin and isospin of each state and the GT transition strengths for transitioning between those states (recall that the strengths of Fermi transition strengths are not required directly, but are calculated from the spin and isospins of the nuclear states).

For *sd*-shell nuclei with $18 \leq A \leq 38$ the atomic masses, excitation energies of the parent and daughter nuclei and GT transition strengths between each pair of parent-daughter states for β^\pm -decay and e^\mp -capture are calculated using a shell model code (e.g. Richter, Mkhize & Brown 2008). The shell model code used by Toki et al. (2013) to calculate the transition strengths—and hence, the weak reaction rates—that were used in the present work considers the USD (universal *sd*) interaction (Wildenthal 1984) along with the USDA and USDB (versions A and B) updates to the Hamiltonian.

4.2.4 Neutrino fluxes and γ -ray heating rates

For each reaction, one would also need to calculate the neutrino luminosity ϵ_ν and the γ -ray heating rate ϵ_γ . These terms are important when using weak reaction rates in calculations of stellar evolution or supernovae. For example, the neutrino luminosity appears in the equation of energy conservation of stellar structure (equation 2.5).

For neutrino fluxes, ϵ_ν (MeV/s), an extra factor of $Q_{ij} \pm w$, the neutrino energy, is introduced into the integrand of the phase space integral. Yet to be mentioned is the γ -ray heating rate of a reaction. For every transition to an excited state in the daughter nucleus, a γ -ray will be emitted upon its decay to the ground state. Assuming that the daughter nucleus will instantaneously decay to the ground state if it is created in an excited state (an assumption held for the calculations associated with this work), emitting the aforementioned γ -ray, then the γ -ray heating rate, ϵ_γ (MeV/s), is given by equation 4.3 with an extra factor of E_j in the final summation (over the daughter states). As I will explain in section 4.3, in order to calculate the averaged net energy production due to a weak reaction, one need only consider either $\langle E_\nu \rangle$ or $\langle E_\gamma \rangle$ – the average neutrino and gamma-ray energies, respectively – not both. Since the neutrino luminosity is simply energy removed from the star per second and assuming the daughter nucleus decays instantaneously to the ground state, $\langle E_\nu \rangle$ is generally considered the more useful quantity.

4.2.5 Screening of weak reactions

At high densities, the Coulomb interaction of the electron ‘background’ and the nuclei becomes non-negligible. In order to produce the most accurate, up-to-date rate calculations, Coulomb corrections to the nuclear chemical potential, μ_i and to the electron chemical potential, μ_e must be accounted for. The former manifests itself as a correction to the transition Q -value Q_{ij} in the phase space integrals (4.8–4.11). The treatment of the Coulomb corrections follows that of Juodagalvis et al. (2010), which is summarised below.

The self-manifested Coulomb field in which the ion and electron gas exists promotes interactions between the particles, altering the energy of the particles in the system. The correction to the chemical potential of species i , assuming that the nuclear charges do not affect the background distribution of electrons, is (Yakovlev & Shalybkov 1989)

$$\mu_{i,C} = k_B T f_C(\Gamma_i), \quad (4.13)$$

making the corrected nuclear chemical potential

$$\mu_i = \mu_{i,0} + \mu_{i,C}, \quad (4.14)$$

where $\mu_{i,0}$ is the uncorrected nuclear chemical potential from Boltzmann statistics. Γ is the ion-coupling parameter – the ratio of the potential energy of the ions (due to Coulomb interactions) to their thermal energy. f_C is the Coulomb free energy per ion; for $\Gamma > 1$ (the ‘free energy regime’) an analytical expression for the Coulomb free energy per ion is given by Yakovlev & Shalybkov (1989) with fitting coefficients from Ichimaru (1993). The Coulomb free energy per ion for $\Gamma < 1$ is also given by Yakovlev & Shalybkov (1989). In the case of $\Gamma \ll 1$, Coulomb interactions are negligible however they do become significant while Γ is still well below unity. In that regime, the Debye-Hückel limit is reproduced by the Yakovlev & Shalybkov (1989) formula for f_C in the case that $\Gamma < 1$ (Juodagalvis et al. 2010; see also Cox & Giuli 1968 section 15.5).

The resulting correction to the reaction Q -value is

$$\Delta Q_C = \mu_C(Z - 1) - \mu_C(Z), \quad (4.15)$$

(Couch & Loumos 1974), yielding the screened transition energy

$$Q_{ij}^s = Q_{ij} + \Delta Q_C. \quad (4.16)$$

For electron capture, $\Delta Q_C < 0$ and thus the threshold energy is increased (since Q_{ij} itself is negative) and the electron capture rate is reduced for a given thermodynamic condition. The screening potential, V_s , is assumed to be constant inside the nucleus with a value evaluated at the nuclear radius given by Itoh et al. (2002) as an analytical fitting formula.

The screening potential results in a distorted electron distribution that is now given by

$$S_e = [e^{(E_e + V_s - \mu_e)/k_B T} + 1]^{-1}, \quad (4.17)$$

which one can equivalently describe as a modification of the electron chemical potential, using the fact that

$$S_e(E_e + V_s, \mu_e, T) = S_e(E_e, \mu_e - V_s, T). \quad (4.18)$$

This yields screened weak reaction rates by using the same formalism for the phase space integrals that is outlined above in section 4.2.2, and replacing Q_{ij} with $Q_{ij}^s = Q_{ij} + \Delta Q_C$ and μ_e with $\mu_e^s = \mu_e - V_s$.

4.3 Implementation in a stellar evolution code (MESA)

In section 4.2, the calculation of β^\pm -decay and e^\mp capture was outlined, along with the method of calculation of their respective neutrino emission and γ -ray heating rates. These rates ($\log_{10} \lambda^\alpha$, $\log_{10} \epsilon_\nu$ and $\log_{10} \epsilon_\gamma$) are tabulated in $\log_{10}(\rho Y_e) - T_9$ space. This section will describe how the weak reaction rates are implemented inside the MESA stellar evolution code. First, in section 4.3.1 I will summarise the chapter so far before the implementation is described in section 4.3.2.

4.3.1 A quick reality check

During the very late stages of the 8.75 and $8.8 M_{\odot}$ stars electron captures by sd -shell nuclei become crucial to the fate of the star. In the degenerate core, there is a very sharp jump in the rates of these electron captures, which corresponds to a threshold density at which the electron chemical potential, μ_e , exceeds the threshold energy for the reaction to proceed. Tabulated electron capture rates that are used as input for the models must properly resolve this steep transition if one wants to know at what density the oxygen deflagration is ignited. One should want to know that density so that it can be determined whether nuclear energy release from burning the core to nuclear statistical equilibrium (NSE) composition is high enough to exceed the gravitational binding energy of the core and thus lead to its explosion (Gutierrez et al. 1996). Otherwise, the core would collapse to a neutron star following its deleptonisation through electron captures on ^{20}Ne , iron-group isotopes and free protons.

Because the rates are so sensitive to density, any form of interpolation cannot properly represent the physical situation without some input from knowledge of the nuclear physics. This is why several groups employ an interpolation of effective $\log ft$ values (Fuller, Fowler & Newman 1985). I have explained that the effective $\log ft$ value for a reaction is related to its raw rate by the relationship in equation 4.2, where ϕ_{GS} is the ground-state to ground-state phase space integral, and that the aim is to produce a quantity that varies smoothly with T and ρ . From this new, smoothly varying quantity, the raw rate may be obtained within a stellar evolution calculation by approximation of the phase space integral at the desired conditions. I concluded that while this method is considered to be relatively robust for those weak rates for which ground-state to ground-state transitions dominate, it is not valid for the reactions of interest in electron-capture supernova progenitors. The change in Y_e is not the only important facet of the electron captures; they also possess a strong heating effect. The heating is due to the γ -decay of the daughter nuclei to their ground state from the excited states in which they were created. Hence this demonstrates the importance of excited states when one attempts to normalise the reaction rate using simplifications

or approximations such as the $\log\langle ft \rangle$ formalism.

Having concluded that there are two possible sets of desired quantities, either grids of weak reaction rates for sd -shell nuclei that are appropriately resolved through the threshold density or $\log ft$ values that incorporate all important transitions in the normalisation of the rate, I have approached solving the problem with the former method. The rationale here is that there are contributions from many states of the parent and daughter nuclei for these reactions and to perform phase space integral routines (see section 4.2) within a stellar evolution code to account for this could be exceptionally inefficient². It is also important to use β^\pm -decay and neutrino-loss rates calculated with the same physics and grid resolution to ensure consistency when one examines the impact of the URCA process on the evolution. More generally, since the energy production is calculated from the tabulated neutrino luminosity (see 4.34, where ϵ_ν is the neutrino luminosity), consistent grids are required for any weak rate, not just those operating as part of an URCA pair.

4.3.2 Implementing weak reactions into the stellar evolution code

As in any nuclear reaction network, the abundance change of a species i is given in equation 2.48. Weak reactions contribute to the first term in this equation (one-body). As such, the rate of change in abundance of species i that is undergoing, for example, electron capture, is simply given by

$$\dot{Y}_i = -Y_i \lambda_i^{ec}(\log_{10} \rho Y_e, T_9), \quad (4.19)$$

where λ has been interpolated from the rates produced using methods akin to those in section 4.2, for the appropriate $\log_{10}(\rho Y_e), T_9$ coordinate.

The energetics of an electron capture reaction are illustrated in Figure 4.4. Conservation of energy requires that

²The rates are in fact dominated by transitions from the ground state of the parent nucleus to excited states in the daughter nucleus.

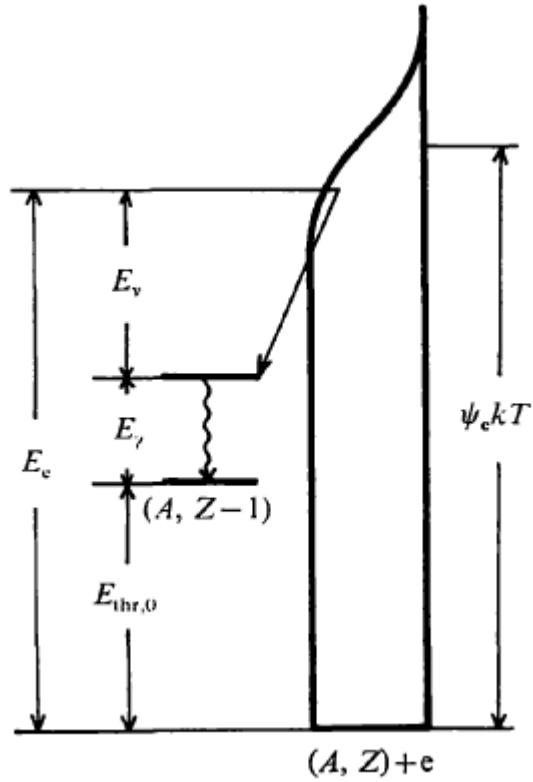


Figure 4.4: Schematic diagram illustrating the energetics of electron capture from Miyaji et al. (1980). The parent (A, Z) and daughter $(A, Z-1)$ nuclei are shown along with the electron distribution. The electron chemical potential is labelled as $\psi_e kT$ and the neutrino and gamma-ray energies are E_ν and E_γ , respectively. $E_{\text{thr},0}$ is the ground-state to ground-state transition energy.

$$M_{p,0}c^2 + E_p + E_e = M_{d,0}c^2 + E_d + E_\nu, \quad (4.20)$$

where $M_{p,0}c^2$, $M_{d,0}c^2$, E_p and E_d are the ground state and excitation energies of the parent and daughter nuclei respectively, E_e is the energy of the captured electron and E_ν is the energy of the emitted neutrino. Since I assume that the daughter nucleus decays instantaneously to the ground state, one can replace E_d directly with E_γ ,

$$M_{p,0}c^2 + E_p + E_e = M_{d,0}c^2 + E_\gamma + E_\nu, \quad (4.21)$$

where E_γ is the energy of the γ -ray from the decay of the daughter nucleus if it is created in an excited state. In the case for which all transitions are from the ground state of the parent nucleus, $E_p = 0$, and if all transitions are directly to the ground state of the daughter nucleus, $E_d = E_\gamma = 0$. For a transition to a fixed state in the daughter nucleus, the higher the initial state of the parent, the higher the energy of the emitted neutrino for the reaction. Similarly, a transition from a fixed state in the parent nucleus yields a higher neutrino energy for a lower final state in the daughter.

In Figure 4.4, ψ_e is the degeneracy parameter, which is related to the electron chemical potential, μ_e , by

$$\mu_e = \psi_e kT. \quad (4.22)$$

By definition,

$$\mu_e = - \left. \frac{\partial E}{\partial N_e} \right|_s. \quad (4.23)$$

Using the notation of Miyaji et al. (1980), the threshold energy for the reaction is

$$E_{thr} = (M_{d,0}c^2 + E_d) - (M_{p,0}c^2 + E_p). \quad (4.24)$$

Substituting E_{thr} into equation 4.20 and rearranging gives

$$E_e = E_{thr} + E_\nu, \quad (4.25)$$

and for electron capture in general, $E_{thr} = -Q_{ij} > 0$. Assuming the daughter nucleus decays directly to the ground state and that the parent nucleus is almost always in the ground state, $E_{thr} = E_{thr,0} + E_\gamma$ and the expression becomes

$$E_e = E_{thr,0} + E_\nu + E_\gamma. \quad (4.26)$$

We have seen from the detail of the rate calculations in section 4.2 that it is not possible to deal with each reaction explicitly within the stellar evolution code (or in most applications). Instead, the averages of quantities are calculated tables and as such, equation 4.26 becomes

$$\langle E_e \rangle = E_{thr,0} + \langle E_\nu \rangle + \langle E_\gamma \rangle, \quad (4.27)$$

taking

$$\langle E_\nu \rangle = \frac{\epsilon_\nu}{\lambda_{ec}}, \quad (4.28)$$

$$\langle E_\gamma \rangle = \frac{\epsilon_\gamma}{\lambda_{ec}}, \quad (4.29)$$

with both ϵ and λ terms found by interpolation with respect to the position in the $(\log_{10} Y_e \rho, T_9)$ plane. $\langle E_e \rangle$ is the average energy of a captured electron, and in theory should be given by integrating the electron distribution function from E_{thr} for each transition (the electron energy at which the capture is possible) as in equation 4.30.

$$\frac{\langle E_e \rangle}{m_e c^2} = \frac{\int_{E_{thr}/m_e c^2}^{\infty} w S_e(w, \mu_e, T) dw}{\int_{E_{thr}/m_e c^2}^{\infty} S_e(w, \mu_e, T) dw} \quad (4.30)$$

The average energy of the captured electron for each transition will therefore depend upon E_{thr} for the transition. Moreover, there are large contributions from several states in the daughter nuclei, as I have discussed already in section 4.1.

To consider the net energy production from a given reaction, I refer to Figure 4.4, which illustrates the fate of the energy of the captured electron. Its energy is distributed between (i) the nuclear potential energy (rest mass) of the daughter nucleus compared to the parent nucleus, (ii) the energy of the neutrino and (iii) the energy of the γ -ray, should the daughter be created in an excited state. Hence, except for the energy that will be returned to the system via the γ -decay of the daughter, the entire energy of the captured electron is ‘lost’ in the emitted neutrino and the extra energy in the ground state of the newly created daughter nucleus (compared to its parent). A simple rearrangement of equation 4.23,

$$\partial E = -\mu_e \partial N_e, \quad (4.31)$$

shows that under fixed conditions, electron capture will increase the thermal energy of the system by an amount μ_e . This means that one may then write an expression for the net energy production per reaction, E_{ec} , in terms of these average quantities as

$$E_{ec} = \mu_e + \langle E_\gamma \rangle - \langle E_e \rangle. \quad (4.32)$$

The implications are such that if the electron chemical potential is lower than the threshold energy for the reaction ($\mu_e < E_{thr,0}$) the reaction will proceed slowly since the number of electrons with energy of at least $E_{thr,0}$ will be extremely low. Under these circumstances, the reaction will actually be endothermic because $\langle E_e \rangle > \mu_e$.

Re-writing equation 4.32 by substituting in $\langle E_e \rangle$ as it is given in equation 4.27, since one does not wish to repeatedly calculate it within the stellar evolution code, gives

$$E_{ec} = \mu_e - E_{thr,0} - \langle E_\nu \rangle, \quad (4.33)$$

which now contains only a constant from nuclear physics, the electron chemical potential from the equation of state (EOS) and $\langle E_\nu \rangle$, which is taken from the weak reaction rate tables as described in equation 4.28. This gives the expression for the net energy production (MeV s^{-1}) due to a particular electron capture reaction from tables,

$$\epsilon_{ec} = \left(\mu_e - E_{thr,0} - \frac{\epsilon_\nu}{\lambda_{ec}} \right) \lambda_{ec}. \quad (4.34)$$

One may follow a similar derivation for the process of β^- -decay (' bm '), yielding

$$\epsilon_{bm} = \left(E_{thr,0} - \mu_e - \frac{\epsilon_\nu}{\lambda_{bm}} \right) \lambda_{bm}, \quad (4.35)$$

and likewise for positron capture and β^+ decay.

These quantities must be included when solving the energy equation of stellar structure (2.5). Clearly, ϵ_{ec} , ϵ_{bm} and their respective ϵ_ν terms will contribute some fraction of the net ϵ and ϵ_ν in the energy equation. This fraction will vary depending upon the composition and thermodynamic conditions of the stellar plasma, but is highest in compact, degenerate conditions such as the cores of white dwarfs, the cores of intermediate-mass and massive stars during the late stages of their evolution and the crusts of neutron stars.

4.4 Impact of new weak reaction rates on the stellar models

New weak reaction rates have been computed for the $A = 23, 25$ and 27 classical URCA pairs (Toki et al. 2013) and for the $A = 20$ and 24 nuclei that are important during the late phases of electron capture supernova progenitors (Martínez-Pinedo et al. 2014). In this section the properties of the rates themselves are examined and compared with rates that were previously available in the literature (Takahara et al. 1989; Oda et al. 1994). The impact of these new rates on the evolution of failed massive stars is then presented and discussed.

4.4.1 URCA rates

In chapter 3, it was shown that the evolution of stars at the transition between super-AGB and massive stars is dominated by weak reactions. This is illustrated in the central evolution of the 8.75 and $8.8 M_{\odot}$ models in Figures 3.3 and 4.5. The onset of the URCA process modifies significantly the evolution during the neon-oxygen shell burning phase of failed massive stars and aids the central contraction, so long as some degree of mixing between the convective shell and underlying radiative layer operates. In massive super-AGB stars, the Chandrasekhar mass is also reduced when electrons are captured during the URCA process and the evolution of the core is accelerated towards the critical central density at which electron captures by ^{24}Mg are activated. Thus, it is imperative to treat the URCA process as accurately as possible to best predict the fate of $8 - 12 M_{\odot}$ stars.

Motivated by the present work, Toki et al. (2013) have produced well resolved ($\Delta \log_{10} \rho Y_e / \text{g cm}^{-3} = 0.02$ and $\Delta \log_{10} T / \text{K} = 0.05$) reaction and neutrino loss rates for the $A = 23, 25$ and 27 URCA pairs under the conditions $7.0 \leq \log_{10} (T/\text{K}) \leq 9.2$ and $8.0 \leq \log_{10} (\rho Y_e / \text{g cm}^{-3}) \leq 9.2$. The difference between the Oda et al. (1994) compilation and the newly calculated Toki et al. (2013) rates that are available to use in stellar evolution calculations for the $A=25$ pair is shown in Figure 4.6. The most

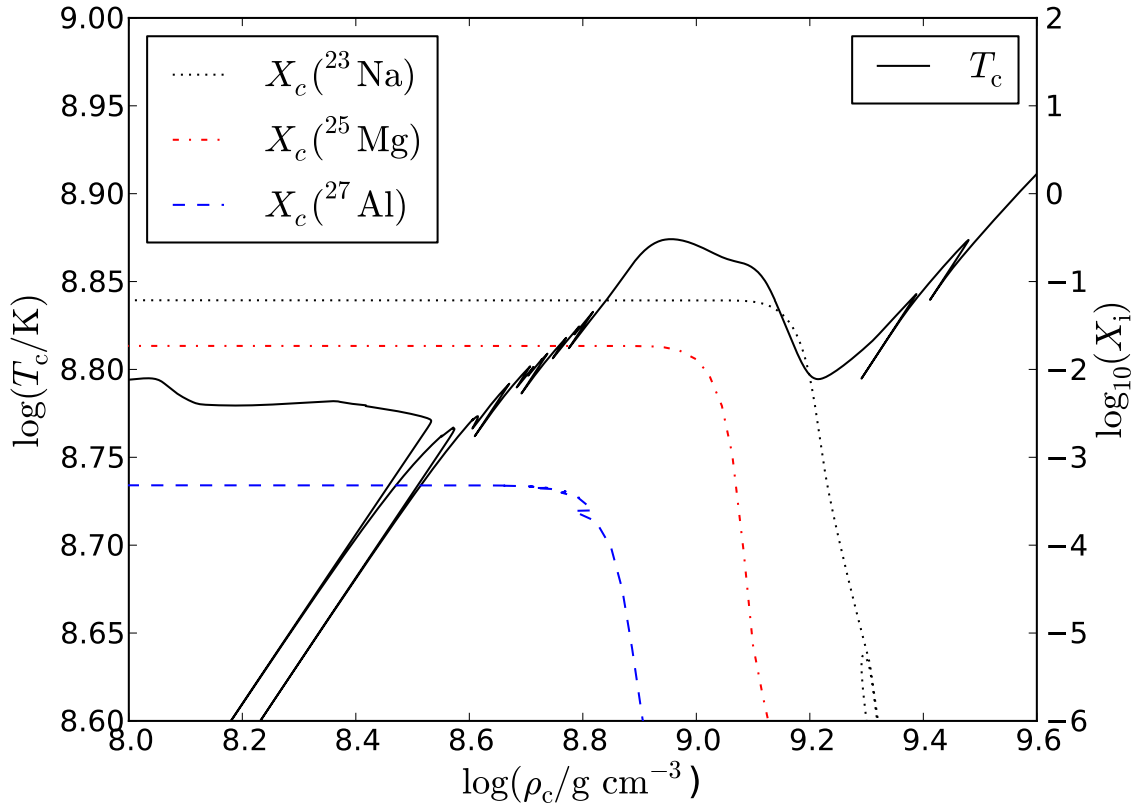


Figure 4.5: Evolution of the $8.8 M_{\odot}$ model in the $\rho_c - T_c$ plane along with the central abundances (right axis) of the key URCA process isotopes. This calculation used the weak reaction rates of Oda et al. (1994). Electron captures on ^{25}Mg and ^{23}Na cool the central regions while those on ^{27}Al provide little contribution due to the low abundance of fuel and the Pauli blocking of $^{27}\text{Mg} \rightarrow ^{27}\text{Al} + \beta^- + \bar{\nu}$. The $A = 23$ pair provides stronger cooling than the $A = 25$ pair.

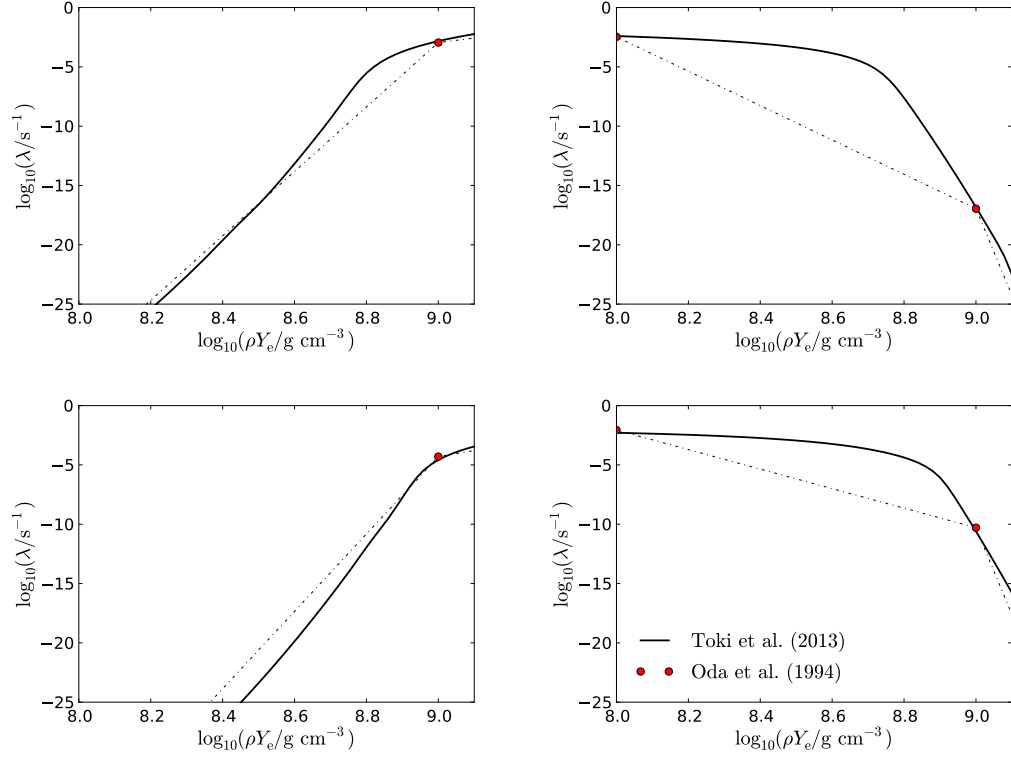


Figure 4.6: ^{25}Mg electron capture rate (top left panel) and ^{25}Na beta decay rate (top right panel) at $T = 4 \times 10^8$ K from the compilation of Oda et al. (1994) and the new calculation by Toki et al. (2013). The lower panel shows the same for the $A = 23$ pair $^{23}\text{Na} \leftrightarrow ^{23}\text{Ne}$. These particular rates from Toki et al. (2013) do not include Coulomb corrections for the purpose of more direct comparison with the Oda et al. (1994) rates, which do not include these corrections either.

striking difference between the linear interpolation of the Oda et al. (1994) rates and the Toki et al. (2013) rates can be seen for the ^{25}Na β^- -decay rate in the top right panel of Figure 4.6. The maximum discrepancy between the linearly interpolated Oda et. al. rate and the new Toki et. al. rate is almost 10 orders of magnitude! As I have discussed in section 4.2.5, the most up-to-date rates should include the effects of Coulomb screening. The rates from Toki et al. (2013) in Figure 4.6 for the $A = 25$ and 23 pairs do not include the effects of Coulomb corrections purely for the purposes of a more direct comparison to the interpolation of the Oda et al. (1994) rates, with which

I intend to illustrate the large discrepancies.

As I described in detail in section 3.1.3, the URCA process operates in regimes where the forward (electron-capture) and reverse (β -decay) rates between a pair of nuclei (${}^A Z$ and ${}^A(Z-1)$) are both high. Under these conditions, energy is rapidly removed via the production of neutrinos and the process produces a net cooling effect. For a given pair of nuclei linked in this way, the potential strength of the URCA process for that pair can be illustrated by plotting the product of the electron-capture and β -decay rates as a function of density for relevant temperatures. Such a plot for the $A = 23, 25$ and 27 pairs is shown in Figure 4.7 for the rates of Toki et al. (2013). The figure shows that the cooling should be strong from the ${}^{25}\text{Mg} \leftrightarrow {}^{25}\text{Na}$ and ${}^{23}\text{Na} \leftrightarrow {}^{23}\text{Ne}$ pairs. For the ${}^{27}\text{Al} \leftrightarrow {}^{27}\text{Mg}$ pair, the β -decay rate is blocked before the electron capture rate becomes significant and hence there is a negligible cooling effect. Instead, the heating due to the electron capture reaction ${}^{27}\text{Al} + e^- \rightarrow {}^{27}\text{Mg} + \nu + \gamma$ has a stronger impact. This is a known result for the classical $A = 27$ URCA pair (see Ritossa, García-Berro & Iben 1999 and section 3.1.3). Also plotted in Figure 4.7 are the quantities λ^{ec} , λ^{β^-} and $\lambda^{ec}\lambda^{\beta^-}$ for the neutron-rich counterparts of the classical URCA pairs, i.e. ${}^{23}\text{Ne} \leftrightarrow {}^{23}\text{F}$, ${}^{25}\text{Na} \leftrightarrow {}^{25}\text{Ne}$ and ${}^{27}\text{Mg} \leftrightarrow {}^{27}\text{Na}$. These could be considered a second set of URCA pairs where the electron-capture parent is the electron-capture daughter of its classical URCA process pair counterpart. One can see that the two (the classical URCA and the neutron-rich URCA) do not operate under the same thermodynamic conditions; the neutron rich pairs all have higher Q -values and thus operate at higher electron densities. Although these neutron-rich pairs display generally higher values of $\lambda^{ec}\lambda^{\beta^-}$ (recall that this quantity is an indication of the strength of the cooling), the evolution of stars at these densities is much more rapid than at those where the classical URCA process operates. Moreover, under these thermodynamic conditions the rate of ${}^{24}\text{Mg} + e^- \rightarrow {}^{24}\text{Na} + \nu$ is already several orders of magnitude higher than any of the electron-capture rates by the neutron-rich URCA parent nuclei ${}^{23}\text{Ne}$, ${}^{25}\text{Na}$ and ${}^{27}\text{Mg}$ (see section 4.4.2).

The same type of plot for the same rates, this time from the compilation of Oda et al. (1994) with linear interpolation is shown in Figure 4.8. Putting the somewhat

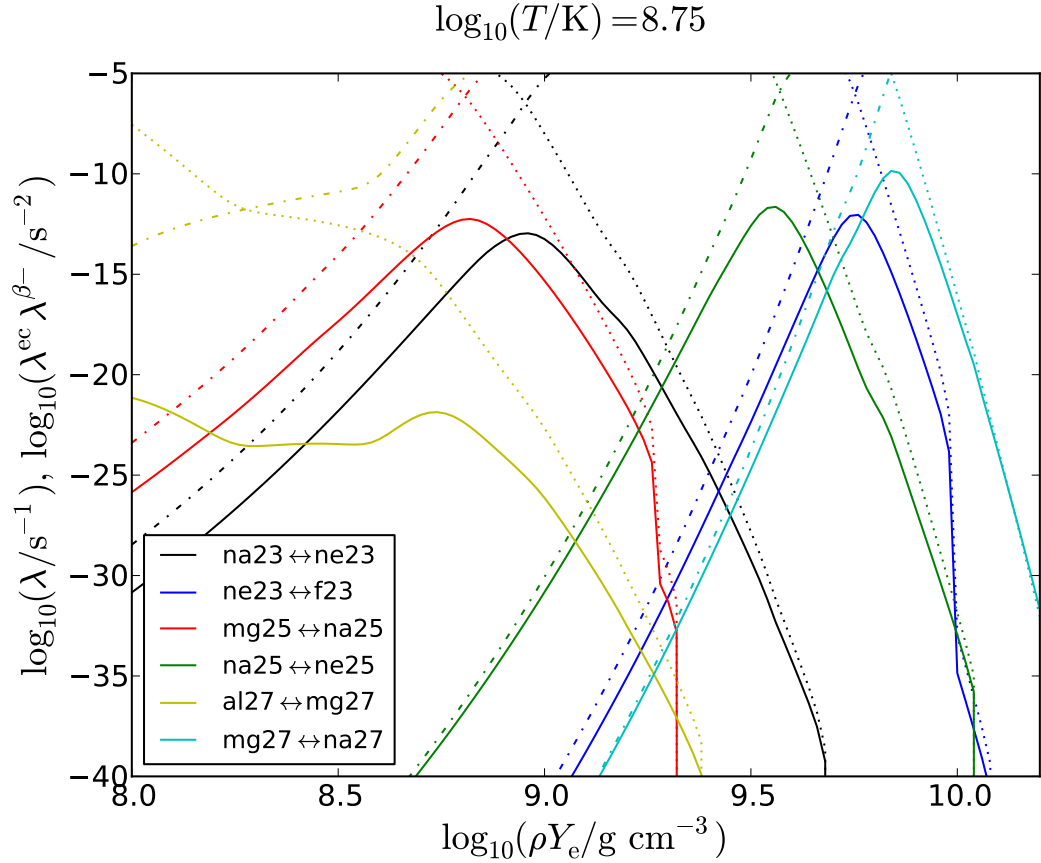


Figure 4.7: Product of electron-capture and β -decay rates for $A=23, 25$ and 27 (solid lines) using the newly calculated rates from Toki et al. (2013) including Coulomb corrections. The dot-dashed lines show the respective electron-capture rates and the dotted lines show the β -decay rates. A peak in each solid line shows roughly where a given pair of nuclei will induce cooling via the URCA process, and the height of the peak gives an indication of the strength of the cooling. The classical URCA pairs are in yellow, red and black, and one can clearly see that the $A = 27$ pair does not produce a significant cooling effect.

obvious shortcomings aside, the figure resembles the behaviour seen in Figure 4.7 for the rates of Toki et al. (2013). For example, cooling is provided by the $A = 23$ and 25 pairs but not the $A = 27$ pair. The $A = 23$ pair produces stronger cooling than the $A = 25$ pair, which is the opposite of what is seen in the new Toki et al. (2013) rates. The electron density of strongest cooling is the same for both $A = 23$ and 25 pairs, which is an artefact of the sparse grid resolution. In Figure 4.7 it is clear that cooling from the $A = 25$ pair taking place at lower electron densities (earlier in the evolution) than the $A = 23$ pair, due to the lower magnitude of the Q -value for the $A = 25$ reactions. Although the Toki et al. (2013) rates in Figure 4.7 include Coulomb corrections, it is difficult to comment on the differences this causes when compared to the Oda et al. (1994) rates in Figure 4.8 because of the resolution issues. In fact, the inclusion of Coulomb corrections in the Toki et al. (2013) calculations shift the curves in Figure 4.7 by about 0.05 dex to the right (higher electron density).

The impacts of these new, well-resolved rates compared to those of Oda et al. (1994) on failed massive star models at $Z = 0.014$, 0.001 and 10^{-5} are shown in Figure 4.9. Not only is the cooling effect more pronounced, as predicted by the close examination of the rates above, but the reaction thresholds are more clearly identifiable in the central evolution and occur at higher densities than with the rates of Oda et al. (1994). A neon-oxygen shell flash occurs in the model with $Z = 0.001$ when ^{23}Na is almost depleted in the centre. As I described in section 3.1.3, the centre's response to the shell flash is expansion and cooling along the adiabatic slope (down and leftwards in the plot). This brings the centre of the star back to the electron density where some heating is produced by $^{25}\text{Mg}(e^-, \nu)^{25}\text{Na}$, producing a different central trajectory during the flash compared with the same model using the rates of Oda et al. (1994). When the shell extinguishes and the core once more contracts, the central regions again evolve through the electron densities where the $A = 23$ pair can provide cooling. The timescale is shorter than before, and so only a small amount of cooling takes place this time.

All of the failed massive star models in which the Coulomb corrected rates of Toki et al. (2013) were used are cooler in the centre than their equivalent models using the

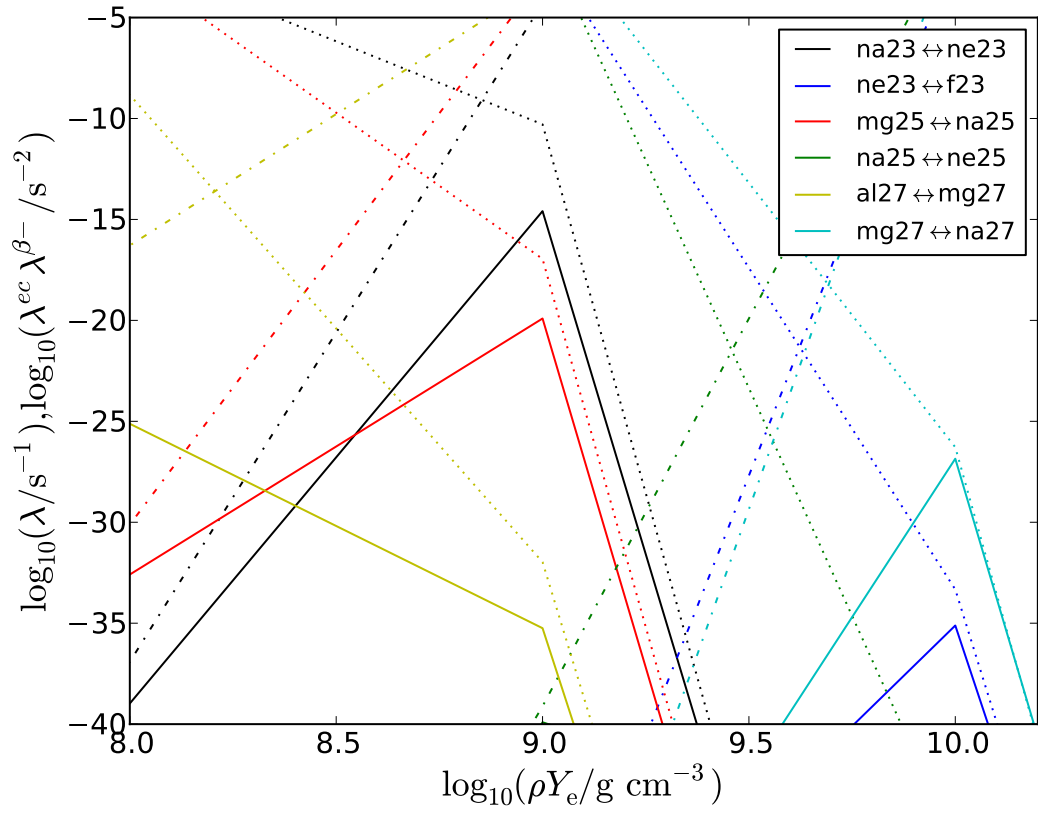


Figure 4.8: Same as Figure 4.7 but for the rates of Oda et al. (1994).

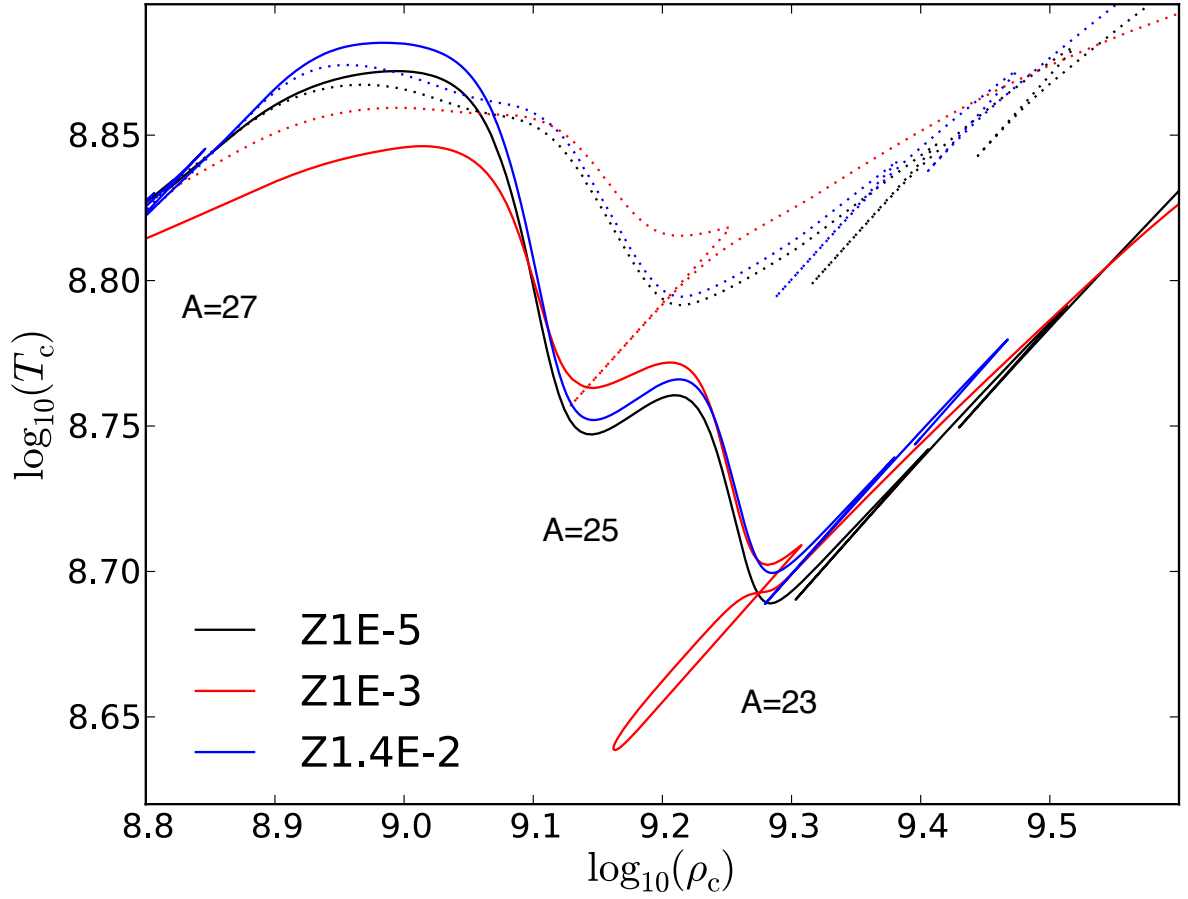


Figure 4.9: Central evolution of the failed massive stars at 3 metallicities ($Z = 0.014$, 0.001 and 10^{-5}) governed by the URCA process. Dashed lines show the models where the weak rates of Oda et al. (1994) were used and solid lines those where the new rates of Toki et al. (2013) including Coulomb corrections were used.

Oda et al. (1994) rates. This lower temperature makes the transition from low to high rates at the reaction thresholds for electron captures by ^{24}Mg and ^{20}Ne much steeper functions of the electron density. This is because the step at $E_e = \mu_e$ in the Fermi-Dirac distribution becomes more defined with decreasing temperature. Hence, at lower temperature it is less probable for an electron to have an energy greater than the μ_e and the reaction proceeds extremely slowly when only electrons from the exponential tail of the distribution can contribute (see section 4.3.2). Thus, the effect of the lower temperatures on the rate thresholds mean that the impact of the $A = 24$ and 20 weak reactions occurring later in the evolution will be felt by the star at higher densities. This is a similar effect that the operation of the URCA process has on carbon ignition in degenerate CO cores and WDs. The models of Paczyński (1973) showed that with increasing abundances of odd- A nuclei (i.e. the stronger the cooling effect), the ignition density of carbon in the degenerate material would be greater. However, one can not draw too many parallels to this work.

4.4.2 $A = 20$ and 24 rates

The sensitivity of the oxygen-deflagration ignition density to the threshold density of $A = 20$ electron captures has been demonstrated by Gutierrez et al. (1996). Coulomb corrections cause an increase in the threshold density for those electron captures. There were some shortcomings of the work of Gutierrez et al. (1996), in which the authors only implemented screening corrections to the sparsely resolved tabulated rates of Oda et al. (1994) and not to the (parent, daughter and electron) chemical potentials.

An increase in the threshold density of $^{20}\text{Ne}(e^-, \nu)^{20}\text{F}$ would cause the oxygen deflagration to ignite under denser conditions in the super-AGB progenitors. However in the failed massive star case the centre is approaching the ignition temperatures of Ne and O almost adiabatically, and so the oxygen deflagration could ignite before $^{20}\text{Ne}+e^-$ becomes significant if there were an increase in its threshold density.

The $A = 20$ and 24 reaction rates have different properties to the $A = 23, 25$ and 27 reaction rates. These differences stem from the underlying nuclear physics (section 4.4.2.1) and propagate to their effect on the evolution of stars (section 4.4.2.2).

4.4.2.1 Different behaviour from Nuclear physics

Martínez-Pinedo et al. (in prep.) have calculated new weak reaction rates linking ^{20}Ne , ^{20}F , ^{20}O , ^{24}Mg , ^{24}Na and ^{24}Ne . The method used to calculate the rates is the same as I have described in section 4.2 and screening corrections were also included in the same way. One significant difference between these newly calculated $A = 20$ and 24 rates and the new URCA process rates ($A = 23, 25$ and 27; Toki et al. 2013) is that some of the GT strengths were re-determined experimentally. Martínez-Pinedo et al. also found a forbidden transition (not measured experimentally) to make a significant contribution to the rate for $^{20}\text{Ne}(e^-, \nu)^{20}\text{F}$.

The newly calculated rates are shown in Figure 4.10. The plot is the same style as Figure 4.7 where electron capture rates are plotted with a dot-dashed line style, β -decay rates with a dotted line style and the product of the two competing rates

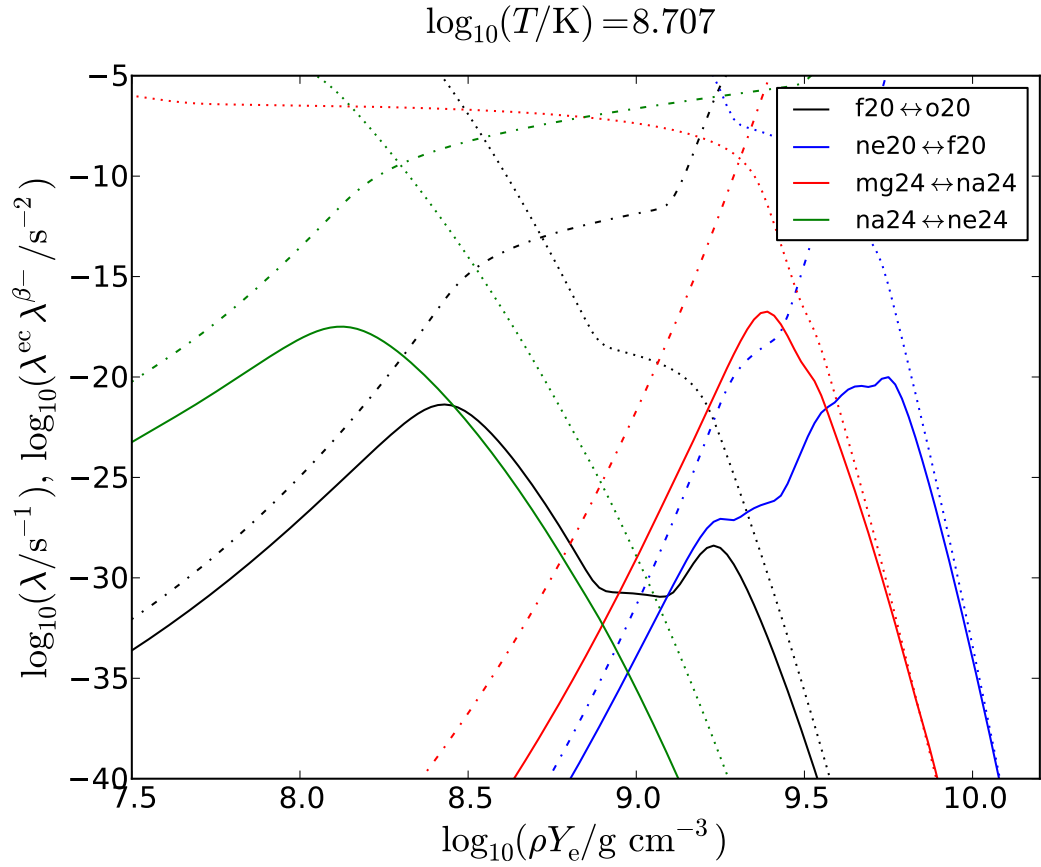


Figure 4.10: Product of electron-capture and β -decay rates for $A = 20$ and $A = 24$ using the newly calculated rates of Martínez-Pinedo et al. (in prep.) including experimentally determined GT transition strengths.

($\lambda^{ec}\lambda^{\beta^-}$) with a solid line. Comparing Figure 4.10 with Figure 4.7, one can see that the solid peaks have lower magnitudes for the $A = 20$ and 24 rates (Figure 4.10) than for the URCA process rates (Figure 4.7). This indicates that the $A = 20$ and 24 nuclei will not provide strong cooling like the URCA pairs because there is a smaller window in which both the forward and reverse rates are high. Another important feature is that for the odd- A nuclei (23, 25, 27, Figure 4.7), the secondary (more neutron-rich) pair for each A has a higher Q -value, and thus operates at higher density than the primary pair. In contrast, for the even- A nuclei (20 and 24, Figure 4.10), the secondary pair has a lower Q -value than the primary pair and thus operates at lower density. As a result of this behaviour for the even- A nuclei ($A = 20$ and 24 , Figure 4.10), the URCA process does not operate and instead the following sequence occurs. ^{24}Mg begins to capture electrons, producing some ^{24}Na . The ^{24}Na will likely not β^- -decay back to ^{24}Mg since there is only a very narrow window where both the forward and reverse rate of $^{24}\text{Mg} \leftrightarrow ^{24}\text{Na}$ is reasonably high (still 3 orders of magnitude lower at the crossing point than for any of the odd- A pairs). However, because the Q -value (and thus threshold density) is much lower for the secondary pair, $^{24}\text{Na} \leftrightarrow ^{24}\text{Ne}$, the ^{24}Na almost instantaneously captures another electron, producing ^{24}Ne . The ^{24}Ne is created for the first time in such dense conditions where the fermi energy is so high that its β^- -decay channel is completely blocked, and the reaction chain ceases. The same order of events occurs for the $A = 20$ chain, $^{20}\text{Ne} \leftrightarrow ^{20}\text{F} \leftrightarrow ^{20}\text{O}$. The net effect is that both ^{24}Mg and ^{20}Ne undergo double electron captures, where each nucleus effectively removes 2 electrons from the plasma.

The simplest way to understand the physical reason for the different behaviour of the odd- A and even- A nuclei is to consider the expression for the binding energy of the nucleus in the semi-empirical mass formula (e.g. Krane 1987, page 68, 3.28),

$$B = a_v A - a_s A^{2/3} - a_c Z(Z-1)A^{-1/3} - a_{sym} \frac{(A-2Z)^2}{A} + \delta. \quad (4.36)$$

The formula consists of volume, surface, Coulomb and symmetry terms (terms 1–4, respectively). The last term, δ , is a pairing term. Protons and neutrons are fermions and as such their spin quantum numbers are $\pm \frac{1}{2}$. As fermions, the nucleons obey the

Pauli exclusion principle and thus no proton may exist with the same set of quantum numbers as another; the same is true for neutrons. It is more energetically favourable for the protons and neutrons to couple together and form spin-zero pairs because in this configuration there is a strong overlap of the spatial wave function of the two protons or two neutrons. The pair will thus spend more time closer together within the range of the strong nuclear force and be more tightly bound (higher binding energy; Lilley 2001, page 40). For nuclei with even A (e.g. the $A = 20$ and 24 nuclei), either both the proton and neutron number will be even (even-even) or both will be odd (odd-odd). When both are even, the protons and neutrons will be coupled in spin 0 pairs, adding to the binding energy ($\delta > 0$). For both N and Z odd, there will be an unpaired proton and an unpaired neutron, and the nucleus as a result will be less tightly bound ($\delta < 0$). The pairing energy δ is given in Krane (1987) as $\pm a_p A^{-3/4}$ with $a_p = 34$ MeV. For nuclei with an odd atomic mass number A , either Z or N must be odd, and so there is always one nucleon that will be unpaired. Thus for the odd- A nuclei, the pairing term $\delta = 0$.

To illustrate the relevance of this discussion of the pairing term, I show the curves of binding energy (magnitude) per nucleon ($|B|/A$) for nuclides with $A = 23$ and 24 in Figures 4.11 and 4.12, respectively. The solid curves are simply quadratic fits to the values of $|B|/A$ calculated using the formula in 4.36, since the binding energy for constant A is a second order function of Z . There are two solid curves in Figure 4.12, corresponding individually to the even-even and odd-odd cases.

The electron capture process transforms a nucleus of ${}^A Z$ into a nucleus of ${}^A(Z-1)$, i.e. reducing the proton number by 1 for the same atomic mass number (β -decay is of course the opposite process). For the odd- A nuclei, Figure 4.11 illustrates the electron capture process (drawn with a dashed line) as a transformation from the parent nucleus to the daughter nucleus, where both nuclei lie on the same binding energy curve. For all odd- A nuclei, the pairing energy $\delta = 0$, as described above, and hence all odd- A nuclei lie along the same curve. Conversely, in Figure 4.12 the non-zero pairing energy of the $A = 24$ nuclei means that the parent and daughter nuclei always lie on different curves (alternating between odd-odd and even-even).

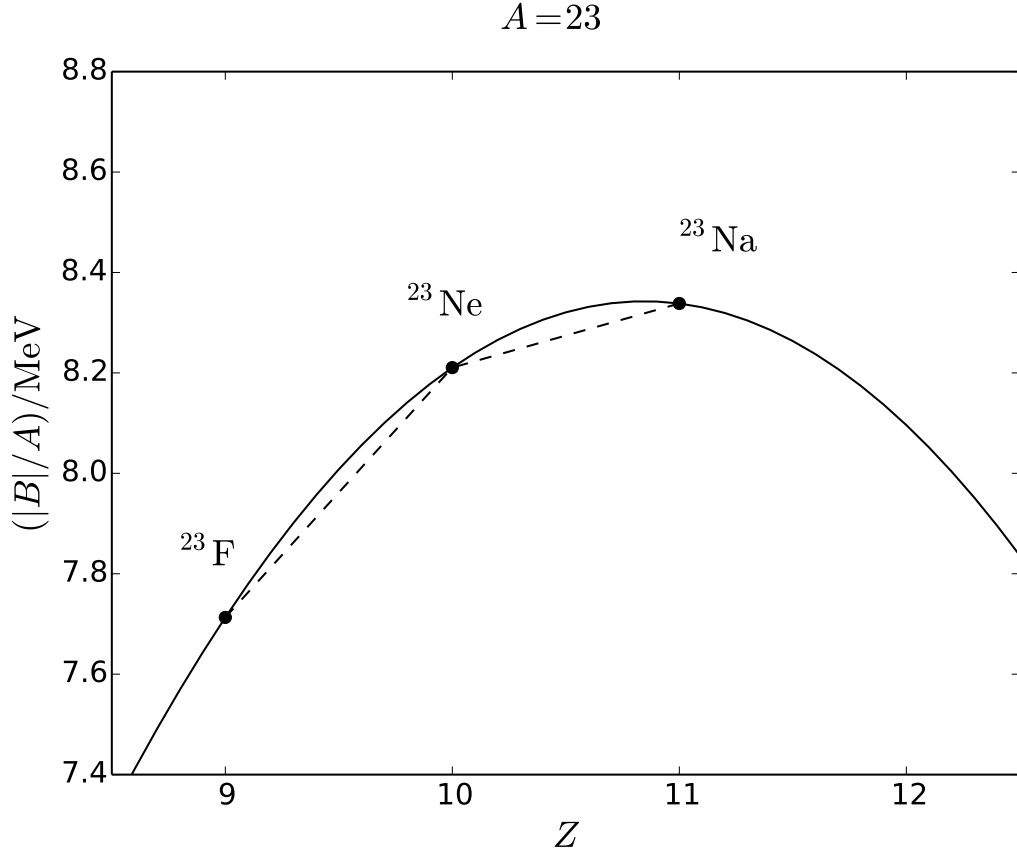


Figure 4.11: Binding energy per nucleon (MeV) as a function of proton number Z for $A = 23$ nuclei (odd-even or even-odd) calculated using the expression from the semi-empirical mass formula (SEMF), equation 4.36. The solid curve shows a quadratic interpolation since for constant A , $|B|$ is a second order function of Z . The dashed lines show the transitions between nuclei undergoing electron capture (to lower Z) or beta decay (to higher Z). The y -component of the dashed lines is related to the threshold energy of the ground-state to ground-state transition. Because the binding energy per nucleon drops steeply from its maximum as Z decreases, the threshold energy of the secondary reaction $^{23}\text{Ne}(e^-, \nu)^{23}\text{F}$ is higher than that of the primary, $^{23}\text{Na}(e^-, \nu)^{23}\text{Ne}$, and thus is activated at higher densities where the electron chemical potential is higher.

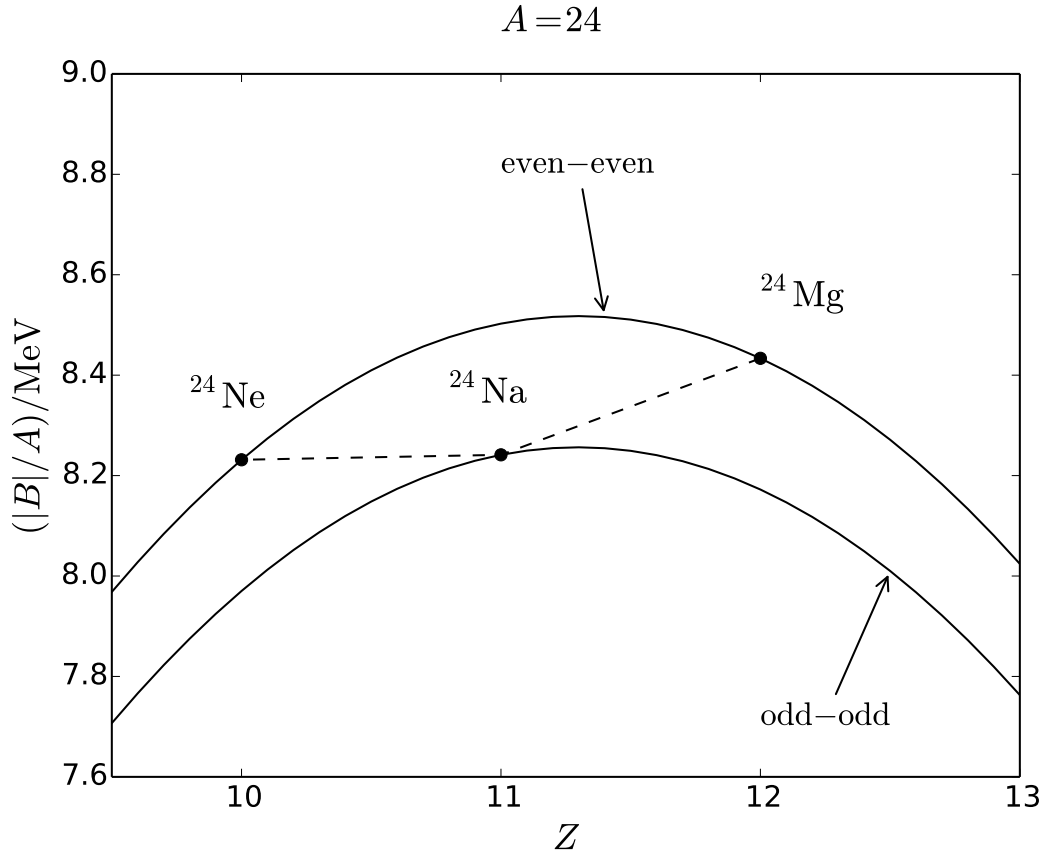


Figure 4.12: Same as Figure 4.11 but for $A = 24$ nuclei. Even- A nuclei can be either even-even or odd-odd, which have separate solid curves for $|B|/A$ against Z . The parent and daughter nuclei never lie on the same curve when A is even because of the difference in the pairing energy for even-even ($\delta > 0$) and odd-odd ($\delta < 0$) nuclei (see equation 4.36 and the text for more details). Converse to the odd- A nuclei, an example of which is shown in Figure 4.11, the threshold energy of the secondary reaction $^{24}\text{Na}(e^-, \nu)^{24}\text{Ne}$ is much lower than that of the primary, $^{24}\text{Mg}(e^-, \nu)^{24}\text{Na}$. As a result, the secondary reaction is activated at lower densities, however its reactant ^{24}Na is only produced once the primary reaction is activated at high density. By this point, the secondary reaction rate is very high and effectively the ^{24}Mg undergoes a rapid double electron capture.

The most abundant nuclei produced in stars will generally be the most stable (near the maximum of the $|B|/A$ curves in Figures 4.11 and 4.12, e.g. ^{23}Na and ^{24}Mg). The (Q -value) ground-state to ground-state threshold energy $E_{thr,0}$ for the weak reactions is related to the difference in $|B|/A$ of the parent and daughter nuclei (the y -component of the dashed lines). Because the curve steeply drops off with decreasing Z and all of the nuclei lie on the same curve, the threshold energy is higher for the secondary reaction $^{23}\text{Ne}(e^-, \nu)^{23}\text{F}$ than for the primary reaction $^{23}\text{Na}(e^-, \nu)^{23}\text{Ne}$ for the odd- A nuclei. In the stellar interior, the secondary reaction is thus activated at higher densities than the primary, where the electron chemical potential is higher. Conversely, the threshold energy is lower for the secondary reaction $^{24}\text{Na}(e^-, \nu)^{24}\text{Ne}$ than for the primary reaction $^{24}\text{Mg}(e^-, \nu)^{24}\text{Na}$ for the even- A nuclei ($A = 24$) because of the fluctuation of the pairing energy δ with Z . This means that the secondary reaction is activated at lower densities than the primary reaction, and because the secondary reaction can only operate once the primary has produced its reactant (^{24}Na), the rate of the secondary reaction is already very high once it can proceed. This is why the $A = 20$ and 24 nuclei, upon reaching their threshold densities in the stellar interior, essentially undergo double electron captures.

4.4.2.2 Results of the new calculations

I have simulated the evolution of failed massive stars (FMS) that experience off-centre neon and oxygen ignition which is recurrently quenched by mixing at the convective boundary (see chapter 3) for three metallicities: $Z = 0.014$ (solar composition), $Z = 10^{-3}$ and $Z = 10^{-5}$. These models were calculated using the rates of Oda et al. (1994) for the $A = 23, 25$ and 27 URCA pairs, and later using both the rates of Oda et al. (1994) and Martínez-Pinedo et al. (in prep) for the $A = 20$ and 24 rates. I have described these new rates themselves in the previous section (4.4.2.1). The evolution of the three models using the two different sets of rates in the $\rho_c - T_c$ plane is shown in Figure 4.13. The solid lines show the models with the new rates from Martínez-Pinedo et al. (in prep.) and the dotted lines show the models with the rates of Oda et al.

(1994).

During this late evolutionary phase, the physics assumptions of the models are modified slightly. Instead of assuming the Schwarzschild criterion to define convective instability, the Ledoux criterion is used. The choice to modify the physics assumptions in this way is motivated by the previous work of Miyaji et al. (1980) and Gutierrez et al. (1996). As I described in chapters 1 and 2, the Ledoux criterion accounts for the stabilising effect of mean molecular weight gradients in the stellar material, while the Schwarzschild criterion does not. The activation of rapid electron captures on such an abundant nuclide as ^{20}Ne greatly increases the mean molecular weight in the central regions and produces a steep μ gradient. Moreover, the evolutionary timescale of this phase is very short and as such, there is little time for the over-stability in the would-be semi-convective region to develop into mixing. Under these conditions, the convection criterion would quite strictly adhere to that of Ledoux, whereas in other evolutionary phases where μ gradients form the evolutionary timescale is significantly long for semi-convection to potentially chemically homogenise the region (in that case, the convection criterion would become identical to that of Schwarzschild).

The general shape of the evolution shows the almost adiabatic increase in temperature of the central region as the core is contracts. As the threshold density for electron captures by ^{20}Ne to be activated is surpassed in the stellar centre, the energy released by the γ -decay of the daughter nuclei begins to heat up the material. As a result, the temperature begins to increase more steeply. In some of the models (the model at $Z = 10^{-3}$ using both rates and the models at $Z = 10^{-5}$ and, to a lesser extent, $Z = 0.014$ using the rates of Oda et al. 1994) the temperature rapidly decreases again, leaving a sharp peak in the $\rho_c - T_c$ evolution. This sharp temperature drop occurs when the radiative temperature gradient that would be required to transport the luminosity becomes so large that convection is induced. The convective luminosity transports heat away from the centre and the region rapidly cools. As expected, the new weak reaction rates for the $A = 20$ nuclei increase the ignition density of the oxygen deflagration (Figure 4.13). The effect is most pronounced for the case with $Z = 10^{-3}$.

I would like to stress at this point of the discussion that the treatment of convec-

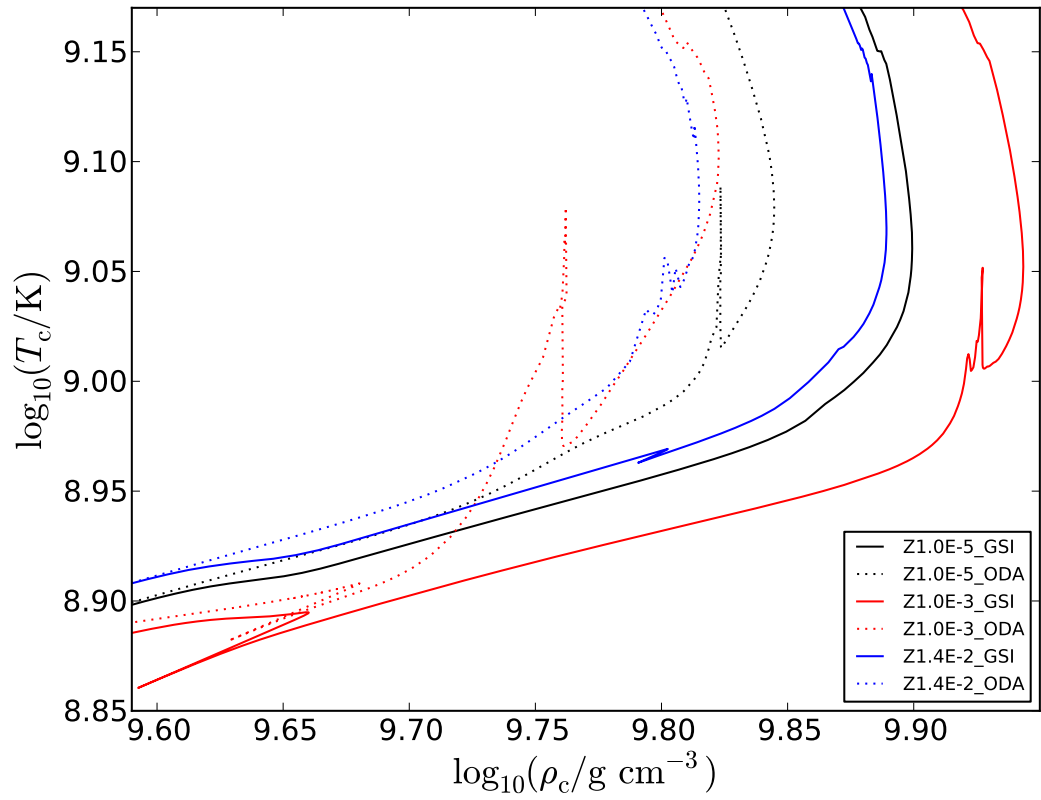


Figure 4.13: Late evolution of the failed massive star (FMS) models at three metallicities ($Z = 0.014$, 10^{-3} and 10^{-5}) using the rates of Oda et al. (1994) and Martínez-Pinedo et al. (in prep.; ‘GSI’).

tion in the present stellar models becomes rather unphysical at such small evolutionary timescales. The mixing length theory of convection (MLT; see section 2.2.1 for a full description) treats the behaviour of convection effectively as a single eddy with velocity v . Many of the caveats of this treatment and their implications are discussed in section 1.4, however during these short evolutionary timescales a different problem arises. The evolutionary timescale becomes comparable to the convective turnover timescale, making the averaging assumptions of the MLT rather inappropriate. For example, once a region becomes convective, the average flux is calculated based on the assumption that the fluid parcels have an average velocity v . If the time step is of the order of several times the convective turnover timescale, this assumption is relatively safe. If not, then the average only holds if there is instantaneous acceleration of the fluid and thus a different method to calculate v should be used for these situations, taking into account its time-dependency.

The time-dependent formulation of the mixing length theory of convection was derived by Unno (1967) for the treatment of stellar pulsations. Two coupled differential equations for the convective velocity v and the average temperature fluctuation \overline{DT} are introduced, while the remaining equations of the MLT remain unchanged. In previous studies of the progenitors of electron capture supernovae (Nomoto 1987; Gutierrez et al. 1996; Takahashi, Yoshida & Umeda 2013), during the late phases the equation of hydrostatic balance is also modified to include an acceleration term. Clearly, it is agreed that the assumptions of hydrostatic equilibrium and the mixing length theory of convection are not valid in this regime and the problem becomes one of hydrodynamics. Moreover, the oxygen deflagration of electron capture supernova progenitors is a phenomenon in which the coupling of turbulent convection and combustion, transonic flow and strong asymmetries are all likely to be important. In the progenitors of type Ia (carbon-deflagration supernovae), a similar deflagration scenario develops, but in the case of type Ia supernovae, the energy released by the deflagration is sufficient to unbind the core, leaving no compact remnant. In the literature, the consensus is that the asymmetrical effects are so crucial to determining the properties of the explosion and the composition of the ejecta that one-dimensional simulations are no longer

considered to be a satisfactory approach.

5 Conclusions and future work

It has been known for a few decades that super-AGB stars with $8 \lesssim M/M_{\odot} \lesssim 10$ could be the progenitors of supernovae triggered by electron captures on sd -shell nuclei (Miyaji et al. 1980; Nomoto 1984; Nomoto 1987; Ritossa, García-Berro & Iben 1999; Poelarends et al. 2008). Further progress was made in uncovering the behaviour of stars across the transition in initial mass (or helium core mass) from super-AGB stars to massive stars that would produce iron cores before collapsing (Woosley, Weaver & Taam 1980; Nomoto 1984; Habets 1986; Nomoto & Hashimoto 1988). The studies modelled the evolution of helium stars with the exception of Woosley, Weaver & Taam (1980), who simulated the full star including the envelope. However, the calculations of Woosley, Weaver & Taam (1980) suffered from poor spatial resolution in a stellar evolution code optimised for massive stars (rather than AGB stars).

I have shown in chapter 3 that with the MESA code, it is possible to simulate full stars (including their envelope) across this transition using a consistent set of input physics. Whilst keeping the many parameters and assumptions of stellar evolution constant functions of the initial mass of the stars is certainly not physically motivated, it is an essential step on the road to characterising the evolution of these stars both individually and collectively.

For the super-AGB progenitors of electron capture supernovae (EC-SNe), the entire thermal pulse phase has been simulated from the end of the second dredge-up (2DUP) to the activation of electron captures by ^{20}Ne in the centre of the core. The ability to simulate the entire TP-SAGB phase was a long-standing goal of the community that had previously not been achieved, and is also a testament to the stability of the MESA stellar evolution code. The structure of the star at the pre-supernova stage is very similar to the classical models of Nomoto (1984), with a compact oxygen-neon core surrounded by a hydrogen envelope; at their interface, the density drops 16 orders of magnitude.

The physics behind the outstanding uncertainties in the efficiency of the third

dredge-up and mass loss rate during the super-AGB phase have not been addressed in the present work, but instead it has been shown that within the current picture (given the physics assumptions made here), an $8.75 M_{\odot}$ star at solar metallicity ($Z = 0.014$) should produce an electron capture supernova. However, if the high mass loss rates of Blöcker (1995) are accurate, then the models suggest, like those of Poelarends et al. (2008), that super-AGB stars cannot produce EC-SNe. These conclusions are, however, drawn from using mass loss rates as functions of luminosity, effective temperature and surface composition.

The mechanisms driving mass loss from the stellar surface are complex and hard to constrain. When a dynamical instability is triggered in the 1-D stellar models, the authors typically conclude that the envelope will be ejected, producing an oxygen-neon white dwarf (ONeWD). These dynamical instabilities could well be transient behaviour, and following a brief period of mass-ejection hydrostatic equilibrium could be restored.

The efficiency of third dredge-up is not a new problem in the (super-) AGB community. A combination of hydrodynamical simulations and nucleosynthesis calculations make it possible to prescribe an appropriate amount of mixing at the convective boundary in certain simulations, however it is not clear how this parameterised treatment depends upon initial mass and metallicity (or rather, on the underlying physics). Hot dredge-up and proton ingestion during the TP-SAGB phase could provide a boost in the luminosity and therefore both enhance the mass loss rate and the efficiency of the 3DUP, narrowing the channel for EC-SNe from super-AGB stars. More careful study of these phenomena at different metallicities should provide better constraints on the evolution of super-AGB stars towards EC-SNe.

My models suggest that stars in the mass range $8\text{--}10 M_{\odot}$ that ignite neon and oxygen burning off-centre could potentially contribute to the EC-SN rate. If mixing takes place across the lower convective boundary of the neon-oxygen burning shell, the flame is recurrently quenched and re-ignited. Upon the quenching of the flame, the core contracts. This intermittent contraction allows the star to reach the conditions for the URCA process to operate in the centre of an $8.8 M_{\odot}$ star, and accelerated cooling and contraction leads to the ignition of an oxygen-deflagration. The fate of the same

model with strictly no mixing at the convective boundary is not certain, but could produce an iron core and thus collapse as a core collapse supernova (FeCCSN). The extent to which mixing takes place at the lower boundary of such a convective shell is at present not clear. However, 3D simulations of oxygen shell burning presented by Meakin & Arnett (2007) suggest that mixing processes do indeed extend beyond the convective boundaries—as they would be defined using the Schwarzschild criterion—in these advanced evolutionary stages.

In computing the evolution of progenitors for electron capture supernovae for this thesis, it became clear that the present status of available weak reaction rates were insufficient to represent accurately the physics that dominates the last years of the lives of these stars. I found that using the $\log\langle ft \rangle$ formalism of Fuller, Fowler & Newman (1985) was inappropriate for the weak reactions that are relevant for 8–10 M_{\odot} stars since there is a significant contribution from transitions not directly involving the ground state of the nuclei. As a result, new weak reaction rates for important nuclei were computed by Toki et al. (2013; see chapter 4). The new weak rates include Coulomb corrections, effectively shifting the rate for a given temperature to higher densities. A log-linear interpolation of the better resolved rate tables represents the nuclear physics much more accurately than using the same method with the available rates of Takahara et al. (1989) and Oda et al. (1994). I implemented the new rates into the stellar evolution code MESA and showed that their impact indeed takes place at higher densities than the older rates of Oda et al. (1994). The new rates also provide stronger cooling, increasing the ignition density of the oxygen deflagration in the star prior to its collapse and explosion.

Future work and scientific outlook

Moving forward, progress in the field of stellar evolution and supernovae should be driven by the improvement of physics considerations in numerical models. The uncertainties related to the progenitors of electron capture supernovae are certainly not new

additions to the list of big problems in stellar astrophysics at present:

- Convective and non-convective mixing processes
 - Super-adiabatic (inefficient) convection
 - Turbulence and mixing at convective boundaries
 - Semi-convection and thermohaline mixing
 - Internal waves and oscillations

- Mass loss
 - Stellar pulsation
 - Dynamical effects
 - Opacity-driven winds
 - Dust formation
 - Enshrouding and CSM interaction

These problems themselves are enough to keep the community busy for years to come, and will be developed and tested alongside improvements in the treatments of rotation and magnetic fields.

Observational data for supernovae (the ejected mass of ^{56}Ni , amount of circumstellar medium interaction, light curves), their remnants (isotopic yields, gravitational mass and spin period of neutron stars) and their progenitors (pre-supernova position in the Hertzsprung-Russell diagram, rotation rates and surface abundances) will become more abundant and the measurements more constrained as new instruments are developed. The new generation of gravitational wave and neutrino detectors will also provide constraints previously unobtainable, and new asteroseismological missions will complement the current efforts to understand the behaviour of convection and turbulence. Ultimately, however, to explain the observations is the job of theory and simulation, and while 1-D stellar models are still an excellent tool – the only viable

method by which to simulate the entire lifetime of a star – they must evolve alongside more specialised physical experiments and numerical simulations.

For the case of electron capture supernova progenitors, hydrodynamical simulations of the thermal pulse phase will uncover the behaviour of the pulse driven convective zone and the extent of the third dredge-up. This will lead to more accurate estimates of the dredge-up efficiency and hence the core growth rate. These simulations would also predict the time evolution of the hydrogen burning luminosity during the thermal pulse phase, which directly influence the mass loss rate from the stellar surface.

Mixing across the convective boundary has also been shown in this thesis to affect the propagation of the neon-oxygen burning front towards the stellar centre, allowing for contraction towards an EC-SN fate, rather than FeCCSN. A similar flame quenching has been found by Denissenkov et al. (2013b), resulting in the formation of hybrid white dwarfs (an inner core of CO composition surrounded by an ONe outer layer). Accretion onto these hybrid white dwarfs could potentially result in peculiar type Ia supernovae.

The oxygen deflagration during the final evolutionary stages of electron capture supernova progenitors is a fine example of reactive hydrodynamics in degenerate material. This is a phenomenon that is similar to the carbon deflagration in carbon-oxygen white dwarfs, producing type Ia supernovae. It has been shown that multi-dimensional effects during the carbon deflagration have a strong impact on the energetics and the nucleosynthetic yields of type Ia supernovae, and so far there is no evidence to suggest that similar asymmetrical effects would not have an impact during the oxygen deflagration of electron capture supernovae. In fact, it is the formation of neutron-rich pockets in multi-dimensional simulations of the resulting explosion of electron capture supernovae that produces the heaviest elements (Wanajo, Janka & Müller 2011), although only elements up to atomic number of about 40 are produced. Multidimensional simulations of type Ia supernovae also show that if the carbon burning flame begins as a detonation, the models cannot reproduce the amount of intermediate alpha elements (e.g. Si and S). This has led to the delayed-detonation model in which the carbon

burning begins first as a deflagration and later becomes supersonic (Seitenzahl et al. 2013 and references therein).

Simulating the supernova explosion of the new ($8.75 M_{\odot}$) super-AGB progenitor model from chapter 3 would be a good first verification step, for which the results can be compared to those obtained using the Nomoto (1984) progenitor model. I expect that the differences in the explosion itself would be minimal since the density profile is so similar and both models would suffer from the same caveats related to the deflagration. Once the new URCA process rates of Toki et al. (2013) have been included in the super-AGB models, significant differences may occur in the explosion. In either case, I expect that the nucleosynthetic yields from the present calculations would be significantly different from those calculated from Nomoto’s models since I include the TP phase. Both the $^{13}\text{C}(\alpha, n)^{16}\text{O}$ and $^{22}\text{Ne}(\alpha, n)^{25}\text{Mg}$ neutron sources operate in the TP-SAGB phase, which should be accounted for in galactic chemical evolution (GCE) models. The GCE models at present do not include the yields of $8-10 M_{\odot}$ stars because of the gap in the available yields (Doherty et al. 2014). Simulating the explosion of the $8.8 M_{\odot}$ failed massive star model could produce interesting nucleosynthetic yields due to the intermediate-density shell located between the ONe core and the envelope (see section 3.3).

In simulating the oxygen deflagration in three dimensions, the first 3D progenitor models for electron capture supernovae will be produced. This would lead to a breakthrough in linking progenitors and explosion models. Such a link is also much needed between massive stars (the progenitors of FeCCSN) and supernova simulations (Ugliano et al. 2012; Couch & Ott 2013). The case of massive stars is potentially more difficult because of the complicated shell structure, but ultimately the effects of mixing, burning and angular momentum transport should be considered.

Close attention should be paid to the steep behaviour of weak reaction rates with respect to density in the future. In particular, accurate weak reaction rates should be used for the four applications outlined in section 1.3: the URCA process, calculating the neutron excess in stellar models, the de-leptonisation during core collapse supernovae and neutron capture nucleosynthesis. Using finely resolved grids of weak reaction

rates could potentially prove cumbersome in large multi-zone network calculations. An alternative procedure could be to use the analytical formulae for the phase space integral from Fuller, Fowler & Newman (1985) to compute the contribution from a number of transitions for each rate. The computational overhead of this method would need to be compared to that of interpolating finely resolved (pre-processed) tables within a stellar evolution or nucleosynthesis post-processing code. The number of transitions that were included using the analytical method would probably need to be limited to only the dominant transitions, and the significance of weaker transitions would need to be tested.

Publications

5.1 Refereed publications

1. **Jones, S.**, Hirschi, R., Nomoto, K.: “The final fate of stars that ignite neon and oxygen off-centre: electron capture or iron core-collapse supernova?”. Submitted to: The Astrophysical Journal.
2. Pignatari, M., Herwig, F., Hirschi, R., Bennett, M., Rockefeller, G., Fryer, C., Timmes, F. X., Heger, A., **Jones, S.**, Battino, U., Ritter, C., Diehl, S., Dotter, A., Frischknecht, U., Hungerford, A., Magkotsios, G., Travaglio, C., Young, P. (2013): “NuGrid stellar data set. I. Stellar yields from H to Bi for stars with metallicity $Z=0.02$ and $Z=0.01$ ”. Submitted to: The Astrophysical Journal, revision requested.
3. **Jones, S.**, Hirschi, R., Nomoto, K., Fischer, T., Timmes, F. X., Herwig, F., Paxton, B., Toki, H., Suzuki, T., Martínez-Pinedo, G., Lam, Y. H., Bertolli, M. G. (2013): “Advanced burning stages and fate of 8-10 solar mass stars”. Published in: The Astrophysical Journal ApJ, 772, 150
4. Toki, H., Suzuki, T., Nomoto, K., **Jones, S.**, Hirschi, R. (2013): “Detailed β -transition rates for URCA nuclear pairs in 8-10 solar-mass stars”. Published in: Physical Review C Vol.88, No.1

5.2 Other Publications

1. Lam, Y. H., Martínez-Pinedo, G., Langanke, K., **Jones, S.**, Hirschi, R., Zegers, R., Brown, A.: “ Electron Capture and Beta-Decay Rates for the Collapse of O+Ne+Mg Cores”, Submitted to: Proceedings of INPC 2013

2. Bertolli, M. G., Möller, P., **Jones, S.** (2013): “Uncertainties astrophysical beta-decay from the FRDM”. Accepted for publication in: Proc. Intl. Conf. Nucl. Data 2013 in Nucl. Data Sheets.
3. **Jones, S.**, Hirschi, R., Herwig, F., Paxton, B., Timmes, F. X., Nomoto, K. (2012): “Progenitors of electron-capture supernovae”. Published in: Proceedings of the International Astronomical Union, IAU Symposium, Volume 279, p. 341-342

5.3 Publications in preparation for submission to refereed journals

1. **Jones, S.**, Hirschi, R., Heger, A., Pignatari, M., Georgy, C., Nishimura, N., Fryer, C., Herwig, F.: “Code dependencies of pre-supernova evolution and nucleosynthesis in massive stars”, to be submitted to MNRAS.
2. Herwig, F., **Jones, S.**, Pignatari, M., Bertolli, M., Paxton, B., VandenBerg, D.: “H-combustion and the i process at low metallicity super-AGB stellar models with convective boundary mixing”, to be submitted to The Astrophysical Journal.

5.4 Talks

1. Seminar, IPMU, Tokyo, Japan. (**Invited**) **2013.11.05**
2. “Supernovae from 8-12 solar mass stars: new stellar models”, Supernovae and Gamma-ray bursts 2013, Kyoto, Japan. **2013.10.29**
3. ”Low mass (type II) supernova (progenitors): the transition”, NuGrid collaboration meeting 2013 University of Victoria, BC, Canada **2013.06.18**

4. "Advanced evolution and fate of 8-10 Mo stars", Massive stars: from Alpha to Omega, Rhodes, Greece **2013.06.13**
5. "Progenitors of electron capture supernovae and related nuclear physics uncertainties", "Astrophysics and Nuclear structure" (International Workshop XLI on Gross Properties of Nuclei and Excitations), Hirschegg, Kleinwalsertal, Austria. **(Invited)** **2013.01.29**
6. "Impacts of convective boundary mixing and weak reaction uncertainties on 8-12 solar-mass stars", EUROGENESIS MACHE meeting, Department of Physics, Goethe University, Frankfurt, Germany. **2012.11.26**
7. "The transition from super-AGB to massive star", GSI Helmholtzzentrum für Schwerionenforschung (Heavy Ion Research), Darmstadt, Germany. **2012.07.08**
8. "Electron-capture supernova progenitor modelling", Massive stars and Supernovae one-day workshop, Institute of Astronomy, University of Cambridge, UK. **2011.09.05**
9. "Comprehensive nucleosynthesis simulations in Massive and super-AGB star models", NuGrid Collaboration meeting Open Day, University of Victoria, BC, Canada. **2011.07.06**

5.5 Conference Posters

1. "Final evolution and fates at the transition between massive and super-AGB stars", ESO/MPA/MPE/Excellence Cluster Universe Conference - "Supernovae Illuminating the Universe: from Individuals to Populations", Garching, Germany. **2012.09.10**
2. "Life at the edge: Progenitors of the lowest mass core-collapse supernovae", IAU Symposium 279 - "Death of Massive Stars: Supernovae and Gamma-Ray Bursts", Nikko, Japan **2012.03.12-16**

Bibliography

- Adams J. B., Ruderman M. A., Woo C.-H., 1963, *Physical Review*, 129, 1383
- Aerts C., Christensen-Dalsgaard J., Kurtz D. W., 2010, *Asteroseismology*
- Anderson J. P., Habergham S. M., James P. A., Hamuy M., 2012, *Monthly Notices of the RAS*, 424, 1372
- Angulo C., 1999, *American Institute of Physics Conference Series*, 495, 365
- Angulo C., Arnould M., Rayet M., Descouvemont P., Baye D., Leclercq-Willain C., Coc A., Barhoumi S., Aguer P., Rolfs C., Kunz R., Hammer J. W., Mayer A., Paradellis T., Kossionides S., Chronidou C., Spyrou K., degl'Innocenti S., Fiorentini G., Ricci B., Zavatarelli S., Providencia C., Wolters H., Soares J., Grama C., Rahighi J., Shotter A., Lamehi Rächti M., 1999, *Nuclear Physics A*, 656, 3
- Arnett W. D., Meakin C., 2011, *Astrophysical Journal*, 733, 78
- Arnett W. D., Thielemann F.-K., 1985, *Astrophysical Journal*, 295, 589
- Asplund M., Grevesse N., Sauval A. J., Allende Prieto C., Kiselman D., 2004, *Astronomy and Astrophysics*, 417, 751
- Asplund M., Grevesse N., Sauval A. J., Scott P., 2009, *Annual Review of Astronomy and Astrophysics*, 47, 481
- Barkat Z., Wheeler J. C., 1990, *Astrophysical Journal*, 355, 602
- Beaudet G., Petrosian V., Salpeter E. E., 1967, *Astrophysical Journal*, 150, 979
- Becker S. A., Iben, Jr. I., 1979, *Astrophysical Journal*, 232, 831
- Becker S. A., Iben, Jr. I., 1980, *Astrophysical Journal*, 237, 111

- Belczynski K., Kalogera V., Rasio F. A., Taam R. E., Zezas A., Bulik T., Maccarone T. J., Ivanova N., 2008, *Astrophysical Journal, Supplement*, 174, 223
- Bionta R. M., Blewitt G., Bratton C. B., Casper D., Ciocio A., 1987, *Physical Review Letters*, 58, 1494
- Blöcker T., 1995, *Astronomy and Astrophysics*, 297, 727
- Blondin J. M., Mezzacappa A., 2007, *Nature*, 445, 58
- Böhm-Vitense E., 1958, *Zeitschrift fuer Astrophysik*, 46, 108
- Bono G., Caputo F., Cassisi S., Marconi M., Piersanti L., Tornambè A., 2000, *Astrophysical Journal*, 543, 955
- Boothroyd A. I., Sackmann I.-J., Ahern S. C., 1993, *Astrophysical Journal*, 416, 762
- Botticella M. T., Pastorello A., Smartt S. J., Meikle W. P. S., Benetti S., Kotak R., Cappellaro E., Crockett R. M., Mattila S., Sereno M., Patat F., Tsvetkov D., van Loon J. T., Abraham D., Agnoletto I., Arbour R., Benn C., di Rico G., Elias-Rosa N., Gorshanov D. L., Harutyunyan A., Hunter D., Lorenzi V., Keenan F. P., Maguire K., Mendez J., Mobberley M., Navasardyan H., Ries C., Stanishev V., Taubenberger S., Trundle C., Turatto M., Volkov I. M., 2009, *Monthly Notices of the RAS*, 398, 1041
- Buchler J. R., Yueh W. R., 1976, *Astrophysical Journal*, 210, 440
- Burbidge E. M., Burbidge G. R., Fowler W. A., Hoyle F., 1957, *Reviews of Modern Physics*, 29, 547
- Busso M., Gallino R., Wasserburg G. J., 1999, *Annual Review of Astronomy and Astrophysics*, 37, 239
- Canuto V. M., Mazzitelli I., 1991, *Astrophysical Journal*, 370, 295
- Canuto V. M., Goldman I., Mazzitelli I., 1996, *Astrophysical Journal*, 473, 550

- Cassisi S., Castellani V., 1993, *Astrophysical Journal*, Supplement, 88, 509
- Cassisi S., Castellani V., Tornambe A., 1996, *Astrophysical Journal*, 459, 298
- Cassisi S., Potekhin A. Y., Pietrinferni A., Catelan M., Salaris M., 2007, *Astrophysical Journal*, 661, 1094
- Castellani V., Giannone P., Renzini A., 1971, *Astrophysics and Space Science*, 10, 355
- Cescutti G., Matteucci F., François P., Chiappini C., 2007, *Astronomy and Astrophysics*, 462, 943
- Chandrasekhar S., 1939, *An introduction to the study of stellar structure*
- Charbonnel C., Zahn J.-P., 2007, *Astronomy and Astrophysics*, 467, L15
- Chiappini C., Frischknecht U., Meynet G., Hirschi R., Barbuy B., Pignatari M., Decressin T., Maeder A., 2011, *Nature*, 474, 666
- Chiappini C., Matteucci F., Gratton R., 1997, *Astrophysical Journal*, 477, 765
- Chieffi A., Limongi M., 2013, *Astrophysical Journal*, 764, 21
- Chieffi A., Domínguez I., Limongi M., Straniero O., 2001, *Astrophysical Journal*, 554, 1159
- Chieffi A., Limongi M., Straniero O., 1998, *Astrophysical Journal*, 502, 737
- Chiu H.-Y., Morrison P., 1960, *Physical Review Letters*, 5, 573
- Clayton D. D., 1983, *Principles of stellar evolution and nucleosynthesis*
- Couch R. G., Loumos G. L., 1974, *Astrophysical Journal*, 194, 385
- Couch S. M., Ott C. D., 2013, *Astrophysical Journal*, Letters, 778, L7
- Cox J. P., Giuli R. T., 1968, *Principles of stellar structure*

- Cyburt R. H., Amthor A. M., Ferguson R., Meisel Z., Smith K., Warren S., Heger A., Hoffman R. D., Rauscher T., Sakharuk A., Schatz H., Thielemann F. K., Wiescher M., 2010, *Astrophysical Journal, Supplement*, 189, 240
- de Jager C., Nieuwenhuijzen H., van der Hucht K. A., 1988, *Astronomy and Astrophysics Supplement Series*, 72, 259
- Denissenkov P. A., 2010, *Astrophysical Journal*, 723, 563
- Denissenkov P. A., Herwig F., Bildsten L., Paxton B., 2013, *Astrophysical Journal*, 762, 8
- Denissenkov P. A., Herwig F., Truran J. W., Paxton B., 2013, *Astrophysical Journal*, 772, 37
- Doherty C. L., Siess L., Lattanzio J. C., Gil-Pons P., 2010, *Monthly Notices of the RAS*, 401, 1453
- Doherty C. L., Gil-Pons P., Lau H. H. B., Lattanzio J. C., Siess L., 2014, *Monthly Notices of the RAS*, 437, 195
- Dominguez I., Chieffi A., Limongi M., Straniero O., 1999, *Astrophysical Journal*, 524, 226
- Eddington A. S., 1926, *The Internal Constitution of the Stars*
- Eggenberger P., Meynet G., Maeder A., Hirschi R., Charbonnel C., Talon S., Ekström S., 2008, *Astrophysics and Space Science*, 316, 43
- Eggleton P. P., 1971, *Monthly Notices of the RAS*, 151, 351
- Eldridge J. J., Tout C. A., 2004, *Monthly Notices of the RAS*, 353, 87
- Eldridge J. J., 2005, PhD thesis, PhD Thesis, University of Cambridge, 171 pages,
- Eldridge J. J., Mattila S., Smartt S. J., 2007, *Monthly Notices of the RAS*, 376, L52

Fischer T., 2014, in preparation

Fischer T., Whitehouse S. C., Mezzacappa A., Thielemann F.-K., Liebendörfer M., 2010, *Astronomy and Astrophysics*, 517, A80

Fowler W. A., Hoyle F., 1964, *Astrophysical Journal*, Supplement, 9, 201

Freytag B., Steffen M., Ludwig H.-G., Wedemeyer-Böhm S., Schaffenberger W., Steiner O., 2012, *Journal of Computational Physics*, 231, 919

Freytag B., Ludwig H.-G., Steffen M., 1996, *Astronomy and Astrophysics*, 313, 497

Frischknecht U., Hirschi R., Thielemann F.-K., 2012, *Astronomy and Astrophysics*, 538, L2

Fuller G. M., Fowler W. A., Newman M. J., 1980, *Astrophysical Journal*, Supplement, 42, 447

Fuller G. M., Fowler W. A., Newman M. J., 1982, *Astrophysical Journal*, 252, 715

Fuller G. M., Fowler W. A., Newman M. J., 1982, *Astrophysical Journal*, Supplement, 48, 279

Fuller G. M., Fowler W. A., Newman M. J., 1985, *Astrophysical Journal*, 293, 1

Fynbo H. O. U., Diget C. A., Bergmann U. C., Borge M. J. G., Cederkäll J., Dendooven P., Fraile L. M., Franchoo S., Fedosseev V. N., Fulton B. R., Huang W., Huikari J., Jeppesen H. B., Jokinen A. S., Jones P., Jonson B., Köster U., Langanke K., Meister M., Nilsson T., Nyman G., Prezado Y., Riisager K., Rinta-Antila S., Tengblad O., Turrion M., Wang Y., Weissman L., Wilhelmsen K., Äystö J., ISOLDE Collaboration, 2005, *Nature*, 433, 136

Gallino R., Arlandini C., Busso M., Lugaro M., Travaglio C., Straniero O., Chieffi A., Limongi M., 1998, *Astrophysical Journal*, 497, 388

Garcia-Berro E., Iben I., 1994, *Astrophysical Journal*, 434, 306

- Garcia-Berro E., Ritossa C., Iben, Jr. I., 1997, *Astrophysical Journal*, 485, 765
- Girardi L., Bressan A., Bertelli G., Chiosi C., 2000, *Astronomy and Astrophysics Supplement Series*, 141, 371
- Glebbeek E., Gaburov E., de Mink S. E., Pols O. R., Portegies Zwart S. F., 2009, *Astronomy and Astrophysics*, 497, 255
- Gutierrez J., Garcia-Berro E., Iben, Jr. I., Isern J., Labay J., Canal R., 1996, *Astrophysical Journal*, 459, 701
- Habets G. M. H. J., 1986, *Astronomy and Astrophysics*, 167, 61
- Hansen C. J., Primas F., Hartman H., Kratz K.-L., Wanajo S., Leibundgut B., Farouqi K., Hallmann O., Christlieb N., Nilsson H., 2012, *Astronomy and Astrophysics*, 545, A31
- Heger A., Woosley S. E., Martínez-Pinedo G., Langanke K., 2001, *Astrophysical Journal*, 560, 307
- Heger A., Fryer C. L., Woosley S. E., Langer N., Hartmann D. H., 2003, *Astrophysical Journal*, 591, 288
- Heger A., Langer N., Woosley S. E., 2000, *Astrophysical Journal*, 528, 368
- Herwig F., Austin S. M., 2004, *Astrophysical Journal, Letters*, 613, L73
- Herwig F., 2000, *Astronomy and Astrophysics*, 360, 952
- Herwig F., 2004, *Astrophysical Journal*, 605, 425
- Herwig F., 2005, *Annual Review of Astronomy and Astrophysics*, 43, 435
- Herwig F., Freytag B., Hueckstaedt R. M., Timmes F. X., 2006, *Astrophysical Journal*, 642, 1057

- Herwig F., Freytag B., Fuchs T., Hansen J. P., Hueckstaedt R. M., Porter D. H., Timmes F. X., Woodward P. R., 2007, in Kerschbaum F., Charbonnel C., Wing R. F., eds, *Why Galaxies Care About AGB Stars: Their Importance as Actors and Probes*, p. 43
- Herwig F., Pignatari M., Woodward P. R., Porter D. H., Rockefeller G., Fryer C. L., Bennett M., Hirschi R., 2011, *Astrophysical Journal*, 727, 89
- Herwig F., Vandenberg D. A., Navarro J. F., Ferguson J., Paxton B., 2012, *Astrophysical Journal*, 757, 132
- Hillebrandt W., Nomoto K., Wolff R. G., 1984, *Astronomy and Astrophysics*, 133, 175
- Hirata K., Kajita T., Koshiha M., Nakahata M., Oyama Y., 1987, *Physical Review Letters*, 58, 1490
- Hirschi R., Meynet G., Maeder A., 2004, *Astronomy and Astrophysics*, 425, 649
- Hofmeister E., Kippenhahn R., Weigert A., 1964, *Zeitschrift fuer Astrophysik*, 60, 57
- Hubbard W. B., Lampe M., 1969, *Astrophysical Journal, Supplement*, 18, 297
- Hurley J. R., Tout C. A., Wickramasinghe D. T., Ferrario L., Kiel P. D., 2010, *Monthly Notices of the RAS*, 402, 1437
- Hurley J. R., Pols O. R., Tout C. A., 2000, *Monthly Notices of the RAS*, 315, 543
- Iben, Jr. I., Livio M., 1993, *Publ. Astron. Soc. Pacific*, 105, 1373
- Iben, Jr. I., Renzini A., 1982, *Astrophysical Journal, Letters*, 259, L79
- Iben, Jr. I., Renzini A., 1983, *Annual Review of Astronomy and Astrophysics*, 21, 271
- Iben, Jr. I., 1975, *Astrophysical Journal*, 196, 525
- Iben, Jr. I., Ritossa C., Garcia-Berro E., 1997, *Astrophysical Journal*, 489, 772

- Ichimaru S., 1993, *Reviews of Modern Physics*, 65, 255
- Iglesias C. A., Rogers F. J., 1993, *Astrophysical Journal*, 412, 752
- Iglesias C. A., Rogers F. J., 1996, *Astrophysical Journal*, 464, 943
- Imbriani G., Costantini H., Formicola A., Bemmerer D., Bonetti R., Brogini C., Corvisiero P., Cruz J., Fülöp Z., Gervino G., Guglielmetti A., Gustavino C., Gyürky G., Jesus A. P., Junker M., Lemut A., Menegazzo R., Prati P., Roca V., Rolfs C., Romano M., Rossi Alvarez C., Schümann F., Somorjai E., Straniero O., Strieder F., Terrasi F., Trautvetter H. P., Vomiero A., Zavatarelli S., 2004, *Astronomy and Astrophysics*, 420, 625
- Ishimaru Y., Wanajo S., 1999, *Astrophysical Journal, Letters*, 511, L33
- Itoh N., Hayashi H., Nishikawa A., Kohyama Y., 1996, *Astrophysical Journal, Supplement*, 102, 411
- Itoh N., Tomizawa N., Tamamura M., Wanajo S., Nozawa S., 2002, *Astrophysical Journal*, 579, 380
- Janka H.-T., 2001, *Astronomy and Astrophysics*, 368, 527
- Janka H.-T., Müller B., Kitaura F. S., Buras R., 2008, *Astronomy and Astrophysics*, 485, 199
- Janka H.-T., Marek A., Mueller B., Scheck L., 2008b, *AIP Conf. Proc.*, 983, 369
- Janka H.-T., Hanke F., Huedepohl L., Marek A., Mueller B., Obergaulinger M., 2012, *ArXiv e-prints*, 1211.1378
- Jennings Z. G., Williams B. F., Murphy J. W., Dalcanton J. J., Gilbert K. M., Dolphin A. E., Fouesneau M., Weisz D. R., 2012, *Astrophysical Journal*, 761, 26
- Jones S., Hirschi R., Nomoto K., Fischer T., Timmes F. X., Herwig F., Paxton B., Toki H., Suzuki T., Martínez-Pinedo G., Lam Y. H., Bertolli M. G., 2013, *Astrophysical Journal*, 772, 150

- Juodagalvis A., Langanke K., Hix W. R., Martínez-Pinedo G., Sampaio J. M., 2010, Nuclear Physics A, 848, 454
- Käppeler F., Gallino R., Bisterzo S., Aoki W., 2011, Reviews of Modern Physics, 83, 157
- Karakas A. I., Lattanzio J. C., Pols O. R., 2002, Publ. Astron. Soc. Aust., 19, 515
- Kato S., 1966, Publications of the ASJ, 18, 374
- Kippenhahn R., Weigert A., 1990, Stellar Structure and Evolution
- Kippenhahn R., Thomas H. C., Weigert A., 1965, Zeitschrift fuer Astrophysik, 61, 241
- Kippenhahn R., Thomas H. C., Weigert A., 1966, Zeitschrift fuer Astrophysik, 64, 373
- Kitaura F. S., Janka H.-T., Hillebrandt W., 2006, Astronomy and Astrophysics, 450, 345
- Knigge C., Coe M. J., Podsiadlowski P., 2011, Nature, 479, 372
- Kohyama Y., Itoh N., Obama A., Mutoh H., 1993, Astrophysical Journal, 415, 267
- Krane K. S., 1987, Introductory Nuclear Physics
- Kunz R., Fey M., Jaeger M., Mayer A., Hammer J. W., Staudt G., Harissopulos S., Paradellis T., 2002, Astrophysical Journal, 567, 643
- Langanke K., Martínez-Pinedo G., 2000, Nuclear Physics A, 673, 481
- Langer N., Fricke K. J., Sugimoto D., 1983, Astronomy and Astrophysics, 126, 207
- Lau H. H. B., Gil-Pons P., Doherty C., Lattanzio J., 2012, Astronomy and Astrophysics, 542, A1
- Lau H. H. B., Stancliffe R. J., Tout C. A., 2009, Monthly Notices of the RAS, 396, 1046

- Lauterborn D., Refsdal S., Weigert A., 1971, *Astronomy and Astrophysics*, 10, 97
- Lesaffre P., Podsiadlowski P., Tout C. A., 2005, *Monthly Notices of the RAS*, 356, 131
- Lilley J. S., 2001, *Nuclear Physics: Principles and Applications*
- Limongi M., Straniero O., Chieffi A., 2000, *Astrophysical Journal, Supplement*, 129, 625
- Maeder A., Meynet G., 2001, *Astronomy and Astrophysics*, 373, 555
- Maeder A., 2009, *Physics, Formation and Evolution of Rotating Stars*
- Martínez-Pinedo G., Lam Y. H., Langanke K., Zegers R. G. T., Sullivan C., 2014, *ArXiv e-prints*, 1402.0793
- Martínez-Pinedo G., Langanke K., Dean D. J., 2000, *Astrophysical Journal, Supplement*, 126, 493
- Mattsson L., Höfner S., Herwig F., 2007, *Astronomy and Astrophysics*, 470, 339
- Meakin C. A., Arnett D., 2007, *Astrophysical Journal*, 667, 448
- Meyer B. S., 2002, *Physical Review Letters*, 89(23), 231101
- Meynet G., Ekstrom S., Maeder A., Eggenberger P., Saio H., Chomienne V., Haemmerlé L., 2013, *Lecture Notes in Physics*, Berlin Springer Verlag, 865, 3
- Miyaji S., Nomoto K., 1987, *Astrophysical Journal*, 318, 307
- Miyaji S., Nomoto K., Yokoi K., Sugimoto D., 1980, *Publications of the ASJ*, 32, 303
- Mocák M., Müller E., Weiss A., Kifonidis K., 2009, *Astronomy and Astrophysics*, 501, 659
- Mocák M., Meakin C. A., Müller E., Siess L., 2011, *Astrophysical Journal*, 743, 55
- Mueller B., Janka H.-T., Heger A., 2012, *ArXiv e-prints*, 1205.7078

- Ning H., Qian Y.-Z., Meyer B. S., 2007, *Astrophysical Journal, Letters*, 667, L159
- Nomoto K., Hashimoto M., 1988, *Physics Reports*, 163, 13
- Nomoto K., Kondo Y., 1991, *Astrophysical Journal, Letters*, 367, L19
- Nomoto K., 1984, *Astrophysical Journal*, 277, 791
- Nomoto K., 1987, *Astrophysical Journal*, 322, 206
- Nugis T., Lamers H. J. G. L. M., 2000, *Astronomy and Astrophysics*, 360, 227
- Oda T., Hino M., Muto K., Takahara M., Sato K., 1994, *Atomic Data and Nuclear Data Tables*, 56, 231
- Paczynski B., 1973, *Acta Astronomica*, 23, 1
- Paxton B., Bildsten L., Dotter A., Herwig F., Lesaffre P., Timmes F., 2011, *Astrophysical Journal, Supplement*, 192, 3
- Phillips A. C., 1999, *The Physics of Stars*, 2nd Edition
- Pignatari M., Gallino R., Heil M., Wiescher M., Käppeler F., Herwig F., Bisterzo S., 2010, *Astrophysical Journal*, 710, 1557
- Podsiadlowski P., Langer N., Poelarends A. J. T., Rappaport S., Heger A., Pfahl E., 2004, *Astrophysical Journal*, 612, 1044
- Poelarends A. J. T., Herwig F., Langer N., Heger A., 2008, *Astrophysical Journal*, 675, 614
- Pols O. R., Schröder K.-P., Hurley J. R., Tout C. A., Eggleton P. P., 1998, *Monthly Notices of the RAS*, 298, 525
- Potekhin A. Y., Chabrier G., 2010, *Contributions to Plasma Physics*, 50, 82
- Prialnik D., 2000, *An Introduction to the Theory of Stellar Structure and Evolution*

- Pumo M. L., Siess L., 2007, in Kerschbaum F., Charbonnel C., Wing R. F., eds, *Why Galaxies Care About AGB Stars: Their Importance as Actors and Probes*, p. 133
- Pumo M. L., Turatto M., Botticella M. T., Pastorello A., Valenti S., Zampieri L., Benetti S., Cappellaro E., Patat F., 2009, *Astrophysical Journal, Letters*, 705, L138
- Pumo M. L., Siess L., Zappalà R. A., 2007, *Mem. Societa Astronomica Italiana*, 78, 804
- Raiteri C. M., Gallino R., Busso M., Neuberger D., Kaeppeler F., 1993, *Astrophysical Journal*, 419, 207
- Reimers D., *Circumstellar envelopes and mass loss of red giant stars*, p. 229, 1975
- Richter W. A., Mkhize S., Brown B. A., 2008, *Physical Reviews C*, 78(6), 064302
- Riess A. G., Filippenko A. V., Challis P., Clocchiatti A., Diercks A., Garnavich P. M., Gilliland R. L., Hogan C. J., Jha S., Kirshner R. P., Leibundgut B., Phillips M. M., Reiss D., Schmidt B. P., Schommer R. A., Smith R. C., Spyromilio J., Stubbs C., Suntzeff N. B., Tonry J., 1998, *Astronomical Journal*, 116, 1009
- Ritossa C., Garcia-Berro E., Iben, Jr. I., 1996, *Astrophysical Journal*, 460, 489
- Ritossa C., García-Berro E., Iben, Jr. I., 1999, *Astrophysical Journal*, 515, 381
- Rogers F. J., Nayfonov A., 2002, *Astrophysical Journal*, 576, 1064
- Rosswog S., Korobkin O., Arcones A., Thielemann F.-K., Piran T., 2014, *Monthly Notices of the RAS*, 439, 744
- Salpeter E. E., 1955, *Astrophysical Journal*, 121, 161
- Sana H., de Mink S. E., de Koter A., Langer N., Evans C. J., Gieles M., Gosset E., Izzard R. G., Le Bouquin J.-B., Schneider F. R. N., 2012, *Science*, 337, 444

- Saumon D., Chabrier G., van Horn H. M., 1995, *Astrophysical Journal*, Supplement, 99, 713
- Schaller G., Schaerer D., Meynet G., Maeder A., 1992, *Astronomy and Astrophysics Supplement Series*, 96, 269
- Scheck L., Kifonidis K., Janka H.-T., Müller E., 2006, *Astronomy and Astrophysics*, 457, 963
- Schwab J., Podsiadlowski P., Rappaport S., 2010, *Astrophysical Journal*, 719, 722
- Seitzzahl I. R., Ciaraldi-Schoolmann F., Röpke F. K., Fink M., Hillebrandt W., Kromer M., Pakmor R., Ruiter A. J., Sim S. A., Taubenberger S., 2013, *Monthly Notices of the RAS*, 429, 1156
- Siess L., Pumo M. L., 2006, *Mem. Societa Astronomica Italiana*, 77, 822
- Siess L., 2006, *Astronomy and Astrophysics*, 448, 717
- Siess L., 2007, *Astronomy and Astrophysics*, 476, 893
- Siess L., 2009, *Astronomy and Astrophysics*, 497, 463
- Siess L., 2010, *Astronomy and Astrophysics*, 512, A10+
- Smartt S. J., 2009, *Annual Review of Astronomy and Astrophysics*, 47, 63
- Smartt S. J., Eldridge J. J., Crockett R. M., Maund J. R., 2009, *Monthly Notices of the RAS*, 395, 1409
- Smith N., 2013, *Monthly Notices of the RAS*, 434, 102
- Spruit H. C., 1992, *Astronomy and Astrophysics*, 253, 131
- Stancliffe R. J., Dearborn D. S. P., Lattanzio J. C., Heap S. A., Campbell S. W., 2011, *Astrophysical Journal*, 742, 121

- Stothers R. B., Chin C.-W., 1991, *Astrophysical Journal*, 374, 288
- Stothers R. B., Chin C.-W., 1995, *Astrophysical Journal*, 440, 297
- Strang E. J., Fernando H. J. S., 2001, *Journal of Fluid Mechanics*, 428, 349
- Sugimoto D., Nomoto K.-I., 1974, in Tayler R. J., Hesser J. E., eds, *Late Stages of Stellar Evolution*, p. 105
- Sugimoto D., 1970, *Progress of Theoretical Physics*, 44, 375
- Sweigart A. V., Gross P. G., 1978, *Astrophysical Journal, Supplement*, 36, 405
- Takahara M., Hino M., Oda T., Muto K., Wolters A. A., Glaudemans P. W. M., Sato K., 1989, *Nuclear Physics A*, 504, 167
- Takahashi K., Yoshida T., Umeda H., 2013, *Astrophysical Journal*, 771, 28
- Thielemann F. K., Arnett W. D., 1985, *Astrophysical Journal*, 295, 604
- Thorpe S. A., 1968, *Journal of Fluid Mechanics*, 32, 693
- Timmes F. X., Swesty F. D., 2000, *Astrophysical Journal, Supplement*, 126, 501
- Timmes F. X., Woosley S. E., 1992, *Astrophysical Journal*, 396, 649
- Timmes F. X., Woosley S. E., Taam R. E., 1994, *Astrophysical Journal*, 420, 348
- Timmes F. X., Woosley S. E., Weaver T. A., 1996, *Astrophysical Journal*, 457, 834
- Toki H., Suzuki T., Nomoto K., Jones S., Hirschi R., 2013, *Physical Reviews C*, 88(1), 015806
- Toonen S., Nelemans G., Portegies Zwart S., 2012, *Astronomy and Astrophysics*, 546, A70
- Tornambe A., Chieffi A., 1986, *Monthly Notices of the RAS*, 220, 529

- Trampedach R., Asplund M., Collet R., Nordlund Å., Stein R. F., 2013, *Astrophysical Journal*, 769, 18
- Traxler A., Garaud P., Stellmach S., 2011, *Astrophysical Journal, Letters*, 728, L29
- Turner J. S., 1986, *Journal of Fluid Mechanics*, 173, 431
- Ugliano M., Janka H.-T., Marek A., Arcones A., 2012, *Astrophysical Journal*, 757, 69
- Umeda H., Nomoto K., Yamaoka H., Wanajo S., 1999, *Astrophysical Journal*, 513, 861
- Unno W., 1967, *Publications of the ASJ*, 19, 140
- van Loon J. T., Cioni M.-R. L., Zijlstra A. A., Loup C., 2005, *Astronomy and Astrophysics*, 438, 273
- Ventura P., Zeppieri A., Mazzitelli I., D'Antona F., 1998, *Astronomy and Astrophysics*, 334, 953
- Vink J. S., de Koter A., Lamers H. J. G. L. M., 2001, *Astronomy and Astrophysics*, 369, 574
- Wagenhuber J., Weiss A., 1994, *Astronomy and Astrophysics*, 290, 807
- Wanajo S., Tamamura M., Itoh N., Nomoto K., Ishimaru Y., Beers T. C., Nozawa S., 2003, *Astrophysical Journal*, 593, 968
- Wanajo S., Nomoto K., Janka H.-T., Kitaura F. S., Müller B., 2009, *Astrophysical Journal*, 695, 208
- Wanajo S., Janka H.-T., Müller B., 2011, *Astrophysical Journal, Letters*, 726, L15
- Wanajo S., Janka H.-T., Müller B., 2013, *Astrophysical Journal, Letters*, 767, L26
- Wanajo S., Janka H.-T., Müller B., 2013, *Astrophysical Journal, Letters*, 774, L6
- Wildenthal B. H., 1984, *Progress in Particle and Nuclear Physics*, 11, 5

- Winteler C., Käppeli R., Perego A., Arcones A., Vasset N., Nishimura N., Liebendörfer M., Thielemann F.-K., 2012, *Astrophysical Journal, Letters*, 750, L22
- Wongwathanarat A., Janka H.-T., Müller E., 2010, *Astrophysical Journal, Letters*, 725, L106
- Wood P. R., Faulkner D. J., 1986, *Astrophysical Journal*, 307, 659
- Woosley S. E., Heger A., Weaver T. A., 2002, *Reviews of Modern Physics*, 74, 1015
- Woosley S. E., Heger A., Weaver T. A., 2002, *Reviews of Modern Physics*, 74, 1015
- Woosley S. E., Weaver T. A., Taam R. E., 1980, *Texas Workshop on Type I Supernovae*, 1, 96
- Xu H. Y., Li Y., 2004, *Astronomy and Astrophysics*, 418, 213
- Yakovlev D. G., Shalybkov D. A., 1989, *Astrophysics and Space Physics Reviews*, 7, 311
- Yakovlev D. G., Urpin V. A., 1980, *Soviet Astronomy*, 24, 303